Coupling a System Code with Computational Fluid Dynamics for the Simulation of Complex Coolant Reactivity Effects

Abstract

The current doctoral research is focused on the development and validation of a coupled computational tool, to combine the advantages of computational fluid dynamics (CFD) in analyzing complex flow fields and of state-of-the-art system codes employed for nuclear power plant (NPP) simulations. Such a tool can considerably enhance the analysis of NPP transient behavior, e.g. in the case of pressurized water reactor (PWR) accident scenarios such as Main Steam Line Break (MSLB) and boron dilution, in which strong coolant flow asymmetries and multi-dimensional mixing effects strongly influence the reactivity of the reactor core, as described in Chap. 1.

To start with, a literature review on code coupling is presented in Chap. 2, together with the corresponding ongoing projects in the international community. Special reference is made to the framework in which this research has been carried out, i.e. the Paul Scherrer Institute's (PSI) project STARS (Steady-state and Transient Analysis Research for the Swiss reactors). In particular, the codes chosen for the coupling, i.e. the CFD code ANSYS CFX V11.0 and the system code US-NRC TRACE V5.0, are part of the STARS codes system. Their main features are also described in Chap. 2.

The development of the coupled tool, named CFX/TRACE from the names of the two constitutive codes, has proven to be a complex and broad-based task, and therefore constraints had to be put on the target requirements, while keeping in mind a certain modularity to allow future extensions to be made with minimal efforts. After careful consideration, the coupling was defined to be on-line, parallel and with non-overlapping domains connected by an interface, which was developed through the Parallel Virtual Machines (PVM) software, as described in Chap. 3. Moreover, two numerical coupling schemes were implemented and tested: a sequential explicit scheme and a sequential semi-implicit scheme. Finally, it was decided that the coupling would be single-phase and isothermal, leaving to future work the extension to more complex cases. The development work itself is presented in Chap. 3, together with a generic consideration of code-coupling issues and the discussion of a few verification cases.

After the basic development and verification of the coupled tool, an experiment was devised for its initial validation. The employed experimental set-up, presented in Chap. 4, features a double T-junction, connected to a recirculation loop and instrumented with wire-mesh

sensors to measure the concentration of a tracer injected into the flow. The main aim of this experiment has been to challenge the coupled tool with the transport of a tracer in a steady-state flow field. The experimental results, the CFX and TRACE stand-alone simulations, and the CFX/TRACE coupled simulations are compared with each other for validation purposes, as well as for a clear demonstration of the improvements that one can achieve by using a coupled tool. The simulations, at the same time, indicated the occurrence of strong "numerical diffusion" effects in the TRACE simulations, these being found to result from weaknesses in the numerical discretization adopted in the code for the solute tracking equation.

Accordingly, as described in Chap. 5, a third-order upwind scheme for the numerical discretization, namely QUICKEST-ULTIMATE, has been implemented in TRACE to replace the original first-order upwind scheme. The mathematical derivation of the new scheme is presented, together with certain verification and validation tests. In particular, the improvements over the original TRACE scheme are shown in the context of the coupled CFX/TRACE simulations of the double T-junction experiment.

Finally, a second phase of experimental validation was devised for the coupling. To this end, certain qualification tests for the new FLORIS facility at PSI have been used, as presented in Chap. 6. This second facility features a scaled-down, simplified, two-dimensional vertical slice of a BWR vessel. The aim of this second mixing experiment has been, on the one hand, to challenge the momentum equation coupling in the context of the transport of a tracer in a transient flow field, and, on the other hand, to test the performance of the coupled tool for the case of a more complex geometry. Once again, comparisons have been made between experimental results, CFX and TRACE stand-alone simulations, and CFX/TRACE coupled simulations, employing the QUICKEST-ULTIMATE discretization where possible. As before, it is clearly demonstrated that the coupled tool yields much better results than the stand-alone codes. Furthermore, it has been found to be sufficiently robust for being extended to more advanced applications, such as the analysis of PWR transients in which strong reactivity feedback effects occur in the context of complex coolant flow phenomena.

Keywords: NPP transients, code coupling, system codes, CFD, coolant mixing, reactivity feedback, code validation, mixing experiments.

Riassunto

La presente ricerca di dottorato è incentrata sullo sviluppo e la validazione di un codice di calcolo accoppiato, con l'obiettivo di combinare i vantaggi della fluidodinamica computazionale (computational fluid dynamics, CFD) nell'analizzare i complessi campi di moto dei fluidi con i vantaggi dello stato dell'arte nei codici di sistema adottati nelle simulazioni delle centrali nucleari (nuclear power plants, NPP). Lo sviluppo di un simile strumento di calcolo può migliorare considerevolmente l'analisi dei transitori che possono aver luogo nelle NPP, tra cui alcuni scenari incidentali nei reattori ad acqua pressurizzata (pressurized water reactors, PWR), come ad esempio la rottura della conduttura principale del vapore (Main Steam Line Break, MSLB) o la diluizione involontaria del boro, durante i quali forti asimmetrie nel flusso del refrigerante ed effetti di miscelamento multidimensionali influenzano la reattività del nocciolo del reattore, come descritto nel Cap. 1.

In principio, nel Cap. 2 viene presentata una recensione sull'accoppiamento dei codici, comprensiva dei recenti progetti in corso nella comunità scientifica internazionale. Uno spazio speciale è dedicato al progetto quadro in cui è inserita questa ricerca, ovvero il progetto STARS (Steady-state and Transient Analysis Research for the Swiss reactors) all'Istituto Paul Scherrer (PSI). In particolare, i codici selezionati per l'accoppiamento, cioè il codice CFD ANSYS CFX V11.0 e il codice di sistema US-NRC TRACE V5.0, sono parte integrante del sistema di codici utilizzato in STARS. Le principali caratteristiche di questi codici sono anche esse descritte nel Cap. 2.

Lo sviluppo dello strumento computazionale accoppiato, chiamato CFX/TRACE dal nome dei due codici costituenti, si è rivelato essere un compito alquanto vasto e complesso, e pertanto alcuni limiti sono stati posti sulle specifiche richieste, pur tenendo in conto una certa modularità per rendere possibili future estensioni con sforzi ridotti. Dopo una attenta considerazione, l'accoppiamento scelto è state definito come *on-line*, parallelo e a domini non sovrapposti connessi da un'interfaccia, sviluppata tramite il software Parallel Virtual Machines (PVM), come descritto nel Cap. 3. Inoltre, due schemi numerici di accoppiamento sono stati implementati e utilizzati: uno schema sequenziale esplicito e uno schema sequenziale semi-implicito. Per concludere, è stato deciso di sviluppare un accoppiamento monofase e isotermo, lasciando al futuro l'estensione a casi più complessi. Il lavoro di sviluppo del codice è descritto nel Cap. 3, insieme ad alcune considerazioni generali sui problemi relativi all'accoppiamento di codici

ed alla discussione di alcuni casi per verifiche numeriche.

Dopo lo sviluppo e la verifica dello strumento di calcolo accoppiato, è stato definito un esperimento per la validazione iniziale del codice. L'apparato sperimentale utilizzato, mostrato nel Cap. 4, consiste in una giunzione a doppia T, connessa ad un circuito di ricircolo chiuso e dotata di sensori wire-mesh per la misura della concentrazione di un tracciante iniettato nel fluido del sistema. L'obiettivo principale dell'esperimento è stato quello di collaudare il codice accoppiato con il trasporto di un tracciante in condizioni di deflusso stazionario. I risultati sperimentali, insieme alle simulazioni indipendenti di CFX e TRACE, ed alle simulazioni accoppiate di CFX/TRACE, sono messi a confronto col proposito di validare il codice e di mostrare i chiari vantaggi che si hanno nell'utilizzo di un codice accoppiato. Nel contempo, le simulazioni hanno dimostrato una forte effetto di "diffusione numerica" nelle simulazioni di TRACE, dovute alle intrinseche debolezze della discretizzazione adottata nel codice per l'equazione di convezione del soluto.

Di conseguenza, come descritto nel Cap. 5, uno schema numerico upwind del terzo ordine, più precisamente QUICKEST-ULTIMATE, è stato implementato in TRACE per rimpiazzare lo schema originale del tipo upwind del primo ordine. Viene presentata la derivazione matematica del nuovo schema, complementata da alcuni test per la verifica e la validazione. In particolare, i miglioramenti rispetto allo schema originale presente in TRACE sono mostrati nel contesto delle simulazioni accoppiate CFX/TRACE dell'esperimento della giunzione a doppia T.

In conclusione, è stata organizzata una seconda fase di validazione sperimentale dell'accoppiamento. Per questo fine, sono stati utilizzati alcuni dei test di qualificazione del nuovo apparato sperimentale FLORIS al PSI, come descritto nel Cap. 6. Questo secondo esperimento consiste in una sezione verticale di un vessel BWR, opportunamente scalata e semplificata. L'obiettivo di questo secondo esperimento di miscelamento è, da un lato, di collaudare l'accoppiamento dell'equazione della quantità di moto nel contesto del trasporto di un tracciante in condizioni di deflusso transitorio, e, dall'altro lato, di mettere a prova l'efficienza dello strumento computazionale in caso di geometrie complesse. Ancora una volta, i risultati sperimentali, insieme alle simulazioni indipendenti di CFX e TRACE, ed alle simulazioni accoppiate di CFX/TRACE, sono messi a confronto, utilizzando la discretizzazione QUICKEST-ULTIMATE dove possibile. Come in precedenza, viene mostrato che lo strumento di calcolo accoppiato produce risultati molto migliori dei singoli codici usati separatamente. Inoltre, tale strumento si è dimostrato sufficientemente robusto da poter essere esteso ad applicazioni avanzate, come l'analisi di quei transitori nei PWR dove sono presenti forti effetti di feedback sulla reattività nel contesto di complessi fenomeni legati al deflusso del refrigerante.

Parole chiave: transitori NPP, accoppiamento di codici, codici di sistema, CFD, miscelamento del refrigerante, feedback di reattività, validazione di codici, esperimenti di miscelamento.

Contents

Nomenclature

Abbreviations

1D one-dimensional

2D two-dimensional

3D three-dimensional

ABWR Advanced Boiling Water Reactor

AGR Advanced Gas Reactors

ATWS Anticipated Transient Without Scram

BC Boundary Condition

BOC Beginning Of Cycle

BWR Boiling Water Reactor

CEL CFX Expression Language

CFD Computational Fluid Dynamics

CFL Courant-Friedrichs-Lewy

CVCS Chemical and Volume Control System

ECC Emergency Core Cooling

ENSI Eidgenössisches NuklearSicherheitsInspektorat

EOC End Of Cycle

EPR European Pressurized Reactor

ESBWR European Simplified Boiling Water Reactor

FBR Fast Breeder Reactor

GFR   Gas-cooled Fast Reactors

HPSI High Pressure Safety Injection

LBLOCA Large Break Loss-Of-Coolant Accident

LCFR Lead-Cooled Fast Reactors

LOCA Loss-Of-Coolant Accident

LPSI Low Pressure Safety Injection

LRS   Laboratory for Reactor physics and System behavior

LS   Loop Seal

LTH   Laboratory for ThermoHydraulics

LWR   Light Water Reactor

MMS   Memory Management System (of CFX)

MPI   Message Passing Interface

MSLB Main Steam Line Break

NPP   Nuclear Power Plant

OT   Operational Transient

PHWR Pressurized Heavy Water Reactor

PKL   PrimärKreisLauf

PSI   Paul Scherrer Institute

PVM   Parallel Virtual Machines

PWR   Pressurized Water Reactor

QUICKEST Quadratic Upwind Interpolation for Convective Kinematics with Estimated Streaming Terms

QUICK Quadratic Upwind Interpolation for Convective Kinematics

R&D   Research and Development

RANS Reynolds Averaged Navier-Stokes equations

RBMK Reaktor Bolshoy Moshchnosti Kanalniy (High Power Channel-type Reactor)

Re   Reynolds number

RPV   Reactor Pressure Vessel

RS   Reynolds Stress turbulence model

SBLOCA Small Break Loss-Of-Coolant Accident

SG   Steam Generator

SNAP   Symbolic Nuclear Analysis Package

SST   Shear Stress Transport turbulence model

STARS   Steady-state and Transient Anaysis Research for the Swiss reactors

TIM   Time Interpolation Modeling

TRACE   TRAC/RELAP Advanced Computational Engine

ULTIMATE Universal Limiter for Transient Interpolation Modeling of the Advective Transport Equation

VHTR   Very High Temperature Reactor

VVER   Vodo-Vodyanoi Energetichesky Reactor (Water-Water Energetics Reactor)

IAEA   International Atomic Energy Agency

IEA   International Energy Agency

Greek Letters

α void Fraction

Γ dimensionless diffusion coefficient

ε error on the pulse amplitude of the Gaussian distribution

Φ integral solute concentration (kg solute)

ϕ solute concentration (kg solute / m^3 liquid)

φ generic scalar function

μ mean of the Gaussian distribution

Ψ control surface

ρ density (kg/m^3)

σ standard deviation of the Gaussian distribution

τ dummy time variable used during integration

ϑ dimensionless mixing scalar

ξ conductivity (S/cm)

Ω control volume

Roman Letters

A cell flow area

B normalization coefficient of the Gaussian distribution

C Courant number

c solute concentration (kg_{solute}/kg_{liquid})

D diffusion coefficient

f generic function

K total number of side junctions for the considered cell

k k-th side junction for the considered cell

M wire-mesh sensor raw measured value (positive integer)

m m-th explicit time step inside the (semi-) implicit time step

$\mathbf{n}$ normal vector to the control surface

p pressure

q generic weight

S source term

t time coordinate

u velocity (m/s)

$\mathbf{u}$ velocity vector

V cell volume

W mass flow rate

w weight

X generic fluid variable

x space coordinate

$\mathbf{x}$ space coordinate vector

Subscripts

$_0$ lower value

$_1$ higher value

$_j$ index of the side junction connected cell

$_l$ liquid

$_n$ n-th time step

$_t$ time derivative $\partial/\partial t$

$_{tt}$ time derivative $\partial^2/\partial t^2$

$_x$ space derivative $\partial/\partial x$

$_{xx}$ space derivative $\partial^2/\partial x^2$

$_y$ space derivative $\partial/\partial y$

$_z$ space derivative $\partial/\partial z$

Superscripts

^{A} advection

^{D1} diffusion, 1st order

^{D2} diffusion, 2nd order

^{i} i-th cell

^{n} n-th time step

$^\sim$ time-averaged variable

Symbols

Δt temporal discretization

Δx spatial discretization

∇ gradient - in Cartesian coordinates, for $f(x, y, z)$: $\nabla f = (f_x, f_y, f_z)$

$\boldsymbol{\nabla}\cdot$ divergence - in Cartesian coordinates, for $\mathbf{u} = (u, v, w)$: $\boldsymbol{\nabla} \cdot \mathbf{u} = u_x + v_y + w_z$

$\boldsymbol{\nabla}\times$ curl - in Cartesian coordinates, for $\mathbf{u} = (u, v, w)$: $\boldsymbol{\nabla} \times \mathbf{u} = (w_y - v_z, u_z - w_x, v_x - u_y)$

Chapter 1

Introduction

In this opening chapter, the global scenario for nuclear energy is presented first (Sec. 1.1). Thereafter, certain basic notions are given concerning safety analyses for nuclear reactors (Sec. 1.2). Then, the most common type of nuclear power plant (NPP), the pressurized water reactor (PWR), is introduced (Sec. 1.3), followed by a brief description of two reference PWR accident scenarios that are fundamental for understanding the main motivation of the current research (Sec. 1.4). Later on, the thesis objectives are described (Sec. 1.5), followed by a presentation of its outline (Sec. 1.6).

1.1   Global nuclear energy scenario

1.1.1   Historical development

Following the start of the interest in nuclear power for civil purposes after World War II, the nuclear industry and related research made rapid progress. This culminated in the operation of the first commercial pressurized and boiling water reactor (PWR, BWR) units in 1960. At about the same time, other NPP types were also put in operation (gas-cooled, graphite-moderated, as also heavy-water moderated and cooled reactors). However, it is light water reactors, i.e. PWRs and BWRs, which have since then dominated the nuclear energy scene, as can be seen from the actual worldwide NPP fleet composition in Tab 1.1 [1].

From the late 1970s to about 2000, the nuclear power industry suffered some decline and stagnation, with the exception of a few Asian countries (Japan and Korea). Rising economic costs (related to extended construction times, largely due to regulatory changes and inflation) [3], public pressure from anti-nuclear groups (especially after the Three-Miles Island and Chernobyl accidents, in 1979 and 1986, respectively) and falling fossil fuel prices made nuclear power plants then under construction less attractive. More than two-thirds of all nuclear plants ordered after January 1970 were eventually cancelled [4]. In the 1980s (U.S.) and 1990s (Europe), flat load growth and electricity liberalization also made the addition of

Reactor type	Main Countries	Number	GWe[a]	Fuel	Coolant	Moderator
Pressurised Water Reactor (PWR)	US, France, Japan, Russia, China	265	251.6	enriched UO2	water	water
Boiling Water Reactor (BWR)	US, Japan, Sweden	94	86.4	enriched UO2	water	water
Pressurised Heavy Water Reactor "CANDU" (PHWR)	Canada	44	24.3	natural UO2	heavy water	heavy water
Gas-cooled Reactors (AGR & Magnox)	UK	18	10.8	natural U (metal), enriched UO2	carbon dioxide	graphite
Light Water Graphite Reactor (RBMK)	Russia	12	12.3	enriched UO2	water	graphite
Fast Breeder Reactor (FBR)	Japan, Russia	2	1.0	PuO2 and UO2	liquid sodium	none
Other	Russia	4	0.05	enriched UO2	water	graphite
Total		439	386.5			

[a]Gross capacity.

Table 1.1: Nuclear power plants in commercial operation in the year 2010 [1, 2].

large new baseload capacity unattractive. Few new reactors were ordered, while the number coming on line from the mid 1980s little more than matched retirements, though capacity increased by nearly one third and output increased by about 60% due to power uprates and improved load factors. The share of nuclear in world electricity from mid 1980s remained fairly constant at 16-17%. As mentioned, many reactor orders from the 1970s were cancelled. The uranium price dropped accordingly, also because of an increase in secondary supplies from dismissed nuclear warheads. Oil companies which had entered the uranium field bailed out, and there was a consolidation of uranium producers [1].

In the new century, several factors have combined to revive the prospects for nuclear power:

- the scale of projected increased electricity demand worldwide, particularly in rapidly developing countries;

- awareness of the importance of energy security, especially after many oil crises;

- the need to limit carbon emissions due to concern about global warming.

These factors coincide with the availability of a new generation of nuclear power reactors. By the late 1990s, the first of the so-called third-generation reactors was commissioned in Japan - a 1350 MWe Advanced BWR (ABWR). In 2004, another type of third-generation unit was ordered by Finland - a 1600 MWe European Pressurized Reactor (EPR). A similar NPP is being built in France, as the first unit of a full-fleet replacement there. In the USA, the 2005 Energy Policy Act provided incentives for establishing new-generation power reactors. Many European countries, other than France and Finland, are currently reviewing their nuclear policies and are getting ready for the construction of new reactors. China, India, Japan and South Korea are also raising their installed capacity. China alone plans a sixfold increase in nuclear power capacity by 2020, and has more than one hundred further large units proposed and backed by credible political determination and popular support (most of them are third-generation, western design). This is a clear sign of the world nuclear industry reprise, which is commonly referred to as "nuclear renaissance" [1].

In March 2011, following the Tohoku earthquake and tsunami in Japan, a severe accident took place at the Fukushima Daiichi nuclear site. Three out of the four units suffered meltdown, with a considerable release of radioactivity, thus giving the accident a rating of 7 on the INES scale. As a direct consequence of the accident, Germany immediately shut down several of its operating reactors and has decided to abandon its nuclear program totally by 2022; Switzerland has opted for a phase-out, canceling its new nuclear power plant projects; Italy has revoked its earlier intention to restart its nuclear program. With those exceptions, nuclear programs are continuing as planned in the rest of the world, but at a slowed-down pace, since a series of stress tests for existing nuclear power plants is being carried out and is likely to lead to new safety measures for new projects as well [1].

1.1.2 Facts and figures

At the end of 2008, there were 438 nuclear power reactors in operation worldwide, with an installed capacity of 372 GWe and a share of 14% of the global electricity demand; 44 new reactors were under construction (most of them in Asia) for an extra installed capacity of 39 GWe [5].

At least until the global financial crisis, growth targets for nuclear power were raised in many Countries (Russian Federation, China, Canada, USA, some European countries). Moreover, interest in starting new nuclear power programs have remained high. In the past years, many States have expressed, through requests to the International Atomic Energy Agency (IAEA) to participate in technical cooperation projects, their interest in considering the introduction of nuclear power [5]. Consequently, projections from international agencies and organizations foresee an overall increase in the installed nuclear capacity for the next century. However, the quantification of such an increase remains still subject to heavy uncertainties,

as can be evinced from the following projection figures:

- In 2008, the IAEA revised upwards its low and high projections for global growth in nuclear power. In the updated low projection, global nuclear power capacity reaches 473 GWe in 2030 (+27%), compared to a capacity of 372 GWe at the end of 2008. In the updated high projection, it reaches 748 GWe (+101%) [5].

- The Nuclear Energy Agency (NEA) developed two projection scenarios for nuclear electricity supply, showing that global installed nuclear capacity could increase from 372 GWe in 2008 to between 404 GWe (+9%) and 625 GWe (+68%) by 2030, and to between 580 GWe (+56%) and 1400 GWe (+276%) by 2050 [6].

- The International Energy Agency (IEA) reports that world nuclear capacity is projected to rise from 372 GWe to 397 GWe (+7%) by 2015 and to 433 GWe (+16%) by 2030 in their reference scenario. Two additional scenarios are considered, both focused on a stable concentration of greenhouse gases in the atmosphere. The 550 Policy Scenario foresees a stabilization of greenhouse gases around 550 ppm of equivalent CO_2, with a total installed nuclear energy capacity of 533 GWe (+43%) by 2030. The 450 Policy Scenario equates to a stabilization level of 450 ppm of equivalent CO_2 and an increased nuclear capacity of about 680 GWe (+83%) by 2030 [7].

It is important to note that all these projections were made before the financial crisis in late 2008 and, consequently, also before the Fukushima accident in 2011. At the time of writing, no new projections have been published, but it seems quite likely that these will be reduced. It is nevertheless important to underline, in these projections, the significant contribution that nuclear power is supposed to have in reducing carbon dioxide emissions in the coming century, now used as one of the major points to promote nuclear energy.

1.2   NPP transient analyses

As part of the safety assessment and licensing procedure for nuclear power plants, designers have to analyze systems response during a wide variety of accident scenarios[1] and transients such as Large and Small Break Loss Of Coolant Accidents (LOCAs), Operational Transients (OTs), Anticipated Transients Without Scram (ATWS), etc. For this purpose, specific computer codes are used to evaluate the time evolution of the thermal-hydraulic flow parameters in such scenarios; they can be grouped into two categories: system codes and Computational Fluid Dynamics (CFD) codes . However, while system codes are currently accepted as licensing tools, this is not the case for CFD codes.

---

[1] These are usually called Design Basis Accidents (DBAs), and are the set of accidents for which the designer needs to ensure that his design has adequate capability to deal with them, while remembering that specific, more severe accidents can occur. DBAs are usually those accidents which the regulatory body requires the designer to have analyzed in detail.

1.2.1 System codes

Different so-called, best-estimate system codes have been (and are still being) developed. In such codes, the partial differential equations (mass, momentum and energy balance equations) that describe the two-phase flow and the heat transfer are usually solved by finite differences based on one-dimensional approximations. Since the conservation equations are not by themselves a closed mathematical system, the thermal-hydraulic model is completed by a set of correlations and physical models (so-called closure relationships) which describe, among other things, the mass, energy, and momentum transfers at the interface between the gas and the liquid phase. Finally, the thermal-hydraulic model of a nuclear power plant is built by connecting one-dimensional modular components (pipes, tees, pumps, valves, heat structures, etc.) with each other.

Since many components with heterogeneous characteristics have to be modeled and connected, it is clear that the complexity of system codes is very high, and many physical and geometrical simplifications have to be made in order to obtain a solution within an acceptable time (or a solution at all, in case some knowledge of the phenomena involved is lacking).

Some of the existing best-estimate system codes (TRACE, CATHARE, RELAP-3D, etc.) (see, for example, [8]) also provide the capability to account for multi-dimensional flows, for instance in the reactor pressure vessel. However, the three-dimensional solution offered by system codes is based on an approximate formulation of the momentum balance equations (inviscid Eulerian). Thus, in the multi-dimensional solution provided by best-estimate system codes, turbulence is not resolved. In addition, because of the inviscid Eulerian approximation, the three-dimensional momentum balance equations are not able to model the evolution of a velocity profile along a pipe, since the wall-friction is distributed in the computational volumes by means of a sink term in the momentum balance, and shear between adjacent control volumes is not taken into account. This means, for example, that a flat velocity profile input in a three-dimensional component of a best-estimate code, such as TRACE or RELAP-3D, will remain flat. Therefore, even by making use of the 3D components available in best-estimate codes, in which the Reactor Pressure Vessel (RPV) is divided into a certain number of azimuthal sectors (typically 3 or 4), it is not possible to satisfactorily predict the flow streams in the downcomer and the mixing in the lower plenum, and this leads to unreliable predictions of the core inlet conditions and subsequent power response.

1.2.2 Computational fluid dynamics codes

CFD codes are based on the Navier-Stokes formulation of multi-dimensional flow, and turbulent exchange is fully taken into account. This means, for example, that the velocity profile mentioned above will evolve to the expected turbulent or laminar profile after a sufficient number of length-over-diameter ratios. In contrast to system codes, much finer meshes are needed for representing the component to be analyzed. Therefore, in view of the high computational

power required by CFD codes, only single components (or parts of a reactor component) have hitherto been analyzed. Furthermore, it is only in the context of single-phase mixing applications that CFD codes can be considered to have reached a satisfactory level of maturity for providing the complementary capability to system codes for accurately dealing with multi-dimensional flows.

1.3 Pressurized water reactors

As can be seen from Tab. 1.1, most of the world's nuclear reactor fleet is currently constituted by PWRs. While a full description of a nuclear power plant is beyond the scope of this work, some key elements related to this doctoral research will be presented here.

The standard PWR design is constituted by two coolant circuits (Fig. 1.1), in order to keep separated the core cooling fluid, slightly radioactive, from the conventional (non-nuclear) part of the plant. This separation also acts as a supplementary protective barrier against the release of radioactive material to the environment in the case of an accident. The main components of the primary loops are listed below:

- RPV, containing the reactor core with its fuel assemblies, where the heat is generated;

- pressurizer, which regulates the primary system pressure. The pressure in the primary coolant circuit is around 16 MPa to keep the cooling water single-phase at high temperatures (~ 300 °C);

- main reactor coolant pumps, to guarantee the mass flow in the primary loops (usually there are 2 or more loops connected to the RPV);

- steam generators (primary side), one for each loop, where heat is exchanged with the secondary circuit to generate steam for the turbines.
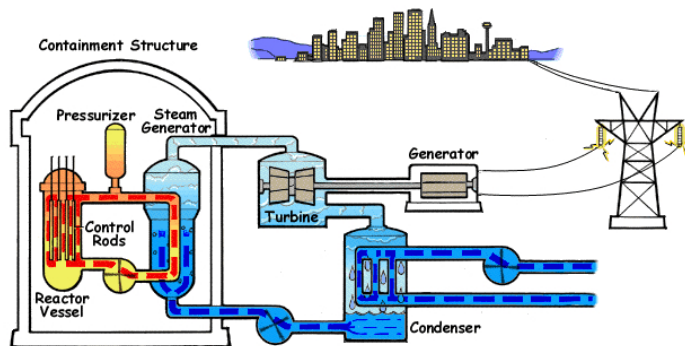

Figure 1.1: Simplified scheme of the power transfer in a pressurized water reactor. The primary coolant is in orange and the secondary coolant (steam and condenser feedwater) is in blue [9].

The main components of the secondary loops follow below:

- steam generators (secondary side), where the steam for the turbines is produced. Pressure is about 7 MPa;

- turbines (high and low pressure), to create mechanical energy from the steam; the mechanical energy is then conveyed to the generator to be transformed into electrical power and sent to the electricity grid;

- condenser, to condense the steam into water after it has passed through the turbines; water or air from the environment is used to cool the condenser (river, sea, cooling towers, etc.);

- pumps, to overcome the hydraulic resistance of the loop.

From among all the above described components, the RPV with its internals is one of the most important and complex components of the power plant; a vertical section of a generic PWR vessel is shown in Fig. 1.2. The water, coming from the cold legs of the primary loops, enters the vessel from the middle-top (inlet nozzles), and descends into an annular duct (the downcomer), where it partially mixes before reaching the lower plenum of the vessel (in which most of the mixing occurs). From there, it enters the core from below and provides cooling and moderation to the fuel bundles. The water then exits the core and collects into the upper plenum, where it leaves the vessel from outlet nozzles located in the upper part.

As a matter of fact, due to the geometrical complexity of the vessel, many secondary and bypass flows are present together with the main flow described above. Therefore, a simple one-dimensional approximation of its thermal-hydraulic behavior requires ad-hoc correlations and may give only very approximate results, especially in the case of an accident, where the flow conditions inside the vessel may largely differ from those under design conditions and where flow asymmetries could be expected. In such cases, a three-dimensional representation and analysis would give a more reliable representation of the complex flow that develops inside the vessel.

1.4 Relevant PWR transients for the current research

In PWRs, certain scenarios are foreseen in which strong asymmetries exist between the states of the coolant entering the RPV from the cold legs. Typically, these asymmetries are due to differences in temperature (for instance during a Main Steam Line Break) or boron concentration (boron dilution scenarios).

1.4.1 Main Steam Line Break

During a Main Steam Line Break (MSLB), it is supposed that the steam line connected to one of the steam generators breaks. The heat transfer of the reactor coolant in the loop
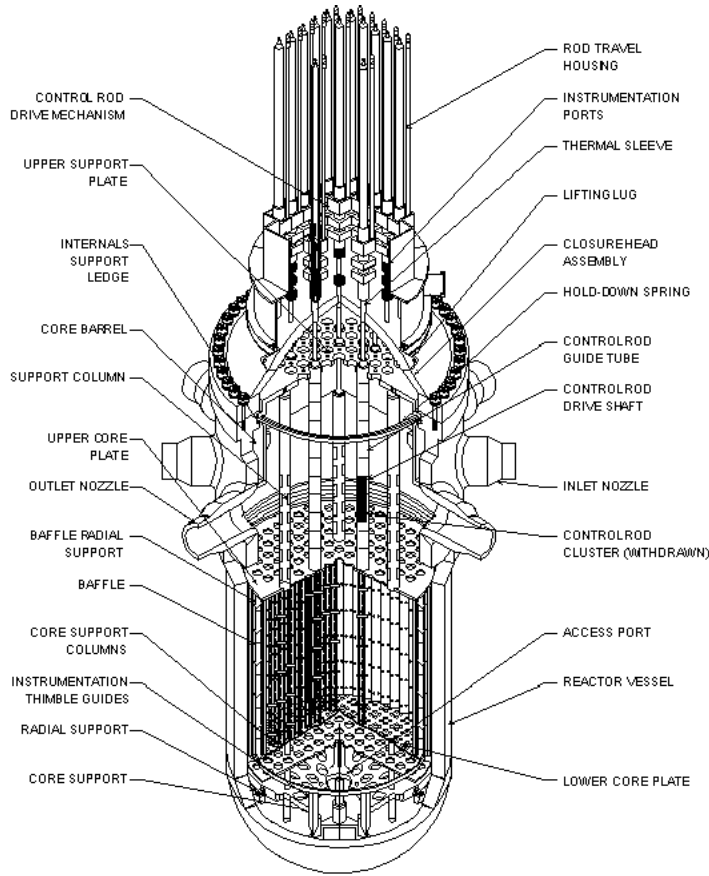
Figure 1.2: Vertical section of a PWR reactor vessel [10].

of the affected steam generator will thus be enhanced due to the increase of the coolant velocity on the secondary side. Consequently, the temperatures in the cold leg of the affected loop can become considerably lower than those in the intact loops. Depending on the flow mixing pattern in the downcomer and in the lower plenum, a strong overcooling of the reactor core might take place. The most severe consequences of such over cooling occur when the moderator temperature reactivity coefficient is strongly negative, and when fuel and coolant are at the same temperature. In this case, no heat is stored in the fuel elements. In view of these facts, MSLB scenarios are mostly severe at the End of Cycle (EOC) and under hot zero-power conditions (i.e. low fuel temperature), when the inventory in the steam generators is higher and a larger subcooling in the cold leg can take place.

Due to the strong asymmetry of the transient, a 3D neutron kinetics code is needed to evaluate the power response of the core. On the other hand, the neutron kinetics code needs a reliable time-dependent temperature distribution at the core inlet, which results from the coolant mixing taking place in the downcomer and in the lower plenum. Such mixing phenomena are strongly three-dimensional, and are influenced by turbulent motions. Therefore, one-dimensional approximations are unsuitable for this class of problem. As a

matter of fact, in order to apply 1-D thermal-hydraulic codes, one has to assume either full mixing, or no mixing at all, when no *a priori* information is available (for instance, from experiments). The first approach is unacceptable, being non-conservative, while the second approach can lead to excessive conservatism.

To take a specific example, Kliem and co-workers [11] have analyzed a MSLB transient for a VVER-440 reactor at EOC and hot zero-power conditions. They found that, if full flow mixing is assumed in the lower plenum, no recriticality of the core is predicted. On the other hand, assuming no mixing, recriticality and return to power were found to occur. The authors tried to achieve a better estimation of the transient consequences by off-line coupling with a CFD model of the reactor downcomer and lower plenum, with the conditions at the cold leg supplied to the CFD code (CFX-4 in this case) as boundary conditions. A stationary off-line CFD calculation was performed, and the temperature distribution at the core inlet was supplied to the system code (DYN3D) to calculate the resulting stationary power distribution. With the temperature distribution obtained by means of the CFD simulation, recriticality of the reactor core was again predicted, but the more realistic temperature distribution yielded a maximum power level 3.5 times lower than that with no mixing assumed. The three-dimensional reactivity feedback effects were very significantly influenced by the coolant mixing assumptions (Fig. 1.3). Thus, a strong asymmetric power response was found to result from the more realistic modeling of the core inlet temperature distribution during the MSLB.

This aforementioned study clearly points out the need for a direct coupling between CFD and system codes, so that the complex reactivity feedback effects which occur in a MSLB event can be reliably modeled.
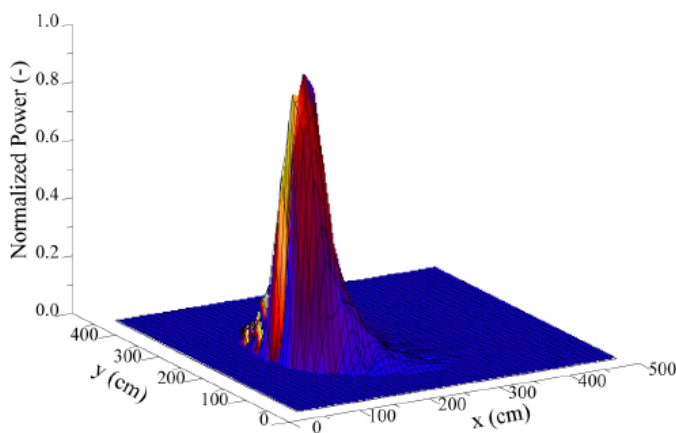

Figure 1.3: Normalized power distribution in the calculation with the CFD-based mixing model (after recriticality) [11].

1.4.2 Boron dilution scenarios

The control of the core reactivity in PWRs, especially at Beginning of Cycle (BOC), is largely achieved through soluble neutron absorbers (usually orthoboric acid) dissolved in the primary system. Boron acts as an effective neutron absorber, thus reducing the multiplication factor of the system. The Chemical and Volume Control System (CVCS) is used to control on-line the quantity of boron dissolved inside the primary loop. Such a reactivity control system can cause severe reactivity insertions if an undetected plug of (partially) unborated water crosses the core such as to cause the reactor to become supercritical. Such transients may then lead to high power excursions, threatening fuel integrity. Local power peaking can be an issue as well.

Such coolant transport can take place as a consequence of certain operational or accident scenarios (for instance, due to a malfunction of the CVCS), during the start-up of a reactor coolant pump or the reestablishment of natural circulation after accidental conditions. Mixing in the downcomer and in the lower plenum of the reactor pressure vessel serves as an inherent protection mechanism, distributing the deborated water more uniformly across the core entrance.

Following initial studies [12, 13] which confirmed the possibility of fuel rod failure due to such transients, more recent analyses [14, 15, 16, 17, 18] have identified and investigated a series of possible scenarios where the concentration of boron can drop substantially, or even become zero in certain stagnant zones of the primary loop. Moreover, the recent trend of increasing fuel cycle length by employing a higher initial excess reactivity relies on the use of higher boron concentrations in the primary loop in order to maintain criticality at the BOC. This clearly enhances the potential effect of diluted boron plugs traveling through the core, making such hypothetical accidents even more severe. Safety concerns have therefore prompted new studies focused on the accurate modeling of boron transport in nuclear systems, and boron dilution scenarios have recently become one of the most important issues in PWR safety [19, 20].

As an example, experiments at the PKL test facility in Germany have demonstrated that, in the case of a postulated Small Break LOCA (SBLOCA) with a reflux condensation cooling phase[2] (see Fig. 1.4), natural circulation does not start up simultaneously in all loops [21]. This means that slugs of condensate (with a lower boron concentration), which might have accumulated in the pump seal during the reflux-condenser mode of operation, would reach the RPV at different times. Experiments on mixing phenomena in model RPVs have also been performed at the Vattenfall test facility in Sweden [22], at the ROCOM facility in Germany

---

[2]During a SBLOCA in a PWR, the primary water level drops to the height of the hot/cold legs, where the break is located. Since steam generator pipes are located at a higher level, they are left without water and vapor flows through them from the vessel. Since the secondary loop is intact and working, it extracts heat from the primary system. By doing so, the vapor inside the steam generator pipes condenses on the pipe walls, and the water flows countercurrent to the vapor (hence, reflux) under the effect of gravity, towards the vessel. This phenomenon serves as an effective way of cooling the primary system under SBLOCA conditions.

[23], at the EDO Gidropress facility in Russia [24], and at the University of Maryland in the U.S.A. [25]. These experiments have shown that the complex flow in the downcomer and in the lower plenum promotes strong mixing in the coolant. However, local unmixed fluid regions are still present, and unmixed slugs arrive at different time instants at the core inlet [20].
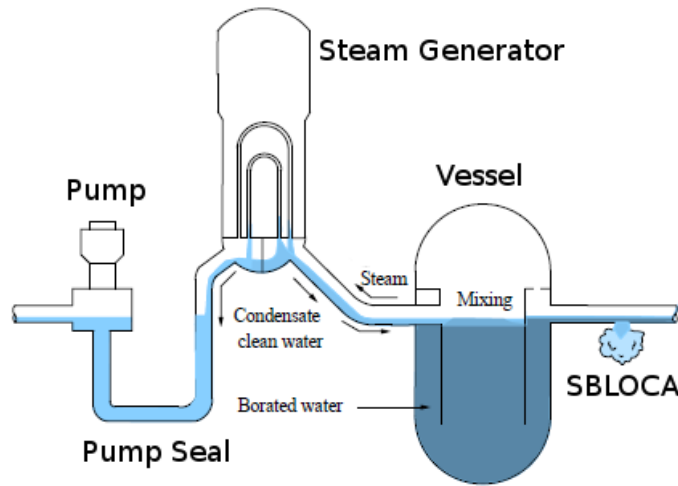
Figure 1.4: Reflux cooling during a SBLOCA [26]. Notice the accumulation of unborated water inside the pump seal.

On the one hand, computational fluid dynamics (CFD) codes have been employed for detailed analyses and have yielded good results in the reproduction of experimental data, also in complex geometries [14, 19, 27, 28]. However, their use is still limited to certain components of the primary loop, mainly the pressure vessel, because of the excessive computational costs and of the limitations in modeling two-phase flow transients. This leads to some arguable simplifications on the boundary conditions adopted, especially in transients where power excursions may affect the thermal-hydraulics (TH) of the full primary loop. The consideration of feedback effects from the entire plant becomes necessary in this case.

On the other hand, some thermal-hydraulics system codes (eventually coupled with core neutronics), while able to account for feedback effects covering the whole plant, are known to have relatively low accuracy when simulating the transport of a solute field because of high numerical diffusion [29]. Moreover, they are not able to provide a detailed treatment of complex geometries, where three-dimensional effects are dominant. This is a major obstacle in the accurate analysis of transients in which boron convection plays an important role [28].

In view of the above mentioned limitations, the off-line coupling between CFD and system codes becomes questionable, and a direct coupling is desirable.

1.5 Thesis objectives

In the light of the arguments presented in Secs. 1.2 and 1.4, a direct coupling between CFD and system codes is a most worthwhile endeavor for nuclear safety applications, especially when applied to the analysis of transients where three-dimensional flow effects play an important role for the consequences of a given accident scenario. This can bring a new quality of results of the analysis and improve the understanding of the coolant reactivity feedback phenomena which occur during MSLB and boron-dilution scenarios. Greater accuracy in determining the corresponding safety margins for PWR power plants can thus be expected.

In order to keep computational costs to a minimum, and at the same time not lose the accuracy of the solution, the concept proposed in this work is to couple a CFD and system code in such a way that only the downcomer and the lower plenum are fully modeled using CFD. The primary coolant loops, the core and the secondary side of the power plant all can be modeled with the system code, including a 3D representation of the neutron kinetics in the core (Fig. 1.5).

While the task of fully developing such a computational concept is very complex and, as such, too large for a single doctoral thesis, it is also quite modular, since the basic framework can be built in a relatively short time and more features can be added later on. Firstly, the range of applicability can be reduced. In particular, we will here deal with the CFD simulation of single-phase flows, the field of multiphase CFD simulations being very broad and still not sufficiently mature for safety applications. Secondly, for the sake of simplicity, the simulations will be limited to constant temperature (and therefore density) conditions. The possibility of convecting a scalar quantity will nevertheless be introduced, although the extension to non-isothermal cases will not be developed here. Thus, the main objective of the present research is to develop and validate a stable and flexible coupling between the computational fluid dynamics code ANSYS CFX V11.0SP1 and the U.S. NRC best-estimate system-code TRACE V5.0, while keeping in mind the above constraints.

Following a "divide and conquer" strategy, the aforementioned thesis goal can be divided into the typical stages of numerical methods development and validation, i.e. development of the code coupling itself, verification on the basis of numerical test cases and validation against experimental data. These three stages are listed below, along with the individual steps involved for each of them.

1. Development of the coupling schemes:

   (a) Choose the most suitable coupling schemes for the task at hand, starting from the existing literature.

   (b) Implement the chosen schemes as subroutines into the selected codes.

   (c) Evaluate possible coupling issues and devise the corresponding solutions.
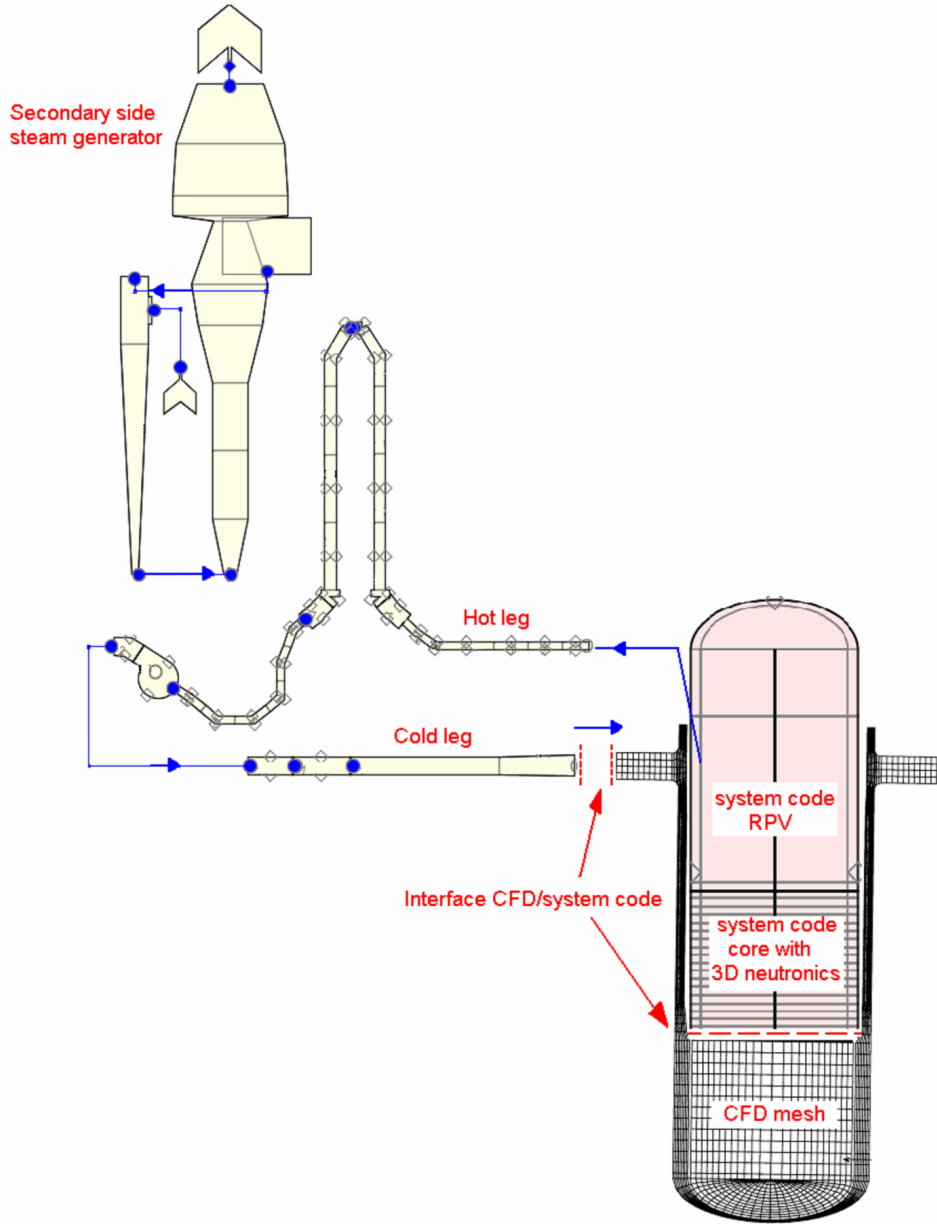
Figure 1.5: Conceptual scheme for the coupling between a system code and a CFD code.

   (d) Develop suitable optimization techniques where possible.

2. Verification of the coupling on the basis of numerical tests:

   (a) Define simple and easy-to-control numerical simulations to test the coupled tool.

   (b) Perform a sensitivity analysis to evaluate the effects of the coupling parameters and determine the parameters which are the most significant for the model; here particular attention has to be given to the interface between the codes and to eventual

numerical instabilities that may arise from the implemented coupling schemes.

(c) Compare the obtained results against stand-alone system code simulations of the same problems.

3. Validation of the coupling through experiments of increasing complexity:

   (a) Design experimental facilities suitable for the validation of the coupled code.

   (b) Assess the capability of the coupling to reach and correctly reproduce steady-state flow conditions.

   (c) Test the capacity of the coupled tool to correctly reproduce the convection of a tracer, thus challenging the coupling of the transport equation for a scalar.

   (d) Investigate the ability of the chosen coupling schemes to correctly reproduce transient flow conditions, thus challenging the coupling of the momentum equation.

   (e) Compare the results obtained from coupled-code simulations against experimental evidence, stand-alone system code results and stand-alone CFD results.

Apart from the above, the present research has involved the improvement of the numerical scheme for solving the solute tracking equation in the TRACE code. This has been achieved via implementation of a third-order upwind scheme, the principal aim being to improve calculation accuracy by reducing numerical diffusion problems identified during Stage 3. The individual tasks involved for the TRACE improvement are:

1. Describe the currently employed numerical scheme and its limitations.

2. Select a suitable non-diffusive scheme from the existing literature.

3. Implement the selected scheme inside TRACE.

4. Verify the newly implemented scheme in simple, controlled scenarios, comparing it against results obtained with the original scheme and against analytical solutions.

5. Validate the new scheme, eventually together with the coupled tool, against experimental results.

1.6 Thesis outline

The thesis outline corresponds to an appropriate linking of the various stages and tasks presented in Sec. 1.5, starting from a review of the state-of-the-art in thermal-hydraulic code-coupling development (Chap. 2), continuing to the development and verification of suitable coupling schemes (Chap. 3), and moving through three chapters on the validation experiments: Chaps. 4 and 6 on the experiment themselves, and Chap. 5 as the intervening improvement

of the TRACE solute tracker. The individual chapters, following the present one, are briefly described below.

Chapter 2 presents the current state-of-the-art in the field of thermal-hydraulic numerical simulations related to NPPs, with emphasis on the various attempts of code coupling carried out in the recent past.

A list of related experiments used for code validation is also provided, as is a brief overview of the project STARS at the Paul Scherrer Institute (PSI), in the framework of which the present work has been carried out. The chapter also describes the principal features of the two codes used in the present work.

Chapter 3 focuses on the development and verification of the TRACE/CFX coupled code, illustrating the issues encountered during the coupled tool development and the solutions adopted to overcome them.

Following an initial review of the available coupling strategies, justification is provided for the choice made for the present work. The developed coupled tool is verified on the basis of two numerical transient experiments: an open pipe simulation and a simple closed loop simulation, respectively.

Chapter 4 contains the validation of the TRACE/CFX coupled code against experimental data from a double-T junction experiment built at PSI. The experiment has been devised to challenge the coupled tool with the transport of a tracer under steady-state flow conditions. The experimental facility is described, and the data obtained from the experiment are presented. Then a comparison is made between experiments, TRACE stand-alone simulations, CFX stand-alone simulations and coupled CFX/TRACE simulations.

Chapter 5 is dedicated to the improvement made of the TRACE solute tracking algorithm. As mentioned earlier, modifications to this algorithm have been necessary in order to overcome the poor precision and the high numerical diffusion of the original upwind scheme adopted in the code.

The developed QUICKEST-ULTIMATE numerical scheme is presented, together with the adaptations to the topology of the TRACE code and a detailed treatment of the issues encountered. The new scheme is then verified via comparisons with simple analytical solutions and with the results from the original TRACE. The implementation is validated using the same experimental data as presented in Chap. 4, as also against certain experimental data from the PKL test facility in Germany.

Chapter 6 describes the validation of the CFX/TRACE coupled code against the FLORIS experiment, recently set up at PSI. With a geometry of greater complexity than the double

T-junction, this experiment is such as to challenge the coupling of the momentum equation with transient flow conditions, while convecting a tracer in the system.

The experimental facility is firstly described, together with the definition of a test matrix through preliminary, pre-test CFD stand-alone simulations. Thereafter, the experimental data are presented, together with comparisons against TRACE stand-alone simulations, CFX stand-alone simulations and coupled CFX/TRACE simulations.

Chapter 7 finally presents conclusions from the performed research, with certain recommendations being made for future work.

Chapter 2

State-of-the-art and codes used

This chapter describes the state-of-the-art in thermal-hydraulic code coupling, as also the two codes used in the present research. Sec. 2.1 deals with the current research and development (R&D) status, with emphasis on the development of coupled-code solutions (Subsec. 2.1.1) and on the design of experiments suitable for their validation (Subsec. 2.1.2). A brief overview of the project STARS at PSI, in the framework of which the present work has been carried out, is given in Subsec. 2.1.3. Sec. 2.2 presents the main characteristics of the codes employed in the development of the coupled tool, i.e. the system code TRACE and the CFD code ANSYS CFX.

2.1 R&D status

2.1.1 Development of coupled-code solutions

As mentioned in Chap. 1, the continuous evolution of available computational power and the increasing level of maturity attained by CFD codes are leading to a growing interest on the part of the nuclear safety community in CFD applications. Up to now, stand-alone CFD simulations have been carried out for a variety of nuclear safety applications, and it is expected that in the near future regulating authorities will demand more accurate evaluations involving CFD. At the same time, in view of the complexity of nuclear power plants and the impossibility of simulating the thermal-hydraulics of an entire plant with CFD codes (both because of the enormous computing power that would be required, and because of the inability of current-day CFD codes to deal with two-phase flows involving a wide range of void fractions), it is also recognized that the importance of system codes in the safety assessment of nuclear reactors will not decrease. The development of coupled solutions involving single-phase CFD and system codes is a logical step. Thus, several research groups have been trying to develop general approaches for the coupling of different types of codes, involving different modeling scales, and including two-phase flows. In the following, the various research activities being

carried out internationally in this context are described briefly:

- Idaho National Laboratory (INL) has started a project aimed at the coupling of its in-house code RELAP5-3D (system code derived from the 1D code RELAP5) with the commercial CFD code FLUENT. The main goals are the application to Very High Temperature Reactors (VHTRs), Gas-cooled Fast Reactors (GFRs), lead-cooled reactors, and liquid-sodium reactors, as well as to certain specific phenomena associated with advanced water-cooled reactors such as supercritical water reactors. The basic coupling of RELAP5-3D and FLUENT has in fact already been achieved [30, 31, 32]. Up till now, however, the coupling between the two codes has been limited to one-dimensional, single-phase pipe flows ignoring turbulence and three-dimensional aspects, i.e. only the numerics of the coupling has been studied and model inconsistencies have been ignored [33, 34].
Most recently, the coupled tool was applied to VHTR simulations at the Texas A&M University [35]. Unfortunately, the results could not be validated against experimental data, thus making this effort principally a verification exercise.

- Penn State University (group of Prof. Mahaffy) has coupled a simplified in-house 1D code with the 3D code NPHASE [36]. A simple demonstration test has been carried out for single-phase flow in pipe geometry. In this simple benchmark, they have shown that inconsistencies arise in the pressure distribution along the pipe if a flat velocity profile is supplied from the 1D code to the 3D code. The inconsistency disappears if a correct velocity profile is supplied, together with the average liquid velocity. The work has been unfortunately terminated at a rather preliminary stage.

- Under a program funded by DOE and EPRI, the project of the so-called Numerical Nuclear Reactor is being extended from PWRs to BWRs. Argonne National Lab, Purdue University and STAR-CD/Adapco are involved in the project [37]. The aim of the project is to couple 3D neutronics, system codes and CFD for application to two-phase flows. First contacts have been made between Idaho National Lab (Dr. Allison) and the Adapco company for a possible coupling between the CFD code STAR-CD and RELAP5 (personal communication by Adapco/STAR-CD staff). At the moment, the efforts are limited to stationary problems with coupled CFD/neutronics codes.

- Collaboration between CEA, EDF, FRAMATOME and IRSN in the framework of the NEPTUNE/DESCARTES projects has been initiated. The EU project NURESIM (6th EU Framework Program) and the follow-up project NURISP (7th EU Framework Program), currently on-going, in part support NEPTUNE. In the project, a coupling between different codes on a common platform is foreseen (system codes, 3D thermal-hydraulics based on a porous body approach, CFD codes, 3D neutron kinetics codes, Monte Carlo codes, Direct Numerical Simulation codes, etc.). Because of the highly

ambitious nature of the program, the full range of results is expected to be delivered only in the very long-term.

- Recently, AREVA has presented calculations of HTR reactors using the 3D neutronic code CRONOS2 (cross-sections supplied by APOLLO2) coupled to the CFD code STAR-CD [38].

- At KTH, in Stockholm, a brief review of the past coupling activities was done, together with a suggestion to use multiscale methods to solve the coupling issue [39].

- Some efforts have been made by ANSYS staff to develop a coupling between ANSYS CFX and the best-estimate system code ATHLET from the German regulatory authority (GRS) [40]; the project was temporarily suspended due to the lack of funds and has been recently resumed [41].

2.1.2   Experimental activities

Extensive experimental investigations have been performed with regard to coolant mixing in the downcomer of a PWR. These studies have been carried out with the aim of gaining more physical insight into the phenomenology of coolant mixing phenomena under various scenarios of interest for reactor safety, and also to provide an experimental data base for code validation. The database has been successfully used for the partial validation of CFD codes. In this chapter, the main experimental facilities are listed:

- Experimental investigations on coolant mixing in the RPV of a PWR have been carried out in the framework of the EU project FLOMIX-R [42, 43]. The experimental database established provides a solid basis for advanced codes validation. The experiments were performed at several different test facilities:

  - ROCOM (Rossendorf Coolant Mixing Model) models a German KONVOI type reactor, and consists of a four-loop test facility with a RPV mock-up made of transparent perspex on a linear scale of 1:5. Both boron and temperature distributions can be measured with high time and spatial resolution (more than 4000 measurement points and a measuring frequency up to 200 Hz).

  - The Vattenfall mixing test facility is a 1:5 scaled model of a Westinghouse PWR. Two loops are included in the model. Components that might be important for the mixing are also modeled (thermal shields, inlet pipe diffusers, structures in the lower plenum, core support plates and core). In total, data from 81 measurement points with a 60 Hz sampling frequency are available.

  - The EDO Gidropress test facility is a model of a Russian VVER-1000 reactor on a scale of 1:5. One loop, with a loop seal, and the reactor coolant pump are

modeled. The other three loops are short-circuited and only their pressure losses are simulated. The model of the core has 151 fuel assembly simulators, with the same pressure drop as regular fuel assemblies. About 100 thermocouples have been installed in the lower part of the downcomer and at the inlet of the core section to study the mixing flow.

– The FORTUM PTS test facility is a 1:2:56 scale model of the Loviisa VVER-440 reactor. The facility contains one half of the circumference of the reactor downcomer and includes three cold legs and the perforated plate in the lower plenum. In total, 62 thermocouples have been installed, most of them located in the downcomer to measure temperature fluctuations at the vessel wall.

- Additional experiments have been performed at the large scale test facilities PKL (PrimärKreisLauf) [44] and UPTF (Upper Plenum Test Facility) [45, 46]. These two facilities have been scaled on the basis of a 1300 MW PWR from Siemens-KWU:

  – The PKL test facility is built in scale 1:145 for volumes and 1:1 for heights, and models the entire primary system, relevant parts of the secondary side, and all important engineered safety and auxiliary systems. Each of the four coolant loops includes a fully scaled steam generator.

  – The UPTF facility consists of a full-scale upper plenum of the RPV, including original internals, the downcomer and the four connected coolant loops.

The two complementary facilities have been built by Siemens-KWU, in order to study the thermal-hydraulic behavior of a PWR under various accident conditions. Up to now, the UPTF experimental results on mixing behavior in the cold legs and in the RPV downcomer are the only ones that have been obtained with the original geometry. The tests carried out at the PKL test facility, in which boron dilution events occurring during SBLOCAs (in reflux-condenser mode and with restart of natural circulation) have been investigated, should be specially mentioned as well, considering the 1:1 scaling for heights of the facility.

- Experiments on coolant mixing have been performed at the B-MOV (Boron-Mixing Optical Vessel) test facility of the University of Maryland . The facility is scaled to 1:4 in length and 1:500 in volume with respect to the prototypical Babcock and Wilcox 2x4 lowered-loop PWR. All the four [25] cold legs are simulated. Additional experiments have been performed in the past at a second scaled integral facility, the University of Maryland 2x4 Thermal-hydraulic Loop Facility [47]. In total, 265 thermocouples were installed in the downcomer and lower plenum.

It has to be noted, however, that none of the experiments listed here were designed with the specific aim of validating system codes. They were mainly designed to validate CFD

codes, with the sole exceptions of PKL and UPTF. PKL has been used for the validation of one-dimensional system codes; UPTF was built to investigate three-dimensional effects experimentally, at a time when CFD analyses were not yet employed for nuclear applications. UPTF is since long closed, and the instrumentation employed was not detailed enough for advanced CFD validation; nevertheless, significant three-dimensional effects could be observed.

2.1.3 The project STARS at PSI

The present research has been carried out in the framework of the LRS[1] project STARS[2], whose main mission is to make available to both the Swiss nuclear regulatory authority (ENSI, former HSK) and the Swiss utilities a broad range of technical expertise related to the safety of nuclear systems [48]. The multi-physics aspects covered include neutronics, thermal-hydraulics, thermo-mechanical fuel behavior and plant behavior. Over the past 15 years, staff within the STARS project has provided expert services, to ENSI and the utilities, on all these aspects.

In order to fulfill the project mission, a comprehensive set of state-of-the-art computer codes has been assembled, covering core dynamics, system transients, LOCA analysis, sub-channel thermal-hydraulics and fuel transient behavior (Fig. 2.1). These codes have been subjected to an extensive program of assessment [49] and validation, in part achieved through participation in international benchmark and assessment programs. These activities have been complemented on some occasions with the development and implementation of improved code models, in collaboration with the code developers.

The constant need for better, more accurate quantification of NPPs safety margins demands increasingly more sophisticated, state-of-the-art safety analysis methods. For this reason, the introduction of a CFD capability, complementary to best-estimate system codes, is considered an important aspect of the project's overall strategy related to the safety analysis of NPPs [51]. In view of the growing level of maturity reached by CFD codes, and the high potential of such codes for applications to reactor safety, their introduction in the STARS code package constitutes a natural development. The complementarity of CFD and system codes will allow further improvement of the prediction of safety margins, with the potential of allowing more flexibility in plant operation.

In-depth experience on a wide range of NPP transients is available at LRS. Analyses of NPP behavior are performed by means of the coupled usage of best-estimate thermal-hydraulics and neutron kinetics codes. Thus, for example, specific experience on MSLB transients analyzed employing such a coupled approach has been already gained in LRS. MSLB scenarios have been simulated for the Beznau NPP (KKB-I) [52]. For such simulations, a thermal-hydraulic model of the complete plant was used, together with a 3D representation

---

[1]Laboratory for Reactor physics and Systems behavior.
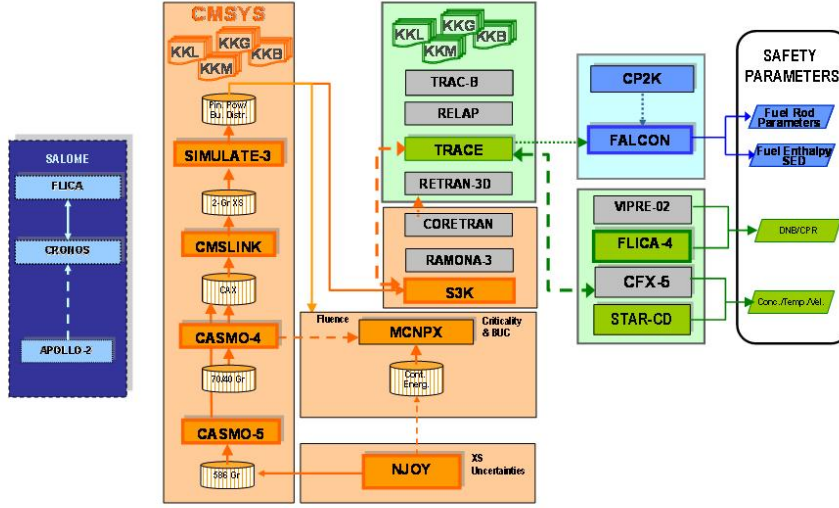[2]Steady-state and Transient Analysis Research for the Swiss reactors.

Figure 2.1: STARS codes system [50].

of the core neutronics. Different assumptions on coolant mixing in the lower plenum have been considered and their impact on the transient severity has been investigated, pointing out to the need for a better representation of the three-dimensional coolant mixing in the downcomer and lower plenum.

At PSI, LTH[3] has a long tradition in the study of single-phase mixing using CFD, both at the fundamental level, as part of PhD programs, and in terms of applied research, as part of ongoing projects. The study of mixing phenomena in Light Water Reactors (LWRs) has been pursued in the context of the European Framework Project FLOWMIX-R for the boron dilution experiments in the Vattenfall test facility [53], in the ECORA project [54], and as part of the analysis of experiments from the OECD/SETH series of tests carried out using the PANDA facility [55]. The laboratory's knowledge on CFD and experience on experimental facilities has been of primary importance in the design, construction and operation of the validation experiments presented in Chaps. 4 and 6.

2.2 Codes used for the coupled tool development

For the present creation of a coupled tool, the choice was restricted to the codes belonging to the STARS project. Therefore, the two codes chosen are the best-estimate system code TRACE V5.0 and the computational fluid dynamic code ANSYS CFX V11.0SP1.

---

[3]Laboratory for Thermal-Hydraulics

In order achieve the coupling, a certain degree of modification of the two source codes is necessary. The TRACE source code (in FORTRAN) is available at PSI through special agreements with US NRC, making it easily accessible and modifiable. ANSYS CFX is a commercial code and no source is delivered by the software vendor. However, some manipulation of the CFX code is possible through a user interface that is also based on FORTRAN. The flexibility of the available interface was found to be adequate for the development of the coupling capabilities of CFX with an external code.

2.2.1 TRACE

Quoting the code manual, TRACE "is the latest in a series of advanced, best-estimate reactor systems codes developed by the U.S. Nuclear Regulatory Commission for analyzing transient and steady-state neutronic-thermal-hydraulic behavior in light water reactors. It is the product of a long term effort to combine the capabilities of the NRC's main systems codes (TRAC-P, TRAC-B and RELAP5) into one modernized computational tool. [...] TRACE has been designed to perform best-estimate analyses of LOCAs, operational transients, and other accident scenarios in PWRs and BWRs. It can also model phenomena occurring in experimental facilities designed to simulate transients in reactor systems. The models used include multi-dimensional two-phase flow, nonequilibrium thermo-dynamics, generalized heat transfer, reflood, level tracking, and reactor point-kinetics" [8].

Governing equations

A full two-fluid (six-equations) hydrodynamic model evaluates gas-liquid flow, thereby allowing important phenomena such as countercurrent flow to be simulated explicitly. A stratified-flow regime has been added to the 1D hydrodynamics; a seventh field equation (mass balance) describes a non-condensable gas field; and an eighth field equation tracks dissolved solute in the liquid field that can be plated out on surfaces when solubility in the liquid is exceeded.

The thermal-hydraulic equations describe the transfer of mass, energy, and momentum between the steam-liquid phases and the interaction of these phases with heat flow from/to the modeled structures. Because these interactions are dependent on the flow topology, a constitutive-equation package dependent on the flow regime has been incorporated into the code. Assessment calculations performed to date indicate that most of the flow conditions can be accurately calculated with this package.

TRACE also performs detailed heat-transfer calculations between fluid and heat structures by including: 2D treatment of conduction heat transfer within metal structures, simulation of heat transfer characteristics of quench fronts, flow-regime-dependent heat transfer coefficients, inner-surface or outer-surface convective heat transfer, tabular or point-reactor kinetics with reactivity feedback, volumetric power sources. One-dimensional or three-dimensional reactor kinetics capabilities are possible through coupling with the Purdue Advanced Reactor Core

Simulator (PARCS) program.

Solution strategy

The partial differential equations that describe two-phase flow and heat transfer are solved using finite-volume numerical methods. The heat transfer equations are evaluated using a semi-implicit time-differencing technique. The fluid-dynamics equations in the spatial one-dimensional and three-dimensional components use, by default, a multi-step time-differencing procedure[4] that allows the Courant limit to be exceeded (App. A). The finite-volume equations for hydrodynamic phenomena form a system of coupled, nonlinear equations that are solved by the Newton-Raphson iteration method. The resulting linearized equations are solved by direct matrix inversion. For the one-dimensional network matrix, this is done by a direct full-matrix solver; for the three-dimensional component matrix, this is done by the capacitance-matrix method using a direct banded-matrix solver.

Component and functional modularity

TRACE takes a component-based approach to modeling a reactor system. Each physical piece of equipment in a flow loop can be represented as some type of component, and each component can be further nodalized into some number of physical volumes (also called cells) over which the fluid, conduction, and kinetics equations are averaged. The number of reactor components in the problem and the manner in which they are coupled is arbitrary. There is no built-in limit for the number of components or volumes that can be modeled; the size of a problem is theoretically only limited by the available computer memory.

Reactor hydraulic components in TRACE include pipes, plenums, pressurizers, BWR fuel channels, pumps, jet pumps, separators, tees, turbines, feedwater heaters, containment, valves, vessels with associated internals (downcomer, lower plenum, reactor core, and upper plenum). Special components are available as well for delivering energy to the fluid via the heat structures[5], hydraulic component walls or directly to the fluid (such as might happen with gamma heating of the coolant). Radiation enclosure components may be used to simulate radiation heat transfer between multiple arbitrary surfaces. Finally, "fill" and "break" components are used to impose flow and pressure boundary conditions, respectively.

The TRACE code is not only modular by component, but also by function, i.e. the major aspects of the calculations are performed in separate modules. For example, the basic 1D hydrodynamics solution algorithm, the wall-temperature field solution algorithm, heat transfer coefficient selection, and other functions are performed in separate sets of routines that can be accessed by all component modules. This modularity allows the code to be readily upgraded

---

[4] Known as stability-enhancing two-step (SETS) numerics [56].

[5] Heat structure components, to model fuel elements or heated walls in the reactor system, are available to compute two-dimensional conduction and surface-convection heat transfer in Cartesian or cylindrical geometries.

with minimal effort, and there is minimal potential for error as improved correlations and test information become available.

Control system

In NPPs, electronic and mechanical systems are put into place to give the operating staff either manual or automatic control over the system behavior. Parameters like temperatures, water levels, pressure, flow rates, and power can be measured and, using predetermined set points, controlled by the emulated electronics logic. Typical component actions include opening and closing valves, turning pumps on/off, and inserting or withdrawing control rods.

The TRACE control procedure is the means by which the code user is given the same level of control over his or her model as a reactor operator has over his or her real reactor system. By implementing the desired control logic, it also allows the user to model automatic control of regulating hardware, as well as abnormal hardware behavior, in a general and flexible way (Fig. 2.2).
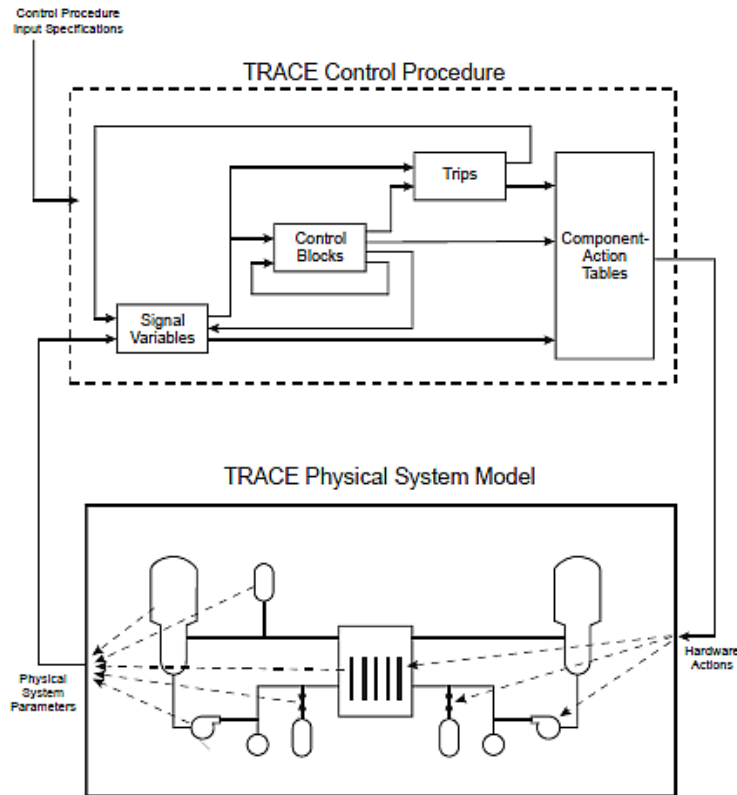

Figure 2.2: Conceptual structure of the TRACE control system and how it interacts with a system model [57].

Physical phenomena considered

The TRACE code can simulate the following physical phenomena:

1. Emergency Core Cooling (ECC) downcomer penetration and bypass, including the effects of counter-current flow and hot walls;

2. lower-plenum refill with entrainment and phase-separation effects;

3. bottom-reflood and falling-film quench fronts;

4. multi-dimensional flow patterns in the reactor-core and plenum regions;

5. pool formation and counter-current flow at the upper-core support-plate region;

6. pool formation in the upper plenum;

7. steam binding;

8. water level tracking,

9. average-rod and hot-rod cladding temperature histories;

10. alternate ECC injection systems, including hot-leg and upper-head injection;

11. direct injection of subcooled ECC water, without artificial mixing zones;

12. critical flow (choking);

13. liquid carryover during reflood;

14. metal-water reaction;

15. water-hammer pack and stretch effects;

16. wall friction losses, and reversible and irreversible form-loss flow effects on the pressure distribution;

17. horizontally stratified flow, including reflux cooling;

18. gas or liquid separator modeling;

19. noncondensable-gas effects on evaporation and condensation;

20. dissolved-solute tracking in liquid flow;

21. reactivity-feedback effects on reactor-core power kinetics;

22. two-phase bottom, side, and top offtake flow of a T-junction.

Limitations

As a general rule, system codes like TRACE are only applicable within their assessment range. In the present case, TRACE has been qualified to analyze the European Simplified Boiling Water Reactor (ESBWR) design, as well as conventional PWR and BWR large and small break LOCAs (excluding B&W designs). Assessment has not yet been officially performed for BWR stability analysis, or other operational transients.

Moreover, the TRACE code is not appropriate for modeling:

- situations in which transfer of momentum plays an important role at a localized level. For example, TRACE makes no attempt to capture, in detail, the fluid dynamics in a pipe branch or plenum, or flows in which the radial velocity profile across the pipe is not developed;

- transients in which there are large changing asymmetries in the reactor-core power (e.g. a control-rod-ejection transient) unless it is used in conjunction with the PARCS spatial kinetics module. In TRACE, the neutronics is evaluated on a core-wide basis by a point-reactor kinetics model with reactivity feedback, and the spatially local neutronic response associated with the ejection of a single control rod cannot be modeled;

- transients in which one expects to observe thermal stratification of the liquid phase in the 1D components. The "vessel" component can resolve the thermal stratification of liquid only within the modeling of its multi-dimensional noding when horizontal stratification is not perfect;

- scenarios where the viscous stresses are comparable to, or larger than, the wall (and/or interfacial, if applicable) shear stresses. The TRACE field equations have been derived assuming that viscous shear stresses are negligible (to a first-order approximation) and explicit turbulence modeling is not coupled to the conservation equations (although turbulence effects can be accounted for with specialized engineering models for specific situations). For example, TRACE is incapable of modeling circulation patterns within a large open region, regardless of the choice of mesh size;

- stress/strain effects of temperature gradients in structures. The effect of fuel-rod gas-gap closure due to thermal expansion or material swelling is not modeled explicitly. Nevertheless, TRACE can be useful as a support to other, more detailed, analysis tools in resolving questions such as pressurized thermal shock;

- scenarios where direct heating of the fluid due to viscosity effects occurs. The TRACE field equations are derived such that viscous heating terms within the fluid are generally ignored. A special model is, however, available within the "pump" component to account for direct heating of fluid by the pump rotor;

27

- phenomena such as collapse of a steam bubble blocking natural circulation through a Babcock & Wilcox "candy cane"[6], or of the details of steam condensation at the water surface in an AP1000 core-makeup tank. Approximations in the wall and interface heat flux terms prevent accurate calculations of such phenomena.

2.2.2 ANSYS CFX

According to the software documentation, ANSYS CFX (or CFX in short) "is a general purpose Computational Fluid Dynamics (CFD) software suite that combines an advanced solver for the Navier-Stokes equations with powerful pre- and post-processing capabilities" [58].

Governing equations

The set of equations solved by ANSYS CFX are the unsteady Navier-Stokes equations in their conservative form, properly closed by the fluid equations of state. Turbulence is treated with different degrees of detail, depending on the model chosen. Scalar transport equations are solved for velocity components, pressure, temperature and other quantities of the fluid. For a multi-component[7] fluid, moreover, additional equations must be solved to determine how the single components of the fluid are transported within the fluid itself. The bulk motion of the fluid is then modeled using single velocity, pressure, temperature and turbulence fields.

Solution strategy

The approach to solve the Navier-Stokes equations involves discretizing the spatial domain into finite control volumes using a mesh. The governing equations are then integrated over each control volume, such that the relevant quantity (mass, momentum, energy, etc.) is conserved in a discrete sense for each control volume. The discretized equations are then solved using a segregated solver[8] or a coupled solver. ANSYS CFX uses a coupled solver, which solves the hydrodynamic equations (for velocity and pressure) as a single system. This solution approach uses a fully-implicit discretization of the equations at any given time step. For steady-state problems, the time step behaves like an "acceleration parameter", to guide the approximate solutions in a physically based manner to a steady-state solution. This reduces

---

[6]Section of pipe carrying water from the reactor to a steam generator.

[7]ANSYS CFX has the capability to model fluid mixtures consisting of an arbitrary number of separate physical components (or "species"). Each component fluid may have a distinct set of physical properties. The ANSYS CFX solver will calculate appropriate average values of the properties for each control volume in the flow domain, for use in calculating the fluid flow. These average values will depend both on component property values and on the proportion of each component present in the control volume.

[8]Segregated solvers employ a solution strategy in which the momentum equations are first solved, using a guessed pressure, and an equation for a pressure correction is obtained. Because of the "predict-and-correct" nature of the linear system, a large number of iterations are typically required, in addition to the need for judiciously selecting relaxation parameters for the variables.

the number of iterations required for convergence to a steady state, or to calculate the solution for each time step in a time-dependent analysis.

Turbulence models

Turbulence consists of fluctuations in the flow field in time and space. It is a three-dimensional, unsteady process which consists of many scales. It can have a significant effect on the characteristics of the flow. Turbulence occurs when the inertia forces in the fluid become significant compared to viscous forces, and is characterized by a high Reynolds number. In principle, the Navier-Stokes equations describe both laminar and turbulent flows without the need for additional information. However, turbulent flows at realistic Reynolds numbers span a large range of turbulent length and time scales, and would generally involve length scales much smaller than the smallest finite-volume mesh which can be practically used in a numerical analysis. The so-called Direct Numerical Simulation (DNS) of these flows would require computing power which is many orders of magnitude higher than that which will be available in the foreseeable future. Therefore, a large amount of CFD research has concentrated on methods which make use of turbulence models, to enable the effects of turbulence to be predicted without recourse to a prohibitively fine mesh.

Most turbulence models - with the exceptions of the Large Eddy Simulation (LES) model and the Detached Eddy Simulation (DES) model for ANSYS CFX - are statistical. As a matter of fact, when looking at time scales much larger than those of turbulent fluctuations, turbulent flow could be said to exhibit average characteristics, with an additional time-varying, fluctuating component. For example, a velocity component may be divided into an average component and a time varying component. In general, turbulence models seek to modify the original unsteady Navier-Stokes equations by the introduction of averaged and fluctuating quantities to produce the Reynolds Averaged Navier-Stokes (RANS) equations. These equations represent the mean flow quantities only, while modeling turbulence effects without a need for the resolution of the turbulent fluctuations; all scales of the turbulence field are being modeled. Turbulence models based on the RANS equations are therefore known as statistical turbulence models due to the statistical averaging procedure employed to obtain the equations. The solution of the RANS equations greatly reduces the computational effort compared to a DNS and is generally adopted for practical engineering calculations. However, the averaging procedure introduces additional unknown terms containing products of the fluctuating quantities, which act like additional stresses in the fluid. These terms, called Reynolds (or turbulent) stresses, are difficult to determine directly and so become further unknowns. Thus, Reynolds stresses need to be modeled by additional equations of known quantities in order to achieve closure of the equation system; such equations define the type of turbulence model.

Closure of the RANS equations is hence realized by providing models for the computation

of Reynolds stresses and Reynolds fluxes. Models adopted by ANSYS CFX can be broadly divided into two classes:

- Eddy Viscosity (EV) models assume that turbulence consists of small eddies which are continuously forming and dissipating, and in which the Reynolds stresses are assumed to be proportional to mean velocity gradients, in a manner analogous to the relationship between the stress and strain tensors in laminar Newtonian flow. Within this approximation, two-equation turbulence models are widely used, as they offer a good compromise between numerical effort and computational accuracy. Both the velocity and length scales are solved, using separate transport equations (hence the term "two-equation"). The $\kappa - \varepsilon$ and $\kappa - \omega$ models, and their derivative models (e.g. the SST[9] model), fall in this category.

- Reynolds Stress (RS) models are based on transport equations for all components of the Reynolds stress tensor and the dissipation rate. The exact production term and the inherent modeling of stress anisotropies theoretically make Reynolds Stress models more suited to complex flows; however, practice shows that they are often not superior to two-equation models.

Program structure

The structure of ANSYS CFX consists, as for many other commercial CFD codes, of three stages. Each stage is executed with one or more specific software modules (Fig. 2.3); a more detailed description of the three stages follows.

Pre-processing

The objectives of this interactive process are:

- geometry and mesh creation, for input to the physics pre-processor. The geometry of the problem and the mesh of control volumes can be produced in any of the many geometry/mesh creation tools (e.g. ICEM). The basic steps involve: defining the geometry of the region of interest; creating regions of fluid flow, solid regions and surface boundary names; setting properties for the mesh;

- model physics definition, to create input required by the solver. The basic steps are: loading of the mesh into the physics pre-processor; selection of the physical models that are to be included in the simulation; specification of the fluid properties and boundary conditions.
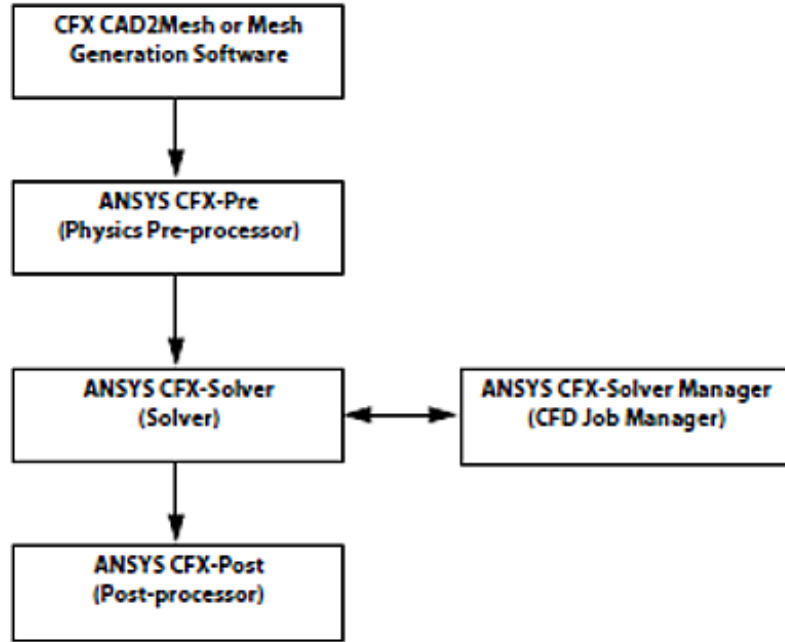
---

[9]Shear Stress Transport.

Figure 2.3: Software modules of ANSYS CFX [58].

Solving

This non-interactive process produces the required results. A CFD problem is solved as follows:

- The partial differential equations are integrated over all the control volumes in the region of interest. This is equivalent to applying a basic conservation law (for example, for mass or momentum) to each control volume.

- These integral equations are converted to a system of algebraic equations by generating a set of approximations for the terms in the integral equations.

- The algebraic equations are solved iteratively. An iterative approach is required because of the nonlinear nature of the equations and, as the solution approaches the exact solution, it is said to converge. For each iteration, an error, or residual, is reported as a measure of the overall conservation of the flow properties. How close the final solution is to the exact solution depends on a number of factors, including the size and shape of the control volumes and the size of the final residuals. The approximated or empirical modeling of complex physical processes contributes to differences between the CFD solution and the real flow.

Post-processing

This process, usually supported by proprietary tools, is used to analyze, visualize and present the results interactively. Post-processing includes anything from obtaining point values to

complex animated sequences.

In addition, some manipulation of the CFX code (commercial and closed-source) is possible through a User FORTRAN Interface, consisting of a set of user-defined subroutines[10] that are linked as shared libraries during runtime. These subroutines allow the user to access the Memory Management System (MMS) of the code, thus giving a very fine control over the simulation and allowing the introduction of almost any external user-made code.

Physical phenomena considered

ANSYS CFX is capable of modeling:

1. steady-state and transient flows;

2. laminar and turbulent flows;

3. subsonic, transonic and supersonic flows;

4. heat transfer and thermal radiation;

5. buoyancy;

6. non-Newtonian flows;

7. transport of non-reacting scalar components;

8. multiphase flows;

9. combustion;

10. flows in multiple frames of reference;

11. particle tracking.

Limitations

One important limitation of CFD modeling is the computing power required to conduct very precise simulations. This limits the size of the computational domain and requires the

---

[10] The CFX subroutines are divided into two types (for more details, refer to [58]):

1. User Junction Box Routines: they can be called at specific pre-defined points during the solver execution, and grant full access to the control of the program. They represent the core component for the coupling.

2. User CEL Functions: they can be called during the solver execution and accept user-defined parameters. They have more or less the same capabilities as the junction box routines, but they are employed to define the boundary conditions.

introduction of models to resolve, for example, turbulence, thus introducing uncertainties and loss of details in the results.

Moreover, in CFD codes, the treatment of multiphase flows is still under research and development. The two-fluid formulation, based on the so-called interpenetrating-media approach, is the most commonly used in current-day codes [59]. With this model, the characteristics of the interfaces between the fluids (i.e. their exact shape and position) are "lost", even if the presence of the interfaces has been considered during the local averaging process. While the absence of topological information about the interfaces is not a shortcoming in many two-phase flow problems, there are situations where the two phases are sharply separated (on a large scale, such as the scale of the channel) and full understanding of the situation requires knowledge of the position and geometry of the interface. In such cases, the implementation of interface tracking and reconstruction methods is necessary to properly resolve the physics of the system without resorting to DNS [59]. These methods are currently under investigation and not yet sufficiently developed for NPP applications.

2.3 Chapter summary

Efforts towards coupling CFD and system codes are being made worldwide, but a systematical approach has still been lacking. While many experiments of varying complexity are being analyzed with either system codes or CFD codes (mostly with the aim to validate such codes), to date coupled-code solutions are mostly being verified on a purely numerical basis. In view of the potential use of such coupled codes for NPP safety analyses, and therefore in view of the corresponding high-quality requirements, it is necessary to establish a proper coupled-code methodology which has been validated against experimental evidence.

Such an approach is clearly of utmost importance to the project STARS, in the framework of which this thesis has been developed, the principal STARS goal being to provide reliable in-depth analyses of the phenomena occurring during safety-relevant transients in the Swiss NPPs. It is with this background that the codes chosen for carrying out the aforementioned coupling are the system code TRACE and the CFD code ANSYS CFX, both of which are used in STARS and have been found to be quite suitable for the present purpose. The development, verification and validation of the new coupled tool will be described in the following chapters.

Chapter 3

CFX/TRACE coupling development and verification

The present chapter is essentially divided into two parts. In the first part (Secs. 3.1 and 3.2), the strategy adopted for the coupling[1] between the thermal-hydraulic system code TRACE and the CFD tool ANSYS CFX is discussed, together with the theoretical and implementation challenges that had to be faced during the development work. The techniques that have been developed and applied to overcome such issues are described as well.

In the second part of the chapter (Secs. 3.3 and 3.4), the results of numerical tests employed to verify the adopted coupling schemes are presented. In particular, Sec. 3.3 describes an open-loop test configuration and Sec. 3.4 describes a closed-loop test configuration.

3.1 Coupling strategy

As mentioned earlier, considerable efforts have been dedicated during the past decade to the development of coupling schemes between thermal-hydraulic system codes and CFD [30, 31, 33, 34, 36, 39, 40]. However, a certain lack of systematization and consistent classification of the coupling approaches is still noticeable in the literature. Moreover, few attempts have been made to improve and standardize the coupling procedures, for example with reference to the coupling between thermal-hydraulic system codes and 3D neutron kinetics [60].

The coupling between two codes can be classified according to:

- code execution (off-line and on-line coupling) - Subsec. 3.1.1;

- code interface (serial integration and parallel processing algorithms) - Subsec. 3.1.2;

---

[1]With *coupling* is here implied the technique necessary to make the *coupled* codes work in synergy, usually to exploit the advantages of the individual codes employed. In such a way, it may become possible to treat more aspects of a given problem, or alternatively to cover reciprocally the deficiencies of each of the individual codes employed to study such a problem.

- spatial domain of the system to be modeled (overlapping and non-overlapping domains) - Subsec. 3.1.3;

- numerical scheme (sequential and parallel schemes; explicit, semi-implicit and implicit schemes) - Subsec. 3.2.3.

In the following subsections, the different issues are addressed separately, and the motivation behind each chosen alternative is discussed.

3.1.1 Code execution

An important generic distinction is between off-line and on-line coupling schemes:

- In an **off-line coupling**, the codes are run independently and sequentially in their own problem domains. Results from one code are used as an educated guess to impose improved boundary conditions and/or fluid properties on the other code. For example, a thermal-hydraulic system code might be employed to calculate a plant transient scenario, and its results would then be used as input for a CFD code, to calculate the evolution of the transient in a limited region of the plant (e.g. the reactor pressure vessel). This coupling strategy is actually the simplest one to adopt, since it does not need any modification of the codes. This type of approach, however, has the disadvantage of lacking the provision of feedback from the second code to the first one, and has therefore a limited applicability.

- In an **on-line coupling** strategy, the codes run concurrently (in parallel or sequentially, as described later in this chapter), with a continuous exchange of information. In such a way, one code feeds information back to the other system and *vice versa*. This allows a better representation of the given plant transient scenario.

The coupled code developed currently is based on the on-line coupling approach.

3.1.2 Code interface for on-line coupling

In developing a coupled tool based on the on-line coupling approach, an interface between the two codes to be coupled has to be developed. The scope of such an interface is to allow the needed variables and data of one code to be transferred to the other code[2], and *vice versa*. While this at first sight may look straightforward, an in-depth knowledge of the numerics and internal structure of the codes to be coupled is required, in order to retrieve the correct data and feed them at the correct location within the code structure. Moreover, each code has its own way of managing information (i.e. data structures), and data manipulation is

---

[2]Since in the present work the coupling is between TRACE and ANSYS CFX, the descriptions are shaped around the presence of two codes; nevertheless, most of what is here described is valid also if three or more codes are involved in the process.

often necessary before transferring data from one code to the other. Special care has to be taken to maintain coherence in the results of the two codes, and consequently in the coupled simulation.

The different approaches to develop such an interface are usually of two kinds:

- A **serial integration algorithm** can be developed, thus integrating one code into the other (both codes are merged and compiled together). The interface is internal to the resulting coupled-code. This approach is usually more efficient and allows one to employ more complex numerical schemes, but it requires major modifications to the source of each code involved in the coupling.

- A so-called **parallel processing algorithm** [60] can be adopted, in which a dynamic data exchange routine between the two codes is established. This solution is relatively easy to implement, since viable code-interface options already exist (PVM[3] or MPI[4]) and only limited modifications to the source of each individual code are needed. It should be noted that the interface may act as bottleneck for the overall performance of the coupled tool.

In the specific case treated here, the latter option has been chosen. Thus, the information exchange between ANSYS CFX and TRACE is realized by means of the PVM[5] software. When two programs are coupled through a third one (the interface), the latter creates an environment in the system memory within which the other two codes are executed. In such an environment, a common terminology is to define one of the two codes as the "master", which bears the task of directing the information exchange with the other code, defined as the "slave".

An alternative to the use of PVM or MPI would consist in compiling the TRACE code as an external library, to be called within a CFX user-defined subroutine. This approach is in between the ones described here; however, it would require more modifications to the source and to the compilation scripts of the TRACE code, and therefore a PVM interface is hereby preferred.

3.1.3   Spatial domains

In order to perform the simulation of a system by means of a coupled code, the system is first divided into computational domains, which are then assigned to the individual codes. Two approaches can be employed, based on so-called overlapping and non-overlapping domains, respectively:

---

[3] Parallel Virtual Machines.

[4] Message Passing Interface.

[5] PVM enables a collection of heterogeneous computer systems to be viewed as a single parallel virtual machine. It handles message routing, data conversion and task scheduling across a network of incompatible computer architectures. See [61] for more information.

- One refers to **overlapping domains**, if the domains into which the system to be computed is divided (and which are assigned to the two codes) are to some extent superimposed. When this approach is used, generally the whole system is modeled with the system code, and specific zones of the system are modeled with the CFD code as well. In such a case, the CFD computation is used to improve the solution of the system code by adding external source and sink terms for the primitive variables and the fluxes.

- On the other hand, one uses the term **non-overlapping domains**, if the system of interest is split into two separate domains, separately computed within the domain of the CFD and the system code, respectively.

In the present work, the non-overlapping strategy has been chosen.

3.2 Coupling numerics

3.2.1 TRACE-TRACE coupling

In order to test and verify the numerical algorithm of the coupling and the correct data exchange between the codes coupled through PVM, a coupling between two application cases of the TRACE code has been tested, before proceeding to the more complex coupling between TRACE and CFX. For the TRACE-TRACE coupling, a simple test was performed by considering a 10-meter long straight pipe with imposed pressure boundary conditions at the inlet and outlet, completely filled with water initially under stagnant conditions at 10 bar. The scenario considered was a transient followed by a steady state. The transient consisted in reducing the outlet pressure from 10 bar to 1 bar over 50 seconds; the outlet pressure was then maintained at 1 bar for additional 10 seconds, in order to reach a steady state. The change in outlet pressure causes an increase of the liquid velocity.

The problem was simulated in two ways, firstly as a single pipe component of 20 cells ("Full pipe"), modeled as a single TRACE case (stand-alone TRACE simulation), and then as two pipes of 10 cells each ("Half pipe"), modeled as separate TRACE cases with TRACE-TRACE coupling. Fig. 3.1 shows the two different layouts and the symbolic notation used throughout the thesis. For the coupled simulation, PVM was used on a single machine running three tasks in parallel: the two different TRACE cases and a third "Master" program which coordinated the other two tasks.

Boundary conditions were set with a "break" element (imposed pressure) both at the beginning and at the end for the "Full pipe". Regarding the "Half pipe", the first half had two "breaks", and the second half an inlet "fill" (imposed mass flow rate) and an outlet "break". Such a configuration at the interface between the two half-pipes seems to be the best one from the point of view of numerical stability. The "break" and the "fill" at the interface were set-up with constant fluid properties and constant boundary conditions: the coupling scheme
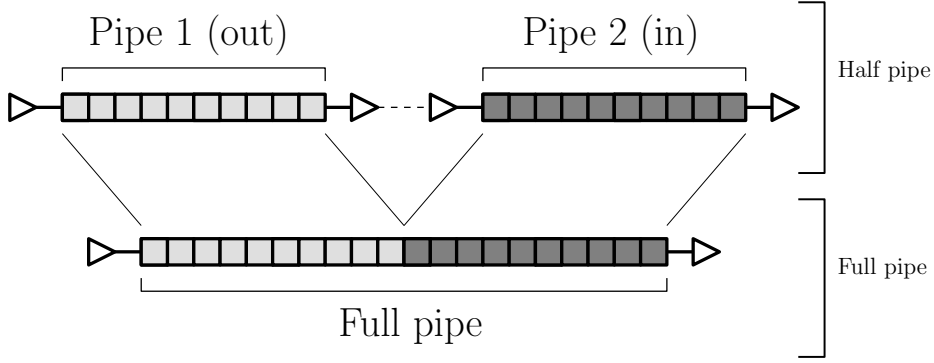
Figure 3.1: "Full pipe" and "Half pipe" layouts.

	Full pipe	Pipe 1	Pipe 2
No. of Cells	20	10	10
Cell length (m)	0.5	0.5	0.5
Fill length (m)	0.5	0.5	0.5
Break length (m)	0.5	0.5	0.5
Pipe length (m)	10	5	5
Hydr. diam. (m)	0.1	0.1	0.1
Wall roughness (m)	5.0E-5	5.0E-5	5.0E-5
Pressure convergence	1.0E-4	1.0E-4	1.0E-4
Starting Temp. (K)	300	300	300
Starting Pressure (Pa)	1.0E6	1.0E6	1.0E6
Break (inlet) pressure (Pa)	1.0E6	1.0E6	1.0E6
Break (outlet) pressure (Pa) at 0 s	1.0E6	1.0E6	1.0E6
Break (outlet) pressure (Pa) at 50 s	0.1E6	1.0E6	0.1E6
Simulation time (s)	60	60	60

Table 3.1: Set-up for TRACE-TRACE coupling simulation.

directly modified the pressure at the exit of the first half pipe and the velocity at the inlet of the second half pipe until the desired convergence was reached. A more detailed description of the test, along with its results, is presented in the following.

The "Full pipe" calculations (TRACE stand-alone) were made with the original version of TRACE (V5.0RC2), while the "Half pipe" calculations (TRACE-TRACE coupling) were carried out with the modified version of TRACE including statements for the linking to the PVM environment (denoted by TRACEPVM from now on). For the sake of simplicity, a single version of TRACEPVM was considered, containing both the calls for the 1st and the 2nd halves of the pipe. Effectively, the "Master" program spawned two copies of the TRACEPVM models and assigned them the tag of "Giver" for the 1st half of the pipe and "Receiver" for the 2nd half. Each copy of TRACE had its own input file. Data used for the set-up of the simulation are listed in Tab. 3.1.

The idea at the base of the coupling is shown in Fig. 3.2: at the end of each time step, the
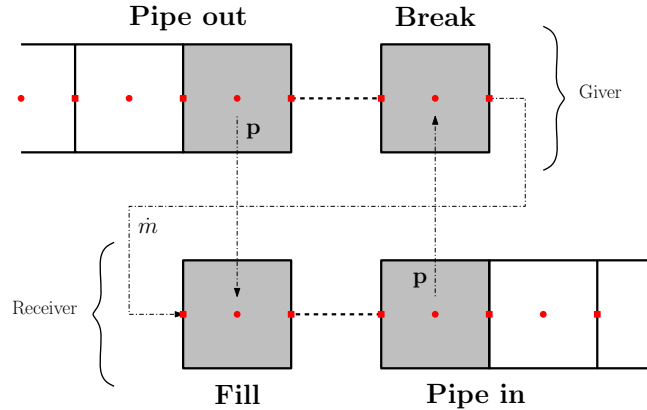
Figure 3.2: Schematic of the coupling used in TRACEPVM.

"Giver" program passes "Pipe out" pressure and mass flow rate to the "Fill" of the "Receiver"; the "Receiver" then proceeds with its own time step and, at the end of it, passes "Pipe in" pressure to the "Break" of the "Giver". The same time step is repeated until convergence is reached, i.e. the old "Break" pressure equals, within the tolerance requested, the new "Pipe in" pressure. Then, the computation is moved to the next time step, and the last obtained pressure value (from the previous time step) is assigned as initial pressure value of the receiving cell.

In Fig. 3.3 is shown the pseudo-code for the coupling featuring both the "Master" program and the double spawn of TRACEPVM, with the structure of the information passing. Particular care is needed to avoid program locks due to an infinite waiting time of one information packet, which may not have been sent at the right instant of the run. Moreover, it is necessary to ensure that both the TRACEPVM programs have the same time step to maintain consistency between the passed data. The commands SPAWN, SEND and RECEIVE are the actions performed by the PVM FORTRAN subroutines. There are extra subroutines which read from an external input file the component number (defined by the user in the input file) of the two pipes, and of the fill and the break at the coupling interface.

"Half pipe" TRACEPVM calculations were compared to the "Full pipe" TRACE runs. Figs. 3.4 and 3.5 show the evolution of both the pressure and the mass flow rate at a certain point in space (for different spatial positions, similar results were obtained). The results obtained with TRACEPVM are seen to be consistent with those obtained with TRACE.

Fig. 3.6 shows TRACEPVM and TRACE time evolutions of the pressure relative error[6] at different positions along the pipe. Fig. 3.7 shows instead the TRACEPVM and TRACE time evolutions of the mass flow rate relative error at the coupling interface. For both the pressure

---

[6] The relative error is here evaluated as:

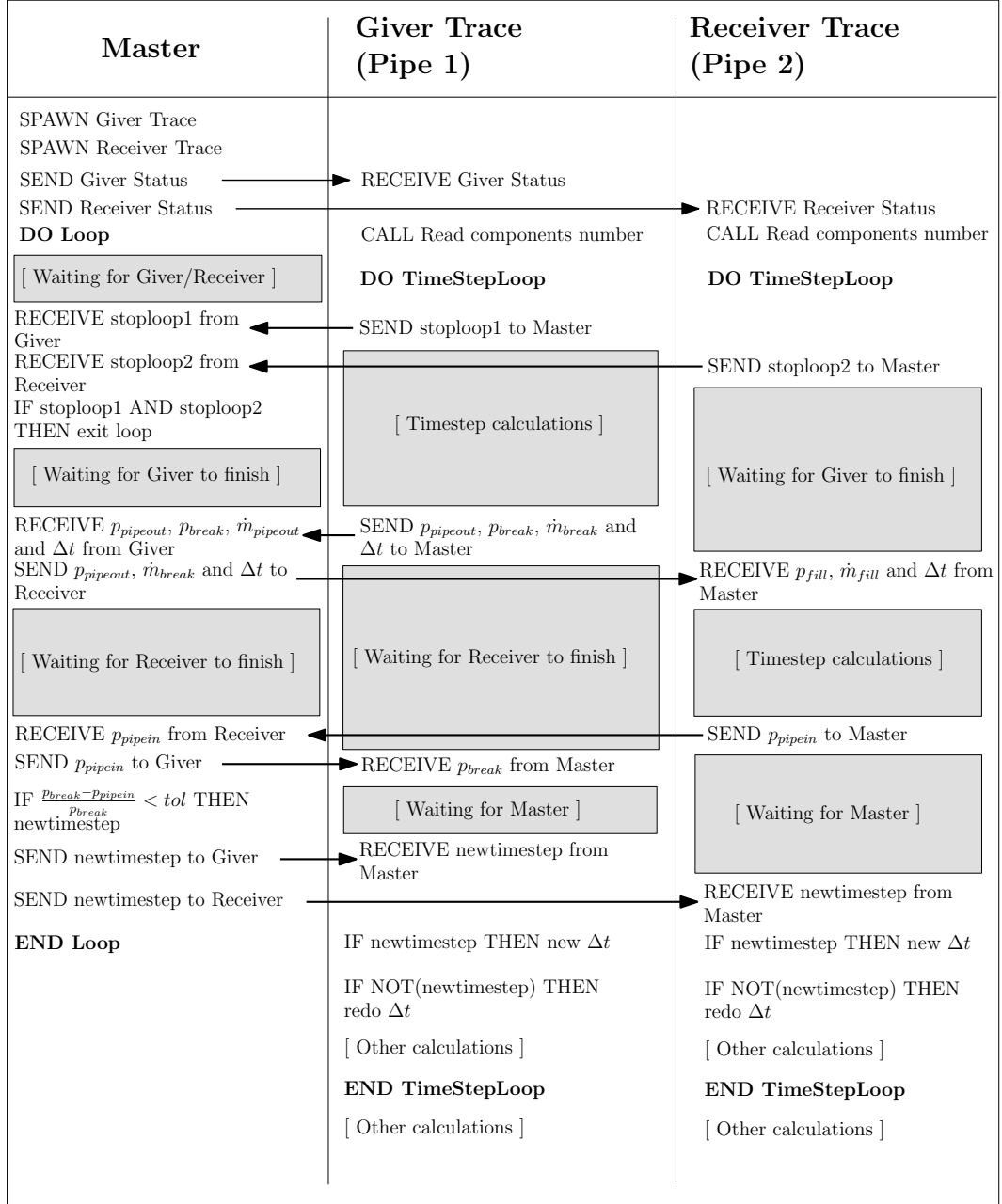$$\varepsilon = \frac{\text{TRACEPVM} - \text{TRACE}}{\text{TRACE}}$$

Master	**Giver Trace (Pipe 1)**	**Receiver Trace (Pipe 2)**
SPAWN Giver Trace		
SPAWN Receiver Trace		
SEND Giver Status ──────►	RECEIVE Giver Status	
SEND Receiver Status ────		──► RECEIVE Receiver Status
DO Loop	CALL Read components number	CALL Read components number
[Waiting for Giver/Receiver]	**DO TimeStepLoop**	**DO TimeStepLoop**
RECEIVE stoploop1 from Giver ◄──	── SEND stoploop1 to Master	
RECEIVE stoploop2 from Receiver ◄──		SEND stoploop2 to Master
IF stoploop1 AND stoploop2 THEN exit loop	[Timestep calculations]	[Waiting for Giver to finish]
[Waiting for Giver to finish]		
RECEIVE $p_{pipeout}$, p_{break}, $\dot{m}_{pipeout}$ and Δt from Giver ◄──	SEND $p_{pipeout}$, p_{break}, $\dot{m}_{break}$ and Δt to Master	──► RECEIVE p_{fill}, $\dot{m}_{fill}$ and Δt from Master
SEND $p_{pipeout}$, $\dot{m}_{break}$ and Δt to Receiver ────		
[Waiting for Receiver to finish]	[Waiting for Receiver to finish]	[Timestep calculations]
RECEIVE p_{pipein} from Receiver ◄──		── SEND p_{pipein} to Master
SEND p_{pipein} to Giver ──────►	RECEIVE p_{break} from Master	
IF $\frac{p_{break}-p_{pipein}}{p_{break}} < tol$ THEN newtimestep	[Waiting for Master]	[Waiting for Master]
SEND newtimestep to Giver ──────►	RECEIVE newtimestep from Master	
SEND newtimestep to Receiver ──────►		RECEIVE newtimestep from Master
END Loop	IF newtimestep THEN new Δt	IF newtimestep THEN new Δt
	IF NOT(newtimestep) THEN redo Δt	IF NOT(newtimestep) THEN redo Δt
	[Other calculations]	[Other calculations]
	END TimeStepLoop	**END TimeStepLoop**
	[Other calculations]	[Other calculations]

Figure 3.3: Pseudo-code for the TRACE-TRACE coupling.
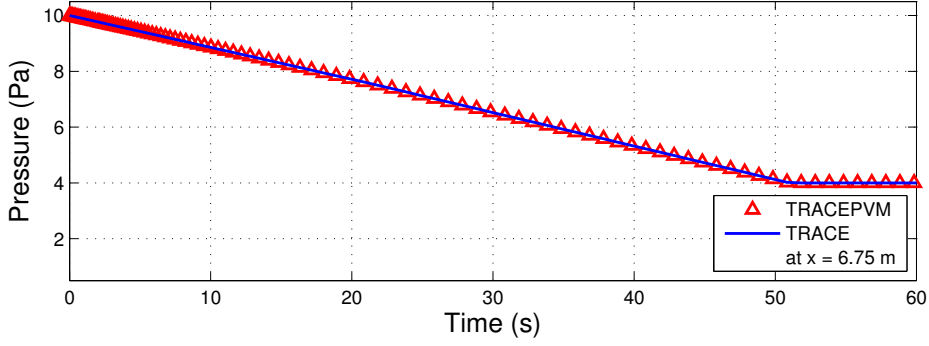
Figure 3.4: Pressure time evolution during the simulation, for both TRACEPVM and TRACE.
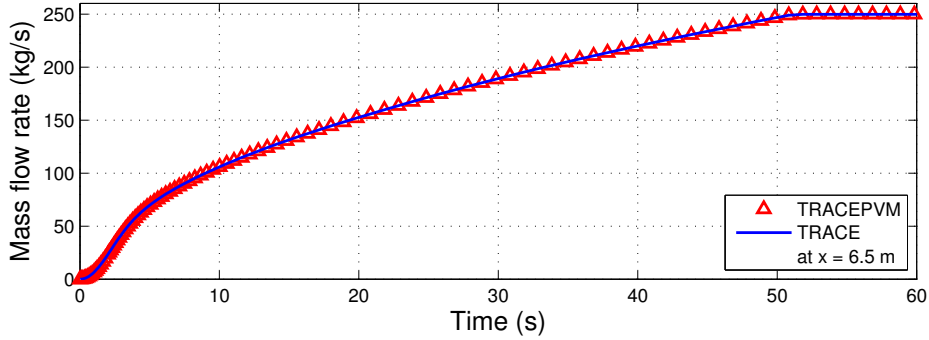
Figure 3.5: Mass flow rate time evolution during the simulation, for both TRACEPVM and TRACE.

and the mass flow rate, the error is lower than 0.1% at any given time. It should be noted that no particular criterion on the interface convergence was implemented in TRACEPVM for this preliminary test. The only modification adopted was pressure weighting (similar to that presented in Subsec. 3.2.6) to avoid having diverging oscillations of the pressure at the interface between the two TRACE half-pipes. Figs. 3.8 and 3.9 show the spatial profiles of TRACEPVM and TRACE, respectively, for the pressure and the mass flow rate at different times.

3.2.2 CFX/TRACE coupling

In the coupling developed between ANSYS CFX and TRACE (Fig. 3.10), the CFD code is defined as "Master" program and is implemented as a CFX junction box routine which is called at several stages during the computation. This routine controls the information exchange with the system code TRACE (defined accordingly as the "Slave" code) and the time-step advancement. Special user-defined CEL functions are employed to set the the boundary conditions in CFX and communicate with the junction box through the Memory Management
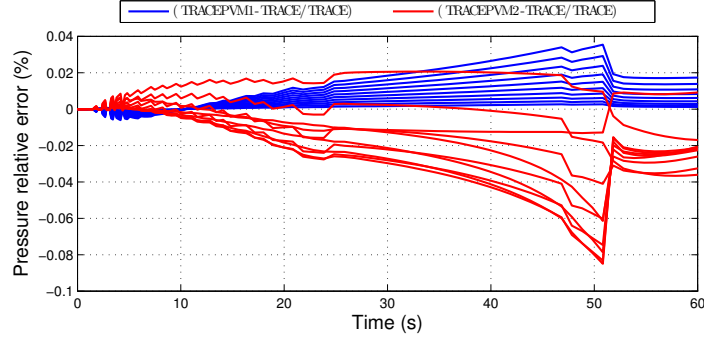
Figure 3.6: Time evolution, at different positions, of TRACEPVM and TRACE pressure relative error. TRACEPVM is divided into two profiles ("TRACEPVM1" and "TRACEPVM2"), corresponding to the "Giver" and "Receiver" of the modified-TRACE models.
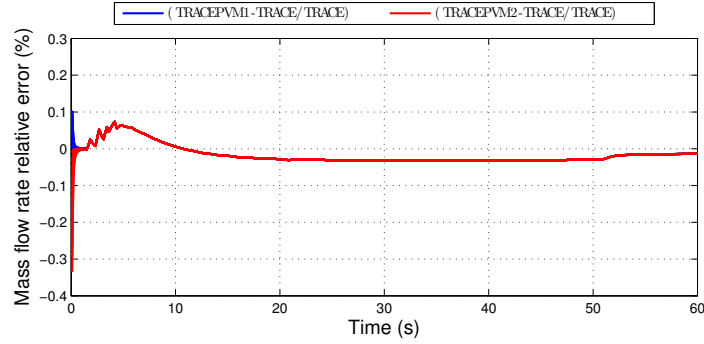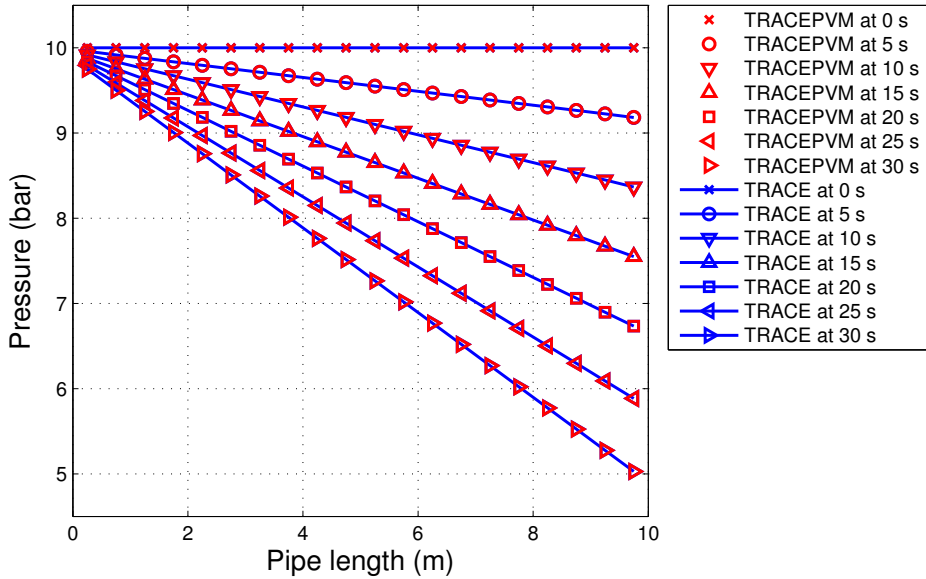

Figure 3.7: Time evolution, at different positions, of TRACEPVM and TRACE mass flow rate relative error. TRACEPVM is divided into two profiles ("TRACEPVM1" and "TRACEPVM2"), corresponding to the "Giver" and "Receiver" of the modified-TRACE models.

Figure 3.8: TRACEPVM and TRACE spatial profiles of pressure during the transient calculation.
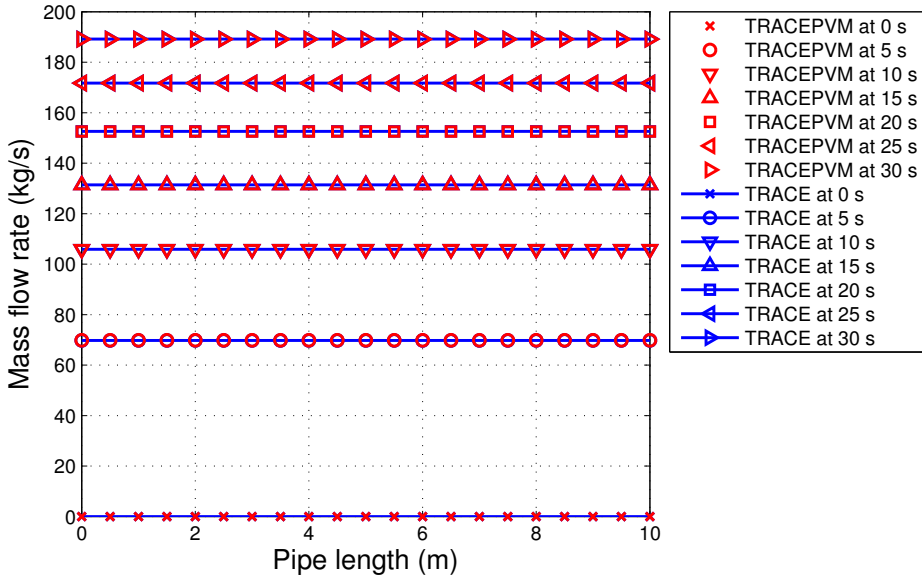
Figure 3.9: TRACEPVM and TRACE spatial profiles of mass flow rate during the transient calculation.
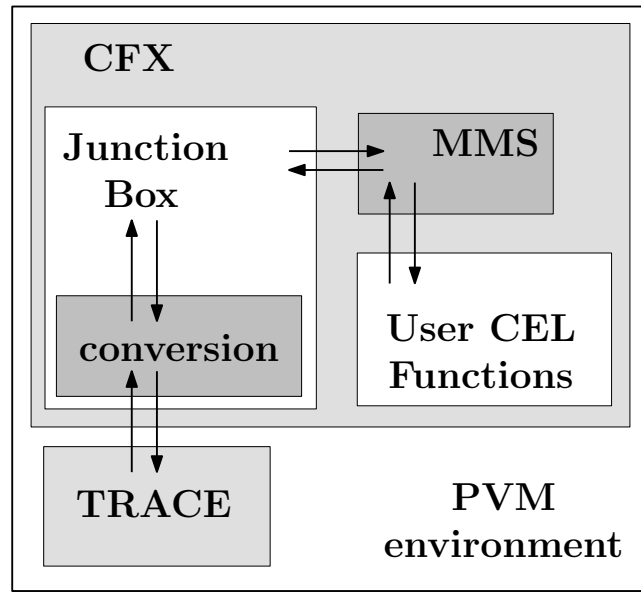
Figure 3.10: Simplified CFX-TRACE coupling scheme.

System (MMS)[7]. The junction box also handles the data conversion and manipulation needed before the data is exchanged between the two codes.

In Fig. 3.11, a flow chart of the coupling structure inside the main junction box is shown. It indicates how the coupling scheme is integrated into the solver of ANSYS CFX.

---

[7]The Memory Management System, is the system used inside CFX to store the data during the computation. See [58] for more detailed information.
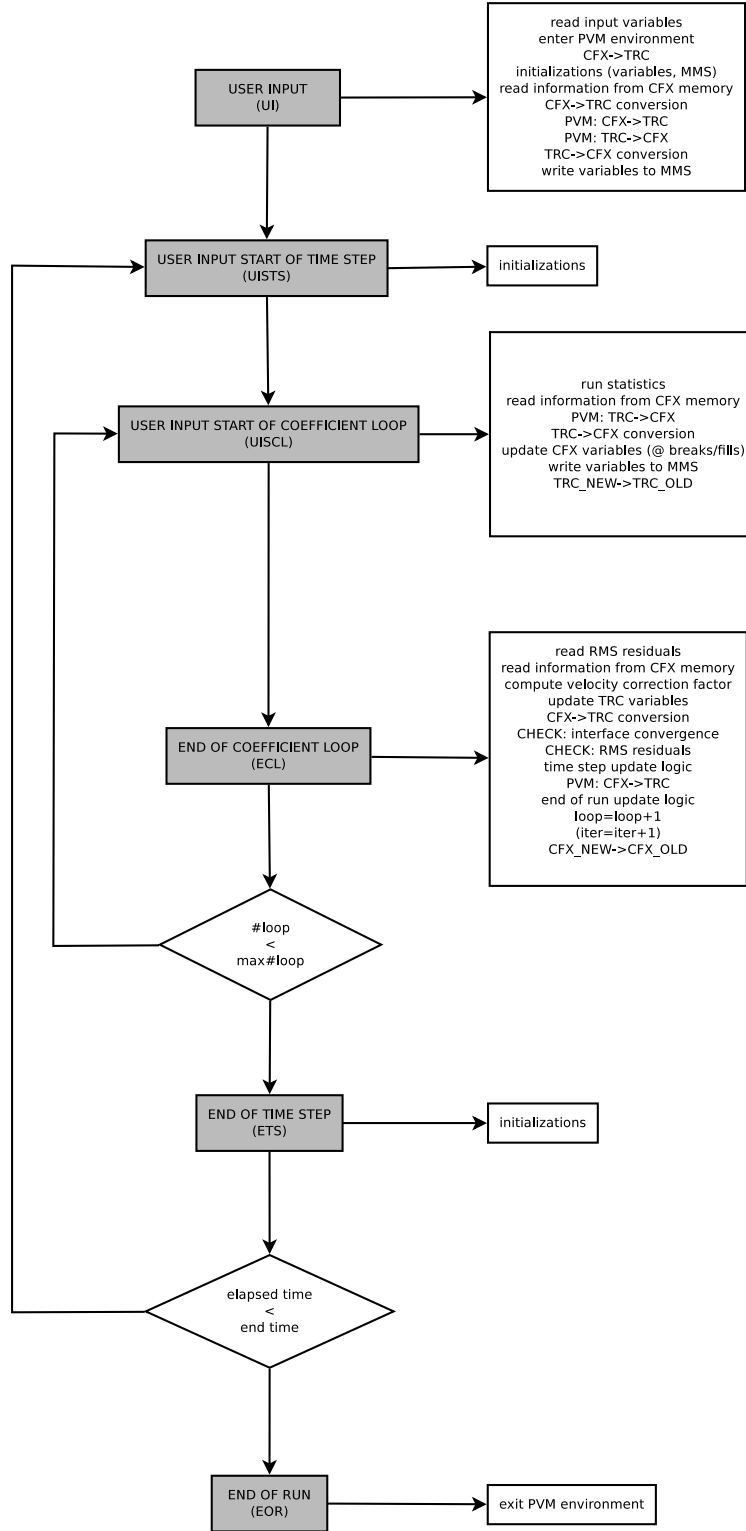
Figure 3.11: Flow chart of the coupling structure inside the main junction box. In gray, on the left, are the points of the solver execution at which the junction box is called. On the right, the main actions taken at each point are listed.

3.2.3   Coupled tool numerical scheme

Different numerical schemes are available to implement the information-passing between the interconnected domains, and thus to achieve an integrated solution between the coupled codes. A first, important distinction is between sequential and parallel schemes:

- In a **sequential** scheme, one code remains idle while the other code is being executed. Usually, one code receives the necessary BCs, computes a time step, exchanges the newly-obtained boundary information with the other code, and then waits for its counterpart to finish the computation and give back new BCs (whether the new BCs will be used to execute a new time step or to re-execute the previous time step depends on the adopted numerical scheme) [62].

- In a **parallel** scheme, both codes work in parallel, thus reducing the dead times. While this option seems attractive from the point of view of computational time optimization (especially if the two codes have comparable execution times), it requires a careful choice of the BCs to be used at each time step, because they are not anymore related with a logical sequence. This may present mass and energy conservation problems, as well as consistency and stability issues, as clearly pointed out in earlier work [62, 63].

The sequential scheme is the most straightforward approach, and it is the one used in the present work. The idle time is not relevant in our case, since the time execution of CFX is much larger than that of TRACE. However, this may become an issue if the coupled codes have similar execution times.

A second kind of classification is based on the definition of explicit, semi-implicit and implicit[8] schemes. In the case of parallel schemes, this definition is related to the numerical scheme used to discretize the equations at the coupling interface. Since in the present work the focus is on the sequential scheme, this distinction will not be detailed further. The following descriptions are suitable for the sequential scheme:

- In the case of an **explicit** coupling scheme, variables in the boundary volumes and faces are held constant during each time step and are updated at the end of the time step. In this case, the convergence of the results at the boundaries of the physical interface is not guaranteed, and a relatively small integration time step has to be employed.

- A **semi-implicit** coupling scheme implies that the variables in the boundary volumes are exchanged between the codes several times during the same time step. The iterations are terminated when convergence of the variable values at the boundaries of the physical interface is reached for both codes.

---

[8]Implicit schemes integrate the solution of the coupled codes in one unique solution process. The numerical solver has to be modified to accomodate such an integration, thus requiring an extensive modification of the source codes of the programs involved in the coupling. Since CFX is a commercial code, its source is not free, and such a coupling procedure cannot be pursued in this thesis. Moreover, by definition, implicit schemes are also parallel schemes and are, therefore, not considered further in this work.

Both explicit and semi-implicit numerical schemes for time advancement have been implemented in the coupled CFX/TRACE code. In specific terms, the coupling in the present work is done by following two different schemes for time advancement: an explicit sequential scheme and a semi-implicit sequential one.

- In the **explicit sequential** scheme (see Fig. 3.12), the solution is computed by TRACE at a certain time step, the results are then passed on as appropriate boundary values to CFX, which computes the same time step for its own computational domain. The results of CFX are passed back as BCs to TRACE, and a new time step is computed. As mentioned earlier, the convergence of the results at the boundaries of the physical interface is not guaranteed, and a relatively small integration time step has to be employed.

- In the **semi-implicit sequential** scheme (Fig. 3.13), the same time step is repeated sequentially in both TRACE and CFX until the convergence of the BC at the interface between the two codes is reached. The convergence criteria are defined by the user.

Independently of the type of coupling scheme employed, each code performs a certain number of internal iterations during each time step, as required by the code internal solver. In the case of CFX, the number of internal iterations can be controlled by the user to reach the desired root mean square (RMS) accuracy; experience dictates that a minimum number of internal iterations should be set for CFX to get acceptable results (usually a minimum of 3 iterations is sufficient). Currently, the developed coupling scheme is limited to single-phase isothermal flows, with the convection of a scalar (e.g. the concentration of a dissolved solute). It can be easily extended to variable temperature flows, as long as the flow regime remains single-phase.

3.2.4 Coupling boundary conditions

The coupling has been developed to deal with multiple boundary conditions. In the present case, TRACE allows the use of two kinds of boundary conditions: a "break" component allows imposing a pressure boundary condition, while a "fill" component allows imposing a velocity boundary condition. CFX allows the definition of a generic "opening" boundary condition that can work both as inlet and outlet (depending on the flow direction), and in which the user can impose a pressure or a velocity profile.

A more detailed illustration of the coupling at the interface between the two codes is shown in Fig. 3.14. The values exchanged here are velocity v and pressure p, with arrows indicating the direction of the information passing. B and F in TRACE are, respectively, a break (imposed pressure) and a fill (imposed velocity). OV and OP are CFX openings with imposed velocity and pressure, respectively. Circles indicate values defined on the cell boundary, crosses indicate values defined at the cell center. If necessary, any other combination
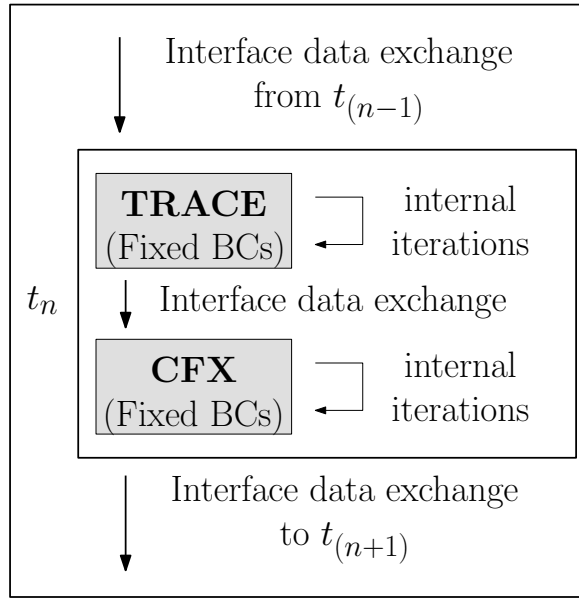
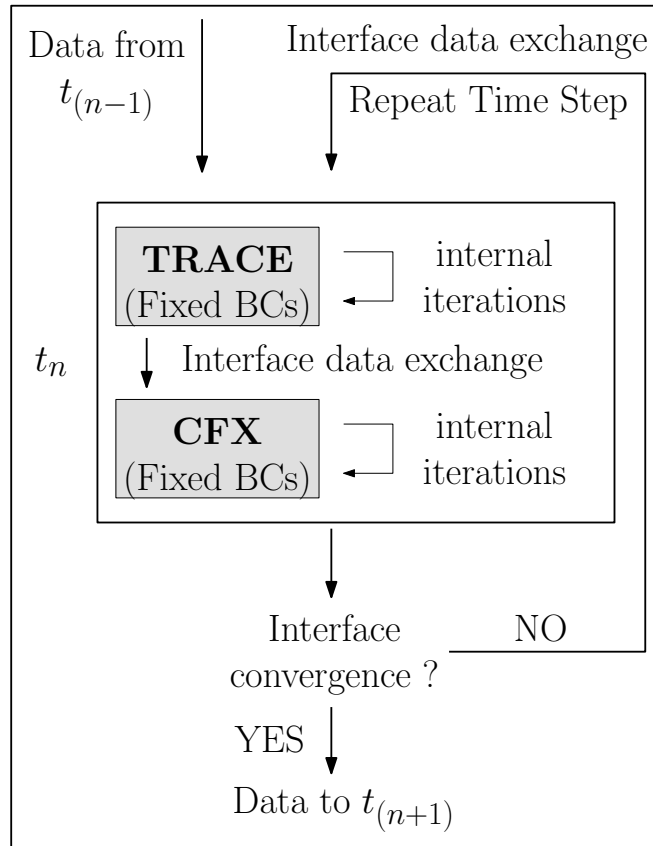Figure 3.12: Sequential explicit numerical coupling scheme for a generic time step.

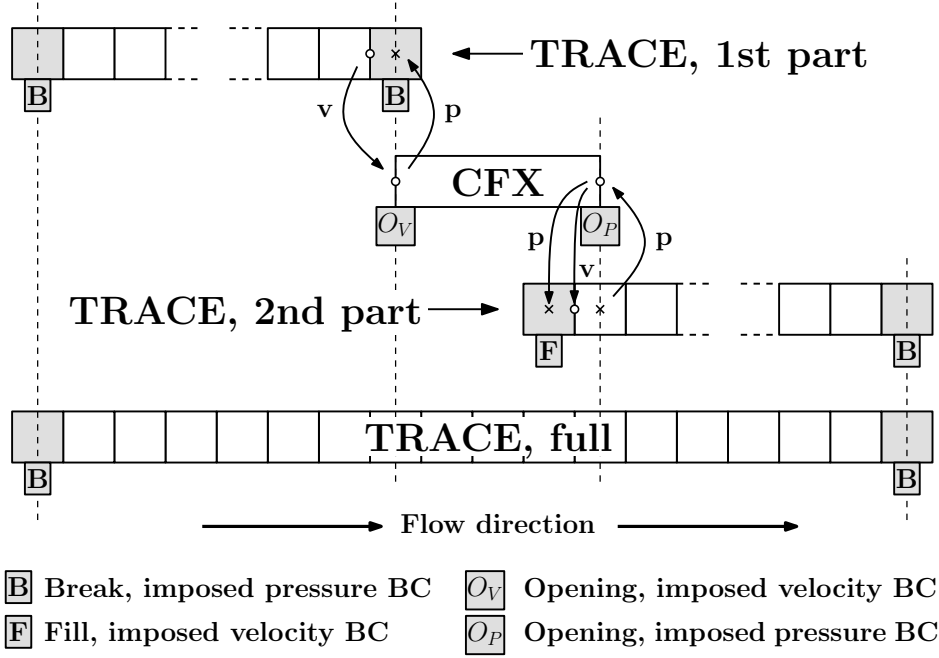Figure 3.13: Sequential semi-implicit numerical coupling scheme for a generic time step.

Figure 3.14: Detailed CFX-TRACE coupling of the boundary conditions.

of fills and breaks at the interface between the two codes is possible, but the general idea remains the same.

3.2.5 Specific coupling issues

It is important to point out that, in the coupling between a 1D code and a 3D code, information from the 3D to the 1D code is lost at the interface. For example, turbulence parameters are lost, because one-dimensional thermal-hydraulic system codes typically do not include turbulence models. Also lost are the cross-section profiles of the exchanged variables, like the velocity profile. Inevitably, cross-section averages have to be computed and single scalar values have to be obtained for the BCs to the system code. While this is not an issue for the 1D code itself, the same information (not available in the 1D solution) is needed at the interface in the other direction, i.e. from the 1D to the 3D code. In this case, cross-section averaged quantities have to be "transformed" into two-dimensional distributions. Moreover, assumptions on the turbulence parameters are necessary. This operation is clearly a source of inaccuracy, and special attention has to be paid to this issue.

Another cause of possible problems is the mesh discretization at the interface. As can be seen in Fig. 3.14, the TRACE solver is based on a staggered mesh (vectorial quantities are defined at the cell edges, while scalar quantities are defined at the cell centers) [8], while CFX uses a co-located grid layout (the control volumes are identical for all transport equations) [64] and thus the variables are considered at the same surface. This is not a problem as long as the discretization of the TRACE mesh at the interface zone is fine enough, so that spatial

variations of the quantities of interest within half a cell are negligible. Experience has shown that, as a rule of thumb, a TRACE discretization of the same order as that adopted in CFX along the flow direction is sufficient to guarantee a stable coupling, but coarser meshes are not excluded *a priori* and should be verified case by case.

3.2.6 Optimization and speed-up techniques

To have a faster interface convergence, an initial pressure drop estimate has been devised as user-defined input. Moreover, to reduce the amplitude of the pressure oscillations at the coupling interface (especially to avoid diverging oscillations, also called overshootings, in the case of open-loop configurations), a pressure weighting has been introduced in the coupling, such that the new pressure value passed as boundary condition is weighted with the old one with a weight $0 \leq w \leq 1$ defined by the user:

- for the 1D-to-3D coupling interface, the adopted weighting is:

$$p_{TRC,out}^{n+1} = (1 - w_{p,in}) \, p_{CFX,in}^{n+1} + w_{p,in} p_{CFX,in}^{n}$$

- for the 3D-to-1D coupling interface, the adopted weighting is:

$$p_{CFX,out}^{n+1} = (1 - w_{p,out}) \, p_{TRC,in}^{n+1} + w_{p,out} p_{TRC,in}^{n}$$

While most of the simulations presented in this thesis could be run without weighting (i.e. with $w = 0$), in a few cases a value of $w = 0.5$ has been necessary to achieve a non-diverging coupling. The value of w has not been found to be clearly dependent on coupling parameters and has been empirically defined, case by case. It has to be noted that, while high values of the weight have a stabilizing effect on the coupling, they also slow down the pressure convergence at the coupling interface. In view of this consideration, weighting should be avoided, or limited in magnitude, whenever possible.

To ensure that proper interface convergence has been reached for the pressure before switching to the new time step in the semi-implicit scheme, an average pressure value is computed at the interface for the internal iteration. This is based on a certain number of last pressure values, the number itself being defined by the user. Without use of such an average, it can happen that certain oscillations bring the pressure values of the two codes very close to convergence (thus inducing the switch to the new time step), while the interface computation is still not truly converged.

3.3   Verification - open-loop

3.3.1   Test description

The developed coupled tool has been verified on a simple problem consisting of a 3 m long straight pipe having a diameter of 50 mm (Fig. 3.15). The pipe is initially filled with stagnant liquid at 10 bar. At time t = 0, the pipe end is opened to a slightly lower pressure environment (9.9 bar), causing a sudden acceleration of the fluid in the pipe (see Tab. 3.2 for details on the simulation).

As coupled problem, the first 2 m of the pipe are modeled with TRACE, while the last 1 m is modeled with CFX (hexa mesh with 150k elements). Fig. 3.16 shows the mesh and Tab. 3.3 provides the related details. The coupled solution has been compared with the results of a TRACE stand-alone simulation.

3.3.2   Convergence studies

Parametric studies have been carried out to verify the sensitivity of the coupling to relevant simulation parameters such as:

- the integration time step;

- the inlet velocity and turbulence BCs at the interface between the TRACE and CFX domains (flat velocity profile, turbulent velocity profile with standard turbulence, tur-
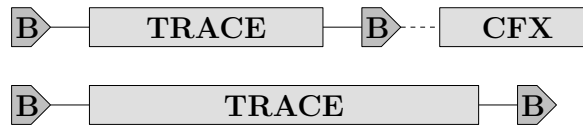
Figure 3.15: Sketch of the open-loop configuration for the coupled simulation (top) and for the TRACE stand-alone reference simulation (bottom). B indicates a TRACE "break" (imposed pressure) component.
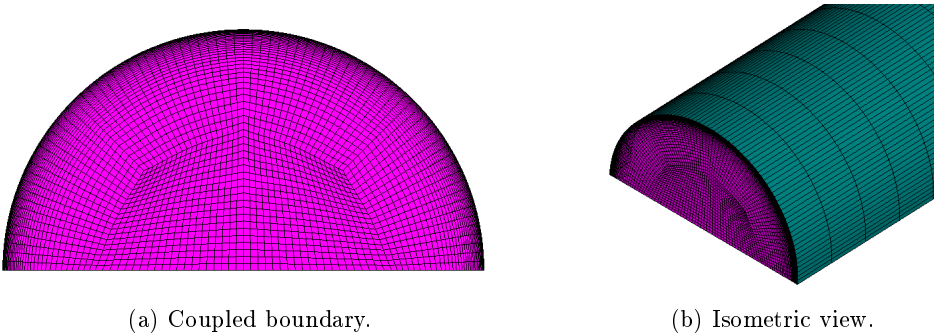

(a) Coupled boundary.　　　　　　(b) Isometric view.

Figure 3.16: CFX mesh for the verification simulations.

Initial conditions	
Temperature	300 K
Pressure	10 bar
Velocity	0 m/s
Boundary conditions	
p_{inlet}	10 bar
p_{outlet}	9.9 bar
TRACE simulation details	
Δt	0.001-0.1 s
Δx	0.2 m
D_h	0.05 m
L	2+1 m
τ_{end}	10 s

Table 3.2: Data sheet for the open-loop test.

Automatic mesh parameters	
Height of wall layer	0.001 m
Height mult. ratio	1.1 m
Max. number of layers	20
Max. mesh size (cross section)	0.001 m
Max. mesh size (wall)	0.01 m
Mesh statistics	
Elements (hexa)	344k

Table 3.3: Data sheet for the CFX mesh and verification simulations.

bulent velocity profile with defined profiles of κ and ω)[9];

- the type of numerical coupling scheme (explicit or semi-implicit).

The performed sensitivity studies are summarized in Tab. 3.4. The table is divided into three sections, one for each variation in the set of boundary conditions exchanged at the coupling interface. Shown are the absolute values of the maximum difference of the velocity (both relative and absolute) between the given case and a reference case representative of that set (the time-converged explicit solution); moreover, for a more extensive comparison, the variance evaluate for the velocity over the whole transient is indicated. The values have been computed as follows:

- absolute difference: $\max\left(\left|v_{ref}\left(t_i\right) - v\left(t_i\right)\right|\right) \quad \forall\, 0 < t_i < t_{end}$;

- relative difference: $\max\left(\left|\dfrac{v_{ref}\left(t_i\right) - v\left(t_i\right)}{v_{ref}\left(t_i\right)}\right|\right) \quad \forall\, 0 < t_i < t_{end}$;

---

[9]Inlet profiles were evaluated through parametric CFD simulations on a pipe of the same diameter, with radial profiles being computed for different mass flow rates and then normalized to the average flow velocity (eventually elevated to an exponent for the turbulent quantities). The resulting analytical expression, dependent on velocity, was then introduced into the boundary condition subroutines of CFX.

Case	Velocity diff. at the coupling interface			Machine	CFX CPU time			
	|Max. (abs.)|	|Max. (rel.)|	Variance		d.	h.	m.	norm.
	(m/s)	(-)	(-)					
pipe, expl., SST, flat, $\Delta t = 0.002$ s	0.0	0.0	0.0	lccfd01	4	22	35	1.00
pipe, expl., SST, flat, $\Delta t = 0.01$ s	$1.53 \cdot 10^{-2}$	$3.42 \cdot 10^{-3}$	$4.56 \cdot 10^{-4}$	lccfd03	1	0	18	0.20
pipe, expl., SST, flat, $\Delta t = 0.1$ s	$1.42 \cdot 10^{-1}$	$3.18 \cdot 10^{-2}$	$3.78 \cdot 10^{-3}$	lccfd01	0	3	6	0.03
pipe, impl., SST, flat, $\Delta t = 0.01$ s	$1.27 \cdot 10^{-2}$	$2.86 \cdot 10^{-3}$	$1.43 \cdot 10^{-5}$	lclrs11	3	17	27	0.75
pipe, impl., SST, flat, $\Delta t = 0.1$ s	$6.03 \cdot 10^{-2}$	$1.35 \cdot 10^{-2}$	$8.13 \cdot 10^{-4}$	lccfd07	0	7	59	0.07
pipe, expl., SST, turb., $\Delta t = 0.01$ s	0.0	0.0	0.0	lccfd05	1	13	10	0.31
pipe, expl., SST, turb., $\Delta t = 0.1$ s	$1.50 \cdot 10^{-1}$	$3.17 \cdot 10^{-2}$	$2.88 \cdot 10^{-3}$	lccfd07	0	3	55	0.03
pipe, impl., SST, turb., $\Delta t = 0.01$ s	$2.16 \cdot 10^{-2}$	$4.57 \cdot 10^{-3}$	$2.82 \cdot 10^{-4}$	lccfd03	2	19	56	0.57
pipe, impl., SST, turb., $\Delta t = 0.1$ s	$7.05 \cdot 10^{-2}$	$1.49 \cdot 10^{-2}$	$1.72 \cdot 10^{-3}$	lclrs14	3	17	28	0.75
pipe, expl., SST, turb. $+ \kappa - \omega$, $\Delta t = 0.01$ s	0.0	0.0	0.0	lccfd07	1	13	27	0.32
pipe, expl., SST, turb. $+ \kappa - \omega$, $\Delta t = 0.1$ s	$1.45 \cdot 10^{-1}$	$3.12 \cdot 10^{-2}$	$2.87 \cdot 10^{-3}$	lccfd01	0	4	13	0.04
pipe, impl., SST, turb. $+ \kappa - \omega$, $\Delta t = 0.01$ s	$2.16 \cdot 10^{-2}$	$4.65 \cdot 10^{-3}$	$2.82 \cdot 10^{-4}$	lccfd05	2	21	33	0.59
pipe, impl., SST, turb. $+ \kappa - \omega$, $\Delta t = 0.1$ s	$6.70 \cdot 10^{-2}$	$1.44 \cdot 10^{-2}$	$1.34 \cdot 10^{-3}$	lccfd05	6	7	17	1.28

Table 3.4: Systematic study of the CFX/TRACE coupling verification with a straight pipe.

- variance: $\frac{1}{N}\sum_{i=1}^{N}\left(v\left(t_i\right)-v_{ref}\left(t_i\right)\right)^2$ with $t_i = i\Delta t$.

In addition, the machine employed to perform each of the computations and the corresponding CPU time consumed are listed in the table, together with a normalization to the longest computation. Even though the computational power is different for some of the machines, a rough comparison of the time used is still possible (see App. B for more details on the technical specifications of the CPUs used). Notice that for non-flat velocity profiles and the semi-implicit coupling scheme, the computation tends to exhibit convergence problems within a given time step, and the corresponding CPU time cannot be easily compared with the other cases. Moreover, while for the majority of the simulations the pressure weight was zero, some of the simulations had to be run with a different pressure weight to be able to reach convergence.

Based on the cases run, the following conclusions can be drawn:

- The pressure profile along the whole pipe at the end of the transient (Figs. 3.17, 3.18 and 3.19), once stationary flow conditions are reached, is not influenced by the integration time step and the type of coupling scheme employed. This is to be expected, since the steady-state solution should not be affected by such parameters. However, while the stand-alone TRACE solution predicts a linear pressure decrease along the pipe length, a clear deviation from linearity at the interface between the CFX and the TRACE domains is observed in the coupled CFX/TRACE solution. The pressure drop in the CFX domain initially deviates from linearity due to the fact that at the interface between the TRACE and CFX domains, the cross-section averaged velocity computed by TRACE is used in CFX as a flat (i.e. uniform) velocity profile. While in TRACE it is assumed that the flow is always fully developed, in the CFD domain the development of the imposed uniform velocity profile into a fully developed turbulent profile is computed, leading to higher pressure drops in the coupled CFX/TRACE solution, compared to the TRACE stand-alone solution.
  In Fig. 3.20 it is seen that a consistent agreement between the TRACE stand-alone solution and the coupled CFX/TRACE solution is obtained when the TRACE cross-section averaged velocity is "transformed" into a fully developed (turbulent) velocity profile, and consistent information on the turbulent kinetic energy is supplied to CFX at the interface between the CFX and the TRACE domains (see curve "impl turb + ko" in Fig. 3.20).

- The time evolution of the velocity at the coupling interface during the transient is presented in Figs. 3.21, 3.22 and 3.23. Again, the TRACE stand-alone solution is shown together with the results of the coupled CFX/TRACE tool obtained for different integration time steps and different coupling schemes (explicit and semi-implicit). The
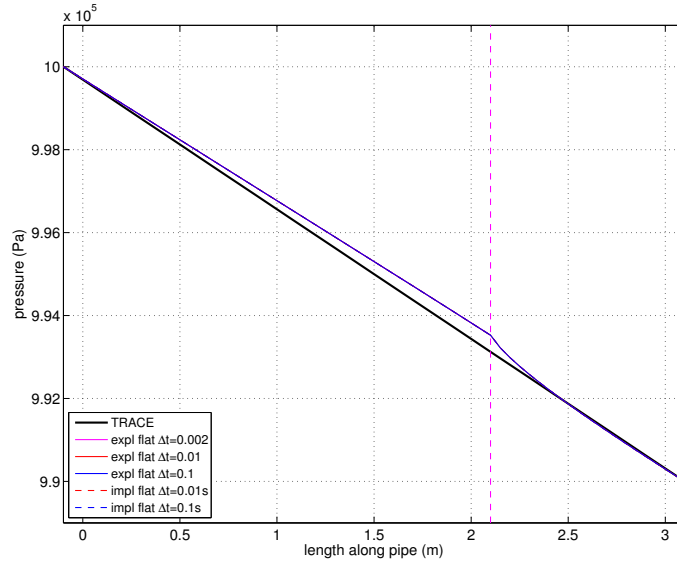
Figure 3.17: Profile of the pressure along the pipe for the explicit and semi-implicit coupling schemes, with a flat velocity profile imposed at the interface. Different time steps are represented.
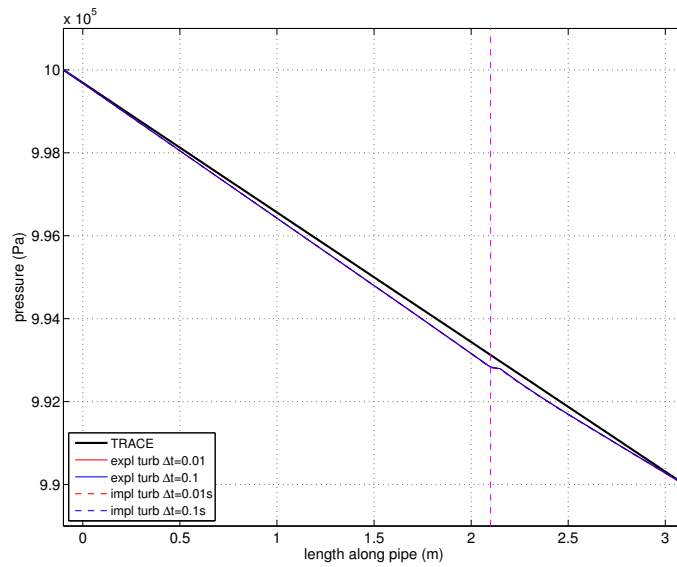

Figure 3.18: Profile of the pressure along the pipe for the explicit and semi-implicit coupling schemes, with a turbulent velocity profile imposed at the interface. Different time steps are represented.
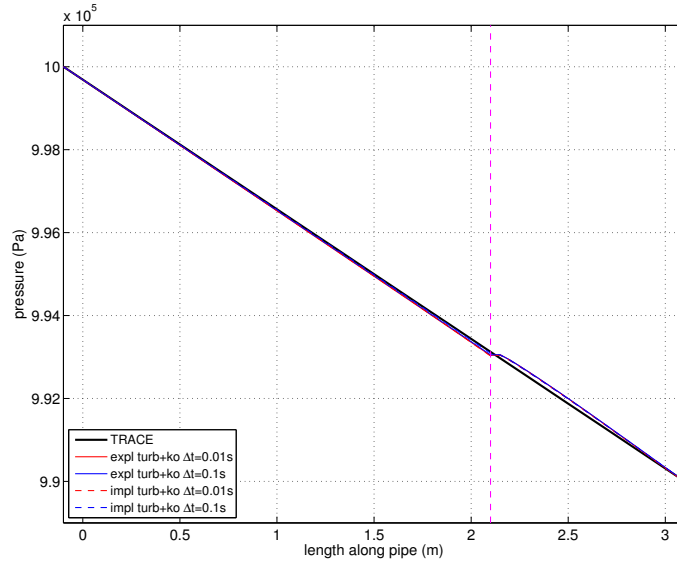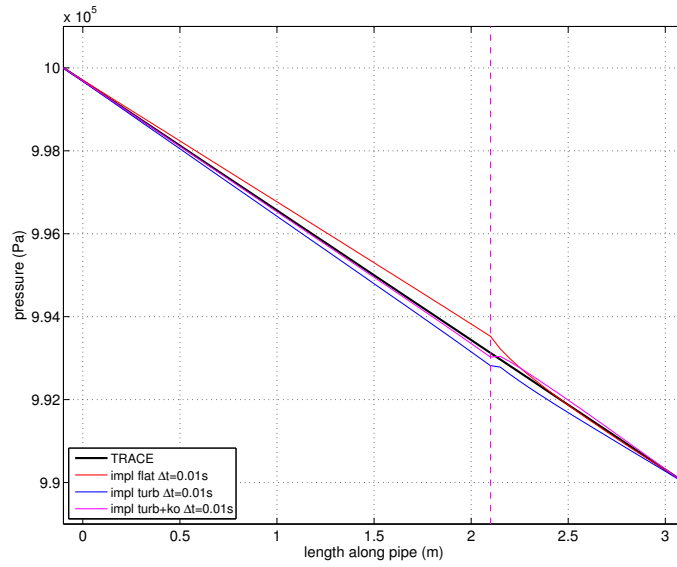
Figure 3.19: Profile of the pressure along the pipe for the explicit and semi-implicit coupling schemes, with a turbulent velocity profile and turbulent quantities k and ω imposed at the interface. Different time steps are represented.

Figure 3.20: Profile of the pressure along the pipe for the semi-implicit coupling scheme and different kinds of velocity and turbulent-quantity profiles imposed at the interface. Constant time step of 0.01 s.
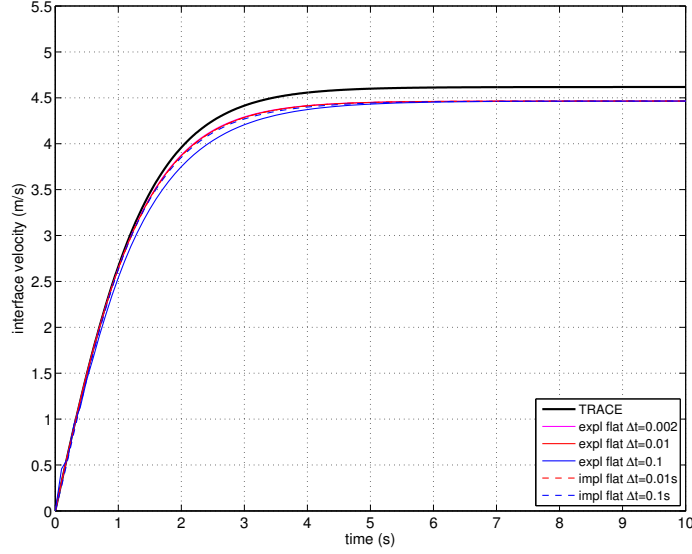
Figure 3.21: Evolution of the velocity at the interface for the explicit and semi-implicit coupling schemes, with a flat velocity profile imposed at the interface. Different time steps are represented.

coupled CFX/TRACE velocity is seen to be asymptotically lower than the TRACE stand-alone solution due to the higher pressure drops computed by CFX/TRACE, as discussed in relation to Figs. 3.17-3.19. Taking as reference the coupled CFX/TRACE solution obtained with an integration time step of 0.002 s, it can be seen that convergence in the solution with the explicit coupling scheme is reached already with an integration time step of 0.01 s. Convergence with the implicit scheme is reached instead with a time step of 0.1 s. Moreover, the semi-implicit scheme is found to give better results than the explicit scheme when the same time step is used (one order of magnitude on the variance), although at the cost of an increased computational time (Tab. 3.4). In Fig. 3.24, it is seen that, consistent with the discussion of Fig. 3.20 with regards to the pressure distribution along the pipe length, satisfactory agreement is obtained between the interface velocity of the stand-alone TRACE solution and that of the coupled CFX/TRACE solution when a turbulent velocity profile and the corresponding turbulence kinetic energy are supplied at the interface between the TRACE and CFX domains.

• Analyzing the time evolution of the pressure at the coupling interface (Figs. 3.25-3.28), it can be seen that the observed oscillations have a periodicity equal to about twice the time step when the explicit scheme is used, since the pressure is exchanged at every time step. If instead the semi-implicit scheme is used, the oscillations disappear very quickly
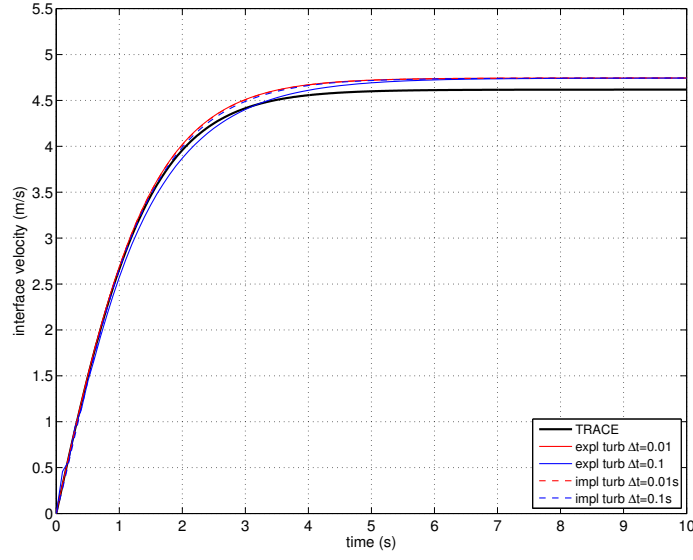
Figure 3.22: Evolution of the velocity at the interface for the explicit and semi-implicit coupling schemes, with a turbulent velocity profile imposed at the interface. Different time steps are represented.
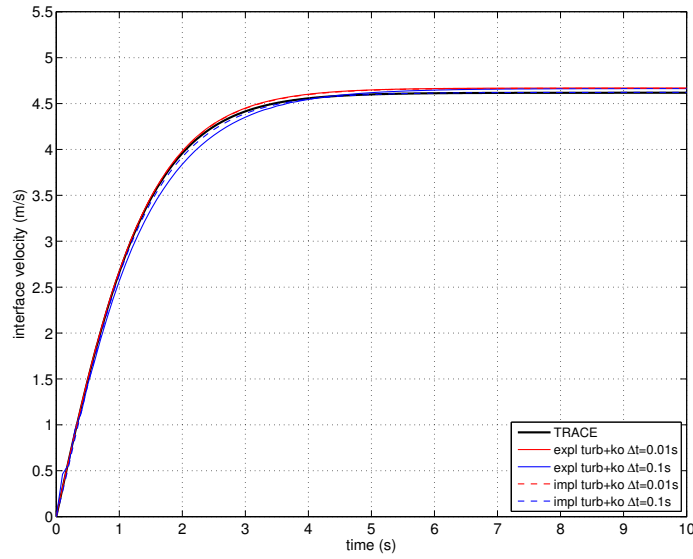

Figure 3.23: Evolution of the velocity at the interface for the explicit and semi-implicit coupling schemes, with a turbulent velocity profile and turbulent quantities k and ω imposed at the interface. Different time steps are represented.
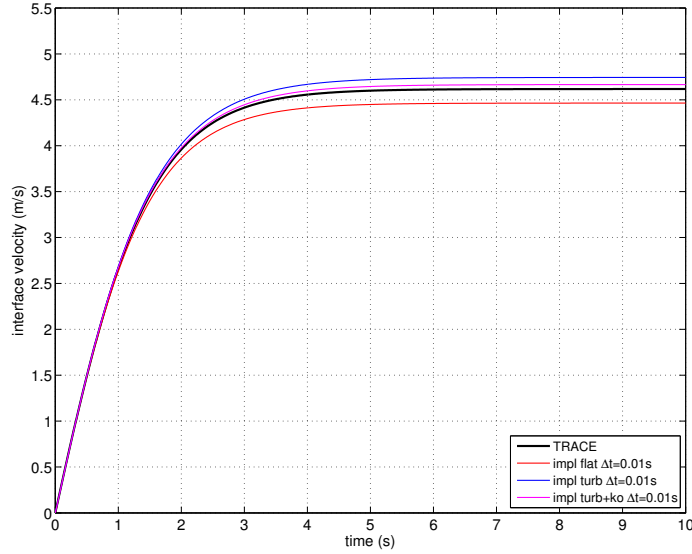
Figure 3.24: Evolution of the velocity at the interface for the semi-implicit coupling scheme and different kinds of velocity and turbulent-quantity profiles imposed at the interface. Constant time step of 0.01 s.

in 2 or 3 time steps and are of limited amplitude (except for the initial oscillation which results from imposition of the initial conditions; this is identical for both the coupling strategies). The way pressure convergence is achieved with the semi-implicit scheme at the interface between TRACE and CFX domains, within the internal iterations of a single time step, can be seen in Figs. 3.29 and 3.30. The number of internal iterations necessary to reach convergence is seen to vary during the transient. Moreover, it can be noted that reducing the integration time step reduces also the number of internal iterations required for achieving convergence.

- To evaluate the decay of the pressure oscillations at the coupling interface, an analysis has been made by fitting the peaks of the oscillations with a correlation of the type:

$$y(t) = ae^{bt} \cos(ct + d)$$

The results are shown in Figs. 3.31, 3.32 and 3.33; the fit was done only on the solutions obtained with the explicit scheme, since as explained earlier the oscillations for the implicit scheme are negligible. It can be seen from Figs. 3.31 and 3.32 that the velocity and turbulence parameters used as boundary conditions do not sensibly affect the decay, while the time step does, in agreement with the previous discussion; this is why only the flat velocity profile is used in Fig. 3.33. As can be seen in Tab. 3.5, the coefficient b scales more or less linearly with the time step. The period of the oscillations is about
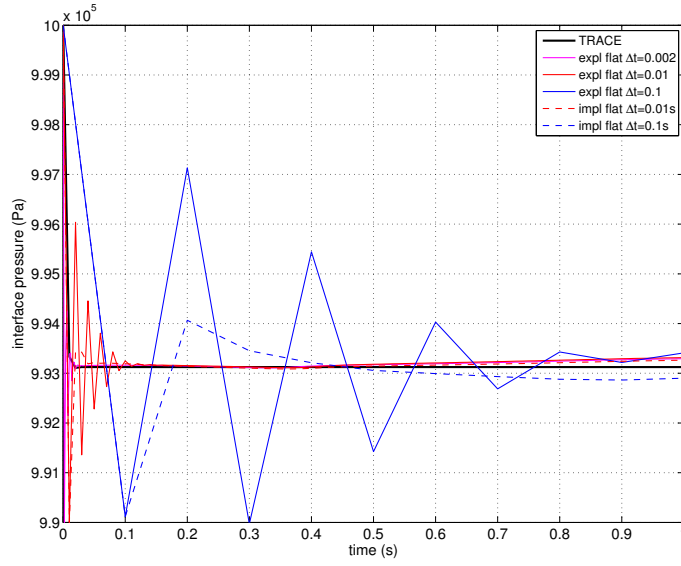
59

Figure 3.25: Evolution (up to 1 s) of the pressure at the interface for the explicit and semi-implicit coupling schemes, with a flat velocity profile imposed at the interface. Different time steps are represented.
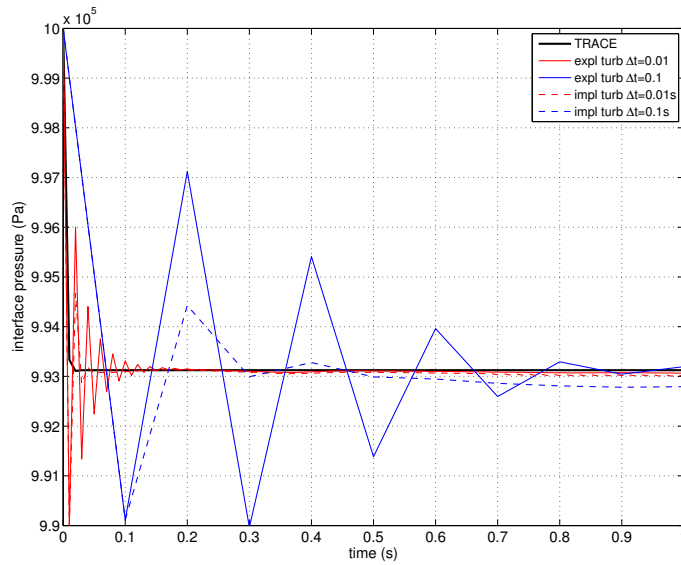

Figure 3.26: Evolution (up to 1 s) of the pressure at the interface for the explicit and semi-implicit coupling schemes, with a turbulent velocity profile imposed at the interface. Different time steps are represented.
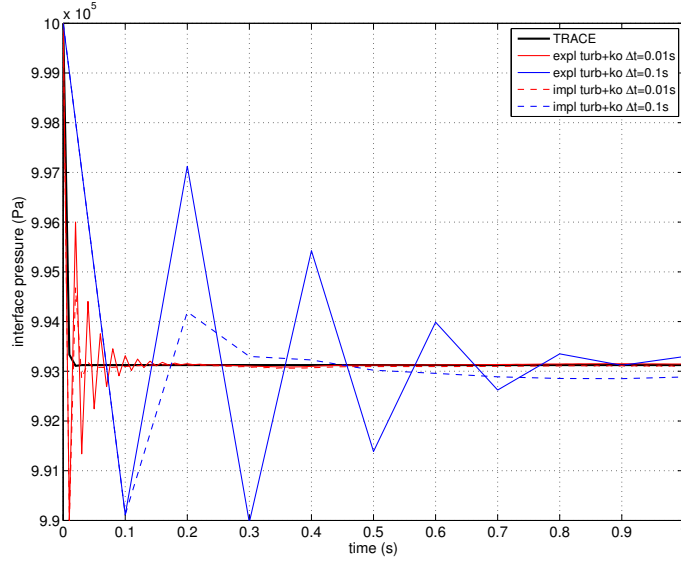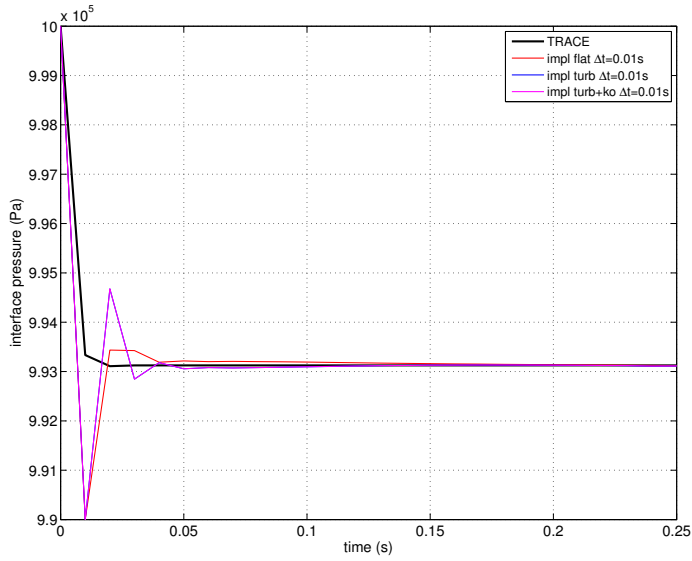
Figure 3.27: Evolution (up to 1 s) of the pressure at the interface for the explicit and semi-implicit coupling schemes, with a turbulent velocity profile and turbulent quantities k and ω imposed at the interface. Different time steps are represented.

Figure 3.28: Evolution (up to 0.25s) of the pressure at the interface for the semi-implicit coupling scheme and different kinds of velocity and turbulent-quantity profiles imposed at the interface. Constant time step of 0.01 s.
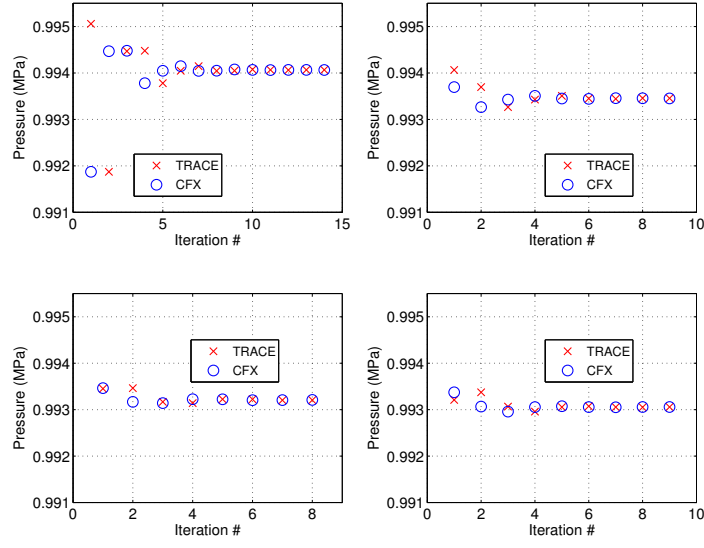
Figure 3.29: Convergence from the 2nd to the 5th iteration loop during the first time step. Results obtained with the semi-implicit coupling scheme with flat velocity profile and 0.1 s time step.
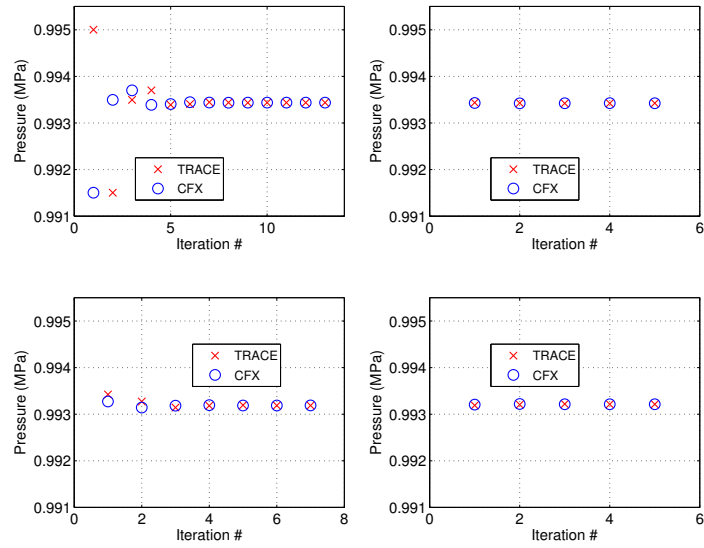

Figure 3.30: Convergence from the 2nd to the 5th iteration loop during the first time step. Results obtained with the semi-implicit coupling scheme with flat velocity profile and 0.01 s time step.

2 time steps for $\Delta t = 0.01$ s and $\Delta t = 0.1$ s, while it is about 3 time steps in the case with $\Delta t = 0.002$ s.

Case	Decay constant b (1/s)	Frequency c (rad/s)	Period $2\pi/c$ (s)
pipe, explicit, SST, flat, $\Delta t = 0.002$ s	-2.02E+02	1.09E+03	5.76E-02
pipe, explicit, SST, flat, $\Delta t = 0.01$ s	-3.02E+01	2.98E+02	2.11E-02
pipe, explicit, SST, flat, $\Delta t = 0.1$ s	-2.53E+00	2.84E+01	2.21E-01

Table 3.5: Time decay constant b, frequency c and oscillation period in the form $ae^{bt}\cos(ct+d)$ for the explicit case with flat velocity profile.

3.4   Verification - closed-loop

3.4.1   Test description

A closed-loop simulation has been run as well, in order to test the stability of the CFX/TRACE coupling. Indeed, in the case of a closed loop, the feedback between the codes is usually stronger than in the case of an open loop, because there are multiple coupling interfaces involved which affect each other and, in turn, may give rise to numerical stability issues. Therefore, the effects of such a configuration have to be verified.

The problem consists of a 11 m long pipe loop having a diameter of 50 mm (Fig. 3.34). The loop is initially filled with liquid at 10 bar, with a starting velocity of 6 m/s. A tee section within the loop is connected to a "break" (9.5 bar). At time t = 0, the system velocity evolves such as to match the constant flow rate imposed by a pump (see Tab. 3.6 for details on the simulation).

Initial conditions	
Temperature	$300\ K$
Pressure	$10\ bar$
Velocity	$6\ m/s$
Boundary conditions	
p_{tee}	$9.5\ bar$
TRACE simulation details	
Δt	$0.01\ s$
Δx	$0.2\ m$
D_h	$0.05\ m$
L	$5+1+5\ m$
τ_{end}	$5\ s$

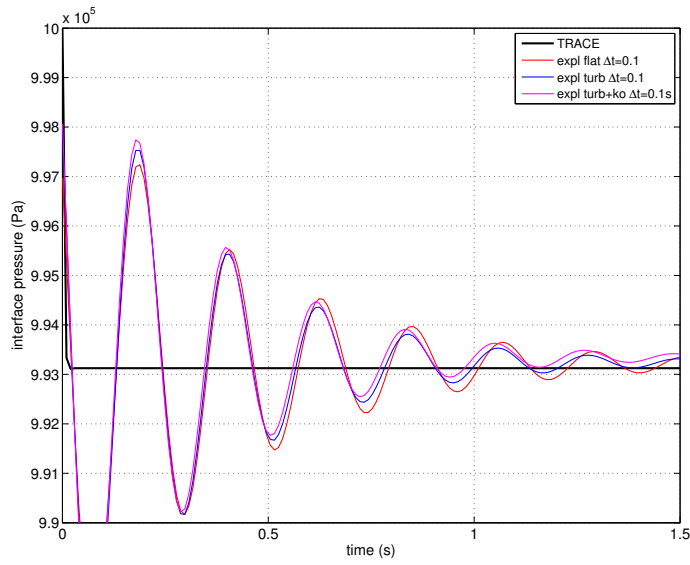Table 3.6: Data sheet for the closed-loop test.

Figure 3.31: Decay (up to 1.5 s) of the pressure peaks at the interface for the explicit coupling scheme, with different kind of velocity and turbulent-quantity profiles imposed at the interface. Constant time step of 0.1 s.
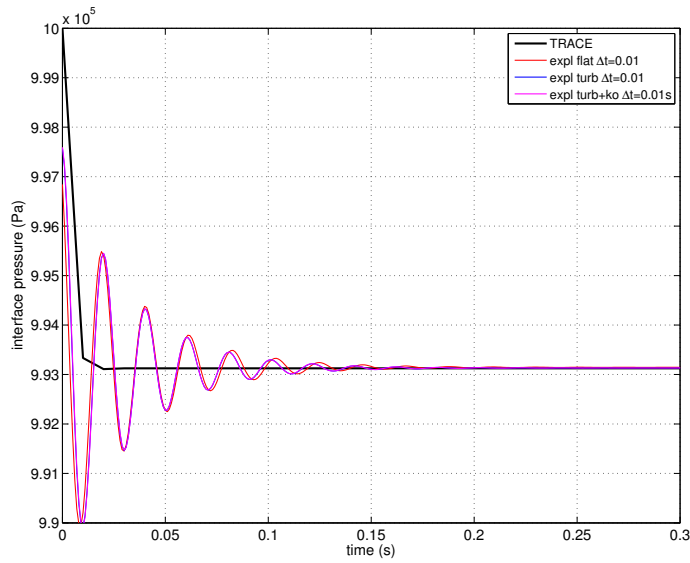

Figure 3.32: Decay (up to 1.5 s) of the pressure peaks at the interface for the explicit coupling scheme, with different kind of velocity and turbulent-quantity profiles imposed at the interface. Constant time step of 0.01 s.
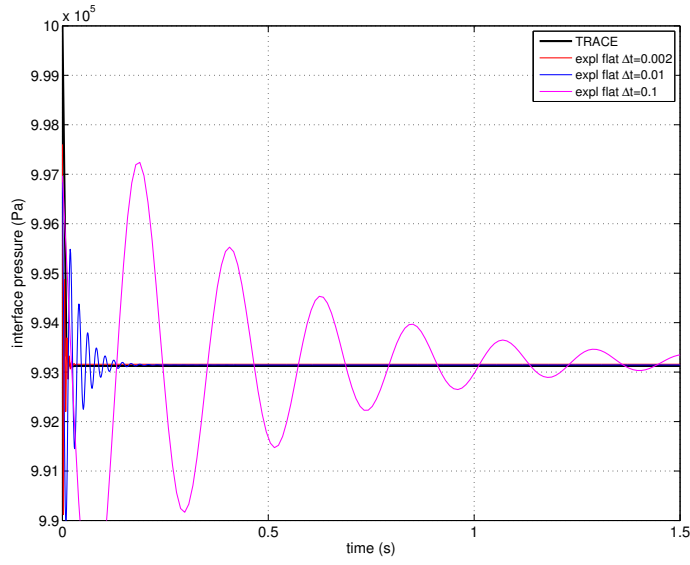
Figure 3.33: Decay (up to 1.5 s) of the pressure peaks at the interface for the explicit coupling scheme, with a flat velocity profile imposed at the interface. Different time steps are represented.
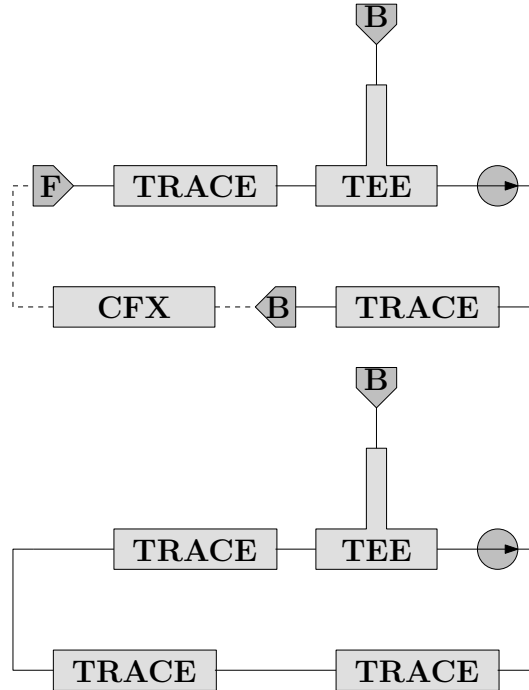

Figure 3.34: Sketch of the closed-loop configuration for the coupled simulation (top) and for the TRACE stand-alone reference simulation (bottom). B indicates a TRACE "break" (imposed pressure) component; F indicates a TRACE "fill" (imposed velocity) component.

As coupled problem, 1 m of the pipe is modeled with CFX (hexa mesh with 150k elements), while the 5 m before and after the CFX section are modeled with TRACE. Fig. 3.16 shows the mesh and Tab. 3.3 provides the related details. As for the open-loop test, the coupled solution has been compared with the results of a TRACE stand-alone simulation.

3.4.2 Convergence studies

Similarly to the open-loop configuration, sensitivities studies for the closed-loop simulation have been carried out by:

- changing the integration time step;

- changing the inlet velocity and turbulence BCs at the interface between the TRACE and CFX domains (flat velocity profile, turbulent velocity profile with standard turbulence, turbulent velocity profile with defined profiles of κ and ω)[10];

- changing the type of numerical coupling scheme (explicit or semi-implicit).

The performed sensitivity studies are summarized in Tab. 3.7. As for the open-loop test, the table is divided into three sections, one for each variation in the set of boundary conditions exchanged at the coupling interface (from TRACE to CFX). Shown are the absolute value of the maximum difference (both relative and absolute) between the given case and a reference case representative of that set (the time-converged explicit solution); moreover, for a more extensive comparison, the variance evaluated for the velocity over the whole transient is indicated. The values have been computed as follows:

- absolute difference: $\max\left(\left|v_{ref}\left(t_i\right) - v\left(t_i\right)\right|\right) \quad \forall\, 0 < t_i < t_{end}$;

- relative difference: $\max\left(\left|\dfrac{v_{ref}\left(t_i\right) - v\left(t_i\right)}{v_{ref}\left(t_i\right)}\right|\right) \quad \forall\, 0 < t_i < t_{end}$;

- variance: $\dfrac{1}{N}\sum\limits_{i=1}^{N}\left(v\left(t_i\right) - v_{ref}\left(t_i\right)\right)^2$ with $t_i = i\Delta t$.

In addition, the machine employed to perform each of the computations and the corresponding CPU time consumed are listed in the table, together with a normalization to the reference computation. Even though the computational power is different for some of the machines, a rough comparison of the time used is still possible (see App. B for more details on the technical specifications of the CPUs used). Notice that for non-flat velocity profiles and semi-implicit coupling, the computation tends to have convergence problems within a given time step and the corresponding CPU time employed cannot be easily compared with the other cases. The implicit coupling in this case takes about 5 to 10 times more time to be completed. Moreover, while for the majority of the simulations the pressure weight was zero, some of the simulations

---

[10]See footnote 9 on page 52.

Case	Velocity diff. at the coupling interface			Machine	CFX CPU time			
	|Max. (abs.)| (m/s)	|Max. (rel.)| (-)	Var. (-)		d.	h.	m.	norm.
loop, expl., SST, flat, $\Delta t = 0.01$ s	0.0	0.0	0.0	lccfd01	0	12	0	1.00
loop, expl., SST, flat, $\Delta t = 0.1$ s	$5.5 \cdot 10^{-1}$	$8.71 \cdot 10^{-2}$	$1.03 \cdot 10^{-3}$	lccfd01	0	1	21	0.11
loop, impl., SST, flat, $\Delta t = 0.01$ s	$1.48 \cdot 10^{-2}$	$2.34 \cdot 10^{-3}$	$1.15 \cdot 10^{-7}$	lccfd03	2	14	17	5.19
loop, impl., SST, flat, $\Delta t = 0.1$ s	$1.95 \cdot 10^{-1}$	$3.09 \cdot 10^{-2}$	$8.26 \cdot 10^{-5}$	lccfd07	0	13	44	1.14
loop, expl., SST, turb., $\Delta t = 0.01$ s	0.0	0.0	0.0	lccfd05	0	17	29	1.00
loop, expl., SST, turb., $\Delta t = 0.1$ s	$5.17 \cdot 10^{-1}$	$8.19 \cdot 10^{-2}$	$8.95 \cdot 10^{-4}$	lccfd05	0	1	51	0.11
loop, impl., SST, turb., $\Delta t = 0.01$ s	$1.51 \cdot 10^{-2}$	$2.39 \cdot 10^{-3}$	$5.24 \cdot 10^{-7}$	lccfd03	6	13	6	8.99
loop, impl., SST, turb., $\Delta t = 0.1$ s	$1.83 \cdot 10^{-1}$	$2.89 \cdot 10^{-2}$	$8.09 \cdot 10^{-5}$	lccfd03	0	18	39	1.07
loop, expl., SST, turb. $+ \kappa - \omega$, $\Delta t = 0.01$ s	0.0	0.0	0.0	lccfd03	0	18	19	1.00
loop, expl., SST, turb. $+ \kappa - \omega$, $\Delta t = 0.1$ s	$5.29 \cdot 10^{-1}$	$8.38 \cdot 10^{-2}$	$9.51 \cdot 10^{-4}$	lccfd03	0	1	57	0.11
loop, impl., SST, turb. $+ \kappa - \omega$, $\Delta t = 0.01$ s	$1.52 \cdot 10^{-2}$	$2.41 \cdot 10^{-3}$	$5.49 \cdot 10^{-7}$	lccfd01	7	21	36	10.35
loop, impl., SST, turb. $+ \kappa - \omega$, $\Delta t = 0.1$ s	$1.84 \cdot 10^{-1}$	$2.92 \cdot 10^{-2}$	$8.90 \cdot 10^{-5}$	lccfd05	0	21	28	1.17

Table 3.7: Systematic study of the CFX/TRACE coupling verification with a closed loop configuration.

had to be run with a different pressure weight to be able to reach convergence; this in turn influenced the convergence speed and thus the computational time.

Based on the cases run, the following conclusions can be drawn.

- The pressure profile along the whole pipe at the end of the transient (Figs. 3.35, 3.36 and 3.37), is not influenced by the integration time step and the type of coupling scheme. This is to be expected, since the steady-state solution should not be affected by such parameters. However, while the stand-alone TRACE solution predicts a linear pressure decrease along the pipe length, a clear deviation from linearity at the interface between the CFX and TRACE domains is observed at the TRACE-to-CFX interface in the coupled CFX/TRACE solution. The pressure drop in the CFX domain initially deviates from linearity due to the fact that, at the interface between the TRACE and CFX domains, the cross-section averaged velocity computed by TRACE is used in CFX as a flat (i.e. uniform) velocity profile. While in TRACE it is assumed that the flow is always fully developed, in the CFD domain the development of the imposed uniform velocity profile into a fully developed turbulent profile is computed, leading to a higher pressure drop in the coupled CFX/TRACE solution, compared to the TRACE stand-alone solution. It should be noted that the same effect does not occur at the CFX-to-TRACE interface, because there the introduction of extra information about the interface profiles is not needed; on the contrary, that same information is lost in the averaging procedure, as pointed out in Subsec. 3.2.5.

    In Fig. 3.38, it is seen that a consistent agreement between the TRACE stand-alone solution and the coupled CFX/TRACE solution is obtained when the TRACE cross-section averaged velocity is "transformed" into a fully developed (turbulent) velocity profile, and consistent information on the turbulent kinetic energy is supplied to CFX at the interface between the CFX and the TRACE domains (see curve "impl turb + ko" in Fig. 3.38). It is also important to point out that the above described TRACE-to-CFX interface effect tends to be a local effect and is often negligible if the pressure drop across the whole pipe is considered, as can be seen in Figs. 3.35-3.38.

- The time evolution of the velocity at the TRACE-to-CFX coupling interface during the transient is presented in Figs. 3.39, 3.40 and 3.41. Again, the TRACE stand-alone solution is shown together with the results of the coupled CFX/TRACE tool obtained for different integration time steps and different coupling schemes (explicit and implicit). The coupled CFX/TRACE velocity is seen to be asymptotically lower than the TRACE stand-alone solution due to the higher pressure drops computed by CFX/TRACE, as discussed in relation to Figs. 3.35-3.37. Convergence in time is supposed to be reached with a time step of 0.01 s, according to the previous experience with the open-loop case; here it is clear that a time step of 0.1 s is not sufficient to achieve convergence of the
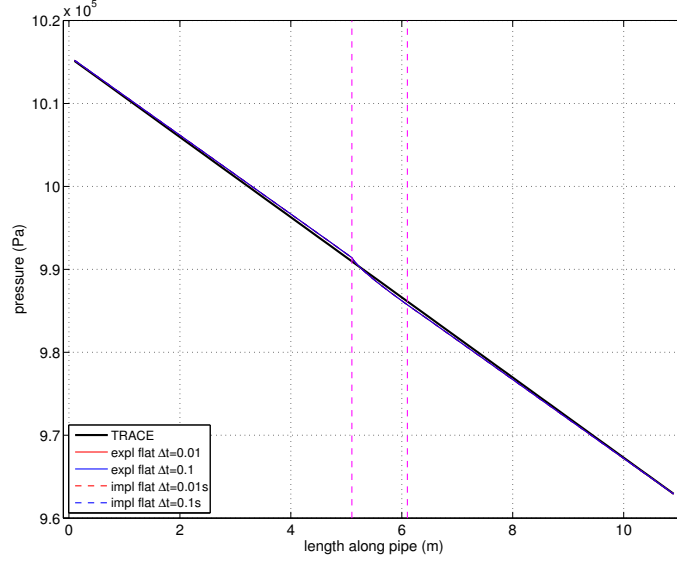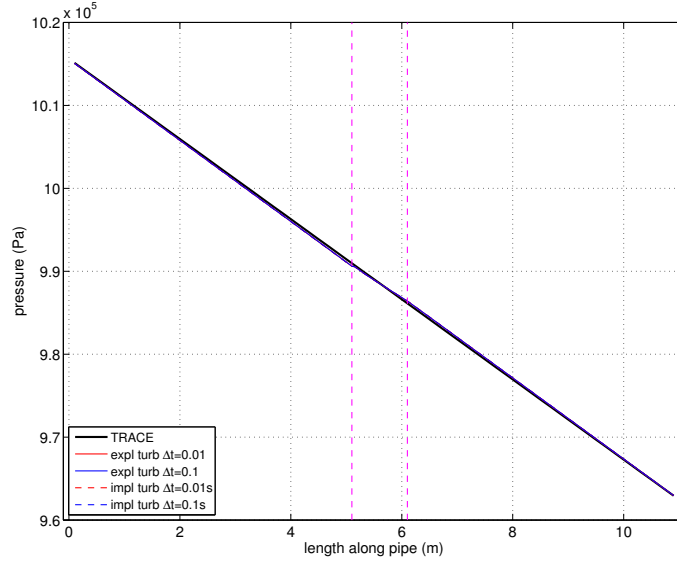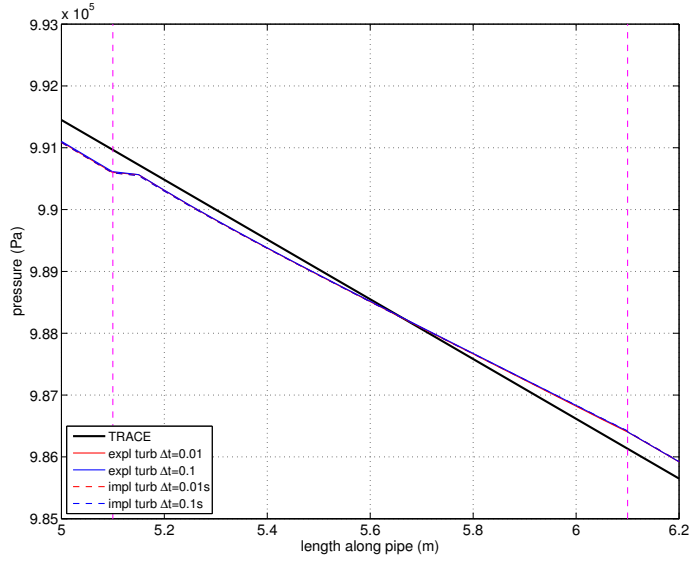
(a) Full-loop view.
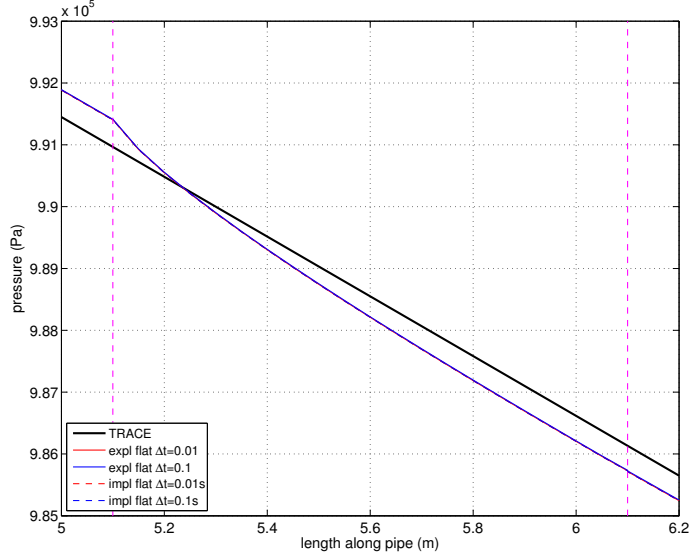
(b) Detailed view of the CFD pipe and of the two interfaces.

Figure 3.35: Profile of the pressure along the pipe under steady-state conditions, for the explicit and semi-implicit coupling schemes, with a flat velocity profile imposed at the interface. Different time steps are represented. The vertical dashed lines show the interface positions.
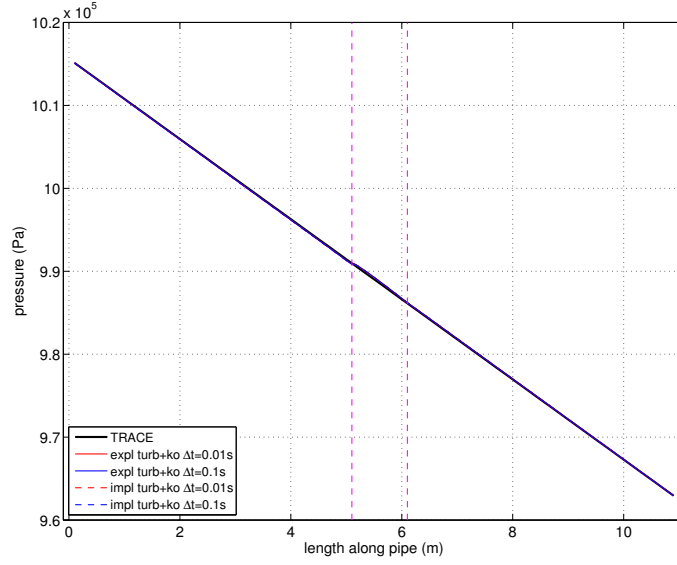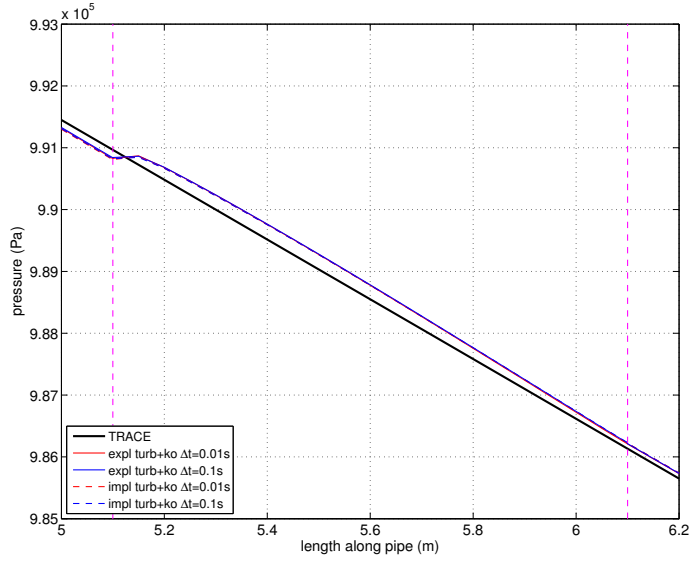
(a) Full-loop view.

(b) Detailed view of the CFD pipe and of the two interfaces.

Figure 3.36: Profile of the pressure along the pipe under steady-state conditions, for the explicit and semi-implicit coupling schemes, with a turbulent velocity profile imposed at the interface. Different time steps are represented. The vertical dashed lines show the interface positions.
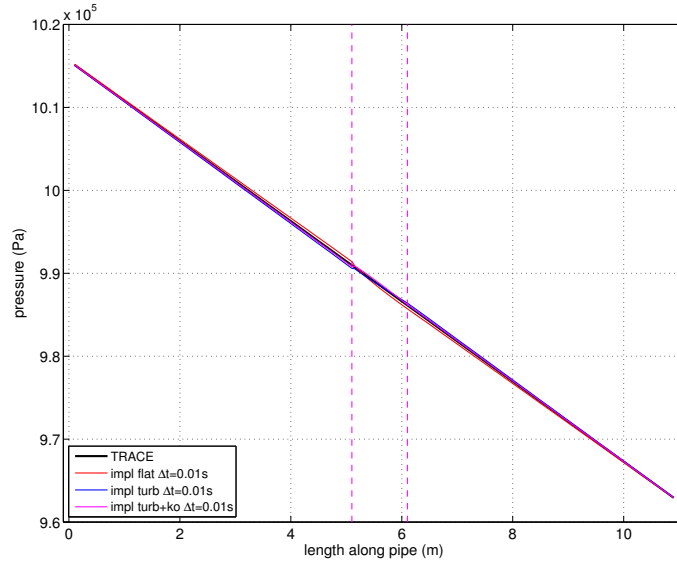
(a) Full-loop view.

(b) Detailed view of the CFD pipe and of the two interfaces.

Figure 3.37: Profile of the pressure along the pipe under steady-state conditions, for the explicit and semi-implicit coupling schemes, with a turbulent velocity profile and turbulent quantities k and ω imposed at the interface. Different time steps are represented. The vertical dashed lines show the interface positions.
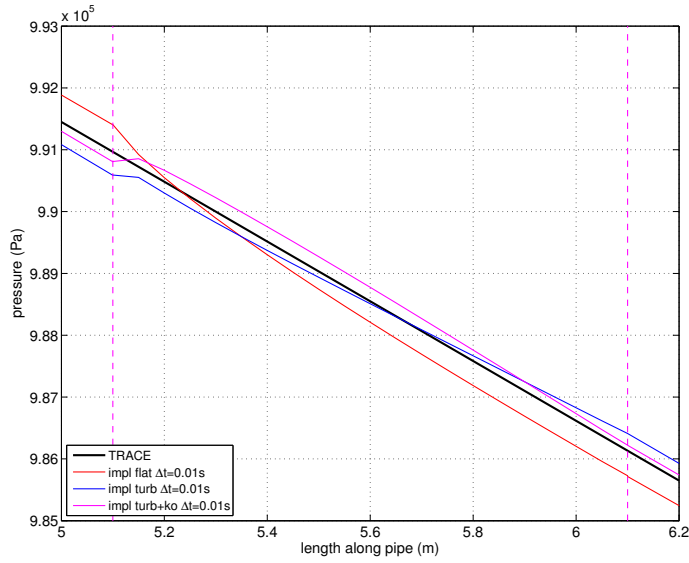
(a) Full-loop view.

(b) Detailed view of the CFD pipe and of the two interfaces.

Figure 3.38: Profile of the pressure along the pipe under steady-state conditions, for the semi-implicit coupling scheme and different kinds of velocity and turbulent-quantity profiles imposed at the coupling interface. Constant time step of 0.01 s. The vertical dashed lines show the interface positions.

results, especially with the simulations obtained with the explicit scheme. Moreover, the semi-implicit scheme proves to give better results than the explicit scheme when the same time step is used (one order of magnitude on the variance), although at the cost of an increased computational time (Tab. 3.7). In addition, the semi-implicit scheme tends to be more prone to convergence problems if the time step is too large, especially when imposing a non-flat velocity profile. In Fig. 3.42, it is seen that, consistent with the discussion of Fig. 3.38 with regard to the pressure distribution along the pipe length, satisfactory agreement is obtained between the interface velocity of the stand-alone TRACE solution and that of the coupled CFX/TRACE solution, when a turbulent velocity profile and the corresponding turbulence kinetic energy are supplied at the interface between the TRACE and CFX domains.

- Analyzing the time evolution of the pressure at the TRACE-to-CFX coupling interface (Figs. 3.43-3.46), it can be seen that some oscillations are present when the explicit scheme is employed, while with the semi-implicit scheme these oscillations decay very quickly. Important to see is also that the initial pressure spike is of greater amplitude in the semi-implicit case with respect to the explicit case, and this is one of the reasons why the robustness of the coupling is weaker for the semi-implicit scheme simulations (at least in this test). It is also clear that neither the velocity profile, nor the turbulent quantities assigned as boundary conditions at the interface, affect significantly the amplitude or the number of oscillations between the time steps.

- To evaluate the decay of the pressure oscillations at the coupling interface, an analysis has been made by fitting the peaks of the oscillations with a correlation of the type:

$$y(t) = ae^{bt} \cos(ct + d)$$

The results are shown in Figs. 3.47, 3.48 and 3.49; the fit was done only on the solutions obtained with the explicit scheme, since as explained previously the oscillations for the implicit scheme are negligible. It can be seen from Figs. 3.47 and 3.48 that the velocity and turbulence parameters used as boundary conditions do not significantly affect the decay, while the time step does, in agreement with the previous discussion; this is why in Fig. 3.49 only the flat velocity profile is used. In Tab. 3.8, the decay coefficients are shown.

3.5   Chapter summary

An on-line coupling between the CFD code ANSYS CFX and the thermal-hydraulic system code TRACE has been developed, with each code being applied to a different sub-domain
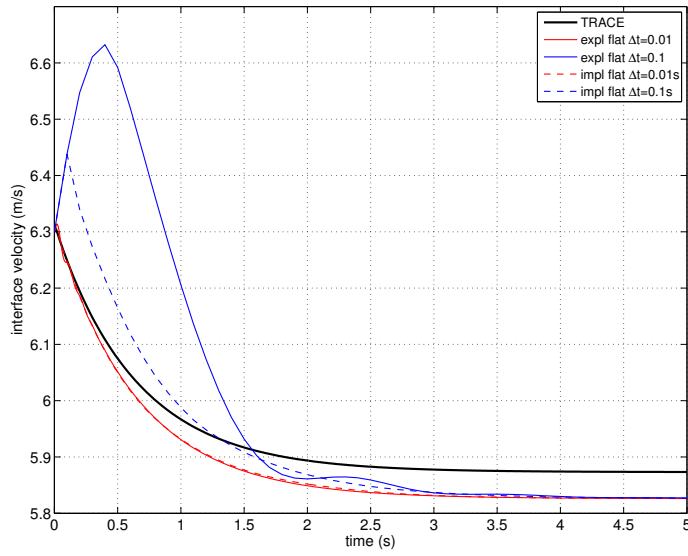
Figure 3.39: Evolution of the velocity at the TRACE-to-CFX coupling interface for the explicit and semi-implicit coupling schemes, with a flat velocity profile imposed at the interface. Different time steps are represented.

Figure 3.40: Evolution of the velocity at the TRACE-to-CFX coupling interface for the explicit and semi-implicit coupling schemes, with a turbulent velocity profile imposed at the interface. Different time steps are represented.

Figure 3.41: Evolution of the velocity at the TRACE-to-CFX coupling interface for the explicit and semi-implicit coupling schemes, with a turbulent velocity profile and turbulent quantities k and ω imposed at the interface. Different time steps are represented.

Figure 3.42: Evolution of the velocity at the TRACE-to-CFX coupling interface for the semi-implicit coupling scheme and different kind of velocity and turbulent-quantity profiles imposed at the interface. Constant time step of 0.01 s.

Figure 3.43: Evolution (up to 1 s) of the pressure at the TRACE-to-CFX coupling interface for the explicit and semi-implicit coupling schemes, with a flat velocity profile imposed at the interface. Different time steps are represented.
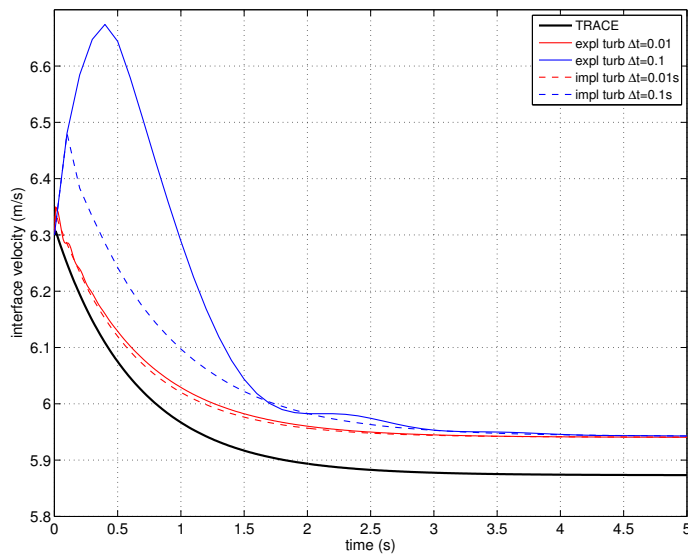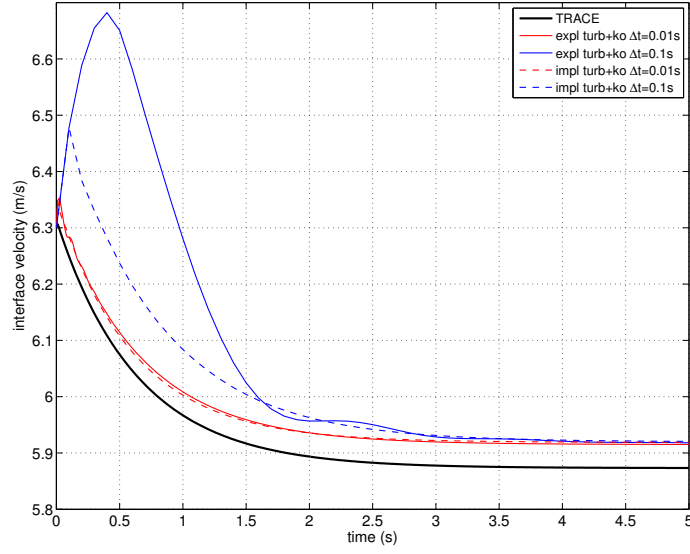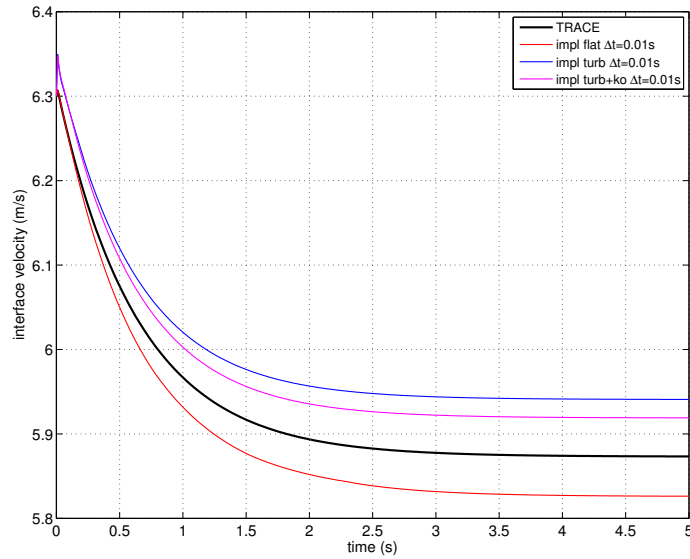

Figure 3.44: Evolution (up to 1 s) of the pressure at the TRACE-to-CFX coupling interface for the explicit and semi-implicit coupling schemes, with a turbulent velocity profile imposed at the interface. Different time steps are represented.
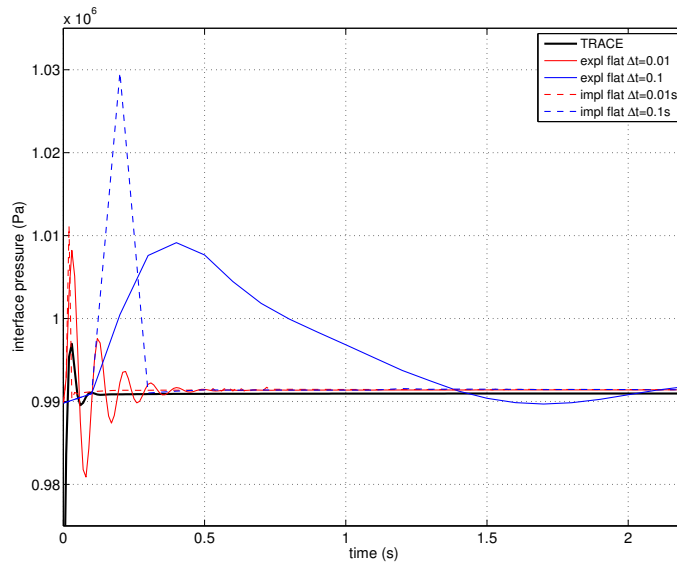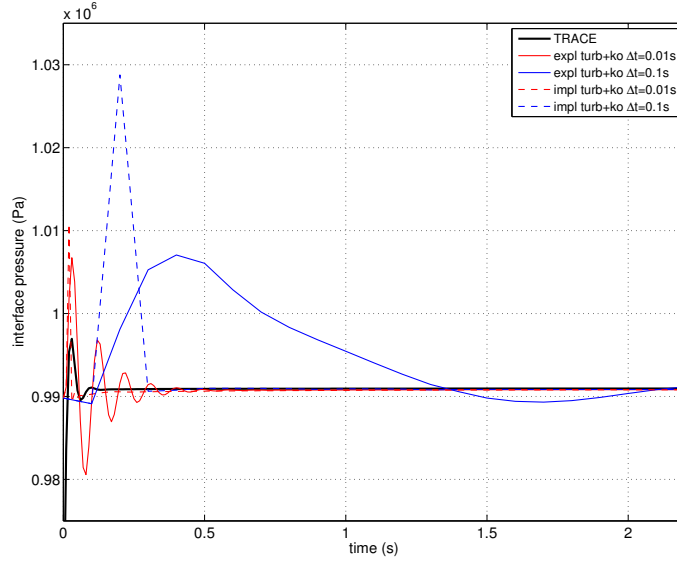
Figure 3.45: Evolution (up to 1 s) of the pressure at the TRACE-to-CFX coupling interface for the explicit and semi-implicit coupling schemes, with a turbulent velocity profile and turbulent quantities k and ω imposed at the interface. Different time steps are represented.
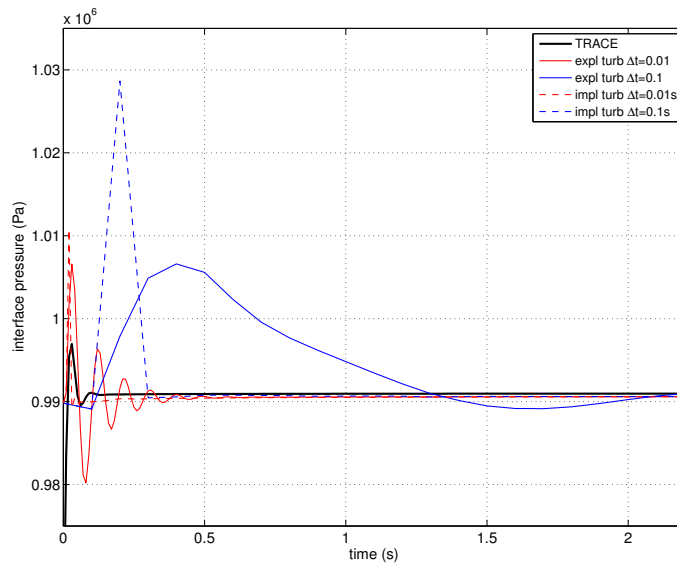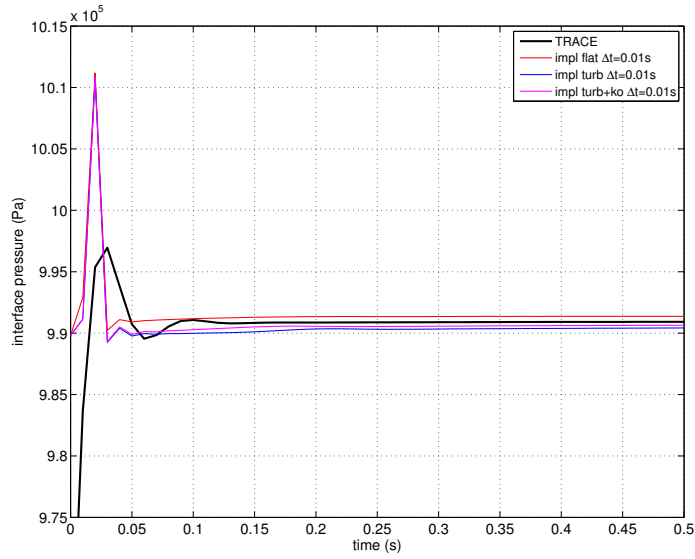

Figure 3.46: Evolution (up to 0.25s) of the pressure at the TRACE-to-CFX coupling interface for the semi-implicit coupling scheme and different kinds of velocity and turbulent-quantity profiles imposed at the same interface. Constant time step of 0.01 s.
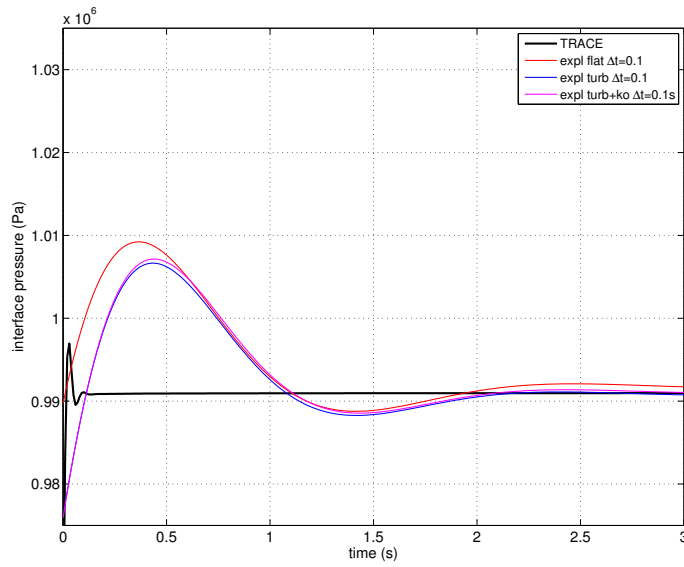
Figure 3.47: Decay (up to 1.5 s) of the pressure peaks at the TRACE-to-CFX coupling interface for the explicit coupling scheme, with different kinds of velocity and turbulent-quantity profiles imposed at the interface. Constant time step of 0.1 s.
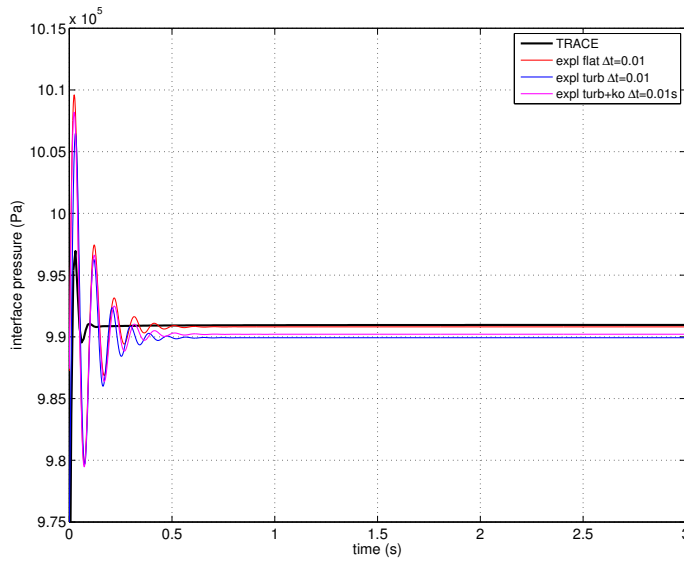
Figure 3.48: Decay (up to 1.5 s) of the pressure peaks at the TRACE-to-CFX coupling interface for the explicit coupling scheme, with different kinds of velocity and turbulent-quantity profiles imposed at the interface. Constant time step of 0.01 s.

Case	Decay constant b (1/s)	Frequency c (rad/s)	Period $2\pi/c$ (s)
loop, explicit, SST, flat, $\Delta t = 0.01$ s	-1.07E+01	6.46E+01	9.73E-02
loop, explicit, SST, flat, $\Delta t = 0.1$ s	-1.65E+00	2.76E+00	2.27E+00

Table 3.8: Time decay constant b, frequency c and oscillation period in the form $ae^{bt}\cos(ct + d)$ for the explicit case with flat velocity profile.
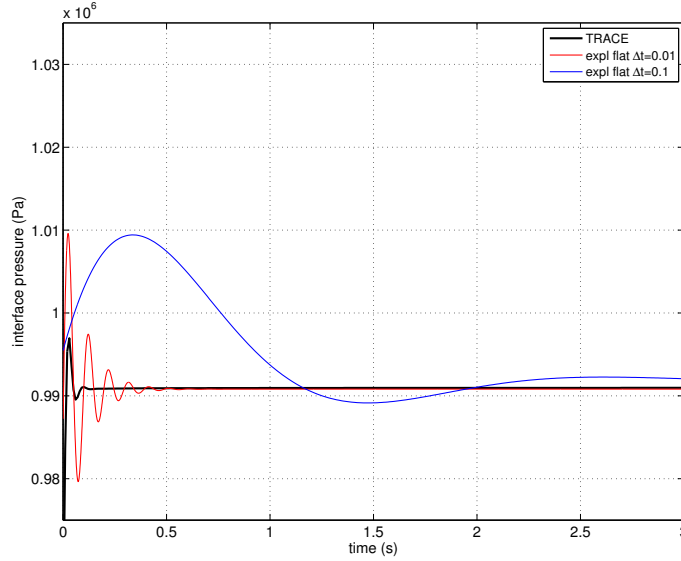
Figure 3.49: Decay (up to 1.5 s) of the pressure peaks at the TRACE-to-CFX coupling interface for the explicit coupling scheme, with a flat velocity profile imposed at the interface. Different time steps are represented.

of the system to be simulated. Both explicit and semi-implicit coupling schemes have been implemented.

The coupling has been verified with two configurations, an open-loop and a closed-loop case, respectively. Parametric studies have been performed, and results have been compared to stand-alone TRACE simulations. Different findings have been made, in particular the strong influence of the boundary conditions at the interface between the one-dimensional and the three-dimensional simulations. Velocity and turbulent-quantity profiles have to be reconstructed or "guessed" from 1D averages before being applied to the 3D mesh, and this may not always be as straightforward as under controlled test conditions.

Another issue that may arise is the convergence at the interface between the domains computed by the two codes. While simulations obtained with the semi-implicit scheme guarantee better results than those obtained with the explicit scheme and with a smaller time step, these are, however, more prone to convergence problems when larger time steps are employed. An appropriate "tuning" of the simulation parameters (e.g. number of internal iterations, number

of interface iterations, weighting of the pressure, etc.) is very important for optimizing the required CPU time, without sacrificing accuracy and stability of the solution.

Following the systematic numerical investigations reported here, the developed coupled tool can be tested against experimental data. This has first been done for a double T-junction configuration (as described in Chap. 4) and later on for the FLORIS facility (as discussed in Chap. 6).

Chapter 4

Coupled code validation: the double T-junction experiment

In this chapter, the initial validation of the coupled CFX/TRACE code against experimental results is presented. A special mixing loop was built at PSI for this purpose. Sec. 4.1 describes the experimental facility, while Sec. 4.2 is dedicated to the tests and the experimental results. In Sec. 4.3, the comparison is discussed between the experimental results and the simulations carried out with the stand-alone CFX and TRACE codes, as also with the coupled CFX/TRACE code. The comparison with the experimental data points out the improvement of the coupled-code solution over the separate use of the individual codes.

4.1 Experimental facility

The experimental set-up consists of two separate loops joined by a double T-junction component (see Fig. 4.1). Two recirculation pumps are present, in the side and main loop, respectively. The latter is in fact an open loop which gets/discharges water from/to the laboratory water distribution system. A tracer can be injected either in the main loop or in the side loop. The double T-junction component is made of Plexiglas and has an inner diameter of 5 cm. The distance between the axes of the junction side connections is 13 cm, and both connections have the same diameter as the main pipe. The system is operated at atmospheric pressure. The working fluid is tap water, while desalinated water is used as tracer. Wire-mesh sensors [65, 66], installed at several locations in the facility, allow the measurement of the two-dimensional mixing patterns in a given pipe cross-section (16x16 measuring points in a single cross-section) with a spatial resolution of 3 mm and a measuring frequency up to 10 kHz. The locations of the wire-mesh sensors are shown schematically in Fig. 4.1.
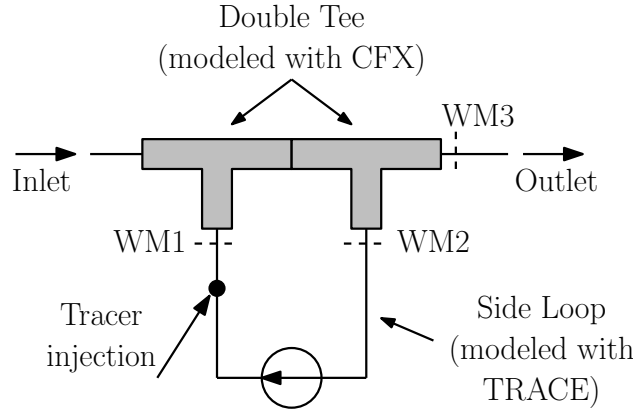
Figure 4.1: Simplified sketch of the mixing set-up with tracer injection in the side loop. WMs are the wire-mesh sensors.

4.2 Tests

4.2.1 Description of the tests

After setting up the desired mass flow rate ratio between the main loop and the side loop, a small quantity of desalinated water (between 10 and 15 ml) was injected in the side loop, just before the wire-mesh sensor. Within the double T-junction component, three-dimensional effects come into play, which determine the time-dependent tracer distribution in the two loops. With the aid of the wire-mesh sensors[1] (used with a sampling rate of 1 kHz) it was possible to measure how the tracer injected in the side loop is split at the T-junction location between main and side loops (by measuring the tracer concentration at the location of WM2 and WM3, respectively, as indicated in Fig. 4.1). The amount of tracer which traveled in the side loop was recirculated into the double T-junction component, so that its splitting among side and main loop repeated over several cycles, until all the tracer was expelled from the system through the main loop discharge.

4.2.2 Experimental results

Several tests were carried out by varying the mass flow rate in the main loop and in the side loop. Due to the fact that the tracer was injected in the side loop, and in view of the topology of the three-dimensional velocity field which develops in the double T-junction component, the tracer had the tendency to flow into the side loop.

In Fig. 4.2, the normalized cross-section averaged tracer concentration as a function of time has been plotted for the three mesh sensors (located in the positions shown in Fig. 4.1) for the case with 1:1 mass flow rate ratio between main and side loop, with a volumetric flow rate of 80 l/min in each loop. From the starting time, the injected concentration measured

---

[1] More details on the calibration of the wire-mesh sensors will be presented in Subsec. 6.3.2.
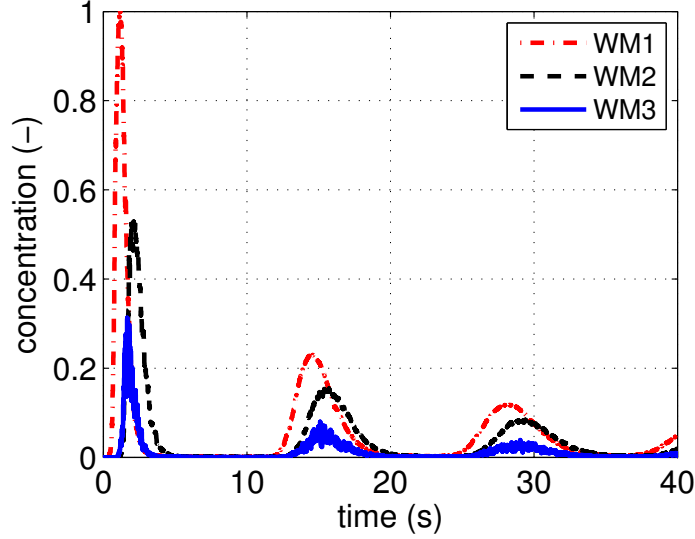
Figure 4.2: Evolution of the experimental tracer concentration (normalized) at the wire-mesh sensor positions; mass flow rate ratio between loops is 1:1.

with WM1 (red line) is seen to be split between the two junction branches WM2 and WM3 with different maximum values (first group of plugs on the left in Fig. 4.2). In particular, a larger quantity of tracer goes into the side branch, where the recirculation loop starts. This quantity, recorded by sensor WM2 (black line), is then recirculated and goes back as injected quantity in sensor WM1 as another plug. The quantity crossing sensor WM3 (blue line) is instead lost to the drain. From the second group of plugs, it can be seen that the shape of the recirculated plug changes, i.e. it becomes lower and wider because of the diffusion (compare the black line in the first group of plugs against the red line in the second one). Again, the tracer is split at the junction and the quantity of tracer recorded by WM2 is recirculated a third time with the same trend as described above. The case presented here has been used as the principal validation basis for the simulations. These, together with their comparison with measurements, are reported in the following section.

4.3   Simulations and comparison with measurements

To gain insights into the performance of the newly developed coupled tool with respect to the individual codes used separately, the double T-junction experiment was simulated not only with the coupled CFX/TRACE code, but also with CFX and TRACE as stand-alone codes.

4.3.1   CFX stand-alone simulations

A 3D CFX model of the double T-junction has been developed (Fig. 4.3). The symmetry in the x-z plane (referring to Fig. 4.3) has been exploited when generating the CFD mesh, thus
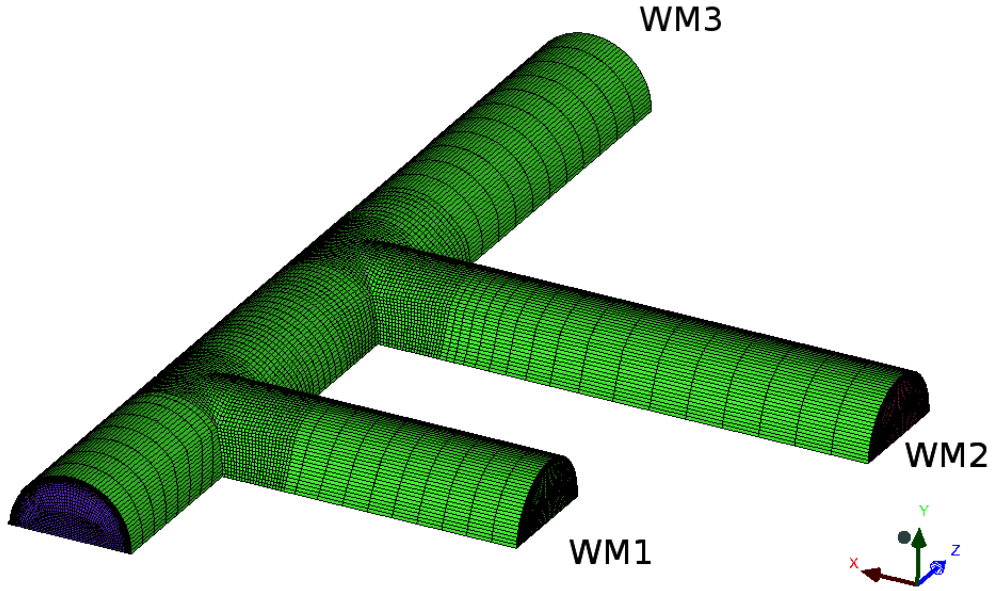
Figure 4.3: CFX mesh for the double T-junction experiment.

effectively cutting by half the size of the model to be computed and reducing the required computational time. Finely refined mesh zones have been created in the proximity of the two junctions in order to better capture the velocity field and the vortices that develop in these regions. In addition, the outlet branch (to WM2) has been meshed over a larger length in order to capture the entire length of the vortex that develops in the side branch and to prevent this vortex from cutting into the outlet surface (WM2 in Fig. 4.3). In this way, the axial velocity (x-direction in Fig. 4.3) over the entire cross-section of the outlet surface WM2 has the same sign. This can be better understood by looking at the velocity field which develops within the double T-junction component at the conditions of the experimental test selected for the code validation (see Fig. 4.4).

A volumetric flow rate of 80 l/min has been imposed at the two inlets (locations "Inlet" and "WM1" in Fig. 4.1) and at the outlet connected to the side loop (location "WM2" in Fig. 4.1). At the other outlet ("WM3" in Fig. 4.1), a constant pressure has been set up. The tracer concentration has been modeled by using a user-defined volumetric variable (i.e. expressed in kg/m^3), subject to the CFX standard non-diffusive transport model [64]. The non-diffusive model (i.e. zero kinetic diffusivity) is justified by the fact that the tracer has the same fluid properties as the main fluid and that the residence time of the fluid in the facility is negligible in comparison to the diffusion time scale. In such a model, the only diffusive effect comes from turbulence (i.e. turbulent diffusivity).

Sensitivity studies were carried out in order to investigate the effects of different parameters such as the integration time step, the mesh size, the turbulence model, the tracer

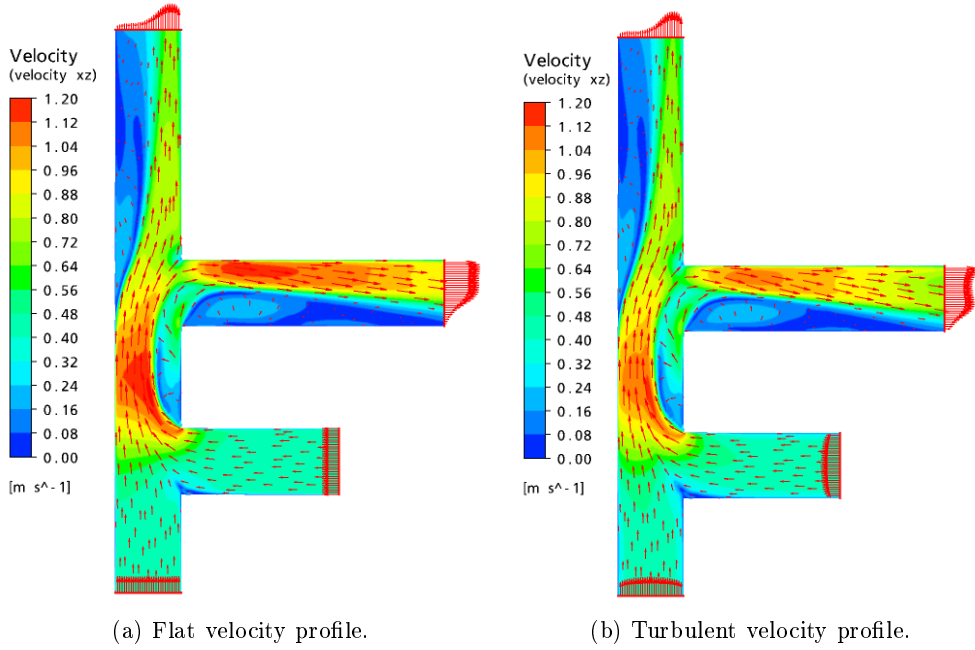(a) Flat velocity profile. (b) Turbulent velocity profile.

Figure 4.4: Velocity magnitude and vector field in the CFX stand-alone steady-state simulations, obtained with two different inlet velocity profiles.

concentration profile at the inlet boundary, as well as the inlet velocity profiles. The CFX results obtained in correspondence to the three measuring locations for the cross-section averaged tracer concentration are shown in Figs. 4.5a and 4.6b. It can be observed that the time step size and the mesh size have little influence on the solution of the time-dependent, cross-section-averaged tracer concentration[2], allowing the use of a relatively coarse mesh (few hundred thousand elements) and relatively large integration time steps (0.1 s) and thus significantly reducing the computational time required for the simulations. The effect of the inlet concentration profile employed for the tracer (see Fig. 4.5a) is also small.

A remarkable effect, however, is observed when a more realistic (i.e. fully developed turbulent) velocity profile is imposed at the loop inlets (locations "Inlet" and "WM1" in Fig. 4.1), instead of a simple flat profile (see Fig. 4.6a), in agreement to what has been seen in Chap. 3. The fully developed turbulent velocity profile was obtained by running a separate CFD simulation for a short pipe having the same diameter as the T-junction loop pipe, and by imposing periodic boundary conditions at the inlet and outlet sections. The velocity field which develops in the double T-junction component when using a flat velocity profile over the inlet cross-sections or a fully developed turbulent velocity profile, is shown in Figs. 4.4a and 4.4b, respectively. The employment of the SST model ($\kappa - \omega$ based) brings additional

---

[2]Plots could be provided of the concentration measured over the entire cross-section of the channel with the wire-mesh sensor, to be compared with the cross-section concentration computed by the CFD code. However, as shown later in this section, the distribution of the tracer over the channel cross-section does not have a significant influence on the results. Therefore, such a comparison has been omitted for the sake of simplicity.

improvement, with respect to the $\kappa - \varepsilon$ model (see Fig. 4.6b). This is because the vortices, which develop at the location of the T-junction and which are responsible for the transport of the tracer in the side junction, are better caught by the SST model [67]. As a matter of fact, it is well known that $\kappa - \omega$ formulations are better able to capture the flow structure in the proximity of walls, with respect to $\kappa - \varepsilon$ formulations, which are instead better suited for the bulk of the flow. This is the reason why the SST model has been developed such to use a $\kappa - \omega$ formulation in the proximity of the walls, and a $\kappa - \varepsilon$ formulation in the flow bulk, with a blending function for the transition between the two models.

The largest disagreement between CFX results and experimental data is seen at the location WM3. In order to understand this result, it has to be pointed out that the cross-section averaged tracer concentration is not a direct measure for the mass of tracer which is effectively transported in the main and side loops. At the location WM3, the velocity profile is much more unstable, confirmed by the fact that larger fluctuations in the measured concentration signal are observed at this location. Thus, while excellent agreement is obtained for the location WM2, the CFD code has more difficulty in reproducing the correct velocity profile for WM3, resulting thus in an erroneous cross-section averaged tracer concentration. All in all, the CFD code is able to predict that the cross-section averaged tracer concentration is lower in the WM3 location than in the WM2 location, even if the flow distribution between the two loops is 1:1.

4.3.2 TRACE stand-alone simulations

A complete 1D model of the experimental set-up has been developed for TRACE (Fig. 4.7) as well. The model includes:

- side loop, containing a pump and a valve with corresponding control system aimed at controlling the mass flow rate; this part of the model has been used also for the coupled CFX/TRACE simulations;

- double T-junction component (modeled with CFX in the coupled solution);

- tracer injection system;

- control system with a pump and a valve to control the mass flow rate in the side loop.

The TRACE solution for the time-dependent tracer concentration at location WM1, after the first recirculation in the double T-junction component, is presented in Fig. 4.8 for different spatial discretizations of the 1D nodalization. It can be observed that the solution does not converge even when using a very fine mesh, because the numerical scheme used in TRACE for the tracer transport is strongly affected by numerical diffusion. Accordingly, for the simulations presented in Subsec. 4.3.3, a pragmatic discretization of 10 mm has been employed, simply since this yields results closer to the experimental values (i.e. the numerical diffusion
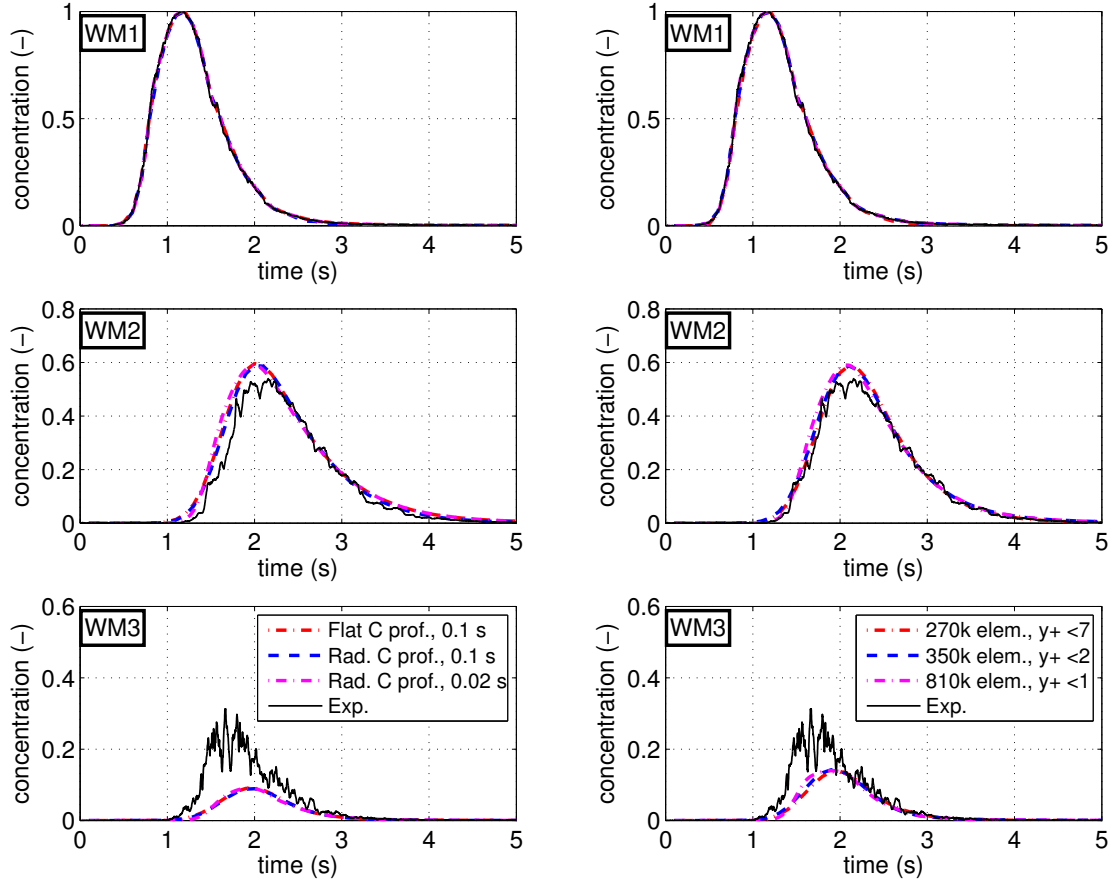
(a) Simulation results for the inlet tracer concentration (WM1, top) and for the concentration splitting in the T-junction in the side loop (WM2, center) and in the main loop (WM3, bottom) at the WM-sensor locations. Parametric study for different inlet concentration (C) profiles and for different time steps; turbulence model is SST and mesh size is 350k elements.

(b) Simulation results for the inlet tracer concentration (WM1, top) and for the concentration splitting in the T-junction in the side loop (WM2, center) and in the main loop (WM3, bottom) at the WM-sensor locations. Parametric study for different mesh sizes. The y+ parameter is the dimensionless distance from the wall, based on the grid size and on the flow characteristics; turbulence model is SST and inlet velocity profile is turbulent.

Figure 4.5: CFX stand-alone simulations of the tracer injection and first splitting (pt. 1).

in this case may be considered as compensating for the physical tracer diffusion which results from turbulent mixing and which is not modeled in TRACE). In Chap. 5, improvements to the numerical scheme of the TRACE solute tracking equation are presented, aimed at the reduction of numerical diffusion in the TRACE solution.

In Fig. 4.9, a comparison is presented between experimental data, the stand-alone TRACE simulation (with 10 mm spatial discretization) and the CFX stand-alone simulation. For the CFX simulation, the SST model has been selected to model turbulence, and a fully developed turbulent velocity profile is imposed as boundary condition at the inlets. CFX correctly predicts, though with slight overestimation, that a higher amount of tracer is recirculated in
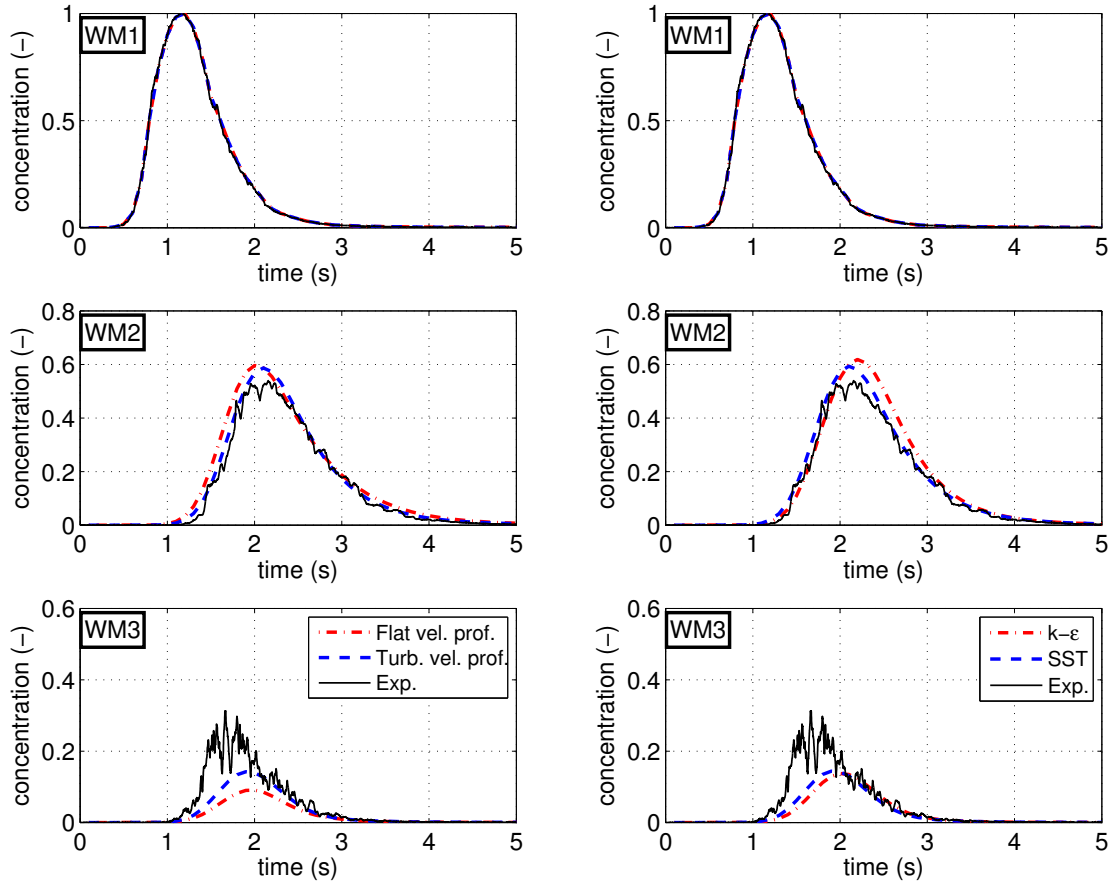
(a) Simulation results for the inlet tracer concentration (WM1, top) and for the concentration splitting in the T-junction in the side loop (WM2, center) and in main loop (WM3, bottom) at the WM-sensor locations. Parametric study for different inlet velocity profiles, flat and turbulent; turbulence model is SST and mesh size is 350k elements.

(b) Simulation results for the inlet tracer concentration (WM1, top) and for the concentration splitting in the T-junction in the side loop (WM2, center) and in the main loop (WM3, bottom) at the WM-sensor locations. Parametric study for different turbulence models; mesh size is 350k elements.

Figure 4.6: CFX stand-alone simulations of the tracer injection and first splitting (pt. 2).

the side loop, while TRACE simply splits the tracer using the mass flow rates as weights (for the particular case under investigation, where a mass flow rate ratio of 1:1 is used, TRACE predicts that 50% of the tracer is recirculated in the side loop). It is thus clear that the combination of a 1D code, such as TRACE, with a CFD code can be expected to provide a considerable improvement in the prediction capabilities for cases where three-dimensional effects are dominant.

4.3.3 Coupled CFX/TRACE simulations

The aim of the coupling is to achieve a more detailed description of the tracer splitting in the T-junction component using CFX, while maintaining the capability of simulating a transient

with several recirculation cycles of the tracer in the side loop.

The simulation has been made with the same three-dimensional geometry model as used for the CFX stand-alone simulations (Subsec. 4.3.1), coupled at the boundaries corresponding to the side loop with the TRACE model of the loop (Subsec. 4.3.2). The injection is simulated as a concentration profile over the inlet boundary from the side loop in CFX; the data are taken from the experiments. The boundary conditions in the TRACE model are imposed with two BREAK components (a BREAK component is used to impose a pressure boundary condition), since the velocity in the side loop is already imposed by controlling the valve downstream of the pump. The velocity of the fluid in the loop is then used as boundary condition for the CFX openings connected to the side loop. The cross-section-averaged velocity provided by TRACE is converted into a fully developed turbulent velocity profile (keeping the same average velocity) before passing this information to the CFX inlet interface. A flat velocity profile approximation would be the simplest to implement, but it would lead to an inaccurate solution, as was shown in Fig. 4.6a. The explicit coupling numerical scheme has been selected for the CFX/TRACE simulation, with a maximum of three CFX internal iterations per time step. An integration time step of 0.05 s has been used, the employed CFX mesh has 350k elements, and the turbulence model is the SST (shear stress transport). The mesh size chosen for TRACE is 10 mm, in order to reduce the numerical diffusion, which would strongly affects
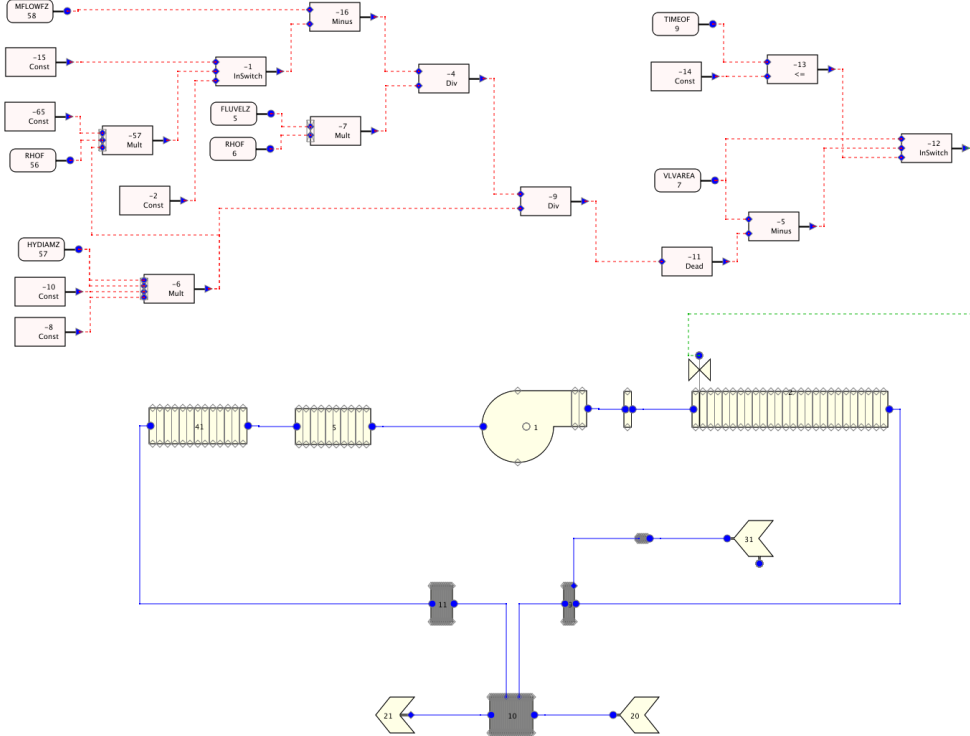

Figure 4.7: TRACE SNAP model of the double T-junction experiment, together with the control system to set the mass flow rate in the side loop.
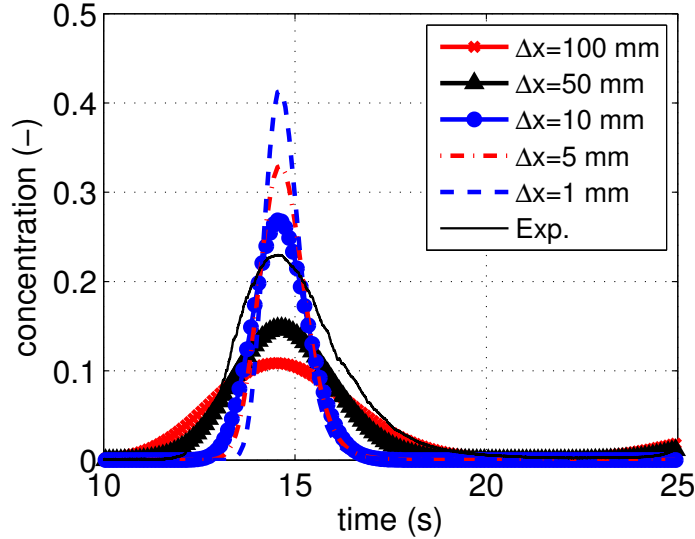
Figure 4.8: Evolution of the normalized tracer concentration at the side loop outlet (WM1) for a TRACE stand-alone simulation, compared with experimental data. Parametric study for different TRACE mesh sizes, with time step fixed at 0.001 s.

the computed tracer concentration, as was seen in Fig. 4.8.

In Fig. 4.10, the results of the coupled CFX/TRACE simulation are presented for the second and third circulations of the injected tracer plug. Obviously, the results for the first circulation (from 0 to 5 s) are identical to those obtained with the stand-alone simulations, already reported in Fig. 4.9. The experimental data are presented as well. Again, TRACE predicts a 50% splitting of the tracer plug at the T-junction location (positions WM2 and WM3). This result is to be expected, since the flow conditions are steady, with the mass flow rate ratio between the two loops remaining fixed at 1:1 during the entire experiment. It must be pointed out that, while the tracer diffusion in TRACE is symmetric, the experimental results show a larger diffusion in the direction of the flow (see Fig. 4.10). This results from turbulent mixing, and the phenomenon is well caught by the CFD simulation.

In Fig. 4.11, the time integral of the cross-section averaged tracer concentration is shown over the entire period considered for the simulation. Also here, it is clearly visible that the TRACE concentration is split in half between the two loops (the value of the integral is the same for WM2 and WM3). Moreover, the integral increases at the same time for the experiment, the stand-alone TRACE, and the coupled CFX/TRACE simulation, demonstrating that the coupling correctly simulates the transport of the tracer plug in the system. Finally, it is possible to see the effect of the diffusion at the plug borders, which reduces the steepness with which the integral increases at the start of each recirculation cycle. For location WM1, where the assumption of a fully developed turbulent velocity profile is justified by the configuration of the experimental set-up, excellent agreement is obtained with the CFX/TRACE coupled tool. This indicates that CFX correctly predicts the amount of tracer mass which is
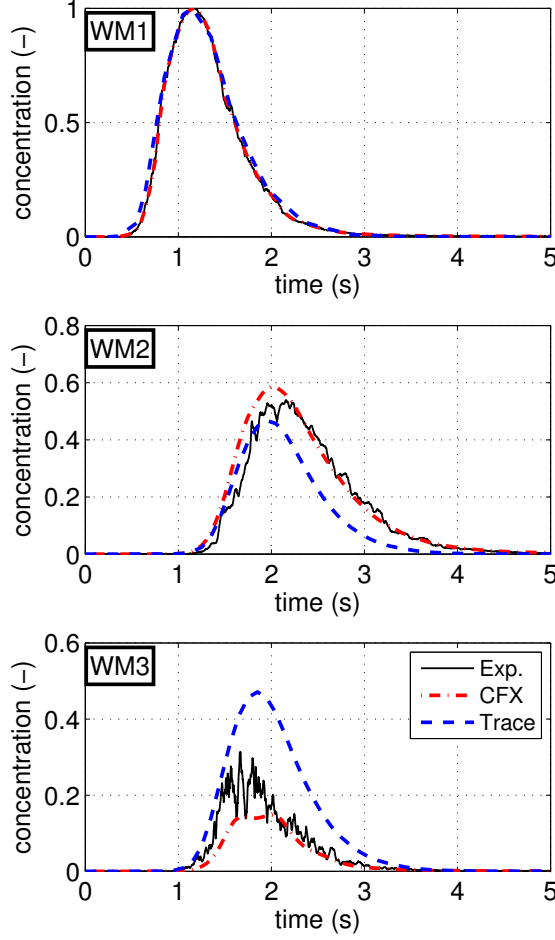
Figure 4.9: Stand-alone CFX and TRACE simulation results for the inlet tracer concentration (WM1, top) and for the concentration splitting in the T-junction in the side loop (WM2, center) and in the main loop (WM3, bottom) at the WM-sensor locations. Comparison between CFX, TRACE and experimental data.

recirculated in the side loop. The fact that the same agreement is not obtained for the locations WM2 and WM3 lies in the less accurate prediction of the velocity profiles at these two locations. Unfortunately, the experimental concentration integral cannot be weighted with the velocity profile, as the latter is not available in the experiment. The fact that a correct prediction of the total mass of tracer recirculated in the side loop is obtained, but that an incorrect cross-section averaged concentration results in the locations WM2 and WM3, points to a disagreement between the experimental and calculated velocity profiles. This disagreement is largest for the WM3 location.
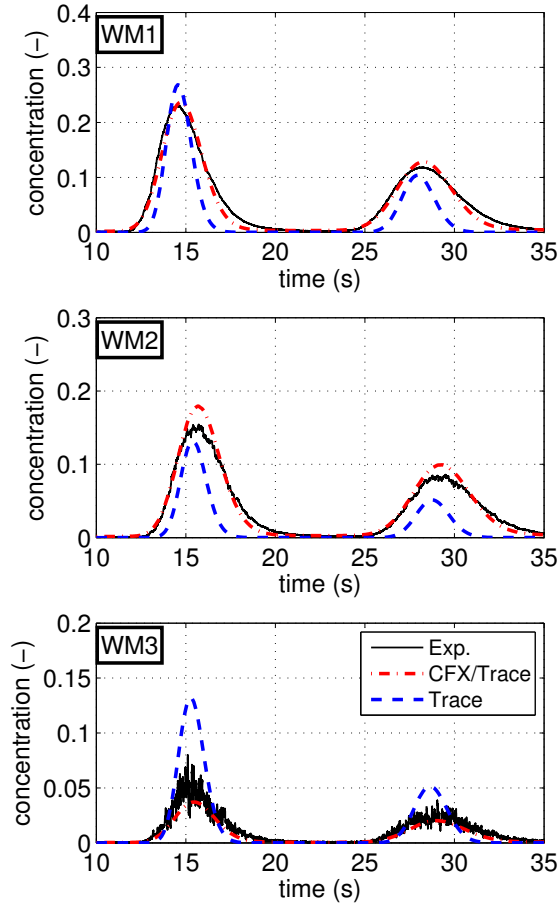
Figure 4.10: Simulation results for the second and third circulations of the tracer. Plots are shown for the concentration at the inlet (WM1, top) and for the concentration splitting in the T-junction in the side loop (WM2, center) and in the main loop (WM3, bottom) at the WM-sensor locations. Comparison between coupled CFX/TRACE, stand-alone TRACE and experimental data.

4.4 Chapter summary

The coupling between the one-dimensional best-estimate code TRACE and the three-dimensional CFD code CFX has been presented and tested on a simple experimental mixing set-up at PSI. The reported results are promising and clearly show the advantages of a 3D simulation over a 1D approximation to capture the complexity of the mixing phenomena when 3D phenomena are important, as in the studied case of the double T-junction component. Finally, the analyses have pointed out that the TRACE prediction of a tracer transport is strongly affected by numerical diffusion. Further improvements in the tracer transport equations of the TRACE code are clearly needed, and the efforts carried out in this direction are presented in Chap. 5. There, the implementation in TRACE of a higher order numerical scheme for the solution of the tracer equation is discussed.

Figure 4.11: Simulation results for the tracer concentration integral at the inlet (WM1, top), in the side loop (WM2, center) and in the main loop (WM3, bottom) at the WM-sensor locations. Comparison between coupled CFX/TRACE, stand-alone TRACE and experimental data.

Chapter 5

Improvement of the one-dimensional solute tracking discretization scheme in TRACE

The system code TRACE adopts a finite-volume, first-order upwind discretization scheme to solve the dissolved-solute convection equation. Such a scheme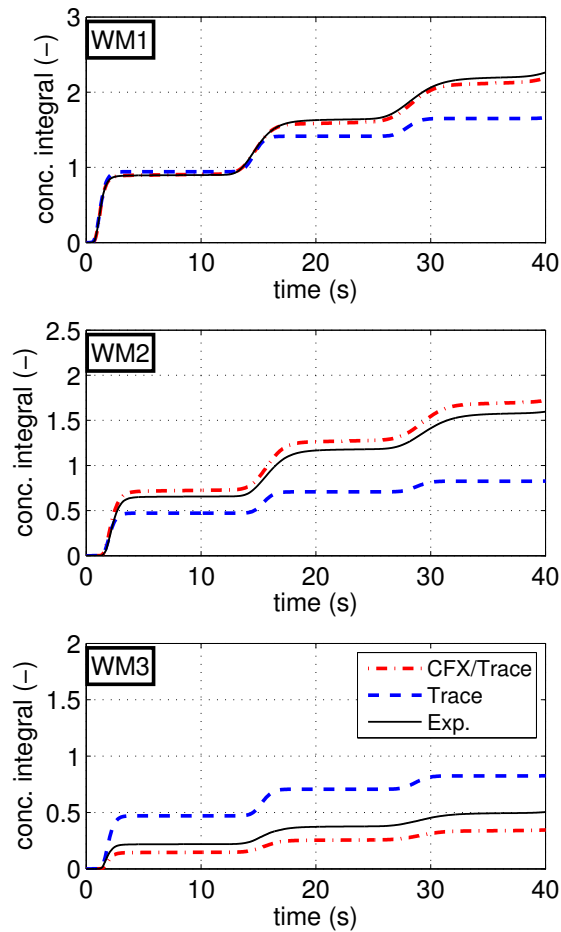 strongly suffers from numerical diffusion (as pointed out in Chap. 4), which can be a significant drawback in analyzing certain safety relevant scenarios in nuclear power plants, e.g. boron dilution (see Chap. 2).

In the present chapter, a modification of the numerical scheme of the TRACE one-dimensional solute tracking equation is presented. The work is largely based on the past studies of Leonard [68, 69, 70] on high order computational schemes, which have previously been used by Macian [71, 72, 73, 74] for the TRAC-PF1/MOD2 code.

Sec. 5.1 describes the features of the solute tracker currently implemented in TRACE and its current limitations. Sec. 5.2 is a brief review of the available discretization methods that can be adopted for the solute tracking equation. Sec. 5.3 addresses the strategy adopted to implement an explicit numerical scheme into a semi-implicit code like TRACE. Sec. 5.4 deals with the implementation of the so-called QUICKEST[1] scheme in TRACE and Sec. 5.5 shows how the ULTIMATE[2] limiter can be applied in our particular case.

Sec. 5.6 compares the new and old schemes with the analytical solutions for a propagating Gaussian wave and for a step function. Sec. 5.7 adopts the new QUICKEST-ULTIMATE discretization for the simulations carried out in Chap. 4 and compares the new and old results, while Sec. 5.8 tests the newly developed scheme against experimental data available in the German PKL facility.

---

[1] Quadratic Upwind Interpolation for Convective Kinematics with Estimated Streaming Terms.
[2] Universal Limiter for Transient Interpolation Modeling of the Advective Transport Equation.

5.1 Current solute tracker in TRACE

TRACE includes the capability of tracking a solute field, in order to simulate the transport of a soluble neutron poison in the primary loop coolant, so that its effect can be taken into account in the evaluation of the reactivity feedbacks to the core power. According to the available documentation [8, 75], the following assumptions are made in the modeling of solute convection:

1. The solute does not affect the hydrodynamics directly (liquid properties, heat transfer). However, the amount of dissolved or plated-out solute in the core affects the neutronics, and therefore indirectly the liquid flow through the change in the reactor heat generation.

2. Plated-out solute affects only the neutronic reactivity feedback. In fact it may affect the surface friction and the wall heat transfer, but this is not modeled by TRACE.

3. Plating-out and re-dissolution occur at an infinite rate.

4. Solubility is a function of the temperature only, and the dependence is considered linear over the defined temperature range.

The equation governing the solute convection is a one-dimensional advection equation, adapted to two-phase flow: :

$$[(1-\alpha)\,c\rho_l]_t + [(1-\alpha)\,c\rho_l u_l]_x = S \tag{5.1}$$

No modeling of boron diffusion is included. However, the effects of numerical diffusion are important (as shown in App. C). In TRACE, the above equation is solved by mean of a first-order upwind finite volume formulation, and the result is appropriately constrained with the solubility limits (App. D). While such discretization is very robust and computationally efficient, its low accuracy and the introduction of significant numerical diffusion leave large room for optimization as regards the improved tracking of sharp solute fronts.

5.2 Review of available discretization methods for the solute tracking equation

The convection of solute in a flow field can be modeled following two different approaches, widely used in fluid dynamics to solve the flow conservation equations. The first methodology is based on the so-called Lagrangian formulation, while the second one is based on the Eulerian formulation.

5.2.1 Lagrangian formulation

The Lagrangian approach is based on the tracking of the mass of solute being transported by the flow. Practically, this can be done by considering the solute as being composed of particles

which move in time within the system according to the velocity field of the fluid, starting from defined initial conditions. Then, through the statistical analysis of the particles ensemble, it is possible to reconstruct the solute field. There are some advantages and drawbacks in this approach. The benefits in using this method are:

- With a good statistics, it is possible to have a very accurate solution (within the limits of the modeling assumptions).

- Physical diffusion needs not to be modeled, since it comes directly from the particles moving in the velocity field.

- This method does not suffer from numerical diffusion.

The disadvantages are:

- The advantage of not modeling the diffusion is counterbalanced by the necessity to model the flow turbulence, which gives the correct velocity field for the particles. This opens up a new set of problematics linked to the modeling of the turbulence, with added computational costs.

- In order to have good statistics, many particles have to be tracked, leading to increased computational costs and memory requirements for the code.

In general, Lagrangian methods are much more computationally intensive than Eulerian methods; this is a major drawback that moves the needle of the balance in favor of the latter.

5.2.2   Eulerian formulation

The Eulerian approach consists in observing what happens to the flow in a defined "control volume" (or, more generally, in a defined domain). From the practical point of view, the flow region is divided into adjacent computational cells. Consequently, the flow variables are defined at discrete locations (usually at the cell center or on the cell faces), the flow equations are discretized and the resulting system of equations is solved with adequate numerical methods. The solute concentration inside each cell is treated like the other flow variables.

The literature on discretization methods for this formulation is extensive. A great number of such methods are based on finite difference (FD), finite volume (FV) or finite element (FE) formulations, but other approaches (spectral schemes, boundary elements methods, cellular automata, etc.) have been developed for special classes of problems. The choice of one method over another depends on many factors, such as the geometry of the problem, the accuracy of the method, the computational efficiency and the stability of the solution.

In this work, the FV method is employed. This uses the integral form of the conservation equations as its starting point, thus enforcing automatically the local and global conservation laws (while FD and FE require special care as regards the approximations adopted). Moreover,

all the terms that have to be approximated have a well defined physical meaning, making it simpler to understand and implement the method. Two kind of approximations are involved, interpolation (to compute the values on the cell faces) and integration (over surfaces and volumes). This method is suitable for any type of grid, so that it can be used for complex geometries as well.

Central difference interpolation

The first schemes developed for the Euler method were based on a simple linear-interpolation approximation of the variables at the cell face. The truncation error of such discretization is relatively low, $O\left(\Delta x\right)^2$, but such schemes can lead to unphysical oscillations of the solution.

Consider for the sake of simplicity the one-dimensional advection equation, with velocity u, discretized on an equally spaced mesh:

$$f_t + (uf)_x = 0 \tag{5.2}$$

Discretizing Eq. (5.2) using the finite difference method, with explicit advancement in time and a central difference scheme for the advective part, the equation becomes:

$$\frac{f_i^{n+1} - f_i^n}{\Delta t} + \frac{u_{i+1/2}f_{i+1}^n - u_{i-1/2}f_{i-1}^n + \left(u_{i+1/2} - u_{i-1/2}\right)f_i^n}{2\Delta x} = 0 \tag{5.3}$$

In Eq. (5.3) the face values were interpolated with the central difference scheme, which is a simple linear interpolation:

$$f_{i-1/2}^n = \frac{f_{i-1}^n + f_i^n}{2}$$

$$f_{i+1/2}^n = \frac{f_i^n + f_{i+1}^n}{2}$$

The sensitivity of the advective term to the variation of f_i^n is purely dependent on the local velocity gradient:

$$\sigma_{A,i} = \frac{\partial\left(\text{inflow}\right)}{\partial f_i} = -\frac{u_{i+1/2} - u_{i-1/2}}{2\Delta x} \sim -\frac{1}{2}\frac{\partial u}{\partial x}$$

From the expression for $\sigma_{A,i}$, it is clear that for a negative velocity gradient the sensitivity is positive and an increase in the value of f_i leads to an increase of the inflow. This is unphysical and can lead to an erroneous accumulation of f in the i-th cell, since the variation in time of f depends on f_i itself and this may cause a positive feedback. Also the case with constant velocity u leads to $\sigma_{A,i} = 0$ and the convective term is completely insensitive to the value of f_i, thus making the scheme intrinsically unstable. This can be partially balanced with the

introduction of a diffusive term:

$$Df_{xx} \sim D \frac{f_{i+1}^n + f_{i-1}^n - 2f_i^n}{(\Delta x)^2} \tag{5.4}$$

which has the sensitivity:

$$\sigma_{D,i} = \frac{\partial \left(\text{diffusion} \right)}{\partial f_i} = -\frac{2D}{(\Delta x)^2}$$

The sensitivity $\sigma_{D,i}$ is always negative by definition (because diffusion is positive) and thus it has a stabilizing effect.

This instability however is not related to the classical stability conditions like the Courant-Friedrichs-Lewy condition (see App. A). It manifests itself with the presence of wiggles, i.e. spatial oscillations, of wavelength $2\Delta x$.

To make the method stable, Lax proposed the following substitution in the time derivative term of Eq. (5.3):

$$f_i^n = \frac{f_{i+1}^n + f_{i-1}^n}{2}$$

obtaining:

$$\frac{f_i^{n+1} - \left(\dfrac{f_{i+1}^n + f_{i-1}^n}{2} \right)}{\Delta t} + u \frac{f_{i+1}^n - f_{i-1}^n}{2\Delta x} = 0 \tag{5.5}$$

This leads to the introduction of a diffusion term in Eq. (5.3), such as that given by Eq. (5.4):

$$\frac{f_i^{n+1} - f_i^n}{\Delta t} + u \frac{f_{i+1}^n - f_{i-1}^n}{2\Delta x} = \frac{f_{i+1}^n + f_{i-1}^n - 2f_i^n}{2\Delta t} \tag{5.6}$$

Although stable, this method only has first-order accuracy and adds significant numerical diffusion to the solution. Further improvements were made to achieve better accuracy (e.g. Lax-Wendroff method) and to adapt the scheme to nonlinear equations (e.g. MacCormack predictor-corrector method) and multidimensional flows. However, being based on the Lax method, they have the same limitations, i.e. the introduction of numerical diffusion.

Other methods were developed as well. Though an extensive review is beyond the scope of this work, it is nevertheless worthwhile to point out that, in general, high-order space-centered methods suffer from strong oscillations around discontinuities, which are usually damped by adding numerical diffusion. As a matter of fact, good accuracy together with low numerical diffusion can be achieved only at the expense of a possibly unstable solution. In system codes, where there are usually many parameters to be taken into account and their range of variation is wide, it is preferable to avoid the use of numerical schemes that can be unstable, since the control of the stability becomes complex and difficult to implement with a good computational efficiency.

Upwind interpolation

To include the directional character of the flow in the numerical solution, a class of upwind biased schemes was developed in the past. The fundamental idea of this methodology is to transport the physical information in the direction of the flow (i.e. according to the sign of the velocity u). Practically, this is done by biasing the computational cell towards upstream nodes.

The simplest approach, which is the most commonly used in system codes, is the first-order upwind differencing (in both explicit and implicit form) because of its robustness and non-oscillatory behavior. The spatial gradient of f is approximated by a backward or forward difference, depending on the sign of the velocity (positive or negative, respectively), leading to two different formulations of Eq. (5.2). These two relationships, using the finite difference method with explicit advancement in time and a central difference scheme for the advective part, can be summarized in one single equation:

$$\frac{f_i^{n+1} - f_i^n}{\Delta t} + \frac{\left(u_{i+1/2} - \left|u_{i+1/2}\right|\right) f_{i+1}^n}{2\Delta x} +$$
$$-\frac{\left[\left(u_{i+1/2} + \left|u_{i+1/2}\right|\right) - \left(u_{i-1/2} - \left|u_{i-1/2}\right|\right)\right] f_i^n}{2\Delta x} +$$
$$-\frac{\left(u_{i-1/2} + \left|u_{i-1/2}\right|\right) f_{i-1}^n}{2\Delta x} = 0$$

In this case, the sensitivity of the advective term to the variation of f_i^n is:

$$\sigma_{A,i} = \frac{\partial\left(\text{inflow}\right)}{\partial f_i} = -\frac{\left[\left(u_{i+1/2} + \left|u_{i+1/2}\right|\right) - \left(u_{i-1/2} - \left|u_{i-1/2}\right|\right)\right]}{2\Delta x}$$

For each combination of the velocities (see Tab. 5.1), the sensitivity is negative and thus the scheme is stable (except when there is only inflow in the i-th cell, and the sensitivity is independent of the variation of f_i, as one can physically expect). Unfortunately, the stability is counterbalanced by the introduction of a strong numerical diffusion, this time due to the truncation error (see App. C). This results in poor resolution when strong discontinuities are present.

To increase the accuracy of the upwind schemes, Godunov in 1959 proposed a new family of methods that assumes a piecewise constant solution in each control volume. This makes the numerical solution at the control volume interfaces discontinuous and, therefore, the flux computation at such interfaces is ambiguous. To overcome this issue, the true flux at the interface is supplanted by a numerical flux function, which gives a single numerical flux at each interface calculated from an exact or approximate local solution of the Riemann problem formulated at the interface. For a more detailed mathematical treatment, see [76].

Another problem arising from using piecewise solutions is that these are so-called weak solutions, i.e. they are usually not unique and require additional criteria to be satisfied in

$u_{i-1/2}$	$u_{i+1/2}$	$\sigma_{A,i}$
> 0	> 0	$-\dfrac{\left|u_{i+1/2}\right|}{\Delta x}$
> 0	< 0	0
< 0	> 0	$-\dfrac{\left|u_{i+1/2}\right| + \left|u_{i-1/2}\right|}{\Delta x}$
< 0	< 0	$-\dfrac{\left|u_{i-1/2}\right|}{\Delta x}$

Table 5.1: Dependence of $\sigma_{A,i}$ on the sign of the velocities $u_{i-1/2}$ and $u_{i+1/2}$.

order to obtain a single solution. This brings additional limitations on monotonicity of the computed numerical fluxes (these requirements go under the name of E-fluxes), and several different formulations exist in the literature.

In 1959, Godunov showed that all linear schemes that preserve the monotonicity of the solution are at most first-order accurate. This motivated the development of new high-order schemes, which essentially use nonlinearity so that monotone resolution of discontinuities and high-order space accuracy away from discontinuities are simultaneously attained. These schemes are known as total variation diminishing (TVD) schemes. Also, higher order time-accuracy schemes, called Strong Stability Preserving (SPP) Runge-Kutta methods, have been developed. The interesting fact about these methods is that they introduce the notion of "limiter" to obtain the correct solution from the discretized equations.

An alternative approach to TVD methods was proposed by Leonard with the QUICK and QUICKEST schemes (for steady-state and transient flows, respectively). The QUICKEST method has been applied in the present work to solve the solute tracking equation of TRACE, thus improving its accuracy.

5.3 Implementation of an explicit high-order scheme inside an implicit or semi-implicit code

5.3.1 Strategy

A strategy to implement an explicit solute tracker inside an implicit or semi-implicit system code was previously developed in [71] and applied successfully to TRAC-PF1/MOD2. A similar strategy has been adopted in the present work to implement the QUICKEST scheme inside TRACE. The basic concept consists in decoupling the solution of the solute convection equation from the solution of the main conservation equations and to solve the former explicitly inside the (semi-) implicit time step. A flow-chart of the solution strategy is given in Fig. 5.1.

After the initialization of the system code, the topological information of the TH system has to be extracted. This is because high-order methods require a more extensive treatment of
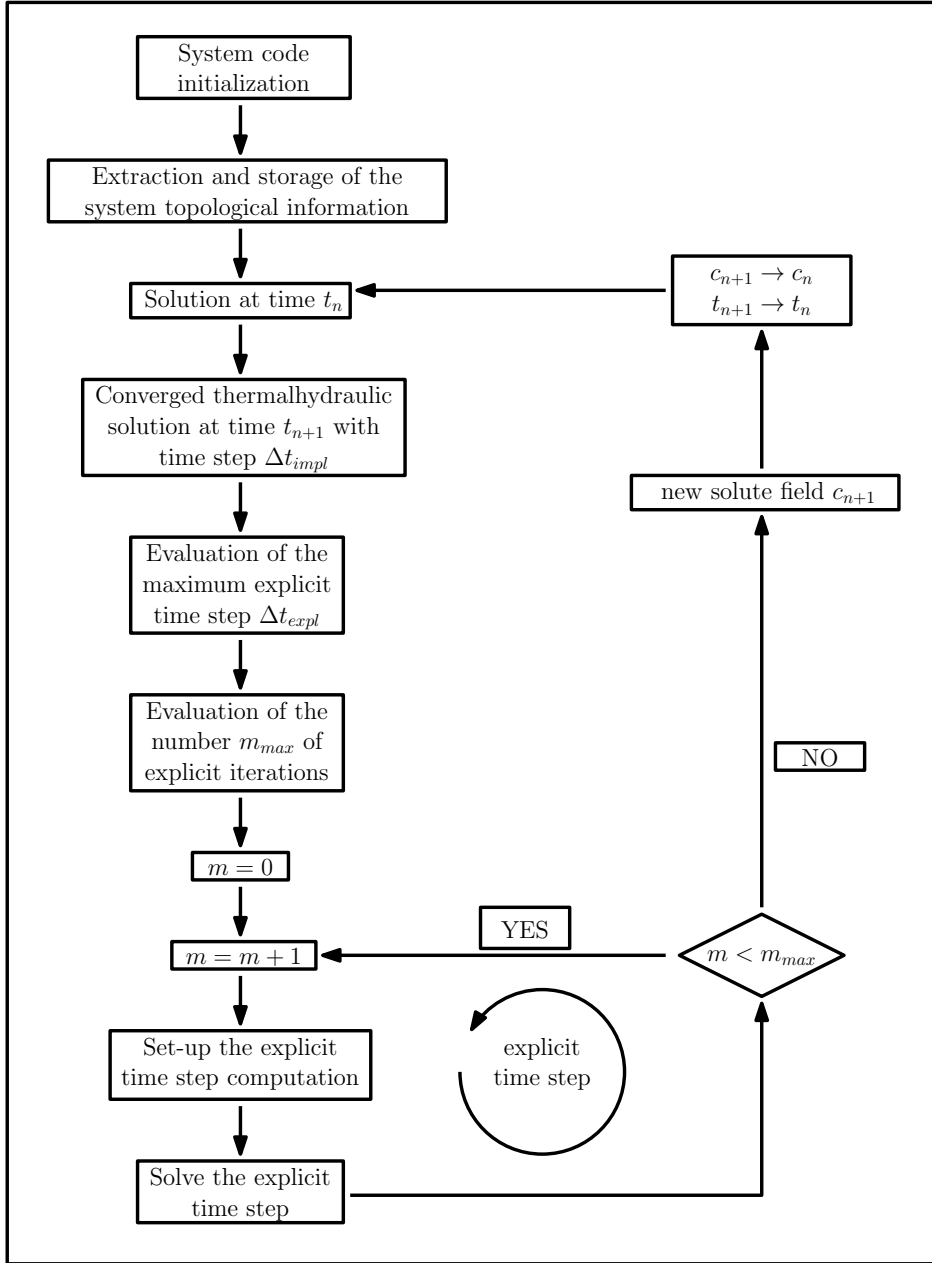
Figure 5.1: Flow chart of the explicit solute tracker implementation inside a (semi-)implicit code.

the component boundaries with respect to first-order codes, since the computational molecule usually involves a wider range of cells. Consequently, it is important to obtain the information on the junctions and on a certain number of cells in the contiguous components.

The solution of the explicit scheme can be merged in the pre-existing (semi-) implicit computational process without perturbing it, since the transport of the solute (i.e. the solution of the corresponding transport equation) does not directly affect the flow field [8]. The only

Figure 5.2: Time-step reference scheme for the explicit solute tracker implementation.
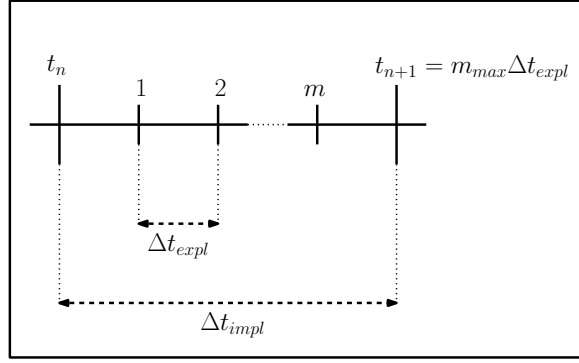
indirect coupling between the flow field and the solute equation takes place through the neutronic response of the core to a change in the concentration of the neutron absorber. This response modifies the core power and thus the temperature field inside the reactor, but again without affecting the (semi-) implicit solution scheme. Therefore, the solute convection equation can be solved independently.

One issue that has to be taken care of is the definition of the explicit time step, since semi-implicit and implicit schemes can exceed the Courant-Friedrichs-Lewy (CFL) condition [77] with larger time steps, while the explicit scheme requires the condition to be fulfilled in order to be stable. The CFL condition can be satisfied by using, when necessary, a time step for the solute tracking algorithm smaller than that employed for the (semi-) implicit scheme.

In Fig. 5.2, a schematic of this procedure is shown. The CFL condition ($C_{CFL} \leq 1$) is applied to each cell in which the high-order solute tracker is used. In this way, the maximum number allowed is found, with the corresponding maximum time step expressed by:

$$\Delta t_{max} = \frac{\Delta t_{impl}}{C_{max}} C_{CFL} \tag{5.7}$$

If $\Delta t_{max} \geq \Delta t_{impl}$, the explicit time step is set to be the same as Δt_{impl}. Otherwise, the number of explicit time steps necessary to cover the (semi-) implicit time step is estimated as:

$$m_{max} = \text{int}\left(\frac{\Delta t_{impl}}{\Delta t_{max}}\right) + 1 \tag{5.8}$$

and the final explicit time step is selected as follows:

$$\Delta t_{expl} = \frac{\Delta t_{impl}}{m_{max}} \tag{5.9}$$

5.3.2 Time averaging

Before actually solving the explicit scheme equations, the values for the fluid properties used during the solutions, as also for the velocities and the diffusion coefficients, have to be evaluated in a manner consistent with the procedure described above. This means that a suitable time averaging procedure has to be defined to interpolate the values inside each (semi-) implicit time step. In general, the options available follow a common scheme:

$$\tilde{X} = (1 - q) X^n + q X^{n+1} \tag{5.10}$$

where X is a generic fluid variable and q is a generic weight. In particular:

- implicit $\rightarrow q = 1$ (use the value at the new time)

- explicit $\rightarrow q = 0$ (use the value at the old time)

- semi-implicit $\rightarrow q = \dfrac{1}{2}$ (use the average value between the new and the old time)

- linear scaling $\rightarrow q = \dfrac{m\Delta t_{expl}}{\Delta t_{impl}}$ (scales the value linearly depending on the explicit time-step size)

Between the presented options, linear scaling is the most appropriate to be applied in the explicit solute tracking procedure described later, since it is more accurate (it is a first-order approximation, while the others are zeroth-order) and relatively inexpensive from the computational point of view.

5.3.3 Evaluation of the explicit time step

Since the discretization scheme adopted in QUICKEST is explicit, the cell Courant number (see Subsec. 5.4.9) has the limit condition $C_Q \leq 1$. TRACE uses a semi-implicit scheme and therefore this condition can in certain situations be relaxed to values greater than one. To avoid convergence problems, the explicit solver has its own time step, which can be equal or smaller than that selected by the TRACE solver. Therefore, in one TRACE time step, it is possible to have more than one explicit time steps for the solution of the solute transport equation.

To evaluate the explicit time step, let us consider the TRACE cell-defined Courant number

$$C_T = \frac{Au\Delta t_T}{V} \quad \longrightarrow \quad \frac{Au}{V} = \frac{C_T}{\Delta t_T} \tag{5.11}$$

and the QUICKEST scheme cell-defined Courant number

$$C_Q = \frac{Au\Delta t_Q}{V} \leq 1 \quad \longrightarrow \quad \frac{Au}{V} \leq \frac{1}{\Delta t_Q} \tag{5.12}$$

Combining Eq. (5.11) and Eq. (5.12), the relationship between the two time steps can be expressed as:

$$\frac{C_T}{\Delta t_T} \leq \frac{1}{\Delta t_Q} \quad \longrightarrow \quad \Delta t_Q \leq \frac{\Delta t_T}{C_T}$$

When the diffusion is taken into account, there is another limitation on the stability: the dimensionless cell-defined diffusion coefficient must satisfy $\Gamma_Q \leq 0.5$. The situation is actually more complex [68], but the limitation presented here is a conservative approximation of the real limit. To evaluate the explicit time step, let us consider the TRACE cell-defined dimensionless diffusion coefficient

$$\Gamma_T = \frac{AD\Delta t_T}{V\Delta x} \quad \longrightarrow \quad \frac{AD}{V\Delta x} = \frac{\Gamma_T}{\Delta t_T} \tag{5.13}$$

and the QUICKEST scheme cell-defined dimensionless diffusion coefficient

$$\Gamma_Q = \frac{AD\Delta t_Q}{V\Delta x} \leq 0.5 \quad \longrightarrow \quad \frac{AD}{V\Delta x} \leq \frac{0.5}{\Delta t_Q} \tag{5.14}$$

Combining Eqs. (5.13) and (5.14), the relationship between the two time steps becomes

$$\frac{\Gamma_T}{\Delta t_T} \leq \frac{0.5}{\Delta t_Q} \quad \longrightarrow \quad \Delta t_Q \leq 0.5\frac{\Delta t_T}{\Gamma_T}$$

5.4 Application of QUICKEST to the solute convection equation

5.4.1 The QUICKEST scheme

The main problem associated with upwind (UDS) and central (CDS) differencing schemes in a finite volume discretization is to obtain a good estimate of the cell-edge values of the dependent variables. While for CDS the estimation is first-order (linear), for UDS the approximation is zeroth-order with the choice of the direction. CDS has stability problems related to the symmetric nature of the scheme [68], and moving to higher order discretizations does not solve them. Leonard [68, 69] accordingly proposed a high-order upwind scheme involving one cell downstream and two cells upstream in the general case (for a maximum stencil size of five cells, in the case of complete inflow into the cell). However, simple cubic interpolation leads to a non-conservative scheme and to numerical problems when the velocity is reversed. Consequently, Leonard proposed a three-point, upstream-weighted quadratic interpolation for each individual cell-edge value, which grants a conservative formulation. The resulting algorithm was named QUICK (Quadratic Upwind Interpolation for Convective Kinematics) and is appropriate for steady-state flows.

Leonard later developed an extension of such a scheme for highly-convective unsteady flows

[68, 69]. The basic idea is that for the case of flows in which the advection term is dominant (with respect to the diffusion and source terms), field variations are carried along at the local fluid velocity. The average cell-edge values can then be estimated by assuming that the solution profile is swept downstream unchanged, using a technique called Time Interpolation modeling (TIM). Such a streaming estimation procedure was used in conjunction with the QUICK scheme and the resulting algorithm was named QUICKEST (QUICK with Estimated Streaming Terms).

Special treatment of tee components and side junctions

A tee component (obsolete in the current version of TRACE), or a side junction, consists of a junction cell where three (or more) flow paths converge and a redistribution of the flow occurs between them. The presence of such flow paths introduces a quasi-two-dimensional component to the discretization. QUICKEST was in the first place developed for one-dimensional geometry [68], so that an extension is required to handle this special case. The idea is to modify the advection and diffusion terms such as to include the contributions of the side junctions [71], without modifying the accumulation term.

In the present work, their treatment has been simplified to avoid unnecessary complications. The simplification works well with the mesh sizes usually adopted in TH system codes, but with very small mesh sizes (around 1 cm and below) some oscillations may appear in the solution around the junction. This is an issue to be aware of, even if such small meshes are seldomly used in typical nuclear power plant simulations, for which representative mesh sizes are several tens of centimeters.

5.4.2 Solute convection equation

The mass conservation equation used in TRACE to model the solute convection is, in its general form (refer to [8] for more details):

$$[(1 - \alpha) \, c\rho_l]_t + \boldsymbol{\nabla} \cdot [(1 - \alpha) \, c\rho_l \mathbf{u_l}] = S \tag{5.15}$$

To simplify the notation, without losing generality, it is possible to make the following substitution:

$$\phi = (1 - \alpha) \, c\rho_l \tag{5.16}$$

Therefore, Eq. (5.15) becomes:

$$\phi_t + \boldsymbol{\nabla} \cdot (\phi \mathbf{u}) = S \tag{5.17}$$

It is worthwhile mentioning that flow turbulence induces enhanced mixing, which in a one-dimensional approximation will result in an equivalent diffusion term in Eq. (5.17). This term is generally neglected in TH system codes. However, the upwind discretization schemes,

commonly adopted, add a numerical diffusion which is not negligible (as explained in App. C). The purpose of the present work is to improve the current solute transport model in TRACE by reducing the numerical diffusion, and by allowing the possibility of including a physical diffusion term. Thus the convection equation can be written, in the following general form, as:

$$\underbrace{\phi_t \left(\mathbf{x}, t\right)}_{\text{accumulation term}} = -\underbrace{\boldsymbol{\nabla} \cdot \left[\phi \left(\mathbf{x}, t\right) \mathbf{u} \left(\mathbf{x}, t\right)\right]}_{\text{advection term}} + \underbrace{\boldsymbol{\nabla} \cdot \left[D \left(\mathbf{x}, t\right) \nabla \phi \left(\mathbf{x}, t\right)\right]}_{\text{diffusion term}} + \underbrace{S \left(\mathbf{x}, t\right)}_{\text{source term}} \tag{5.18}$$

From Eq. (5.18) it is easy to deduce the one-dimensional form of the transport equation:

$$\phi_t \left(x, t\right) = -\left[\phi \left(x, t\right) u \left(x, t\right)\right]_x + \left[D \left(x, t\right) \phi_x \left(x, t\right)\right]_x + S \left(x, t\right) \tag{5.19}$$

In the following, the dependence on $\mathbf{x}$ and t will be omitted when clear.

Finite volume approximation

To define a finite volume approximation of the transport equation, it is necessary to integrate Eq. (5.18) over the control volume Ω:

$$\int_{\Omega} \phi_t d\Omega = -\int_{\Omega} \boldsymbol{\nabla} \cdot \left(\phi \mathbf{u}\right) d\Omega + \int_{\Omega} \boldsymbol{\nabla} \cdot \left(D \nabla \phi\right) d\Omega + \int_{\Omega} S d\Omega \tag{5.20}$$

Using the Divergence Theorem (or Gauss Theorem) on Eq. (5.20):

$$\int_{\Omega} \phi_t d\Omega = -\int_{\Psi} \phi \mathbf{u} \cdot \mathbf{n} d\Psi + \int_{\Psi} D \nabla \phi \cdot \mathbf{n} d\Psi + \int_{\Omega} S d\Omega \tag{5.21}$$

where Ψ is the control surface (i.e. the surface of the control volume Ω) and $\mathbf{n}$ is the normal vector to the control surface.

Since Eq. (5.21) is also time dependent, it is necessary to integrate it over a certain time interval $\Delta \tau$. The final equation is:

$$\int_{\Delta \tau} \int_{\Omega} \phi_t d\Omega d\tau = -\int_{\Delta \tau} \int_{\Psi} \phi \mathbf{u} \cdot \mathbf{n} d\Psi d\tau + \int_{\Delta \tau} \int_{\Psi} D \nabla \phi \cdot \mathbf{n} d\Psi d\tau + \int_{\Delta \tau} \int_{\Omega} S d\Omega d\tau \tag{5.22}$$

To discretize Eq. (5.22), the integration is performed over the i-th volume V_i and the time interval of a generic time step $\Delta t = t_{n+1} - t_n$. The results for the one-dimensional formulation are presented in the following subsections, with each term of Eq. (5.22) being treated separately.

5.4.3   Accumulation term

First the time integration has to be carried out. It is easy to see that:

$$\int\limits_{\Delta t} \phi_t d\tau = \int\limits_{t_n}^{t_{n+1}} \phi_t d\tau = \int\limits_{\phi^n}^{\phi^{n+1}} d\phi = \phi^{n+1} - \phi^n \tag{5.23}$$

Then the integration over the volume has to be performed. For the 1D case, with varying area, it is possible to define an average area for each cell:

$$V_i = \int\limits_{V_i} dV = \int\limits_{\Delta x_i} A(x) dx = <A(x)>_{x_i} \int\limits_{\Delta x_i} dx = <A(x)>_{x_i} \Delta x_i \tag{5.24}$$

$$<A(x)>_{x_i} = A_i = \frac{V_i}{\Delta x_i} \tag{5.25}$$

The volume integration is therefore:

$$\int\limits_{V_i} \phi^{n+1} - \phi^n dV = A_i \int\limits_{-\frac{\Delta x_i}{2}}^{\frac{\Delta x_i}{2}} \phi^{n+1}(x) dx - A_i \int\limits_{-\frac{\Delta x_i}{2}}^{\frac{\Delta x_i}{2}} \phi^n(x) dx = A_i \left(I_i^{n+1} - I_i^n \right) \tag{5.26}$$

The function $\phi^{n+1}(x)$ is then approximated by a Taylor series expansion:

$$\phi^{n+1}(x) = \phi_i^{n+1} + x\ \phi_x|_i^{n+1} + \frac{x^2}{2}\ \phi_{xx}|_i^{n+1} + O(x^3) \tag{5.27}$$

Substituting Eq. (5.27) in Eq. (5.26) gives:

$$I_i^{n+1} = \int\limits_{-\frac{\Delta x_i}{2}}^{\frac{\Delta x_i}{2}} \left[\phi_i^{n+1} + x\ \phi_x|_i^{n+1} + \frac{x^2}{2}\ \phi_{xx}|_i^{n+1} + O(x^3) \right] dx \tag{5.28}$$

Remembering that integrals of odd functions are equal to zero in case of a symmetric integration interval,

$$I_i^{n+1} \cong \phi_i^{n+1} \Delta x_i + \frac{(\Delta x_i)^3}{24}\ \phi_{xx}|_i^{n+1} \tag{5.29}$$

In the same way for the function $\phi^n(x)$:

$$I_i^n \cong \phi_i^n \Delta x_i + \frac{(\Delta x_i)^3}{24}\ \phi_{xx}|_i^n \tag{5.30}$$

Substituting Eqs. (5.29) and (5.30) into Eq. (5.26), the discretization of the accumulation term is obtained as:

$$\int_{V_i} \phi^{n+1} - \phi^n dV \cong A_i \Delta x_i \left[\left(\phi_i^{n+1} - \phi_i^n \right) + \frac{(\Delta x_i)^2}{24} \left(\phi_{xx}\big|_i^{n+1} - \phi_{xx}\big|_i^n \right) \right] \tag{5.31}$$

The problem remains to evaluate the temporal gradient of $\phi_{xx}\big|_i$, since the variables at the time t_{n+1} are unknown. Starting from the original, one-dimensional convection equation:

$$\phi_t + (\phi u)_x = 0 \rightarrow \Delta t \frac{(\Delta x_i)^2}{24} (\phi_t)_{xx} + \Delta t \frac{(\Delta x_i)^2}{24} ((\phi u)_x)_{xx} = 0 \tag{5.32}$$

and differencing:

$$\phi_t \approx \frac{\phi_i^{n+1} - \phi_i^n}{\Delta t} \quad \Rightarrow \quad (\phi_t)_{xx} \approx \frac{\phi_{xx}\big|_i^{n+1} - \phi_{xx}\big|_i^n}{\Delta t}$$

$$(\phi u)_x \approx u^* \frac{\phi_{i+1/2}^n - \phi_{i-1/2}^n}{\Delta x_i} \quad \Rightarrow \quad ((\phi u)_x)_{xx} \approx u^* \frac{\phi_{xx}\big|_{i+1/2}^n - \phi_{xx}\big|_{i-1/2}^n}{\Delta x_i}$$

where u^* is a spatially averaged velocity. Substituting the differentiated terms into Eq. (5.32):

$$\cancel{\Delta t} \frac{(\Delta x_i)^2}{24} \frac{\phi_{xx}\big|_i^{n+1} - \phi_{xx}\big|_i^n}{\cancel{\Delta t}} \cong -u^* \Delta t \frac{(\Delta x_i)^2}{24} \frac{\phi_{xx}\big|_{i+1/2}^n - \phi_{xx}\big|_{i-1/2}^n}{\Delta x_i} \tag{5.33}$$

Notice how the LHS of Eq. (5.33) is the same term that appears in Eq. (5.31); therefore, it is possible to express the temporal gradient of $\phi_{xx}\big|_i$ as a spatial gradient at the time t_n. Finally, Eq. (5.31) becomes:

$$\int_{V_i} \phi^{n+1} - \phi^n dV \cong A_i \Delta x_i \left[\left(\phi_i^{n+1} - \phi_i^n \right) - \frac{u^* \Delta t}{\Delta x_i} \frac{(\Delta x_i)^2}{24} \left(\phi_{xx}\big|_{i+1/2}^n - \phi_{xx}\big|_{i-1/2}^n \right) \right] \tag{5.34}$$

The velocity u^* is a spatially averaged velocity, and can be assumed equal to $\tilde{u}_{i\pm1/2}$ (depending on the cell-edge term being computed) if the velocity field is not too divergent.

5.4.4 Advection term

For the estimation of the advection term, the first integral to be solved is the surface integral. In the 1D case, the values of ϕ and u are constant on each "surface" (because the surface is reduced to one single point) and therefore their area-averaged values are equal to the values at that node. The result is the following:

$$-\int_\Psi \phi \mathbf{u} \cdot \hat{\mathbf{n}} d\Psi \quad \rightarrow \quad \int_{\Psi_{i-1/2}} \phi u d\Psi - \int_{\Psi_{i+1/2}} \phi u d\Psi \quad = \quad [A\phi u]_{i-1/2} - [A\phi u]_{i+1/2} \tag{5.35}$$

Regarding the time integral, the QUICKEST scheme is based on the Time Interpolation modeling (TIM) technique, which transforms the time integration into a spatial interpolation of the scalar field values. The fundamental assumption is that the scalar field is swept downstream unchanged with the local velocity u, plus a correction if diffusion is present [69]:

$$\phi\left(x,\tau\right) = \underbrace{\phi\left(x - u\left(\tau - t\right), t\right)}_{advection} + \underbrace{D\phi_{xx}\left(\tau - t\right)}_{diffusion} \quad \text{with} \quad t \leq \tau \leq t + \Delta t \tag{5.36}$$

where x is an arbitrary location in space, D is assumed locally constant and ϕ_{xx} is assumed independent of time. Eq. (5.36) is practically an approximated convection equation on a generic time step $\Delta\tau = \tau - t$.

The space integration happens over a cell and it is independent of x, while the time integration is over the time step Δt and is therefore independent of t. Consequently, the above equation can be rewritten without losing its generality as:

$$\phi\left(0,\tau\right) = \phi\left(-u\tau, 0\right) + D\phi_{xx}\tau \quad \text{with} \quad 0 \leq \tau \leq \Delta t \tag{5.37}$$

Finally, a new spatial variable is introduced:

$$\xi = u\tau \tag{5.38}$$

$$d\xi = u d\tau \tag{5.39}$$

$$\int_{\Delta\xi} d\xi = \int_{\Delta t} u d\tau \tag{5.40}$$

$$\Delta\xi = \tilde{u}\Delta t \tag{5.41}$$

where $\Delta\xi$ is the distance traveled by the scalar field in the time Δt and $\tilde{u}$ is a time-averaged velocity (Subsec. 5.3.2). Notice also that:

$$d\xi = u d\tau = \frac{dx}{d\tau} d\tau = dx \tag{5.42}$$

and consequently:

$$\phi_{\xi} = \phi_x \tag{5.43}$$

Eq. (5.37) then becomes:

$$\phi\left(\tau\right) = \phi\left(-\xi\right) + D\phi_{\xi\xi}\frac{\xi}{u} \tag{5.44}$$

Remembering that the area has no time dependence, the time integration can be written with Eq. (**??**) as:

$$\int_{\Delta t} A\phi\left(\tau\right) u d\tau = A\int_{\Delta\xi} \left[\phi\left(-\xi\right) + D\frac{\xi}{u}\phi_{\xi\xi}\right] d\xi \tag{5.45}$$

Developing $\phi(-\xi)$ in a Taylor series expansion around the generic time t_n:

$$\phi(-\xi) = \phi^n - \xi\,\phi_\xi|^n + \frac{\xi^2}{2}\,\phi_{\xi\xi}|^n + O(\xi^3) \tag{5.46}$$

and therefore:

$$\int_0^{\Delta\xi} \phi(-\xi)d\xi = \int_0^{\Delta\xi}\left[\phi^n - \xi\,\phi_\xi|^n + \frac{\xi^2}{2}\,\phi_{\xi\xi}|^n + O(\xi^3) + D\frac{\xi}{u}\,\phi_{\xi\xi}|^n\right]d\xi \tag{5.47}$$

Integrating Eq. (5.47):

$$\int_0^{\Delta\xi}\phi(-\xi)d\xi \cong \phi^n\Delta\xi - \frac{(\Delta\xi)^2}{2}\,\phi_\xi|^n + \frac{1}{2}\frac{(\Delta\xi)^3}{3}\,\phi_{\xi\xi}|^n + \tilde{D}\frac{(\Delta\xi)^2}{2\tilde{u}}\,\phi_{\xi\xi}|^n \tag{5.48}$$

Remembering now Eq. (5.43):

$$\int_0^{\Delta\xi}\phi(-\xi)d\xi \cong \phi^n\Delta\xi - \frac{(\Delta\xi)^2}{2}\,\phi_x|^n + \frac{1}{2}\frac{(\Delta\xi)^3}{3}\,\phi_{xx}|^n + \tilde{D}\frac{(\Delta\xi)^2}{2\tilde{u}}\,\phi_{xx}|^n \tag{5.49}$$

Combining Eq. (5.35), Eq. (5.45) and Eq. (5.49), and remembering that $\Delta\xi = \tilde{u}\Delta t$, the final result is obtained as:

$$\int_0^{\Delta t}\left([A\phi u]_{i-1/2} - [A\phi u]_{i+1/2}\right)d\tau \cong \Phi_{i-1/2}^A - \Phi_{i+1/2}^A \tag{5.50}$$

where:

$$\Phi_{i-1/2}^A = A_{i-1/2}\tilde{u}_{i-1/2}\Delta t\left[\phi_{i-1/2}^n - \frac{\tilde{u}_{i-1/2}\Delta t}{2}\,\phi_x|_{i-1/2}^n + \right.$$
$$\left. +\frac{1}{2}\frac{(\tilde{u}_{i-1/2}\Delta t)^2}{3}\,\phi_{xx}|_{i-1/2}^n + \tilde{D}_{i-1/2}\frac{\Delta t}{2}\,\phi_{xx}|_{i-1/2}^n\right] \tag{5.51}$$

$$\Phi_{i+1/2}^A = A_{i+1/2}\tilde{u}_{i+1/2}\Delta t\left[\phi_{i+1/2}^n - \frac{\tilde{u}_{i+1/2}\Delta t}{2}\,\phi_x|_{i+1/2}^n + \right.$$
$$\left. -\frac{1}{2}\frac{(\tilde{u}_{i+1/2}\Delta t)^2}{3}\,\phi_{xx}|_{i+1/2}^n + \tilde{D}_{i+1/2}\frac{\Delta t}{2}\,\phi_{xx}|_{i+1/2}^n\right] \tag{5.52}$$
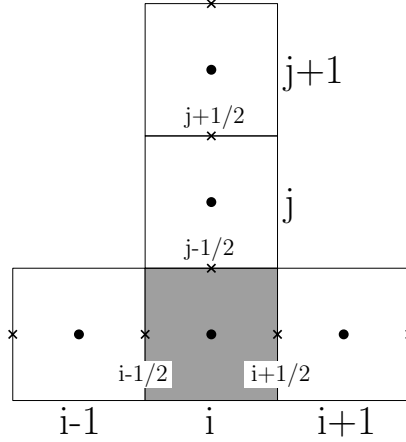
Figure 5.3: Details of the junction cell.

Special case: side junctions

The current version of TRACE allows for one or more side junctions connected to the same cell. Each side junction adds an additional term for the flux across the junction face. The RHS of Eq. (5.35) becomes:

$$[A\phi u]_{i-1/2} - [A\phi u]_{i+1/2} - \sum_{k=1}^{K} [A\phi u]_{j-1/2,k}$$

where $j - 1/2, k$ denotes the side face of the k-th junction cell (Fig. 5.3). Following the procedure described in Subsec. 5.4.4, for the junction cell only Eq. (5.50) becomes:

$$\int_{0}^{\Delta t} \left([A\phi u]_{i-1/2} - [A\phi u]_{i+1/2} - \sum_{k=1}^{K} [A\phi u]_{j-1/2,k} \right) d\tau \cong \Phi_{i-1/2}^{A} - \Phi_{i+1/2}^{A} - \sum_{k=1}^{K} \Phi_{j-1/2,k}^{A} \quad (5.53)$$

where:

$$\Phi_{j-1/2,k}^{A} = A_{j-1/2,k} \tilde{u}_{j-1/2,k} \Delta t \left[\phi_{j-1/2,k}^{n} - \frac{\tilde{u}_{j-1/2,k} \Delta t}{2} \, \phi_x|_{j-1/2,k}^{n} + \right.$$
$$\left. -\frac{1}{2} \frac{\left(\tilde{u}_{j-1/2,k} \Delta t \right)^2}{3} \, \phi_{xx}|_{j-1/2,k}^{n} + \tilde{D}_{j-1/2,k} \frac{\Delta t}{2} \, \phi_{xx}|_{j-1/2,k}^{n} \right] \quad (5.54)$$

Note that here the positive velocity $\tilde{u}_{j-1/2,k}$ is considered to be directed outward of the junction cell i.

5.4.5 Diffusion term

For the diffusion term as well, the first integral to be solved is the surface integral. In the 1D, case the values of ϕ_x and D are constant over the entire "surface" (because the surface is

reduced to one single point) and therefore their area-averaged values are equal to the values at that node, the result being the following:

$$\int_\Psi D\nabla\phi \cdot \hat{\mathbf{n}} d\Psi \rightarrow - \int_{\Psi_{i-1/2}} D\phi_x d\Psi + \int_{\Psi_{i+1/2}} D\phi_x d\Psi = - [AD\phi_x]_{i-1/2} + [AD\phi_x]_{i+1/2} \quad (5.55)$$

Integrating in time Eq. (5.55) and using an explicit treatment of the diffusion (i.e. the derivative is simply that estimated at the old time), the diffusion term can be represented as:

$$\int_0^{\Delta t} \left(- [AD\phi_x]_{i-1/2} + [AD\phi_x]_{i+1/2} \right) d\tau \cong -\Phi^{D1}_{i-1/2} + \Phi^{D1}_{i+1/2} \quad (5.56)$$

where:

$$\Phi^{D1}_{i-1/2} = A_{i-1/2}\tilde{D}_{i-1/2}\Delta t \, \phi_x|^n_{i-1/2} \quad (5.57)$$

$$\Phi^{D1}_{i+1/2} = A_{i+1/2}\tilde{D}_{i+1/2}\Delta t \, \phi_x|^n_{i+1/2} \quad (5.58)$$

and $\tilde{D}$ is a time-averaged diffusion coefficient (Subsec. 5.3.2).

Another more refined way, more consistent with the approach used in the QUICKEST formulation, consists in following a procedure like the one used for the advection term (Subsec. 5.4.4). Remembering that the area has no time dependence, with Eq. (??) and Eq. (5.43) the time integration can be written as:

$$\int_{\Delta t} AD\phi_x d\tau \rightarrow A \int_{\Delta\xi} \phi_\xi \frac{D}{\tilde{u}} d\xi \rightarrow A \frac{\tilde{D}}{\tilde{u}} \int_{\Delta\xi} \phi_\xi d\xi \quad (5.59)$$

where $\tilde{D}$ is a time averaged diffusion coefficient (Subsec. 5.3.2).

Developing $\phi(-\xi)$ in a Taylor series expansion around the generic time t_n and differentiating, Eq. (5.46) becomes:

$$\phi_\xi = - \phi_\xi|^n + \xi \, \phi_{\xi\xi}|^n + O(\xi^2) \quad (5.60)$$

and therefore:

$$\int_0^{\Delta\xi} \phi_\xi d\xi = \int_0^{\Delta\xi} \left[- \phi_\xi|^n + \xi \, \phi_{\xi\xi}|^n + O(\xi^2)\right] d\xi \quad (5.61)$$

Integrating Eq. (5.61):

$$\int_0^{\Delta\xi} \phi_\xi d\xi \cong - \phi_\xi|^n \Delta\xi + \frac{(\Delta\xi)^2}{2} \, \phi_{\xi\xi}|^n \quad (5.62)$$

Remembering now Eq. (5.43):

$$\int_0^{\Delta\xi} \phi_\xi d\xi \cong -\left.\phi_x\right|^n \Delta\xi + \frac{(\Delta\xi)^2}{2}\left.\phi_{xx}\right|^n \tag{5.63}$$

Combining Eqs. (5.55), (5.59) and (5.63), and remembering that $\Delta\xi = \tilde{u}\Delta t$, the final result is obtained as:

$$\int_0^{\Delta t}\left(-[AD\phi_x]_{i-1/2} + [AD\phi_x]_{i+1/2}\right)d\tau \cong -\Phi_{i-1/2}^{D2} + \Phi_{i+1/2}^{D2} \tag{5.64}$$

where:

$$\Phi_{i-1/2}^{D2} = A_{i-1/2}\tilde{D}_{i-1/2}\Delta t\left[\left.\phi_x\right|_{i-1/2}^n - \frac{\tilde{u}_{i-1/2}\Delta t}{2}\left.\phi_{xx}\right|_{i-1/2}^n\right] \tag{5.65}$$

$$\Phi_{i+1/2}^{D2} = A_{i+1/2}\tilde{D}_{i+1/2}\Delta t\left[\left.\phi_x\right|_{i+1/2}^n - \frac{\tilde{u}_{i+1/2}\Delta t}{2}\left.\phi_{xx}\right|_{i+1/2}^n\right] \tag{5.66}$$

Special case: side junctions

Each side junction adds an additional term for the diffusion across the junction face. The RHS of Eq. (5.56) becomes:

$$-[AD\phi_x]_{i-1/2} + [AD\phi_x]_{i+1/2} + \sum_{k=1}^{K}[AD\phi_x]_{j-1/2,k}$$

where $j-1/2, k$ denotes the side face of the k-th junction cell (Fig. 5.3). Following the procedure described in Subsec. 5.4.5, for the junction cell only Eq. (5.56) becomes:

$$\int_0^{\Delta t}\left(-[AD\phi_x]_{i-1/2} + [AD\phi_x]_{i+1/2} + [AD\phi_x]_{j-1/2}\right)d\tau \cong -\Phi_{i-1/2}^{D1} + \Phi_{i+1/2}^{D1} + \sum_{k=1}^{K}\Phi_{j-1/2,k}^{D1} \tag{5.67}$$

where:

$$\Phi_{j-1/2,k}^{D1} = A_{j-1/2,k}\tilde{D}_{j-1/2,k}\Delta t\left.\phi_x\right|_{j-1/2,k}^n \tag{5.68}$$

while Eq. (5.64) becomes:

$$\int_0^{\Delta t}\left(-[AD\phi_x]_{i-1/2} + [AD\phi_x]_{i+1/2} + [AD\phi_x]_{j-1/2}\right)d\tau \cong -\Phi_{i-1/2}^{D2} + \Phi_{i+1/2}^{D2} + \sum_{k=1}^{K}\Phi_{j-1/2,k}^{D2} \tag{5.69}$$

where:

$$\Phi_{j-1/2,k}^{D2} = A_{j-1/2,k}\tilde{D}_{j-1/2,k}\Delta t\left[\left.\phi_x\right|_{j-1/2,k}^n - \frac{\tilde{u}_{j-1/2,k}\Delta t}{2}\left.\phi_{xx}\right|_{j-1/2,k}^n\right] \tag{5.70}$$

Space-averaged diffusion coefficient

Regarding cell-face diffusion coefficients, most system codes (and TRACE is among them [8]) use the staggered grid approach to solve the flow conservation equations. Following this approach, the diffusion coefficient is directly computed at the cell center, and its values on the faces are usually calculated as averages of the cell-centered values of the adjacent cells. Here, different options are possible, e.g.:

- simple average

$$D_{i+1/2} = \frac{1}{2}\left(D_i + D_{i+1}\right)$$

- cell-length weighted average

$$D_{i+1/2} = \frac{\Delta x_i D_i + \Delta x_{i+1} D_{i+1}}{\Delta x_i + \Delta x_{i+1}}$$

- cell-volume weighted average

$$D_{i+1/2} = \frac{V_i D_i + V_{i+1} D_{i+1}}{V_i + V_{i+1}}$$

The volume-weighted average is the recommended option, since the diffusion coefficient is defined over cells with varying area and length. The other two diffusion coefficients needed in the computations are, for the volume-weighted average:

$$D_{i-1/2} = \frac{V_{i-1} D_{i-1} + V_i D_i}{V_{i-1} + V_i}$$

$$D_{j-1/2} = \frac{V_i D_i + V_j D_j}{V_i + V_j}$$

Diffusion coefficient

Different models for the diffusion coefficient were implemented into the code.

- Constant diffusion coefficient D_0 (user defined).

- Levenspiel diffusion coefficient [78, 79]:

$$D = ul\left(\frac{3 \cdot 10^7}{\text{Re}^{2.1}} + \frac{1.35}{\text{Re}^{1/8}}\right)$$

Here the characteristic length scale l is, in the case of pipe flow, the hydraulic diameter d_h, so that:

$$D = ud_h\left(\frac{3 \cdot 10^7}{\text{Re}^{2.1}} + \frac{1.35}{\text{Re}^{1/8}}\right) \tag{5.71}$$

5.4.6   Source term

The source term becomes:

$$\int\limits_{\Delta\tau}\int\limits_{\Omega} S d\Omega d\tau \rightarrow \int\limits_{\Delta t}\int\limits_{V_i} S dV d\tau = \tilde{S}_i V_i \Delta t = \tilde{S}_i A_i \Delta x_i \Delta t \tag{5.72}$$

where $\tilde{S}_i$ is the time- and volume-averaged source inside the i-th cell, and can be expressed by the formulations presented in Subsec. 5.3.2.

5.4.7   Derivatives

The derivatives that appear in the preceding equations are computed as follows. The gradient terms (evaluated at the cell faces) are:

$$\phi_x|_{i-3/2}^n = \frac{\phi_{i-1}^n - \phi_{i-2}^n}{\Delta x_{i-3/2}} \quad \text{with} \quad \Delta x_{i-3/2} = \frac{1}{2}\left(\Delta x_{i-2} + \Delta x_{i-1}\right)$$

$$\phi_x|_{i-1/2}^n = \frac{\phi_i^n - \phi_{i-1}^n}{\Delta x_{i-1/2}} \quad \text{with} \quad \Delta x_{i-1/2} = \frac{1}{2}\left(\Delta x_{i-1} + \Delta x_i\right)$$

$$\phi_x|_{i+1/2}^n = \frac{\phi_{i+1}^n - \phi_i^n}{\Delta x_{i+1/2}} \quad \text{with} \quad \Delta x_{i+1/2} = \frac{1}{2}\left(\Delta x_i + \Delta x_{i+1}\right)$$

$$\phi_x|_{i+3/2}^n = \frac{\phi_{i+2}^n - \phi_{i+1}^n}{\Delta x_{i+3/2}} \quad \text{with} \quad \Delta x_{i+3/2} = \frac{1}{2}\left(\Delta x_{i+1} + \Delta x_{i+2}\right)$$

The curvature terms are:

$$\phi_{xx}|_{i-1/2}^n = \begin{cases} \phi_{xx}|_{i-1}^n = \dfrac{\phi_x|_{i-1/2}^n - \phi_x|_{i-3/2}^n}{\Delta x_{i-1}} & \text{if} \quad \tilde{u}_{i-1/2} \geq 0 \\[3mm] \phi_{xx}|_i^n = \dfrac{\phi_x|_{i+1/2}^n - \phi_x|_{i-1/2}^n}{\Delta x_i} & \text{if} \quad \tilde{u}_{i-1/2} < 0 \end{cases}$$

$$\phi_{xx}|_{i+1/2}^n = \begin{cases} \phi_{xx}|_i^n = \dfrac{\phi_x|_{i+1/2}^n - \phi_x|_{i-1/2}^n}{\Delta x_i} & \text{if} \quad \tilde{u}_{i+1/2} \geq 0 \\[3mm] \phi_{xx}|_{i+1}^n = \dfrac{\phi_x|_{i+3/2}^n - \phi_x|_{i+1/2}^n}{\Delta x_{i+1}} & \text{if} \quad \tilde{u}_{i+1/2} < 0 \end{cases}$$

Notice that the curvature, following the upwind concept, is the cell-centered curvature of the upstream cell.

Special case: side junctions

The extra gradient term between the i-th cell and the k-th junction component is:

$$\phi_x|_{j-1/2,k}^n = \frac{\phi_{j,k}^n - \phi_i^n}{\Delta x_{j-1/2,k}} \quad \text{with} \quad \Delta x_{j-1/2,k} = \frac{\Delta x_{j,k}}{2} + R_i = \frac{\Delta x_{j,k}}{2} + \sqrt{\frac{A_i}{\pi}} \tag{5.73}$$

where R_i is the equivalent radius of the i-th cell. Moreover, the gradient between the last two cells of the side junction is needed:

$$\phi_x|_{j+1/2,k}^n = \frac{\phi_{j+1,k}^n - \phi_{j,k}^n}{\Delta x_{j+1/2,k}} \quad \text{with} \quad \Delta x_{j+1/2,k} = \frac{1}{2}\left(\Delta x_{j,k} + \Delta x_{j+1,k}\right)$$

Regarding the curvature terms, in the first place, the total inflow in the i-th cell has to be defined:

$$m_{\text{in}}^i = \max\left(0, \tilde{m}_{i-1/2}\right) + \max\left(0, -\tilde{m}_{i+1/2}\right) + \sum_{k=1}^{K} \max\left(0, -\tilde{m}_{j-1/2,k}\right)$$

where K is the total number of side junctions. Then the curvature terms for each face are obtained as mass-weighted averages of the inflow-face special curvatures:

$$\phi_{xx}|_{i-1/2}^n = \begin{cases} \phi_{xx}|_{i-1}^n & \text{if} \quad \tilde{m}_{i-1/2} \geq 0 \\[2ex] \dfrac{1}{m_{\text{in}}^i}\max\left(0, -m_{i+1/2}\right)\phi_{xx}|_i^n + \\[1ex] +\dfrac{1}{m_{\text{in}}^i}\displaystyle\sum_{k=1}^{K}\max\left(0, -m_{j-1/2,k}\right)\phi_{xx}|_{j-,k}^n & \text{if} \quad \tilde{m}_{i-1/2} < 0 \end{cases}$$

$$\phi_{xx}|_{i+1/2}^n = \begin{cases} \dfrac{1}{m_{\text{in}}^i}\max\left(0, m_{i-1/2}\right)\phi_{xx}|_i^n + \\[1ex] +\dfrac{1}{m_{\text{in}}^i}\displaystyle\sum_{k=1}^{K}\max\left(0, -m_{j-1/2,k}\right)\phi_{xx}|_{j+,k}^n & \text{if} \quad \tilde{m}_{i+1/2} \geq 0 \\[2ex] \phi_{xx}|_{i+1}^n & \text{if} \quad \tilde{m}_{i+1/2} < 0 \end{cases}$$

$$\phi_{xx}|_{j-1/2,k}^n = \begin{cases} \dfrac{1}{m_{\text{in}}^i}\max\left(0, m_{i-1/2}\right)\phi_{xx}|_{j-,k}^n + \\[1ex] +\dfrac{1}{m_{\text{in}}^i}\max\left(0, -m_{i+1/2}\right)\phi_{xx}|_{j+,k}^n + \\[1ex] +\dfrac{1}{m_{\text{in}}^i}\displaystyle\sum_{h=1}^{K}\max\left(0, -m_{j-1/2,h}\right)\phi_{xx}|_{j,h,k}^n & \text{if} \quad \tilde{m}_{j-1/2} \geq 0 \\[2ex] \phi_{xx}|_{j,k}^n & \text{if} \quad \tilde{m}_{j-1/2} < 0 \end{cases}$$

where the curvature terms are:

$$\phi_{xx}|_{j-,k}^n = \frac{\phi_x|_{j-1/2,k}^n - \phi_x|_{i-1/2}^n}{\Delta x_{j-}}$$

$$\phi_{xx}|_{j+,k}^n = \frac{\phi_x|_{j-1/2,k}^n + \phi_x|_{i+1/2}^n}{\Delta x_{j+}}$$

$$\phi_{xx}|_{j,k}^n = \frac{\phi_x|_{j+1/2,k}^n - \phi_x|_{j-1/2,k}^n}{\Delta x_{j,k}}$$

$$\phi_{xx}|_{j,h,k}^n = \frac{\phi_x|_{j-1/2,h}^n + \phi_x|_{j-1/2,k}^n}{\Delta x_{i\perp}}$$

and:

$$\Delta x_{i\perp} = 2R_i = 2\sqrt{\frac{A_i}{\pi}} \tag{5.74}$$

which is actually the (equivalent) hydraulic diameter of the i-th cell.

It should be noted that, in Eq. (5.73) and Eq. (5.74), the transversal cell length has been calculated with the approximation of circular geometry (i.e. it is the diameter of the cell considered as a circular pipe), because in a one-dimensional code the only information available on the transversal direction is the flow area. Moreover, for $\phi_{xx}|_{j+,k}^n$, the sign is changed to be coherent with the convention used for the flow direction.

To better explain the significance of the above equations, they are applied here to the case of a single side junction. The subscript k, as well as the sum terms, are omitted, since there is only one side connection. Regarding the curvature terms, eight different cases can be encountered. These depend on the sign of the velocities at the junction cell faces (see Fig. 5.4). The following is a list of the cases, each with detailed definitions for the curvature terms:

- **Case 1**

$$\phi_{xx}|_{i-1/2}^n = \phi_{xx}|_{i-1}^n$$
$$\phi_{xx}|_{i+1/2}^n = \phi_{xx}|_i^n$$
$$\phi_{xx}|_{j-1/2}^n = \phi_{xx}|_{j-}^n$$

- **Case 2**

$$\phi_{xx}|_{i-1/2}^n = \phi_{xx}|_{i-1}^n$$
$$\phi_{xx}|_{i+1/2}^n = \phi_{xx}|_{i+1}^n$$
$$\phi_{xx}|_{j-1/2}^n = \frac{\left|\dot{m}_{i-1/2}\right| \phi_{xx}|_{j-}^n + \left|\dot{m}_{i+1/2}\right| \phi_{xx}|_{j+}^n}{\left|\dot{m}_{j-1/2}\right|}$$

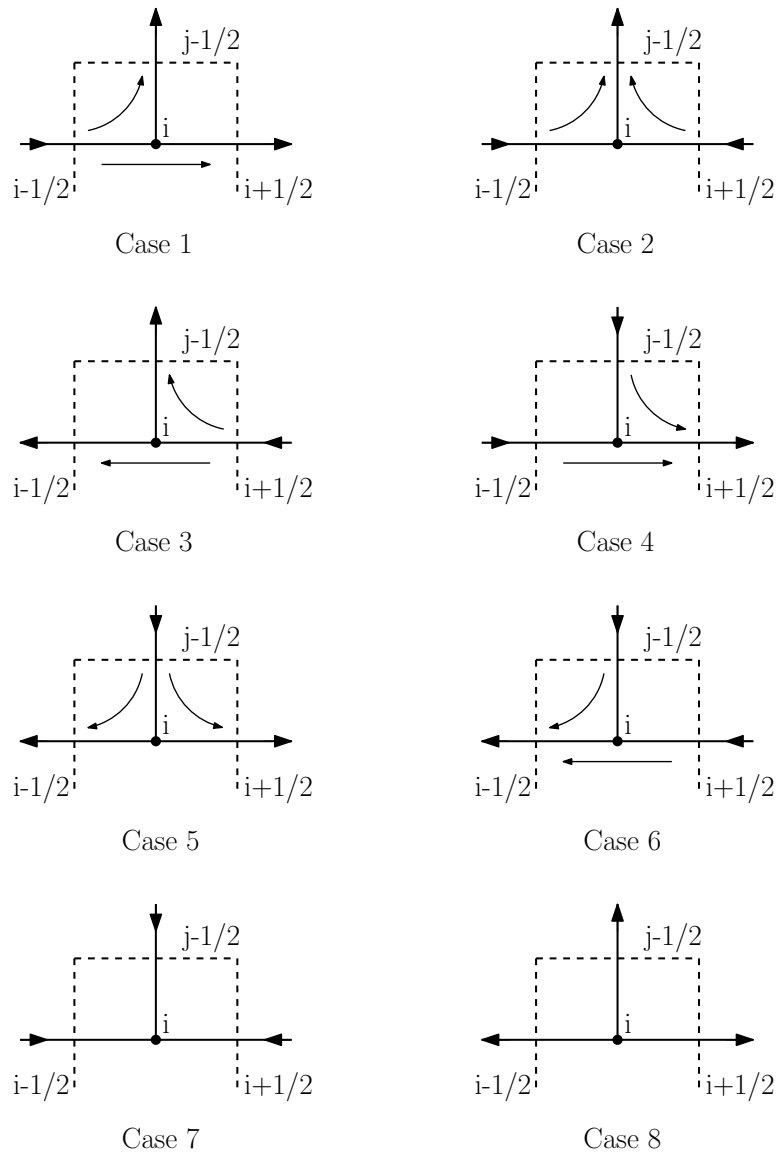Figure 5.4: Possible cases to be found in a junction cell during the evaluation of the curvature terms. Arrows show flow direction.

- **Case 3**

$$\phi_{xx}|_{i-1/2}^{n} = \phi_{xx}|_{i}^{n}$$

$$\phi_{xx}|_{i+1/2}^{n} = \phi_{xx}|_{i+1}^{n}$$

$$\phi_{xx}|_{j-1/2}^{n} = \phi_{xx}|_{j+}^{n}$$

- **Case 4**

$$\phi_{xx}|_{i-1/2}^{n} = \phi_{xx}|_{i-1}^{n}$$

$$\phi_{xx}|_{i+1/2}^{n} = \frac{\left|\dot{m}_{i-1/2}\right| \phi_{xx}|_{i}^{n} + \left|\dot{m}_{j+1/2}\right| \phi_{xx}|_{j+}^{n}}{\left|\dot{m}_{i+1/2}\right|}$$

$$\phi_{xx}|_{j-1/2}^{n} = \phi_{xx}|_{j}^{n}$$

- **Case 5**

$$\phi_{xx}|_{i-1/2}^{n} = \phi_{xx}|_{j-}^{n}$$

$$\phi_{xx}|_{i+1/2}^{n} = \phi_{xx}|_{j+}^{n}$$

$$\phi_{xx}|_{j-1/2}^{n} = \phi_{xx}|_{j}^{n}$$

- **Case 6**

$$\phi_{xx}|_{i-1/2}^{n} = \frac{\left|\dot{m}_{i+1/2}\right| \phi_{xx}|_{i}^{n} + \left|\dot{m}_{j+1/2}\right| \phi_{xx}|_{j-}^{n}}{\left|\dot{m}_{i-1/2}\right|}$$

$$\phi_{xx}|_{i+1/2}^{n} = \phi_{xx}|_{i+1}^{n}$$

$$\phi_{xx}|_{j-1/2}^{n} = \phi_{xx}|_{j}^{n}$$

- **Cases 7 and 8**: these are special cases, with accumulation or depletion of the fluid inside the i-th cell. In this case, the solution is computed following the basic upwind scheme (see App. E for the derivation).

  – Case 7:

$$\phi_{i}^{n+1} = \phi_{i}^{n} + \tilde{C}_{i-1/2}^{i}\phi_{i-1}^{n} - \tilde{C}_{i+1/2}^{i}\phi_{i+1}^{n} - \tilde{C}_{j-1/2}^{i}\phi_{j}^{n}$$

  – Case 8:

$$\phi_{i}^{n+1} = \left(1 + \tilde{C}_{i-1/2}^{i} - \tilde{C}_{i+1/2}^{i} - \tilde{C}_{j-1/2}^{i}\right) \phi_{i}^{n}$$

For the definition of the cell Courant number $\tilde{C}^{i}$, see Subsec. 5.4.10.

5.4.8   Value of ϕ at cell borders

The values of $\phi_{i-1/2}^{n}$ and $\phi_{i+1/2}^{n}$ are computed using the QUICK steady-state approach for second-order upwind weighted interpolation. For example, to find the value of $\phi_{i+1/2}^{n}$, the

procedure starts from the evaluation of ϕ_{i+1}^n using a Taylor series expansion:

$$\phi_{i+1}^n = \phi_{i+1/2}^n + \frac{\Delta x_{i+1/2}}{2}\,\phi_x|_{i+1/2}^n + \frac{1}{2}\left(\frac{\Delta x_{i+1/2}}{2}\right)^2\phi_{xx}|_{i+1/2}^n + O\left(\Delta x\right)^3$$

If we consider a 2nd order approximation, a property of the parabola is that:

$$\phi_x|_{i+1/2}^n = \frac{\phi_{i+1}^n - \phi_i^n}{\Delta x_{i+1/2}}$$

Therefore:

$$\phi_{i+1}^n \cong \phi_{i+1/2}^n + \frac{\phi_{i+1}^n - \phi_i^n}{2} + \frac{\left(\Delta x_{i+1/2}\right)^2}{8}\,\phi_{xx}|_{i+1/2}^n$$

and finally:

$$\phi_{i+1/2}^n \cong \frac{\phi_{i+1}^n + \phi_i^n}{2} - \frac{\left(\Delta x_{i+1/2}\right)^2}{8}\,\phi_{xx}|_{i+1/2}^n$$

The value of the curvature term depends on the sign of the velocity, as described in Subsec. 5.4.7. The final result is, for both faces:

$$\phi_{i-1/2}^n = \frac{1}{2}\left(\phi_i^n + \phi_{i-1}^n\right) - \frac{\left(\Delta x_{i-1/2}\right)^2}{8}\,\phi_{xx}|_{i-1/2}^n$$

$$\phi_{i+1/2}^n = \frac{1}{2}\left(\phi_{i+1}^n + \phi_i^n\right) - \frac{\left(\Delta x_{i+1/2}\right)^2}{8}\,\phi_{xx}|_{i+1/2}^n$$

Special case: side junctions

For the k-th side junction, the extra term is:

$$\phi_{j-1/2,k}^n = \frac{1}{2}\left(\phi_i^n + \phi_{j,k}^n\right) - \frac{\left(\Delta x_{j-1/2,k}\right)^2}{8}\,\phi_{xx}|_{j-1/2,k}^n$$

5.4.9   Cell-defined dimensionless numbers

Since flow area and volume may vary from cell to cell, it is useful to define a cell-dependent Courant number as:

$$\frac{A_{i-1/2}}{V_i}\tilde{C}_{i-1/2}\Delta x_{i-1/2} = \frac{A_{i-1/2}}{V_i}\tilde{u}_{i-1/2}\Delta t = \tilde{C}_{i-1/2}^i$$

$$\frac{A_{i+1/2}}{V_i}\tilde{C}_{i+1/2}\Delta x_{i+1/2} = \frac{A_{i+1/2}}{V_i}\tilde{u}_{i+1/2}\Delta t = \tilde{C}_{i+1/2}^i$$

For a side junction:

$$\frac{A_{j-1/2}}{V_i}\tilde{C}_{j-1/2}\Delta x_{j-1/2} = \frac{A_{j-1/2}}{V_i}\tilde{u}_{j-1/2}\Delta t = \tilde{C}_{j-1/2}^i$$

The same can be done for the face-defined diffusion coefficient:

$$\frac{A_{i-1/2}}{V_i} \frac{\tilde{D}_{i-1/2}\Delta t}{\Delta x_{i-1/2}} = \tilde{\Gamma}^i_{i-1/2}$$

$$\frac{A_{i+1/2}}{V_i} \frac{\tilde{D}_{i+1/2}\Delta t}{\Delta x_{i+1/2}} = \tilde{\Gamma}^i_{i+1/2}$$

and for the side junction:

$$\frac{A_{j-1/2}}{V_i} \frac{\tilde{D}_{j-1/2}\Delta t}{\Delta x_{j-1/2}} = \tilde{\Gamma}^i_{j-1/2}$$

Notice that if the volume is constant, both the cell-defined Courant number and the cell-defined dimensionless diffusion coefficient revert to their respective "classic" versions:

$$C = \frac{u\Delta t}{\Delta x}$$

$$\Gamma = \frac{D\Delta t}{(\Delta x)^2}$$

An important statement has to be made about the velocity used for the Courant number: since the solute is dissolved in the liquid, the velocity used is the liquid velocity provided by TRACE, even in the case of a two-phase mixture flow.

5.4.10   Discretized convection equation

Combining together Eqs. (5.34), (5.50) and (5.72), the QUICKEST scheme can be expressed as:

$$A_i \Delta x_i \left[\left(\phi_i^{n+1} - \phi_i^n \right) - \frac{u^*\Delta t}{\Delta x_i} \frac{(\Delta x_i)^2}{24} \left(\phi_{xx}|_{i+1/2}^n - \phi_{xx}|_{i-1/2}^n \right) \right] =$$

$$A_{i-1/2}\tilde{u}_{i-1/2}\Delta t \left[\phi_{i-1/2}^n - \frac{\tilde{u}_{i-1/2}\Delta t}{2} \phi_x|_{i-1/2}^n + \right.$$

$$\left. \frac{1}{2}\frac{\left(\tilde{u}_{i-1/2}\Delta t\right)^2}{3} \phi_{xx}|_{i-1/2}^n + \tilde{D}_{i-1/2}\frac{\Delta t}{2} \phi_{xx}|_{i-1/2}^n \right] -$$

$$A_{i+1/2}\tilde{u}_{i+1/2}\Delta t \left[\phi_{i+1/2}^n - \frac{\tilde{u}_{i+1/2}\Delta t}{2} \phi_x|_{i+1/2}^n + \right.$$

$$\left. \frac{1}{2}\frac{\left(\tilde{u}_{i+1/2}\Delta t\right)^2}{3} \phi_{xx}|_{i+1/2}^n + \tilde{D}_{i+1/2}\frac{\Delta t}{2} \phi_{xx}|_{i+1/2}^n \right] +$$

$$\tilde{S}_i V_i \Delta t \qquad (5.75)$$

Remembering also that $A_i \Delta x_i = V_i$, and approximating the values of the scalar ϕ on the cell faces with quadratic interpolation, one obtains:

$$
\left(\phi_i^{n+1} - \phi_i^n\right) =
$$

$$
\frac{A_{i-1/2}}{V_i} \tilde{u}_{i-1/2} \Delta t \left[\frac{1}{2}(\phi_i^n + \phi_{i-1}^n) - \frac{\tilde{u}_{i-1/2}\Delta t}{2} \left.\phi_x\right|_{i-1/2}^n\right] -
$$

$$
\frac{A_{i+1/2}}{V_i} \tilde{u}_{i+1/2} \Delta t \left[\frac{1}{2}(\phi_{i+1}^n + \phi_i^n) - \frac{\tilde{u}_{i+1/2}\Delta t}{2} \left.\phi_x\right|_{i+1/2}^n\right] +
$$

$$
\left\{\frac{A_{i-1/2}}{V_i} \tilde{u}_{i-1/2} \Delta t \left[\frac{\left(\tilde{u}_{i-1/2}\Delta t\right)^2}{6} + \tilde{D}_{i-1/2}\frac{\Delta t}{2} - \frac{\left(\Delta x_{i-1/2}\right)^2}{8}\right] - \frac{u^*\Delta t \Delta x_i}{24}\right\} \left.\phi_{xx}\right|_{i-1/2}^n -
$$

$$
\left\{\frac{A_{i+1/2}}{V_i} \tilde{u}_{i+1/2} \Delta t \left[\frac{\left(\tilde{u}_{i+1/2}\Delta t\right)^2}{6} + \tilde{D}_{i+1/2}\frac{\Delta t}{2} - \frac{\left(\Delta x_{i+1/2}\right)^2}{8}\right] - \frac{u^*\Delta t \Delta x_i}{24}\right\} \left.\phi_{xx}\right|_{i+1/2}^n +
$$

$$
\tilde{S}_i \Delta t \quad (5.76)
$$

Substituting u^* (as defined in Subsec. 5.4.3), remembering the classic definition of Courant number $C = \dfrac{u\Delta t}{\Delta x}$, the cell-defined Courant number and the classic definition of the dimensionless diffusion coefficient $\Gamma = \dfrac{D\Delta t}{(\Delta x)^2}$ (Subsec. 5.4.9):

$$
\left(\phi_i^{n+1} - \phi_i^n\right) =
$$

$$
\tilde{C}_{i-1/2}^i \left[\frac{1}{2}(\phi_i^n + \phi_{i-1}^n) - \frac{\Delta x_{i-1/2}}{2}\tilde{C}_{i-1/2} \left.\phi_x\right|_{i-1/2}^n\right] -
$$

$$
\tilde{C}_{i+1/2}^i \left[\frac{1}{2}(\phi_{i+1}^n + \phi_i^n) - \frac{\Delta x_{i+1/2}}{2}\tilde{C}_{i+1/2} \left.\phi_x\right|_{i+1/2}^n\right] +
$$

$$
\tilde{C}_{i-1/2}^i \left[\left(\Delta x_{i-1/2}\right)^2 \left(\frac{\tilde{C}_{i-1/2}^2}{6} + \frac{\tilde{\Gamma}_{i-1/2}}{2} - \frac{1}{8}\right) - \frac{V_i}{A_{i-1/2}}\frac{\Delta x_i}{24}\right] \left.\phi_{xx}\right|_{i-1/2}^n -
$$

$$
\tilde{C}_{i+1/2}^i \left[\left(\Delta x_{i+1/2}\right)^2 \left(\frac{\tilde{C}_{i+1/2}^2}{6} + \frac{\tilde{\Gamma}_{i+1/2}}{2} - \frac{1}{8}\right) - \frac{V_i}{A_{i+1/2}}\frac{\Delta x_i}{24}\right] \left.\phi_{xx}\right|_{i+1/2}^n +
$$

$$
\tilde{S}_i \Delta t \quad (5.77)
$$

Notice that if the spatial discretization is uniform, there is no diffusion, and $C = 1$, then Eq. (5.77) reduces to a point-to-point transfer, i.e. $\phi_i^{n+1} = \phi_{i-1}^n$.

Inserting Eq. (5.64) into Eq. (5.77), to take into account the presence of diffusion, results in the following discretized equation, rewritten to apply the ULTIMATE limiter (Sec. 5.5):

$$
\phi_i^{n+1} = \phi_i^n + \tilde{C}_{i-1/2}^i \phi_{i-1/2}^* - \tilde{C}_{i+1/2}^i \phi_{i+1/2}^* +
$$

$$
-\tilde{\Gamma}_{i-1/2}^i \left.\phi_x\right|_{i-1/2}^* + \tilde{\Gamma}_{i+1/2}^i \left.\phi_x\right|_{i+1/2}^* + \tilde{S}_i \Delta t \quad (5.78)
$$

where the starred scalars are:

$$\phi^*_{i-1/2} = \frac{1}{2}(\phi^n_i + \phi^n_{i-1}) - \frac{\Delta x_{i-1/2}}{2}\tilde{C}_{i-1/2}\ \phi_x|^n_{i-1/2} +$$

$$+ \left[(\Delta x_{i-1/2})^2 \left(\frac{\tilde{C}^2_{i-1/2}}{6} + \frac{\tilde{\Gamma}_{i-1/2}}{2} - \frac{1}{8}\right) - \frac{V_i}{A_{i-1/2}}\frac{\Delta x_i}{24}\right]\phi_{xx}|^n_{i-1/2}$$

$$\phi^*_{i+1/2} = \frac{1}{2}(\phi^n_{i+1} + \phi^n_i) - \frac{\Delta x_{i+1/2}}{2}\tilde{C}_{i+1/2}\ \phi_x|^n_{i+1/2} +$$

$$+ \left[(\Delta x_{i+1/2})^2 \left(\frac{\tilde{C}^2_{i+1/2}}{6} + \frac{\tilde{\Gamma}_{i+1/2}}{2} - \frac{1}{8}\right) - \frac{V_i}{A_{i+1/2}}\frac{\Delta x_i}{24}\right]\phi_{xx}|^n_{i+1/2}$$

$$\phi_x|^*_{i\pm1/2} = \Delta x_{i\pm1/2}\ \phi_x|^n_{i\pm1/2} - \tilde{C}_{i\pm1/2}\frac{\left(\Delta x_{i\pm1/2}\right)^2}{2}\ \phi_{xx}|^n_{i\pm1/2}$$

Analyzing Eq. (5.78), it is easy to see that terms of the kind:

$$\tilde{C}^i_{i\pm1/2}\frac{V_i}{A_{i\pm1/2}}\frac{\Delta x_i}{24}\ \phi_{xx}|^n_{i\pm1/2}$$

make the scheme non-conservative when the cell size Δx_i is not constant. This was not explicitly pointed out in Leonard's work [68, 69, 70], since this involved differentiation based on cells of the same size. Since this is not acceptable in a system code, the scheme will be forced to be conservative during application of the limiter by using the same limited upstream flux for the common face of two adjacent cells.

Special case: side junctions

Considering each of the cells with a side junction component, Eq. (5.78) becomes:

$$\phi^{n+1}_i = \phi^n_i + \tilde{C}^i_{i-1/2}\phi^*_{i-1/2} - \tilde{C}^i_{i+1/2}\phi^*_{i+1/2} - \sum_{k=1}^{K}\left\{\tilde{C}^i_{j-1/2,k}\phi^*_{j-1/2,k}\right\} +$$

$$-\tilde{\Gamma}^i_{i-1/2}\ \phi_x|^*_{i-1/2} + \tilde{\Gamma}^i_{i+1/2}\ \phi_x|^*_{i+1/2} + \sum_{k=1}^{K}\left\{\tilde{\Gamma}^i_{j-1/2,k}\ \phi_x|^*_{j-1/2,k}\right\} + \tilde{S}_i\Delta t \qquad (5.79)$$

where the new starred scalars are:

$$\phi^*_{j-1/2,k} = \frac{1}{2}(\phi^n_i + \phi^n_{j,k}) - \frac{\Delta x_{j-1/2,k}}{2}\tilde{C}_{j-1/2,k}\ \phi_x|^n_{j-1/2,k} +$$

$$+ \left[(\Delta x_{j-1/2,k})^2 \left(\frac{\tilde{C}^2_{j-1/2,k}}{6} + \frac{\tilde{\Gamma}_{j-1/2,k}}{2} - \frac{1}{8}\right)\right]\phi_{xx}|^n_{j-1/2,k}$$

$$\phi_x|^*_{j-1/2,k} = \Delta x_{j-1/2,k} \; \phi_x|^n_{j-1/2,k} - \tilde{C}_{j-1/2,k} \frac{\left(\Delta x_{j-1/2,k}\right)^2}{2} \; \phi_{xx}|^n_{j-1/2,k}$$

5.5 Application of the ULTIMATE conservative difference scheme to the solute convection equation

High-order numerical schemes usually exhibit nonphysical over- and undershoots in the presence of sharp gradients. Various techniques, depending on the specific numerical method adopted, have been developed to solve this problem while still retaining reasonable accuracy. Their principal objective is to guarantee the monotonicity of the solution.

The Universal Limiter (UL) for Transient Interpolation Modeling (TIM) of the Advective Transport Equation (ATE) [70] is a limiter that can be applied to explicit schemes of any order of accuracy that are based on the TIM method (such as QUICKEST). It is devised to impose monotonicity constraints on high-order numerical schemes, in order to avoid the unphysical oscillatory behavior that appears in regions of strong gradients when such schemes are used.

The fundamental idea of the employed strategy is to limit the value of ϕ at the computational cell edge. This limitation produces a bounded solution in which monotonicity is preserved, and the oscillations typical of high-order schemes are eliminated. In particular, the ULTIMATE limiter can be applied to explicit conservative difference schemes of any order of accuracy, and has the property of maintaining the expected accuracy of the numerical scheme it is applied to.

The QUICKEST-ULTIMATE methodology developed by Leonard [70] has currently been applied here, with some modifications to adapt it to the characteristics of a typical TH system code (e.g. variable grid size and variable velocities along the system model, cell-defined Courant number, etc.). The implementation is relatively simple and straightforward.

5.5.1 General treatment

In the case of system codes, the velocity may differ from one cell face to the other. Here the development is based on the downstream face of cell C (see Fig. 5.5). This requires the use of a different local notation for the cell indices based on the velocity sign (see Tab. 5.2), where C_d is defined positive.

Therefore, Eq. (5.78) can be rewritten as:

$$\phi_C^{n+1} = \phi_C^n + C_u^C \phi_u^* - C_d^C \phi_d^* + S_C \tag{5.80}$$

where S_C is a generic source term (which may contain the diffusion term as well, since it is not directly involved in the advective transport).
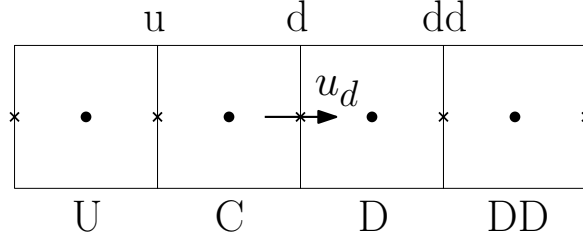
Figure 5.5: Scheme of the ULTIMATE limiter generalized computational cell.

	$u_{i-1/2}$		$u_{i+1/2}$	
	≥ 0	< 0	≥ 0	< 0
$\phi_{\mathbf{U}}$	ϕ_{i-2}	ϕ_{i+1}	ϕ_{i-1}	ϕ_{i+2}
$\phi_{\mathbf{C}}$	ϕ_{i-1}	ϕ_i	ϕ_i	ϕ_{i+1}
$\phi_{\mathbf{D}}$	ϕ_i	ϕ_{i-1}	ϕ_{i+1}	ϕ_i
$\phi_{\mathbf{DD}}$	ϕ_{i+1}	ϕ_{i-2}	ϕ_{i+2}	ϕ_{i-1}
$\mathbf{C_u^C}$	$\tilde{C}_{i-3/2}^{i-1}$	$-\tilde{C}_{i+1/2}^{i}$	$\tilde{C}_{i-1/2}^{i}$	$-\tilde{C}_{i+3/2}^{i+1}$
$\mathbf{C_d^C}$	$\tilde{C}_{i-1/2}^{i-1}$	$-\tilde{C}_{i-1/2}^{i}$	$\tilde{C}_{i+1/2}^{i}$	$-\tilde{C}_{i+1/2}^{i+1}$
$\mathbf{C_d^D}$	$\tilde{C}_{i-1/2}^{i}$	$-\tilde{C}_{i-1/2}^{i-1}$	$\tilde{C}_{i+1/2}^{i+1}$	$-\tilde{C}_{i+1/2}^{i}$
$\mathbf{C_{dd}^D}$	$\tilde{C}_{i+1/2}^{i}$	$-\tilde{C}_{i-3/2}^{i-1}$	$\tilde{C}_{i+3/2}^{i+1}$	$-\tilde{C}_{i-1/2}^{i}$

Table 5.2: Transformations used for the generalized treatment of the ULTIMATE limiter.

First, it has to be established as to whether the profile is monotonic or non-monotonic for the cells U, C and D, i.e. whether C is a maximum or a minimum. Then, if the profile is monotonic, it may be increasing or decreasing. If the profile is non-monotonic, the limiter is not applied and the upwind approximation $\phi_d^* = \phi_C^n$ is used.

In the case of a monotonic profile, the procedure described in the following applies; here only the procedure adopted for an increasing profile is shown, since for a decreasing profile the same relations hold, with the exception that the direction of the inequalities changes. Further below a summary of the procedure is reported for all the possible cases.

If the profile is increasing, the following relation applies:

$$\phi_U \leq \phi_C \leq \phi_D$$

There is therefore a so-called static condition to guarantee the preservation of monotonicity at the time t_n, considering that ϕ_d^* is obtained by interpolation between the cell-center values:

$$\phi_C^n \leq \phi_d^* \leq \phi_D^n$$

Moreover, there are three so-called dynamic conditions in order to preserve the maximum values of the scalar at the cell centers at the time t_{n+1}.

1. $\phi_C^{n+1} \geq \phi_U^n$

Using this condition in Eq. (5.80):

$$\phi_C^{n+1} = \phi_C^n + C_u^C \phi_u^* - C_d^C \phi_d^* + S_C \geq \phi_U^n$$

$$\phi_d^* \leq \frac{1}{C_d^C} \left[\phi_C^n + C_u^C \phi_u^* - \phi_U^n + S_C \right]$$

The value of ϕ_u^* is limited by the static condition $\phi_U^n \leq \phi_u^* \leq \phi_C^n$. The worst limiting condition for ϕ_d^* is when ϕ_u^* is minimum, i.e. $\phi_u^* = \phi_U^n$. Therefore the final limiting condition is:

$$\begin{cases} \phi_d^* \leq \dfrac{1}{C_d^C} \left[\left(C_u^C - 1 \right) \phi_U^n + \phi_C^n + S_C \right] & \text{if} \quad C_u^C \geq 0 \\[2mm] \phi_d^* = \phi_C^n & \text{if} \quad C_u^C < 0 \end{cases}$$

2. $\phi_D^{n+1} \leq \phi_{DD}^n$

   This condition is present because ϕ_d^* appears also in the advection equation for the cell D:

   $$\phi_D^{n+1} = \phi_D^n + C_d^D \phi_d^* - C_{dd}^D \phi_{dd}^* + S_D \leq \phi_{DD}^n$$

   $$\phi_d^* \leq \frac{1}{C_d^D} \left[\phi_{DD}^n + C_{dd}^D \phi_{dd}^* - \phi_D^n - S_D \right]$$

   The value of ϕ_{dd}^* is limited by the static condition $\phi_D^n \leq \phi_{dd}^* \leq \phi_{DD}^n$. The worst limiting condition for ϕ_d^* is when ϕ_{dd}^* is minimum, i.e. $\phi_{dd}^* = \phi_D^n$. Therefore, the final limiting condition is:

   $$\begin{cases} \phi_d^* \leq \dfrac{1}{C_d^D} \left[\left(C_{dd}^D - 1 \right) \phi_D^n + \phi_{DD}^n - S_D \right] & \text{if} \quad C_{dd}^D \geq 0 \\[2mm] \text{no limiter} & \text{if} \quad C_{dd}^D < 0 \end{cases}$$

Notice moreover that:

- The limiter of case 1 is equal to ϕ_C^n if the velocity u_u is negative, since it corresponds to a loss of inventory of the cell from both faces; in this case only, the value of the scalar inside the cell is convected.

- The limiter of case 2 is not used if the velocity u_{dd} is negative, since it corresponds to an injection inside the cell from both faces and the value of ϕ_D^{n+1} can be larger than the surrounding values.

- The limiter of case 2 is not used if ϕ_D^n is a maximum, since the condition become meaningless.

Summary

1. Define the computational cell with the aid of Tab. 5.2

2. Calculate

$$GRAD_{DU} = \phi_D - \phi_U$$

$$AGRAD_{DU} = |GRAD_{DU}|$$

$$ACURV_{DU} = |\phi_D - 2\phi_C + \phi_U|$$

3. If $ACURV_{DU} \geq AGRAD_{DU}$, then the profile is non-monotonic

$$\phi_d^* = \phi_C^n$$

4. If $ACURV_{DU} < AGRAD_{DU}$, then the profile is monotonic

   (a) Calculate

   $$GRAD_{DDC} = \phi_{DD} - \phi_C$$

   $$AGRAD_{DDC} = |GRAD_{DDC}|$$

   $$ACURV_{DDC} = |\phi_{DD} - 2\phi_D + \phi_C|$$

   (b) If $GRAD_{DU} \geq 0$, then the profile is increasing

   i. static condition $\phi_C^n \leq \phi_d^* \leq \phi_D^n$

   ii. dynamic condition $\phi_C^{n+1} \geq \phi_U^n$

   $$\begin{cases} \phi_d^* \leq \dfrac{1}{C_d^C} \left[\left(C_u^C - 1 \right) \phi_U^n + \phi_C^n + S_C \right] & \text{if} \quad C_u^C \geq 0 \\[2ex] \phi_d^* = \phi_C^n & \text{if} \quad C_u^C < 0 \end{cases}$$

   iii. if $ACURV_{DDC} < AGRAD_{DDC}$, then the profile is monotonic

   A. dynamic condition $\phi_D^{n+1} \leq \phi_{DD}^n$

   $$\begin{cases} \phi_d^* \leq \dfrac{1}{C_d^D} \left[\left(C_{dd}^D - 1 \right) \phi_D^n + \phi_{DD}^n - S_D \right] & \text{if} \quad C_{dd}^D \geq 0 \\[2ex] \text{no limiter} & \text{if} \quad C_{dd}^D < 0 \end{cases}$$

   (c) If $GRAD_{DU} < 0$, then the profile is decreasing

   i. static condition $\phi_C^n \geq \phi_d^* \geq \phi_D^n$

   ii. dynamic condition $\phi_C^{n+1} \leq \phi_U^n$

   $$\begin{cases} \phi_d^* \geq \dfrac{1}{C_d^C} \left[\left(C_u^C - 1 \right) \phi_U^n + \phi_C^n + S_C \right] & \text{if} \quad C_u^C \geq 0 \\[2ex] \phi_d^* = \phi_C^n & \text{if} \quad C_u^C < 0 \end{cases}$$

   iii. if $ACURV_{DDC} < AGRAD_{DDC}$, then the profile is monotonic

(a) Positive velocity.　　　　(b) Negative velocity.
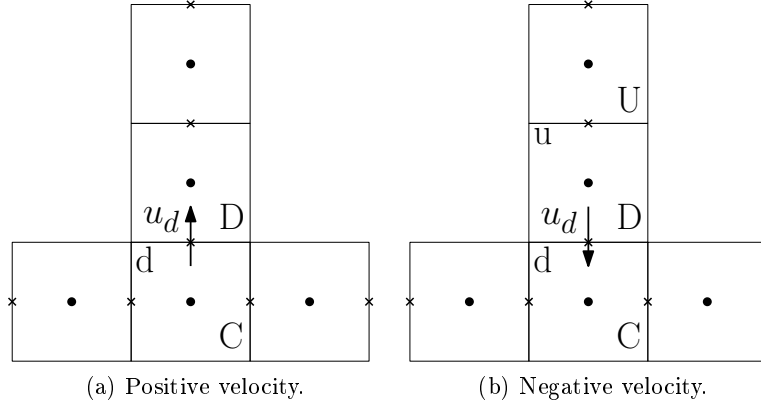
Figure 5.6: Cells involved in the flux limiter for the side junction.

A. dynamic condition $\phi_D^{n+1} \geq \phi_{DD}^n$

$$\begin{cases} \phi_d^* \geq \dfrac{1}{C_d^D} \left[\left(C_{dd}^D - 1 \right) \phi_D^n + \phi_{DD}^n - S_D \right] & \text{if} \quad C_{dd}^D \geq 0 \\[2ex] \text{no limiter} & \text{if} \quad C_{dd}^D < 0 \end{cases}$$

5.5.2　Special case: side junctions

In principle, adding a side junction is equivalent to adding a second dimension; Leonard, however, recommends to use a "locally one-dimensional" limiter, where the chosen direction is that normal to the cell face [70]. This simplifies notably the treatment of the side junction, i.e. Eq. (5.79) is not necessary. The strategy adopted in the present work consists in computing the side junction limiter as simple upwind if the velocity is positive (see Fig. 5.6a) and using only three cells in the case of negative velocity (see Fig. 5.6b), which corresponds to the first two conditions of the limiter.

Regarding the main pipe (faces $i-1$ and $i+1$), to obtain the correct results the contribution from each side junction has to be considered. This leads to the introduction of approximated side junction terms inside the source term of Eq. (5.80), which in our case have been chosen to be:

$$\begin{cases} -\phi_{j,k}^* \left| C_{j-1/2,k}^i \right| & \text{if} \quad C_{j-1/2,k}^i \geq 0 \\[2ex] +\phi_{j,k}^* \left| C_{j-1/2,k}^i \right| & \text{if} \quad C_{j-1/2,k}^i < 0 \end{cases}$$

i.e. a simple upwind estimate of the flux at the side junction.

5.6 Verification

5.6.1 Verification with a Gaussian plug of solute

An effective way to study numerical diffusion consists in injecting a known solute concentration distribution and comparing its computed evolution in time (in a purely advective transient) with the known analytical solution. A Gaussian distribution has been chosen here, since it can be fully characterized by the variance parameter, making the comparison between computed and analytical solutions quite straightforward [80].

Gaussian concentration distribution - analytical solution

Let us consider a purely advective equation of a scalar $\varphi(x, t)$ with constant velocity u:

$$
\begin{aligned}
PDE \quad & \varphi_t + u\varphi_x = 0 \\
IC \quad & \varphi(x, 0) = f(x)
\end{aligned}
\tag{5.81}
$$

The solution to this Initial Value Problem (IVP) is easily found with the method of characteristics [81] and corresponds to

$$
\varphi(x, t) = f(x - ut)
\tag{5.82}
$$

(refer to App. F for the detailed derivation). In our particular case, the function f is the Gaussian function:

$$
f(x) = B \exp\left(-\frac{(x - \mu)^2}{2\sigma^2}\right)
\tag{5.83}
$$

of mean μ and standard deviation σ. B is a normalization coefficient.

Finally, the reference analytical solution that will be considered is:

$$
\varphi(x, t) = B \exp\left(-\frac{[x - \mu_x]^2}{2\sigma_x^2}\right)
\tag{5.84}
$$

Eq. (5.84) is a Gaussian in the space domain with a mean $\mu_x = \mu + ut$ and a standard deviation $\sigma_x = \sigma$. However, it can also be seen as a Gaussian in the time domain with mean $\mu_t = (x - \mu_x)/u$ and standard deviation $\sigma_t = \sigma_x/u$. Most of the Gaussian lies within $\pm\pi\sigma$ from the mean value μ, i.e. in an interval of about $2\pi\sigma$. If N sampling points are needed to have a "smooth" representation of the Gaussian over such an interval, the maximum distance between these points will be $\Delta_{max} = \dfrac{2\pi\sigma}{N}$. Therefore, in the space domain the limit will be $\Delta x_{max} = \dfrac{2\pi\sigma_x}{N}$ and in the time domain $\Delta t_{max} = \dfrac{2\pi\sigma_t}{N} = \dfrac{2\pi\sigma_x}{Nu}$.

Numerical tests and results

The tests have been performed both with the original TRACE code and with TRACE modified with the QUICKEST-ULTIMATE scheme. Physical diffusion was neglected in order to isolate the effects of numerical diffusion.

The test case is a 20 m long straight pipe of 5 cm hydraulic diameter. A velocity of 1.0 m/s is imposed at the pipe inlet for the solute injection and a pressure of 0.1 MPa is imposed at the pipe outlet. The solute injection follows a Gaussian distribution with the following characteristics: μ=-14.0 m, σ=3.0 m, B=0.05. The standard deviation was chosen such as to have about N=20 points in the range of $2\pi\sigma$ in the case of the maximum Δx (1.0 m). The injection starts after 1.5 s to allow the establishment of stationary flow conditions inside the pipe.

Cr		Δx (m)				
		1.00	0.50	0.10	0.05	0.01
Δt (s)	1.00	1.00	-	-	-	-
	0.75	0.75	-	-	-	-
	0.50	0.50	1.00	-	-	-
	0.25	0.25	0.50	-	-	-
	0.10	0.10	0.20	1.00	-	-
	0.075	-	-	0.75	-	-
	0.050	0.05	0.10	0.50	1.00	-
	0.025	-	0.05	0.25	0.50	-
	0.010	0.01	0.02	0.10	0.20	1.00

Table 5.3: Verification tests table: list of the Courant number values for different combinations of spatial and temporal discretizations (u=1.0 m/s).

Tab. 5.3 shows the list of the numerical tests performed. Since the numerical scheme adopted for the QUICKEST discretization is explicit in time, only the cases with $C \leq 1$ have been considered in the comparison, even though TRACE is able to overcome this limit with its semi-implicit scheme. This allows one to have both versions of the code advancing with the same constant time step. To quantify the effects of spatial and temporal discretizations on the numerical damping, it is possible to define the relative error on the pulse amplitude as:

$$\varepsilon = \frac{|B_0 - B_{num}|}{B_0} \tag{5.85}$$

where B_0 is the amplitude of the analytical solution (which remains constant for pure advection) and B_{num} is the amplitude of the computed solution (which is affected by numerical diffusion).

In Figs. 5.7-5.11, the relative error on the pulse amplitude is plotted as a function of the distance from the solute injection for both code versions. It can be seen that:
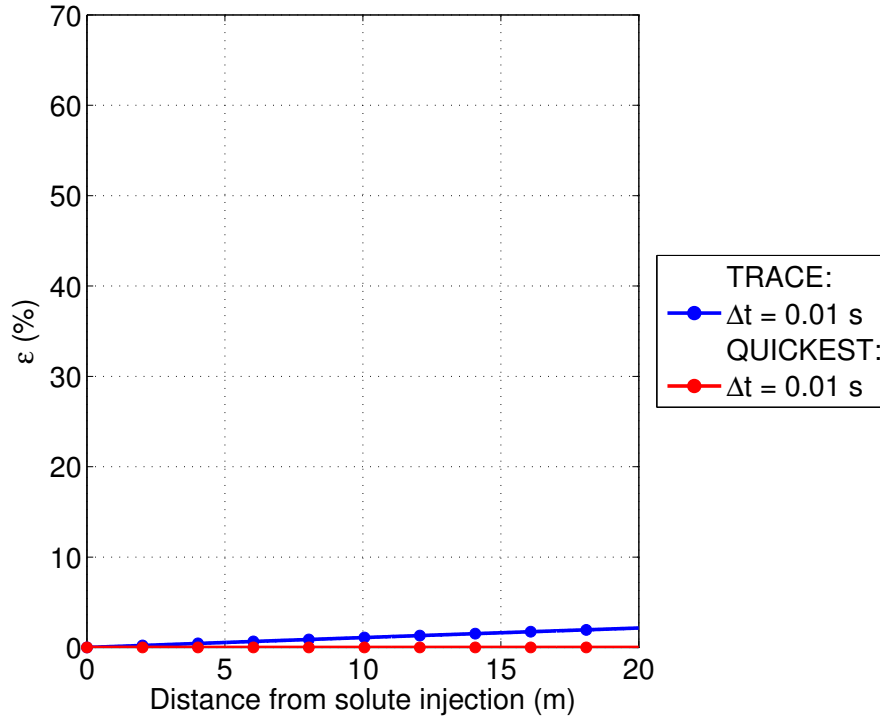
Figure 5.7: Relative error on the pulse amplitude as a function of the distance from the solute injection point; parametric study with fixed $\Delta x = 0.01$ m and varying Δt.
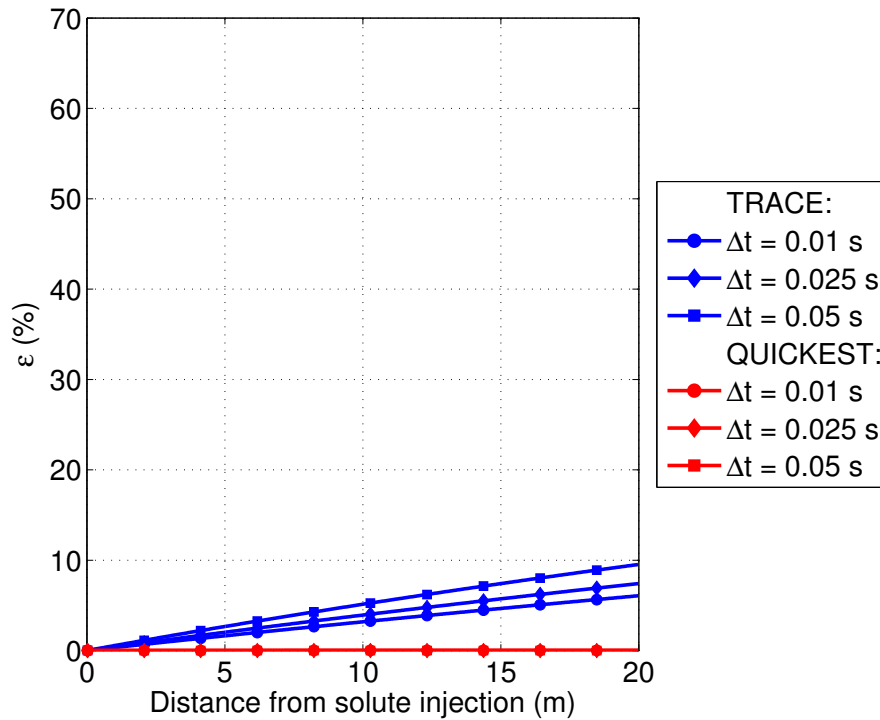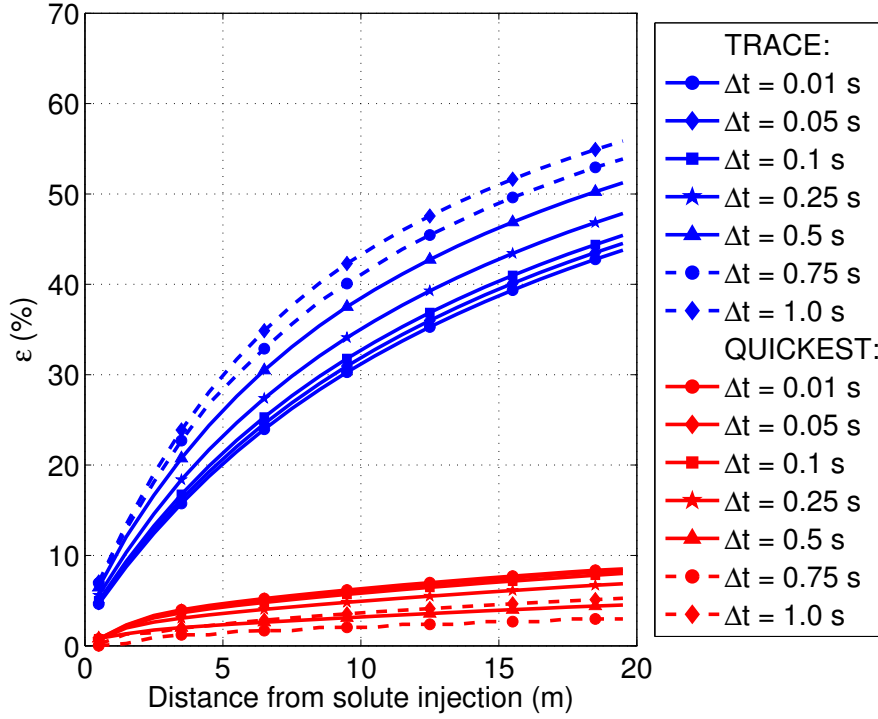

Figure 5.8: Relative error on the pulse amplitude as a function of the distance from the solute injection point; parametric study with fixed $\Delta x = 0.05$ m and varying Δt.
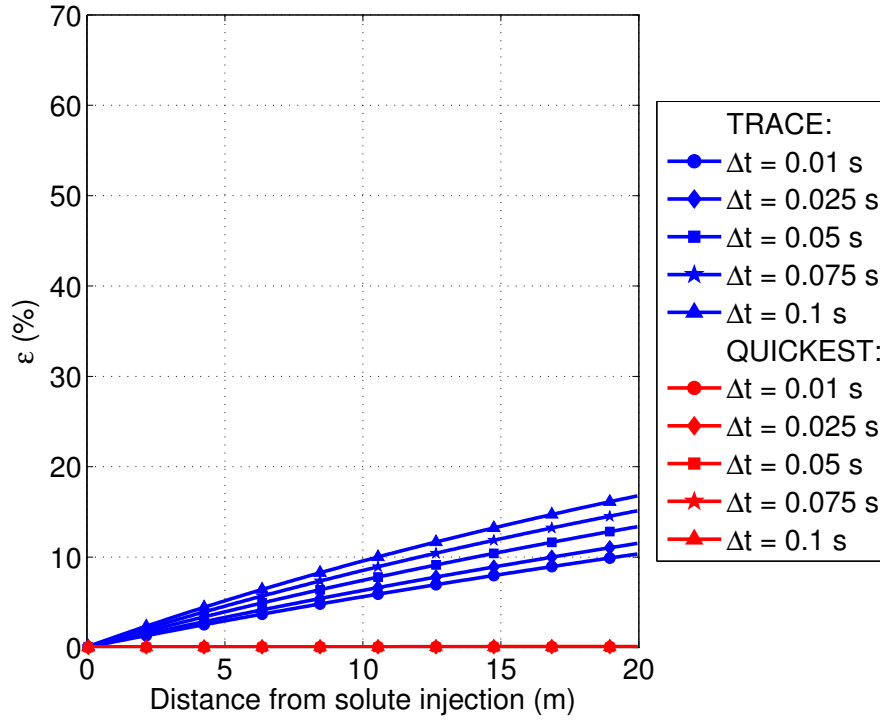
Figure 5.9: Relative error on the pulse amplitude as a function of the distance from the solute injection point; parametric study with fixed $\Delta x = 0.1$ m and varying Δt.
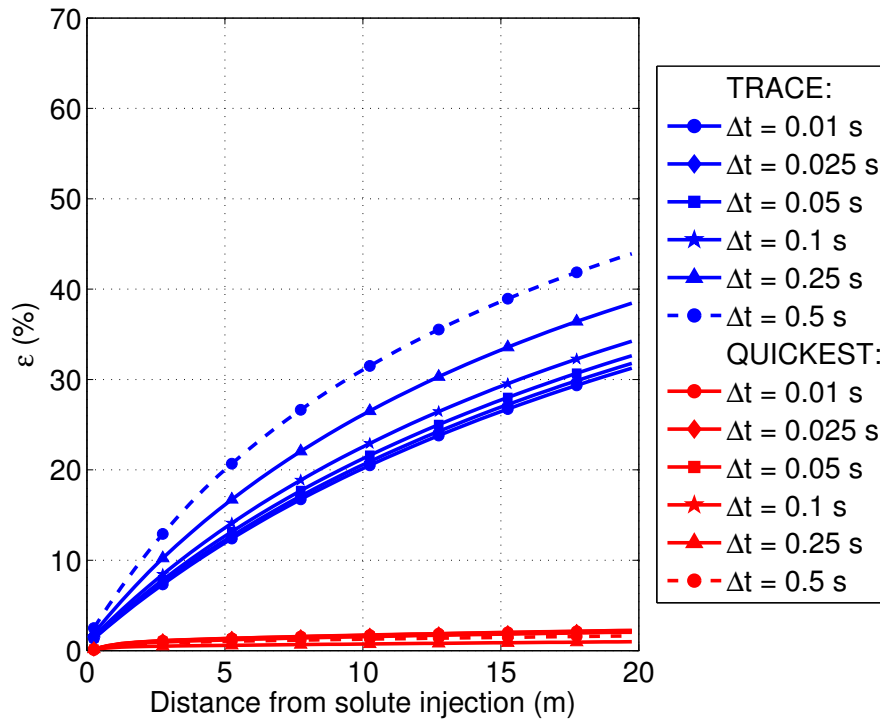
Figure 5.10: Relative error on the pulse amplitude as a function of the distance from the solute injection point; parametric study with fixed $\Delta x = 0.5$ m and varying Δt.

Figure 5.11: Relative error on the pulse amplitude as a function of the distance from the solute injection point; parametric study with fixed $\Delta x = 1.0$ m and varying Δt.

- The solution of the QUICKEST scheme is exact if $C = 1$. In fact, if the geometry does not change, there is no diffusion and, with $C = 1$ (as in the present case), the solution reduces to a point-to-point transfer, i.e. $\phi_i^{n+1} = \phi_{i-1}^n$.

- The case $\Delta x = 0.01$ m is used simply for comparison with the original TRACE, since for the QUICKEST scheme it reduces to a point-to-point transfer (C=1), as indicated above.

- For $\Delta x \leq 0.1$ m, the solution of the QUICKEST scheme is almost immune to numerical diffusion, regardless of the time step chosen (after 20 m, the maximum ε is less than 1% in Fig. 5.9). One can notice that the original TRACE solution is still not converged.

- For $\Delta x > 0.1$ m, there is clearly a saturation of the numerical diffusion error with increasingly reduced integration time step, for both the original TRACE and the QUICKEST scheme. It has to be pointed out that the convergence is reached from above in TRACE and from below in QUICKEST. Moreover, in QUICKEST there is some oscillatory behavior of the error before reaching convergence. For both code versions, however, the error increases with the distance from the inlet, as expected in the presence of numerical diffusion.

- The QUICKEST scheme offers a substantial reduction of numerical diffusion in com-

parison to the original TRACE formulation, even with large spatial discretizations (see the case for $\Delta x = 1.0$ m).

Regarding the computational power required to run the code with the new numerical scheme, there is an increase by about a factor of 6. However, there is clearly still room for speed-up optimization.

5.6.2 Verification with the injection of a step-wave of solute

The QUICKEST scheme implemented in the TRACE code has been further tested and verified by employing a step-wave for the solute injection. Following the same procedure as used in [82], the magnitude of the diffusion coefficient introduced by the numerical scheme can be quantified.

Injection of a step-wave - analytical solution

The pure advection problem is the same as in Eq. (5.81), with a different IC, i.e.

$$f(x) = \begin{cases} C & if \quad x < 0 \\ 0 & if \quad x \geq 0 \end{cases} \tag{5.86}$$

Therefore, the solution is

$$\varphi(x) = \begin{cases} C & if \quad x - ut < 0 \\ 0 & if \quad x - ut \geq 0 \end{cases} \tag{5.87}$$

To quantify the diffusion coefficient introduced by the numerical scheme, the numerical solution of the purely advective equation is compared to the analytical solution of the advective equation with diffusion term. The equation to be solved analytically for the scalar $\varphi(x, t)$ is:

$$\begin{aligned} PDE \quad & \varphi_t + u\varphi_x - D\varphi_{xx} = 0 \\ IC \quad & \varphi(x, 0) = f(x) \end{aligned} \tag{5.88}$$

The generic analytical solution of this problem can be obtained as discussed in App. G. Assuming constant velocity u and constant diffusion coefficient D, the solution is:

$$\varphi(x, t) = \frac{1}{2\sqrt{\pi Dt}} \int_{-\infty}^{+\infty} f(\beta) e^{-(x-ut-\beta)^2/(4Dt)} d\beta \tag{5.89}$$

Imposing the initial condition and thus selecting the particular solution satisfying Eq. (5.87), one obtains:

$$\varphi(x, t) = \frac{C}{2} \left[1 - \mathrm{erf}\left(\frac{x - ut}{2\sqrt{Dt}} \right) \right] \tag{5.90}$$

The time derivative of the previous equation at a generic time $t = u/L$ reads:

$$\varphi_t|_{t=L/u} = \frac{Cu^{3/2}}{2\sqrt{\pi DL}} \tag{5.91}$$

and is a function of the diffusion coefficient, the distance L traveled by the step-wave along the system, and the initial step height C. Therefore, the diffusion coefficient can be expressed as a function of known variables:

$$D = \frac{C^2 u^3}{4\pi L \ \varphi_t|_{t=L/u}} \tag{5.92}$$

Notice that, in the case of pure advection, the step remains sharp (i.e. the derivative in Eq. 5.92 is equal to infinity) and the diffusion coefficient is zero, as expected.

Numerical tests and results

The tests have been performed both with the original TRACE code and the modified TRACE with the QUICKEST-ULTIMATE scheme. Physical diffusion was neglected in order to investigate the effect of numerical diffusion only. The test pipe is the same as described in Subsec. 5.6.1, but the solute injection has been modified to be a step-wave. In a pure advective process, the step would remain sharp. However, due to the effect of numerical diffusion, the step shape of the solute front is not maintained (see Fig. 5.12).

In Tab. 5.4, values are presented of the numerical diffusion coefficient obtained from different numerical tests. It is clear that the QUICKEST-ULTIMATE scheme introduces a numerical diffusion which is at least one order of magnitude smaller than that introduced by the original TRACE scheme (see also Fig. 5.12). In addition, the numerical diffusion drops considerably with decreasing grid size, especially when the QUICKEST-ULTIMATE scheme is employed. The results obtained are consistent with those reported in Subsec. 5.6.1.

5.7 Validation with the coupled tool CFX/TRACE

The experimental testing of the coupled CFX/TRACE simulations described in Chap. 4 (see also [83]) was seen to be strongly affected by the numerical diffusion in the TRACE code. In the particular case investigated, TRACE could not reach convergence even with very small temporal and spatial discretizations, which are not commonly used in system codes. This has, in fact, been the main driving force for the present in-depth investigation of the solute tracking scheme issue.

For the sake of completeness, the studied case, i.e. the flow in a double T-junction with a recirculation loop driven by a pump, is briefly described here again (see Fig. 5.13). The aim has been to simulate how the solute injected in the side loop redistributes within the

D (m^2/s)	Unmodified TRACE - Δx (m)					QUICKEST-ULTIMATE - Δx (m)				
Δt (s)	1.00	0.50	0.10	0.05	0.01	1.00	0.50	0.10	0.05	0.01
1.00	1.0E0	-	-	-	-	8.1E-2	-	-	-	-
0.50	7.6E-1	5.1E-1	-	-	-	7.1E-2	2.6E-2	-	-	-
0.10	5.7E-1	3.1E-1	1.0E-1	-	-	8.5E-2	2.8E-2	2.1E-3	-	-
0.05	5.4E-1	2.8E-1	7.5E-2	5.0E-2	-	8.6E-2	2.9E-2	2.0E-3	7.1E-4	-
0.01	5.2E-1	2.6E-1	5.5E-2	3.0E-2	1.0E-2	8.7E-2	3.0E-2	2.5E-3	8.4E-4	6.1E-5

Table 5.4: Verification tests table for the original TRACE code and for the QUICKEST-ULTIMATE scheme, with the injection of a step-wave of solute: list of values of the numerical diffusion coefficient for different combinations of spatial and temporal discretizations (u=1.0 m/s).
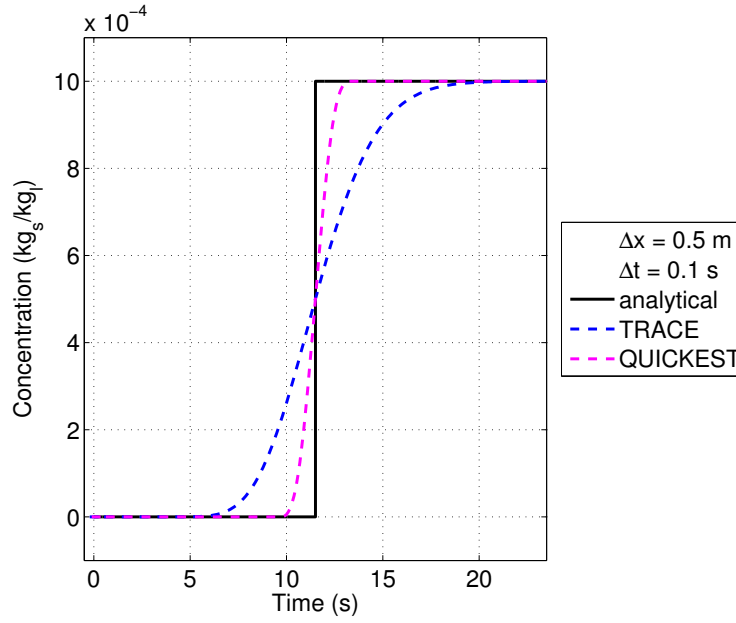
Figure 5.12: Evolution of an injected square wave of solute at $x = 10$ m, for $\Delta x = 0.5$ m and $\Delta t = 0.1$ s. Comparison between the analytical solution, the unmodified TRACE and the QUICKEST-ULTIMATE scheme.
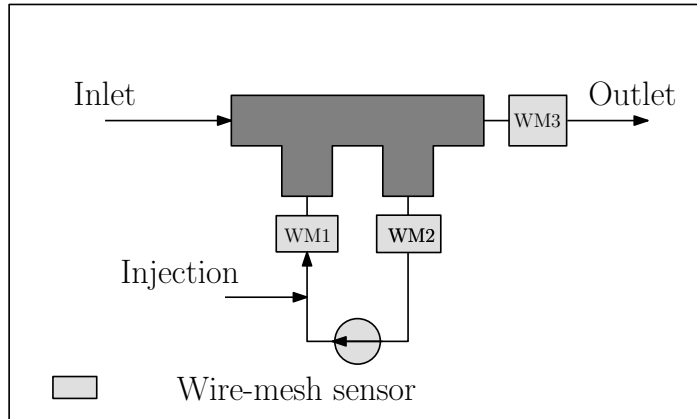
Figure 5.13: Sketch of the double T-junction experiment; the dark gray part is simulated with CFD and TRACE, the side loop and the injection only with TRACE.

side and main loop branches, after the T-junction zone. Both the stand-alone TRACE code and the coupled CFX/TRACE code are used for the purpose. When applying the coupled CFX/TRACE code, the T-junction region (where three-dimensional effects are expected to be dominant) is simulated as a CFX computational domain, while the rest of the loop is simulated within TRACE. The simulation results are compared with experimental values recorded by means of wire-mesh sensors installed at the three indicated locations.

Fig. 5.14 shows a comparison between the earlier reported results obtained with a standard TRACE stand-alone simulation (see Fig. 4.8) and those obtained with the currently
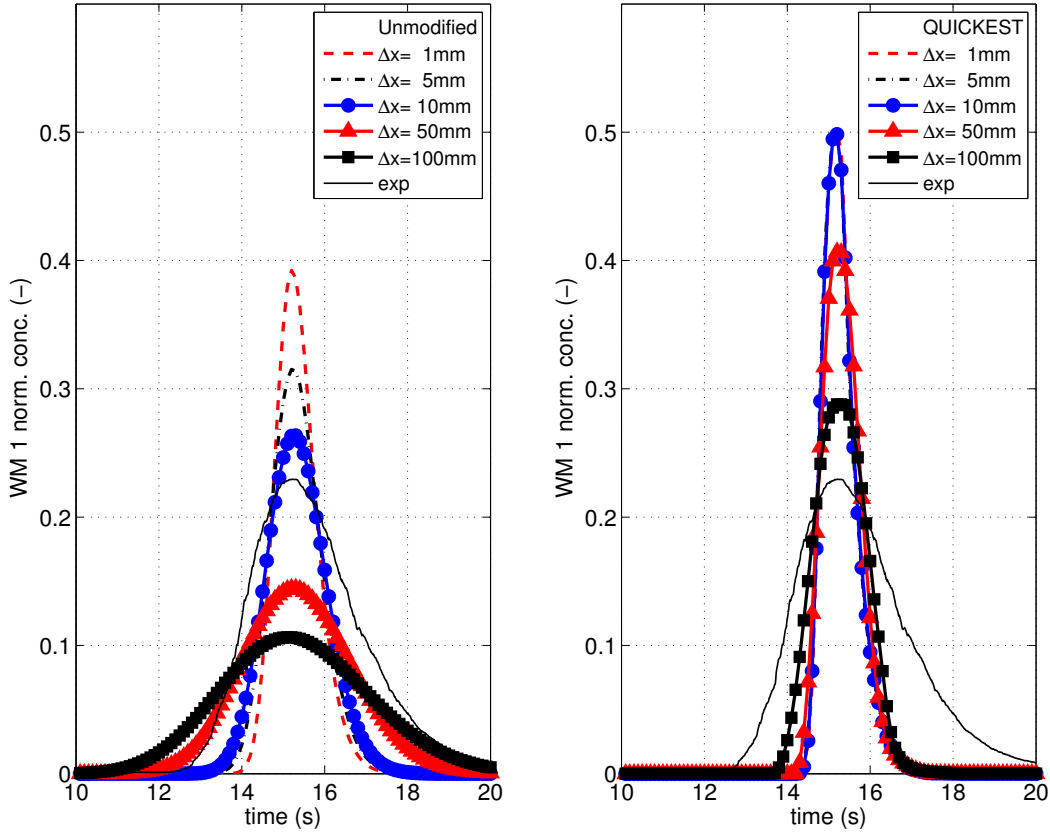
Figure 5.14: Evolution of the normalized solute concentration at the side loop outlet (WM1) for a TRACE stand-alone simulation, compared with experimental data. Parametric study for different TRACE mesh sizes, with time step fixed at 0.001 s. On the left the standard unmodified TRACE results are presented (as reported in Fig. 4.8), while on the right are shown the results with the QUICKEST-ULTIMATE scheme.

implemented QUICKEST-ULTIMATE scheme. Here it is important to note that, with the QUICKEST scheme, the convergence is reached between mesh sizes of 1 cm and 5 cm (in agreement with the results presented in Subsec. 5.6.1). With the standard version of TRACE, on the other hand, the convergence issue remains even when employing very small meshes.

The new scheme has also been applied to re-run the coupled-code simulation reported in Chap. 4, both without physical diffusion and with a constant diffusion coefficient of 0.006 m^2/s (Fig. 5.15). The TRACE mesh size for the case with the QUICKEST scheme was chosen to be 1 cm, in order to completely suppress the numerical diffusion, while the physical diffusion coefficient was chosen to match the value corresponding to the experimental results. The solution obtained with the original TRACE upwind scheme corresponds to a mesh size of 1 cm, chosen earlier to adapt the numerical diffusion to the physical one, as the focus was initially on the importance of correctly modeling three-dimensional effects. It is seen clearly that the numerical diffusion introduced by the original upwind scheme is behaving like
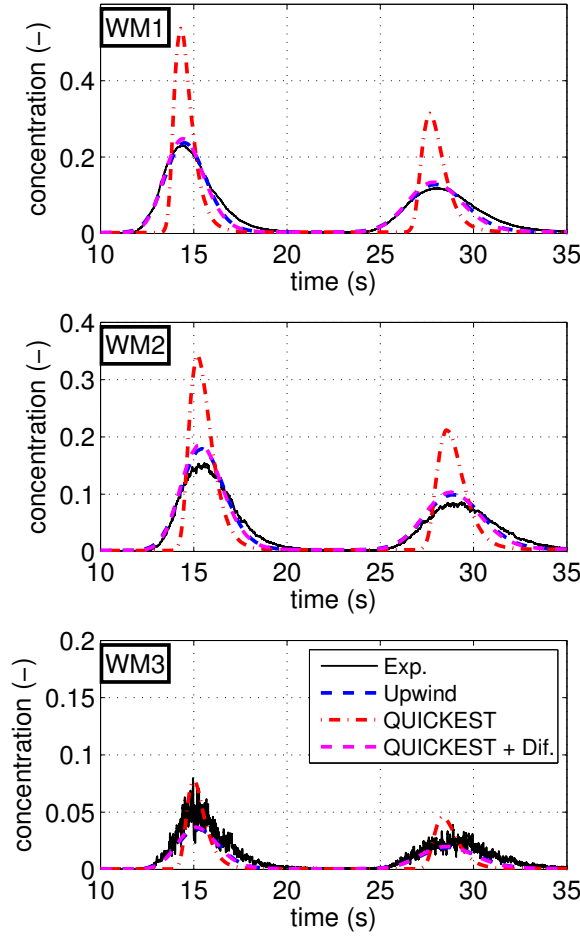
Figure 5.15: Simulation results for the inlet solute concentration (WM1, top) and for the concentration splitting in the T-junction for the side loop (WM2, center) and the main loop (WM3, bottom) at the wire-mesh sensor locations. Comparison between experimental data, TRACE upwind scheme, QUICKEST scheme and QUICKEST scheme with a constant physical diffusion coefficient of 0.006 m^2/s. The plots show the solute loops subsequent to the injection.

physical diffusion.

The simulation versus experiment comparisons shown in both Figs. 5.14 and 5.15 clearly indicate that, in order to correctly model the transport of a solute, reducing numerical diffusion is not sufficient in itself. A physical diffusion term needs to be introduced in the one-dimensional formulation as well, in order to account for the enhanced mixing induced by turbulence (see the results obtained with the QUICKEST scheme, with and without the diffusion term).

In Fig. 5.16, the time integral of the solute concentration at the location WM1 is shown over the entire period considered for the simulation. The absence of diffusion (QUICKEST scheme solution) leads to a sharp increase of the solute concentration integral every time the
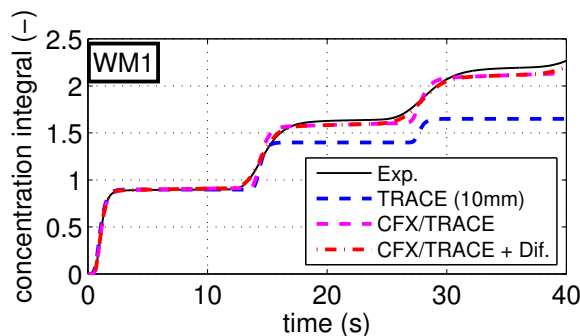
Figure 5.16: Simulation results for the solute concentration integral at the inlet at the wire-mesh sensor location WM1. Comparison between experimental data, TRACE stand-alone with QUICKEST scheme, CFX/TRACE with QUICKEST scheme, and CFX/TRACE with QUICKEST scheme and a constant physical diffusion coefficient of 0.006 m^2/s.

tracer plug recirculates in the loop. The slope is correctly captured if physical diffusion is taken into account. As expected, the diffusion does not influence the total amount of tracer recirculating in the side loop (i.e. the plateau values in Fig. 5.16), which is instead a result of correctly capturing the three-dimensional effects in the T-junction section through the employment of a CFD code. This is clearly demonstrated by looking at the results obtained with the TRACE stand-alone simulation. As mentioned in Subsec. 4.3.3, a 1D system code will wrongly compute the distribution of the tracer plug between main and side loop branches, since this is done only on the basis of the flow ratio between the loop branches.

5.8 Analysis of PKL experiments

PrimärKreisLauf (PKL) is an experimental facility designed to simulate PWRs under accidental conditions [44]. The facility replicates the entire primary system and most of the secondary system (except for the turbine and condenser) of a 4-loop 1300-MW PWR plant, with elevations scaled to 1:1 and volumes and power reduced by a factor of 145. The number of rods in the core and the number of U-tubes in the steam generators are scaled down by a factor of 145 as well. The experiments considered here were performed in the PKL test facility to study the issue of boron dilution from the thermal-hydraulic point of view and are a good reference to both validate and improve thermal-hydraulic codes [84].

The studies on boron dilution within the OECD/PKL II project consisted of two tests:

- Test F1.1 is a clear continuation of the E series of the SETH project [85], related to Small-Break Loss of Coolant Accident (SBLOCA) with boron dilution. In this case, the test is configured such as to resemble a PWR of Westinghouse design, i.e. with a steam generator cool-down rate of about 50 K/h and an Emergency Core Cooling (ECC) injection into all 4 cold legs. The test simulates the accumulation of a maximum amount of lowly borated water in the Loop Seals (LSs) and studies the restart of natural

circulation providing the minimum boron concentration at the reactor pressure vessel inlet [86].

- Test F1.2 was designed to analyze the rate of boron dilution under reflux-condensation conditions depending on the mass inventory in the primary system. The test follows a series of steady states with different mass inventories and with a high steam-generator level maintained in the U-tubes, thus providing experimental evidence regarding the U-tube levels and mass inventories at which the accumulation of condensate in the loop seals occurs [87].

For the purpose of the present validation, both the standard and improved TRACE code versions have been used to analyze Test F1.1. The velocity-dependent Levenspiel diffusion coefficient has been employed with the improved version (see Subsec. 5.4.5).

The analyzed test is a boron dilution transient with a small break located in cold leg no. 1. A High Pressure Safety Injection (HPSI) pump injects symmetrically into the cold leg of each of the loops. Unavailability of Low Pressure Safety Injection (LPSI) and accumulators is supposed. In addition, one of the HPSI pumps is not operable. Since the maximum operating pressure of the PKL test facility is 45 bar, it is not possible to simulate the entire transient of a normal PWR starting from nominal operating pressure (ca. 160 bar). Hence, in the test, the transient starts at a primary pressure of less than 45 bar and with the initial conditions corresponding to those that would prevail in a real plant at this stage of the transient. The initial conditions for Test F1.1 consist of a partially emptied primary system at a pressure of 39 bar with highly borated water in the core and unborated water in the loop seals. In order to reach such conditions, a conditioning phase is performed during which the primary mass inventory is reduced to 50% and reflux-condensation conditions are established in the primary system. During this phase, slugs of boron diluted condensate are formed in the LSs. The conditioning phase was also simulated by TRACE in order to analyze the process of the formation of unborated slugs. For the first 5000 seconds, the primary and secondary pressures decrease following the secondary cool-down. Since the amount of injected water is greater than the discharged mass, the primary system refills. When the primary coolant mass reaches 100%, primary pressure recovers and natural circulation is established. At this moment, the boron diluted slugs are transported to the vessel through the cold legs. Secondary pressure continues falling, bounded by the cool-down, while primary pressure stabilizes at 20 bar until the end of the transient.

The predictions of the boron concentration along loop no. 4 are shown in Fig. 5.17. The boron dilution in the LS is seen to be correctly simulated (bottom plot, Fig. 5.17). The differences between the two sets of TRACE results are very small since the numerical diffusion in TRACE and the physical diffusion in the QUICKEST-ULTIMATE scheme follow a similar pattern (second-order derivative). The main difference is that, whereas the original TRACE results are affected by the time step and the spatial discretization, the results
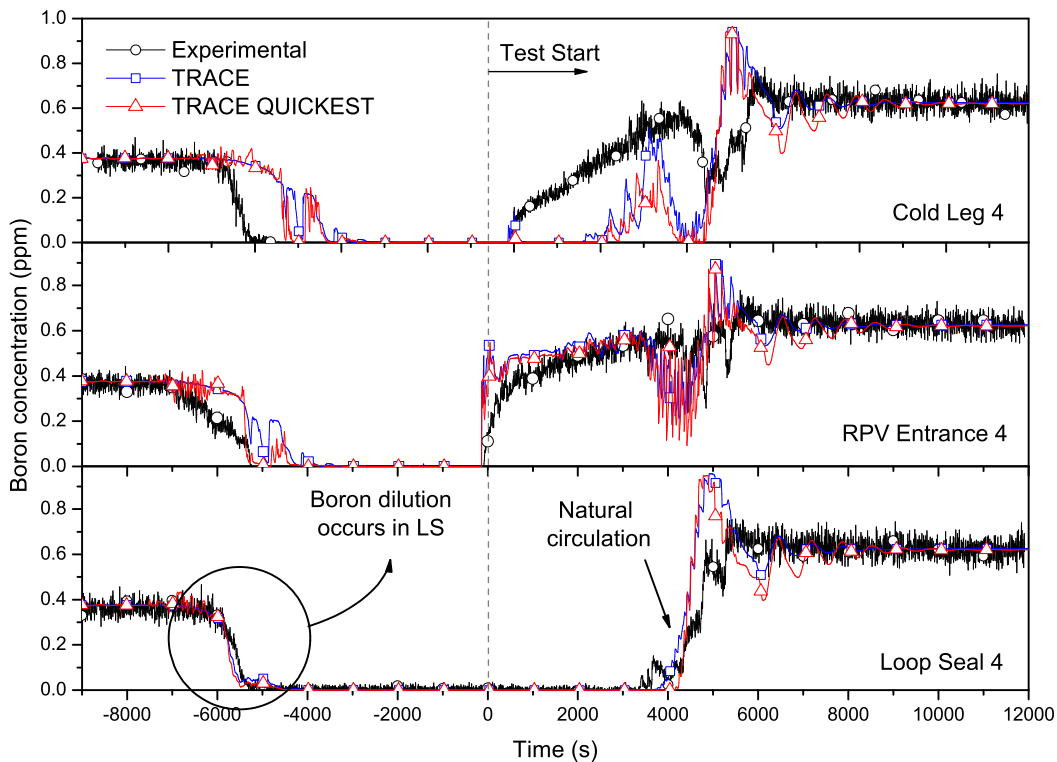
Figure 5.17: Boron concentration along loop 4, PKL Test F1.1.

with the new method are not altered by such changes. It is also important to notice that, with the QUICKEST-ULTIMATE model, the oscillations are less damped because of the less pronounced numerical diffusion.

5.9   Chapter summary

The QUICKEST-ULTIMATE methodology has been successfully applied to the solute tracker used in the TRACE system code. The existing first-order upwind discretization has been replaced with a high-order upwind scheme, which is able to accurately track sharp solute fronts.

Parametric studies for a straight pipe, carried out with both the original and the new solute trackers, have demonstrated that it is possible to greatly reduce (and in some cases eliminate) the errors related to numerical diffusion when the new scheme is applied.

Further optimization is still needed in order to reduce the computational time required by the new scheme (the increase is by about a factor of 6 currently). Moreover, a more sophisticated model for the junction cells should be implemented for obtaining better and more stable results, because the currently adopted simple model sometimes produces nonphysical oscillations for certain mesh sizes (about 1 cm). It should be noted, however, that such small meshes are seldom used and are therefore not of high relevance for plant simulations.

The stand-alone TRACE simulation of the T-junction experiment reported in [83] has been run with the new version of the code. The results are qualitatively consistent with the straight-pipe parametric studies. In addition, the coupled CFX/TRACE simulation has been carried out in conjunction with a constant diffusion coefficient. Thereby, it has been shown that, while the current reduction of the numerical diffusion in TRACE is a positive fact, the effects of physical diffusion clearly need to be introduced into the solute transport equation for obtaining satisfactory agreement with the experimental results. The physical diffusion largely depends on the turbulence characteristics of the flow and on the system geometry. Further efforts are needed to implement an appropriate model for the diffusion coefficient.

As further validation for the QUICKEST-ULTIMATE methodology implementation, simulations of PKL Test F1.1 have been carried out with the new numerical scheme and a variable diffusion coefficient. The results obtained have been compared with both the experimental data and the results of simulations with the unmodified version of TRACE. Agreement with experiment has been found to be quite satisfactory and in line with the standard TRACE results.

Chapter 6

Coupled code validation: the FLORIS experiment

This chapter describes the second phase of experimental validation of the coupled CFX/TRACE computational tool, i.e. the analysis of certain qualification tests carried out at the recently built FLORIS[1] mixing loop at PSI. The new facility has been designed to study the coolant flow behavior in the lower plenum of a LWR during accident scenarios, and the preliminary tests aimed at characterization of the facility have provided an attractive framework to further validate the CFX/TRACE coupling. Thus, while the double T-junction experiments (Chap. 4) have served to challenge the coupled tool with the transport of a tracer under steady-state flow conditions, the FLORIS tests do so with respect to the coupling of the momentum equation with transient flow conditions.

Sec. 6.1 describes in detail the experimental facility and the set-up of the acquisition system. Sec. 6.2 presents the results of pre-test simulations aimed at the establishment of a test matrix. Sec. 6.3 addresses the tests, carried out according to the proposed test matrix, and shows the data obtained from the experiment. Finally, Sec. 6.4 presents the comparisons made between the experimental data and the results obtained on the basis of coupled CFX/TRACE, as well as CFX and TRACE stand-alone, calculations.

6.1 Experimental facility

6.1.1 Facility layout

The new experimental facility FLORIS built at PSI features a scaled-down, simplified, two-dimensional vertical section of a BWR reactor pressure vessel (RPV)[2], made of transparent

---

[1] Flow circulation in the LOwer plenum and RISer.

[2] The FLORIS facility was designed and constructed by W. M. Bissels [88], with the main aim of studying density driven flow phenomena in the lower plenum of a BWR. The current utilization of the facility to provide a complex flow domain for testing the coupled tool is clearly of generic nature. As such, the fact that certain

Plexiglas (Fig. 6.1). The section is about 20 mm thick and comprises the downcomer, the lower and upper plena and the core region, built on a 1:10 scale. The four regions are shaped such as to take into account the presence of jet pumps and fuel assemblies (Fig. 6.2).

The section has two perpendicular inlet pipes in the downcomer region and three perpendicular outlet pipes in the upper plenum. All the openings are connected to two recirculation loops through different sets of valves, in order to allow a high degree of flexibility in the configurations that can be used during the experiments (Fig. 6.3). Each recirculation loop is equipped with a flow-meter and is connected to an external water tank. The two recirculation loops are driven by frequency-controlled pumps, allowing a fine control of transients. A honeycomb section is employed in each loop to reduce the turbulence of the inlet flow. Such a section is followed by a straight pipe (with a length-to-diameter ratio of about 50) connected directly to the vessel inlets, yielding fully developed flow under stationary conditions. The inlet and outlet pipes are also provided with pressure taps to measure the pressure drop inside the vessel model. The same taps can be used to inject a continuous, controlled tracer quantity with an external syringe pump (Fig. 6.4) just before the vessel inlet. Moreover, in each recirculation loop, there is a pipe section that can be insulated from the main flow through two synchronized, rapid-closure automated valves. At such a location, a tracer can be injected to form a high concentration plug, which can thereafter be suddenly released into the system by activating simultaneously the two mentioned valves.

The entire internal surface of the two-dimensional section is equipped with a wire-mesh sensor [65, 66], featuring 112 transmitter wires and 64 receiver wires (see Figs. 6.5 and 6.6). This allows one to effectively measure the tracer concentration over the entire flow domain of the vessel, except at the height of the inlet and outlet sections. A similar layout has already been used successfully in the ROCOM facility [89, 90]. The wire-mesh sensor allows a high spatial- and time-resolved measurement (about 10 mm spatial resolution and up to 1250 Hz sampling rate, respectively, for the whole vessel) of the local concentration of the tracer injected into the system, spreading into the lower plenum and consequently entering the core channels. Unfortunately, because of the presence of a reinforcement metal frame around the vessel, it was not possible to install Particle Image Velocimetry (PIV) instrumentation to measure the temporal evolution of the velocity field inside the lower plenum.

After the pre-test simulations (Sec. 6.2), a 50 mm long and 10 mm thick baffle was added on the side of each jet pump outlet for two reasons:

1. to avoid mixing and flow suction immediately after the jet pump, so that the injected concentration could be measured reliably. As a matter of fact, the jet pumps are metallic and are built in a way that prevents wire-mesh sensor measurements at the inlet of the vessel. Thus, the inlet concentration can effectively be measured only downstream of the jet pump outlet;

BWR geometrical features are represented is not of direct relevance here.

Figure 6.1: Front view of the FLORIS vessel.
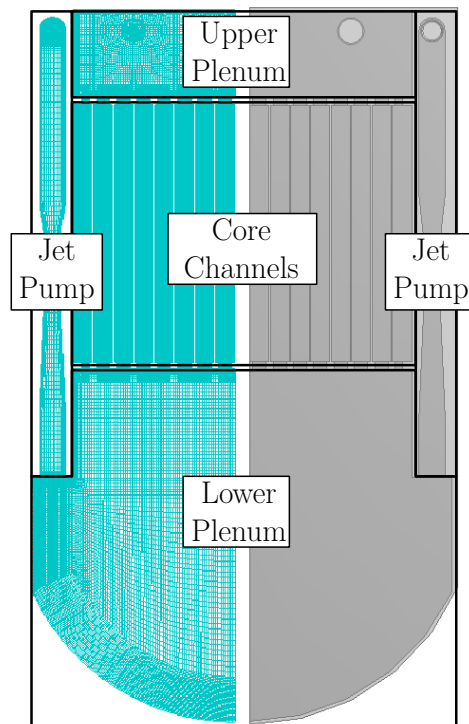
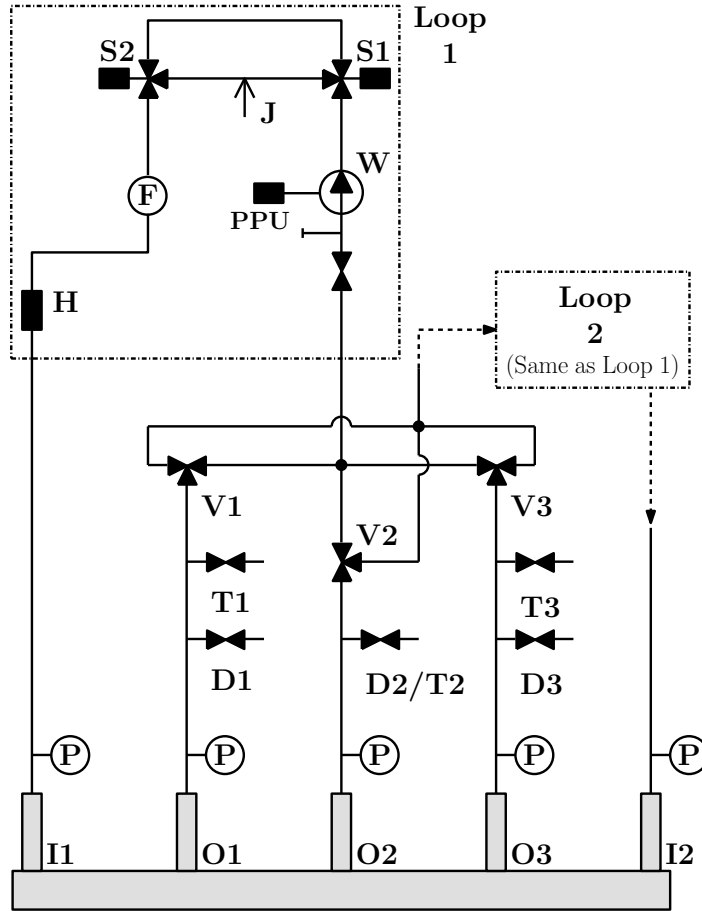Figure 6.2: CAD drawing and sample meshing of the FLORIS facility. The main sections are displayed.

Figure 6.3: Hydraulic scheme of the recirculation loops. I and O denote the vessel inlets and outlets, P the pressure taps, D the connections to the drain, T the connections to the tank, V the three-way valves and W is the frequency-controlled pump. PPU denotes the Power Processing Unit (i.e. the pump frequency controller), S the rapid-closure valves, J the tracer injection, F the flow meter and H the honeycomb section. The top-down view of the two-dimensional FLORIS vessel is shown colored in gray.

Figure 6.4: Syringe pump, able to provide a continuous, controlled injection in the facility. The screw-driven system allows a very precise measurement of the injected mass flow.
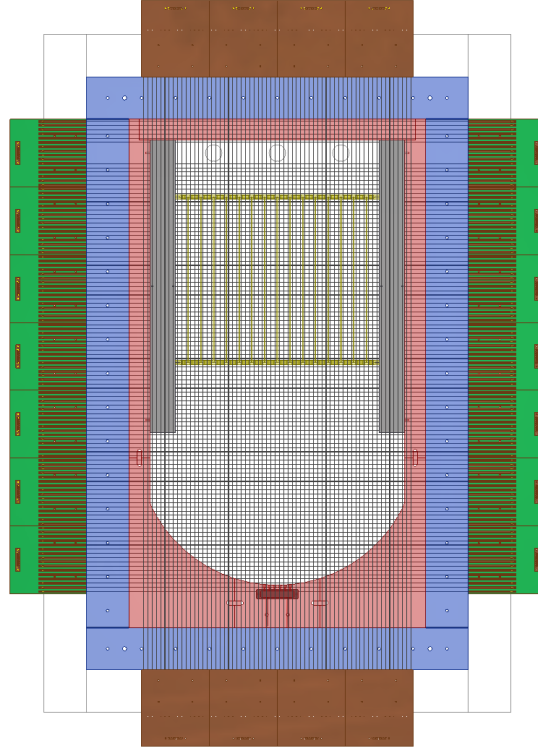
Figure 6.5: FLORIS CAD drawing showing the arrangement of the wire-mesh sensor. The blue part is a metal frame used to reinforce the vessel and hold it in position. The green squares are the transmitting wire-mesh sensor modules (7 in total), while the brown squares are the receiving wire-mesh sensor modules (4 in total).
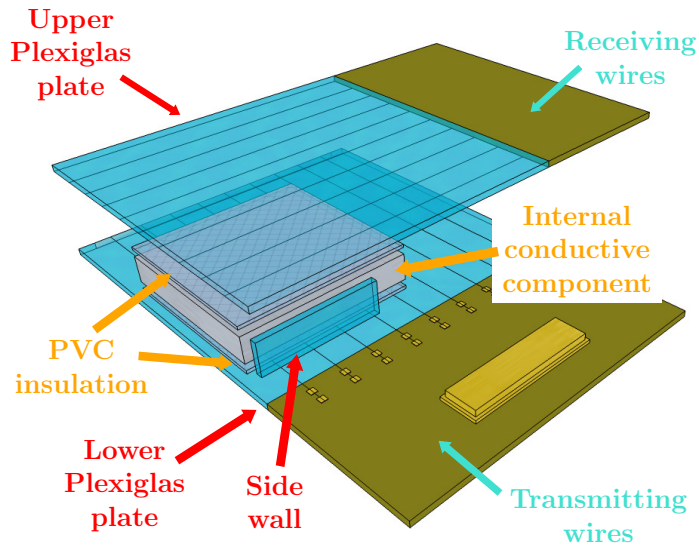
Figure 6.6: Simplified, exploded view of the FLORIS vessel with its internal components.

2. to better stabilize the vortices in the lower plenum and thus avoid possible oscillations of the flow field, which were observed during the symmetric pre-test simulations (see Sec. 6.2 for details).

6.1.2 Acquisition system

The set-up of the acquisition system has been part of the present research. Below, some details are given on the work carried out for the control and signal acquisition of the wire-mesh sensor and the FLORIS facility in general.

Wire-mesh sensor

The wire-mesh sensor acquisition system consists of an electronic box and a graphical program provided by the manufacturer (Fig. 6.7). The data acquisition is implemented in a specific binary format. A set of FORTRAN programs, together with Linux shell and MATLAB scripts, has been developed to process the data (filtering, calibration, normalization, extraction) so as to obtain suitable outputs to be used with the the simulations. The start of the wire-mesh acquisition system is triggered from the FLORIS control and acquisition system (see below), in order to synchronize the timing of all acquired data (i.e. wire-mesh sensor readings, mass flow, pressure and tracer release/injection).

Due to the presence of frequency controllers for the pump, undesired high frequency noise interfered with the wire mesh electronics, resulting in a moderately noisy signal. Certain measures were adopted to reduce the disturbances (insulation transformer, separation of the electronic groundings, current feed from a different line, etc.). Nevertheless, noise could not be eliminated completely; the remaining noise issue was tackled by acquiring the wire-mesh data at a frequency of 1250 Hz (the maximum available) and low-pass filtering these at 50 Hz. This operation gave overall smooth results without sacrificing the accuracy of the measurements.

FLORIS facility

The FLORIS acquisition and control system was devised to:

- vary the pump rotational speed, independently for each of the two loops;

- measure the differential system pressure between inlet and outlets;

- record the mass flow rate in each loop;

- continuously inject the tracer, or release the tracer plugs as required.

The system was set up using a National Instrument cDAQ (compact Data AQuisition) configuration; the cDAQ is an empty chassis with dedicated modules (current input/output, voltage input/output, digital input/output, temperature readings, etc.) that interfaces with
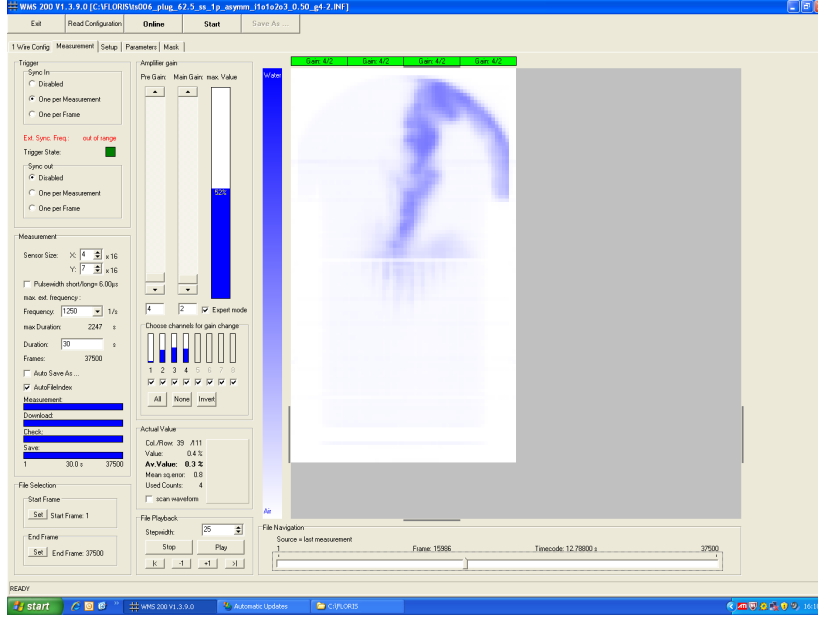
Figure 6.7: Wire-mesh sensor acquisition system interface [91]. On the left, various parameters can be set for the acquisition; on the right, a graphical display of the current measurement is shown. The dark blue cloud indicates the high concentration area caused by the injected tracer traveling in the lower plenum and entering the core.

a PC through a USB port. The graphical user interface to communicate with the cDAQ was set up with LabVIEW (Fig. 6.8).

The acquisition and control system was connected according to the specifications from the component manuals. An extra DC current feed, which was required to supply adequate energy to the instrumentation, was provided separately by a small generator. The wiring was set up on a rack, located on the side of the facility.

6.1.3   Reference schematic sketch

Fig. 6.9, a reference schematic sketch of the FLORIS RPV mock-up, will be referred to during the entire description of the displayed experimental data and simulation results, since it contains the numbering of the core channels and of the relevant wire-mesh sensor rows used for the comparisons. In particular, the rows of interest, as indicated in Fig. 6.9, are the jet pump outlet (WM 34) and three elevations within the core (corresponding to WM 56, WM 75 and WM 93 which are, respectively, the inlet, middle and outlet sections of the core). WM 34 has 5 measurement points over the jet pump outlet cross section (horizontal direction, with respect to the figure), while each of the core rows has 48 points over the core section, 3 for each channel (always in the horizontal direction). The experimental data values and simulation results reported in Secs. 6.3 and 6.4 have, in each case, been averaged over the appropriate number of measurement points.
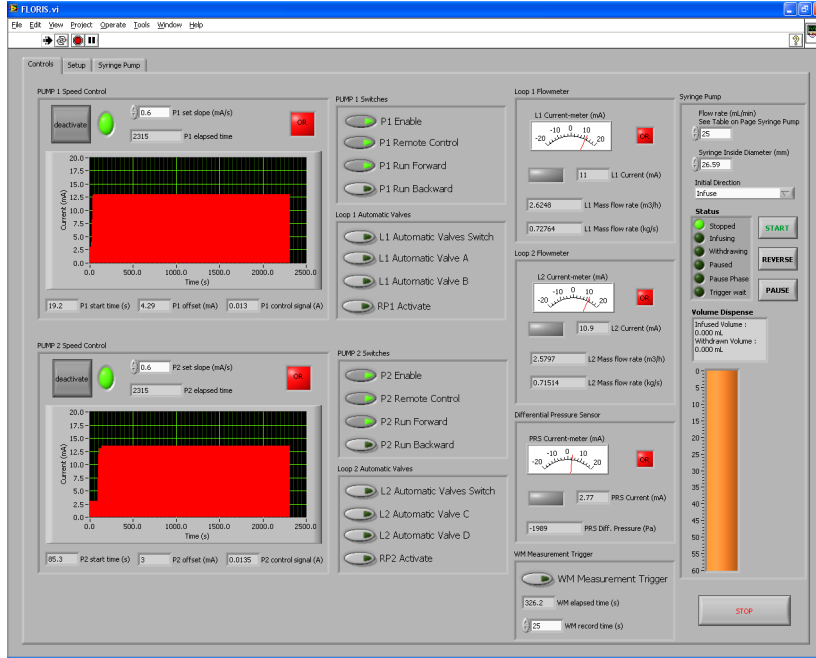
Figure 6.8: FLORIS control and acquisition system interface. On the left are the current controls for the two pumps (top and bottom). In the center-left column are the control switches for the pumps and for the rapid-closure valves (duplicated for each loop). In the center-right column are the measurements from the two flow-meters and from the differential pressure transducer. On the right, the controls for the injection system can be seen.
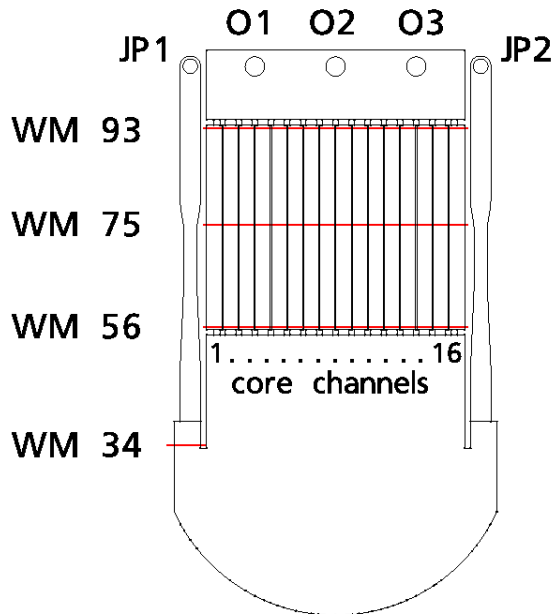
Figure 6.9: Reference schematic sketch of the FLORIS vessel with the relevant measurement positions and the core-channel numbering. JP1 is the jet pump where the tracer injection takes place.

6.2   Pre-test CFD simulations

In order to support the definition of an appropriate test matrix for the experimental campaign on FLORIS, pre-test CFD simulations were performed using ANSYS CFX. The mesh generated for the modeling of the RPV mock-up is symmetric with respect to the vertical axis and fine enough to have values of $y^+ < 2$ for an inlet mass flow rate of 0.67 kg/s. This is a requirement for the employment of the Shear Stress Transport (SST) turbulence model, a variation of the $\kappa - \omega$ model implemented in ANSYS CFX [58]. Even though geometrical symmetry is present, a mesh for the full model was used for the CFD simulations, in order to investigate the eventual development of flow asymmetries or instabilities in the test section. The entire mesh consists of about 6 million hexahedra. To simplify the CFD mesh, the inlets and outlets of the core channel were modeled as square channels (while in fact they have rounded edges). This approximation should not impact the accuracy of the CFD results. Moreover, it should be mentioned that, since the core walls are fixed but not glued inside the facility, a certain bypass flow might take place in between the core channels. This flow, however, is believed to be negligible, in view of the way the core channels are compressed between the two vertical plates of FLORIS; therefore, in the CFD model, all the core channels are assumed to be completely separated from each other.

The intention has been to perform experiments under both steady-state and transient flow conditions in this campaign. Subsec. 6.2.1 presents the pre-test simulations carried out to define the steady-state experiments, while Subsec. 6.2.2 presents those for the transient tests.

6.2.1   Steady-state simulations

Eight ANSYS CFX simulations with stationary boundary conditions were carried out at the nominal mass flow rate of 0.67 kg/s, characterized by different combinations of opened inlets and outlets. The simulations were performed in order to analyze all possible configurations and the corresponding flow patterns. Basically, the following four situations were considered (refer to Fig. 6.9):

1. one open inlet (JP1) and one open outlet: case 1 (O1 opened), case 2 (O2 opened) and case 3 (O3 opened);

2. one open inlet (JP1) and two open outlets: case 4 (O1 and O2 opened), case 5 (O1 and O3 opened) and case 6 (O2 and O3 opened);

3. one open inlet (JP1) and all three outlets opened: case 7;

4. all the inlets and outlets opened.

Situations 1 to 3 are asymmetric configurations, while situation 4 is symmetric. The latter is nevertheless of interest for investigation of the onset of flow instabilities, which might occur when symmetric boundary conditions are applied. In Figs. 6.10-6.12, the results of the steady-state simulations described above are presented. In all the simulations with asymmetric boundary conditions (Figs. 6.10 and 6.11), it is clearly noticeable that a large eddy is present in the central part of the lower plenum, slightly deformed and shifted to the left because of the geometrical configuration and the non-symmetric boundary conditions. A stagnation zone develops in the upper right part of the lower plenum. In addition, during the simulations with the right outlet O3 opened (Figs. 6.10c, 6.11b, 6.11c and 6.11d), a vortex appears in the right zone of the upper plenum, above the corresponding stagnation zone in the lower plenum. As a consequence of these two stagnation areas, the mass flow rate in the core channels 11-16 is close to zero, such that almost the entire flow is concentrated in the other two thirds of the core.

The CFD simulations for situation 4 in steady-state mode resulted in an asymmetric solution when the SST turbulence model was employed, and in a symmetric solution when the $\kappa - \varepsilon$ model was used instead. Situation 4 was therefore calculated also in transient mode. Two cases were analyzed, starting from both symmetric and asymmetric initial velocity fields in the RPV and left to evolve until steady-state conditions were reached. The boundary conditions (velocity at the RPV inlet boundaries) were kept symmetric and constant. The results, obtained with ANSYS CFX using the hexahedral mesh and with the SST turbulence model, were compared to those obtained with a second CFD code, i.e. STAR-CCM+ [92], using a polyhedral mesh and the $\kappa - \varepsilon$ turbulence model. The target criterion for convergence in ANSYS CFX was set to a Root Mean Square (RMS) value of 10^{-4}, while it was set to a RMS value of 10^{-5} for STAR-CCM+[3]. The pressure at the open outlets was set to 1 bar.

In Fig. 6.12a the results, obtained with ANSYS CFX and STAR-CCM+, are shown for situation 4, starting from an asymmetric initial velocity field (case 8a). Under these conditions, even if a symmetric mesh is employed, an asymmetric flow regime is predicted. During the transient run, it was found that, once the solution had stabilized, small flow oscillations were still present, but the overall flow field tended to remain stable in the position shown in Fig. 6.12a. Whether, in the simulations, the flow-field asymmetry develops towards the left or the right side of the model, was found to be very sensitive to the initial conditions, as can be seen from the results obtained from the simulations with the two different codes. This was thus identified as an important factor to be taken into account during the experiments, because the same nominal conditions might lead to different results, depending on inevitable small perturbations in the flow or in the boundary conditions.

If the symmetric transient simulation is started by imposing a symmetric velocity field as initial condition, the development of a symmetric flow regime oscillating around the central

---

[3]The reason behind the choice of a different RMS criterion in the two codes is the different way in which this is evaluated in each code (since the solver algorithms are different).

(a) Velocity streamlines with left inlet and left outlet opened (situation 1, case 1).

(b) Velocity streamlines with left inlet and central outlet opened (situation 1, case 2).

(c) Velocity streamlines with left inlet and right outlet opened (situation 1, case 3).
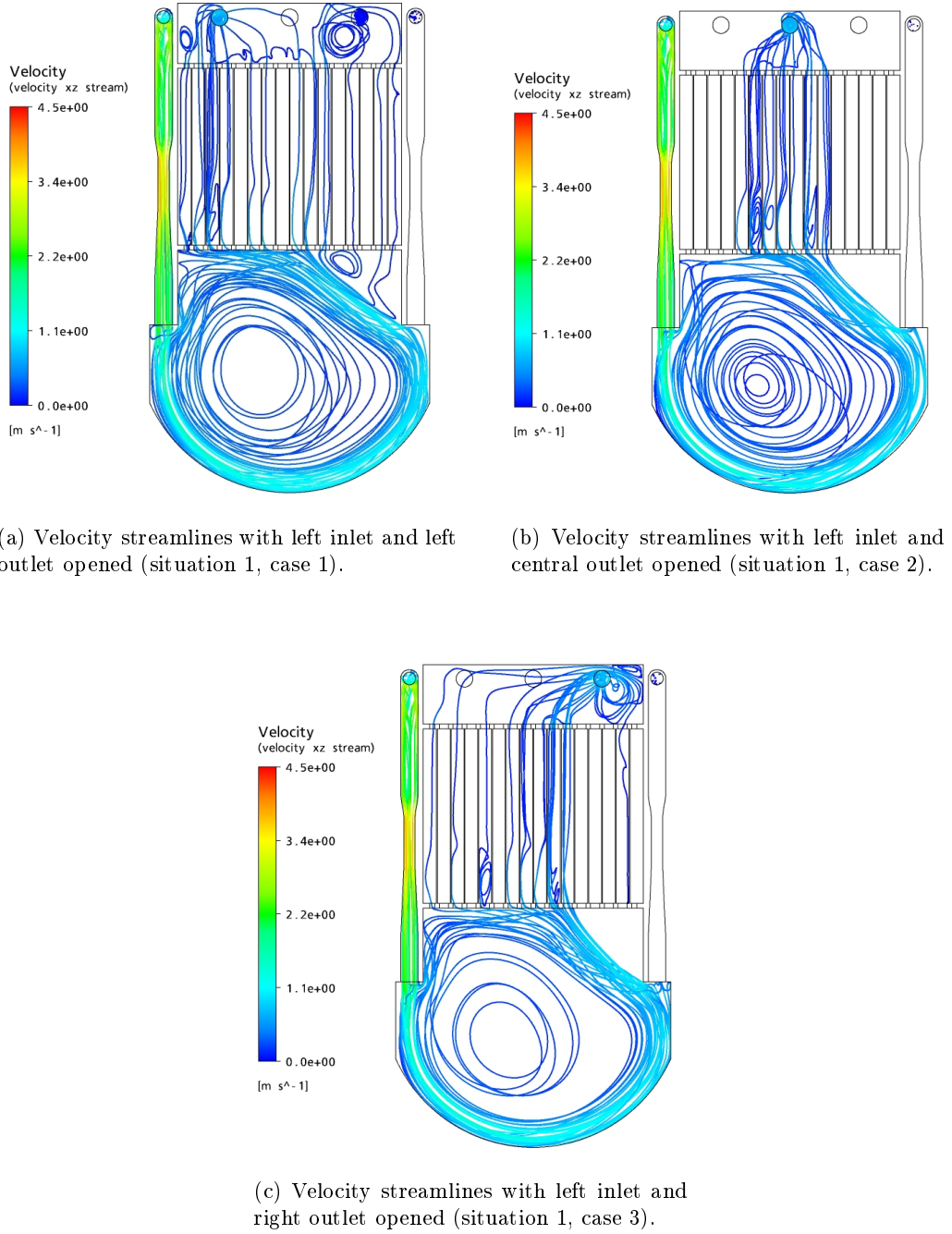
Figure 6.10: Velocity streamlines for the steady-state pre-test simulations. Cases 1 to 3.

axis of the facility is predicted by both codes, as illustrated in Fig. 6.12b. In this case, the pre-test simulations predict the occurrence of a stagnation zone in the central part of the lower plenum. The position of this stagnation zone changes with time, resulting in oscillations of the flow field. It could even happen that the oscillations stabilize into an asymmetric flow-field condition, similar to that shown in Fig. 6.12a. In this case, since the initial conditions
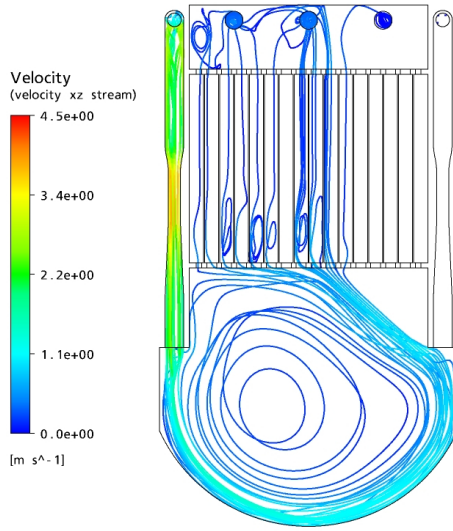
(a) Velocity streamlines with left inlet and left and central outlets opened (situation 2, case 4).
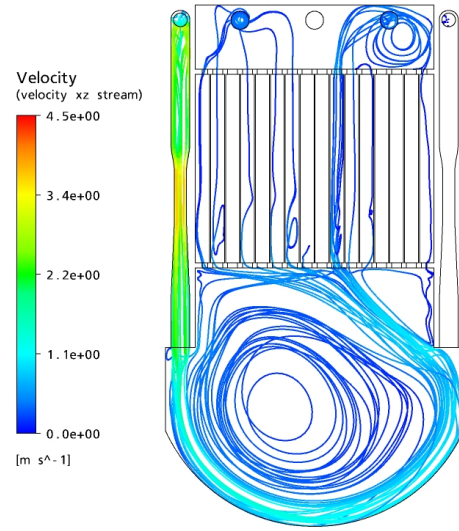
(b) Velocity streamlines with left inlet and left and right outlets opened (situation 2, case 5).
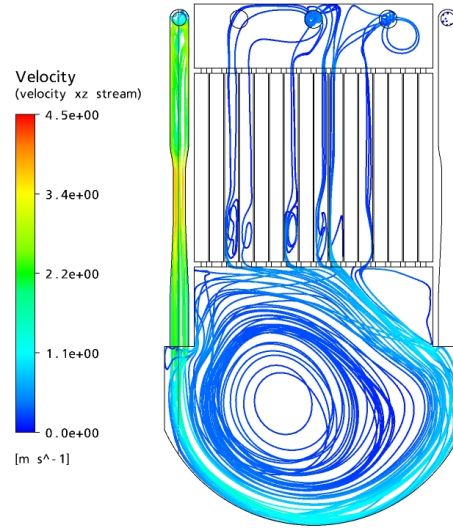
(c) Velocity streamlines with left inlet and central and right outlets opened (situation 2, case 6).
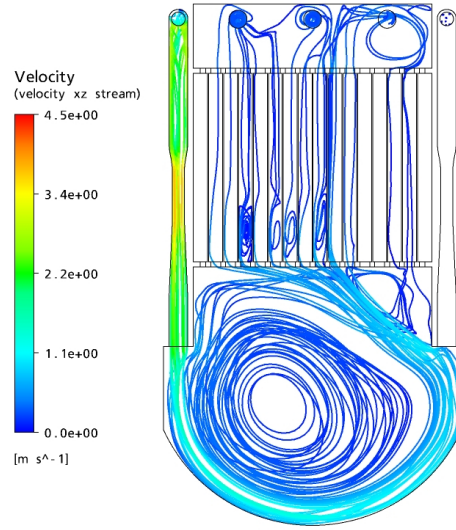
(d) Velocity streamlines with left inlet and all outlets opened (situation 3, case 7).

Figure 6.11: Velocity streamlines for the steady-state pre-test simulations. Cases 4 to 7.

are identical and fully symmetric, it will be the numerical truncation error, which will finally push the flow to one side or the other.
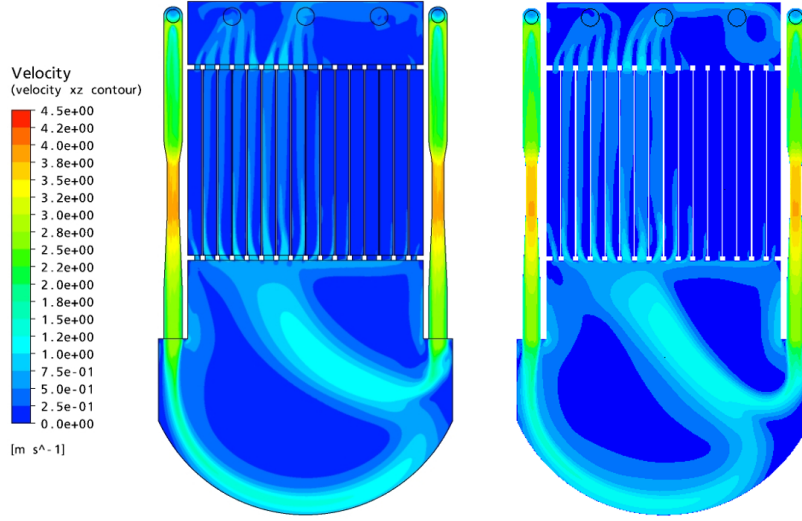
(a) Velocity field with symmetric boundary conditions (situation 4, case 8A), obtained through a transient with asymmetric initial conditions. Comparison between ANSYS CFX (left) and STAR-CCM+ (right).
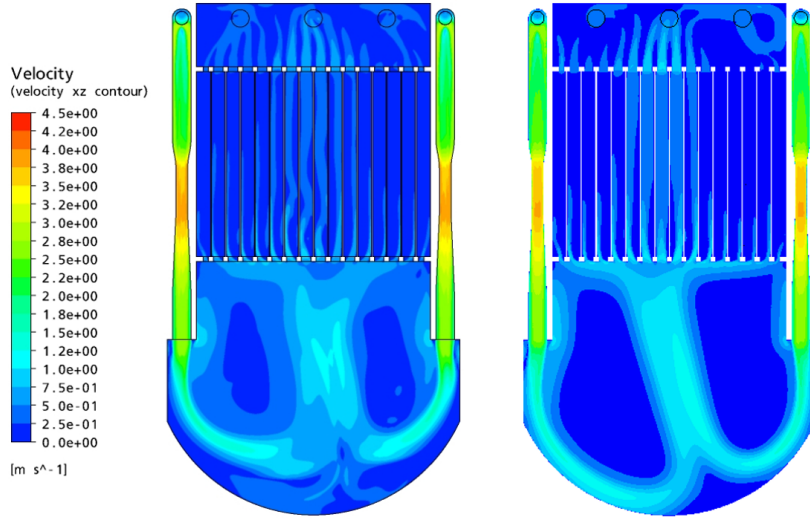
(b) Velocity field with symmetric boundary conditions (situation 4, case 8B), obtained through a transient with symmetric initial conditions. Comparison between ANSYS CFX (left) and STAR-CCM+ (right).

Figure 6.12: Velocity streamlines for the steady-state pre-test simulations. Cases 8A and 8B.

As mentioned, in the experiments themselves, there will clearly be some inevitable small differences in the initial conditions, which will have a destabilizing effect on the flow. Such an occurrence has been observed in earlier CFD calculations for 3D RPV models, e.g. for the ROCOM test facility [42]. In Fig. 6.12b, one can also note that, in the lower section of the lower plenum, the SST model (Fig. 6.12b, left) predicts the occurrence of two additional recirculation regions around the lower plenum stagnation region, just below the two large

eddies in the lower plenum. If one instead uses the $\kappa - \varepsilon$ model (Fig. 6.12b, right), only the stagnation zone and the two large vortices in the lower plenum are predicted (it is a well known fact that $\kappa - \varepsilon$ models fail in correctly reproducing flow detachment). All the steady-state simulations described above are evidence of the complex multi-dimensional field, which can develop in the RPV mock-up. As the results appear to be strongly dependent on the employed turbulence model, the experimental data of the FLORIS facility should clearly provide a valuable contribution towards validating CFD codes.

To avoid the development of asymmetric flow conditions when symmetric boundary conditions are applied, baffles were added to the final design of the facility, as previously described in Sec. 6.1. Baffles have a stabilizing effect on the lower plenum flow field and dampen the aforementioned perturbations which would result from small flow asymmetries.

6.2.2 Transient simulations

Two kinds of transients have been simulated for the planning of the experimental tests:

1. Pump start-up: starting from stagnant conditions and reaching nominal mass flow rate in 5 s (the simulation is continued for an additional 5 seconds in order to reach steady-state conditions).

2. Pump coast-down: starting from the steady-state velocity field at nominal mass flow rate and completing shut-down in 5 seconds (the simulation is continued for an additional 5 seconds in order to exhaust the transient until the flow velocity is zero everywhere).

The initial conditions have been derived from the corresponding results of the steady-state simulations (Fig. 6.11d). Asymmetric transient conditions have been chosen to avoid the stability issue with the symmetric boundary conditions discussed in Subsec. 6.2.1. The integration time-step adopted for the CFD simulations was 0.1 s, while the target criterion for convergence was a RMS value of 10^{-4}; the pressure at the outlets was set to 1 bar.

Relevant time frames of the pump start-up simulation are presented in Fig. 6.13. There, it is seen that a vortex develops in the lower plenum, on the side of the active loop, and grows from the outlet of the jet pump towards the center of the plenum. After the pump has reached steady-state operation and the loop flow rate is thus stabilized to the nominal value, the stagnation zone in the upper right of the lower plenum is formed and the vortex in the lower plenum stabilizes, leading to a similar solution as that found with the steady-state simulations (case 7). The final snapshot presents the same conditions as for the corresponding steady-state run (Fig. 6.13, bottom right, and Fig. 6.11d).

In Fig. 6.14, the salient frames of the pump coast-down simulation are shown. As soon as the mass flow rate of the pump is reduced, the vortices start to collapse; the stagnation zone is lost already after 3 s, while the upper plenum vortex is dissipated after about 5 s. The larger vortex dissipates over a longer time interval.
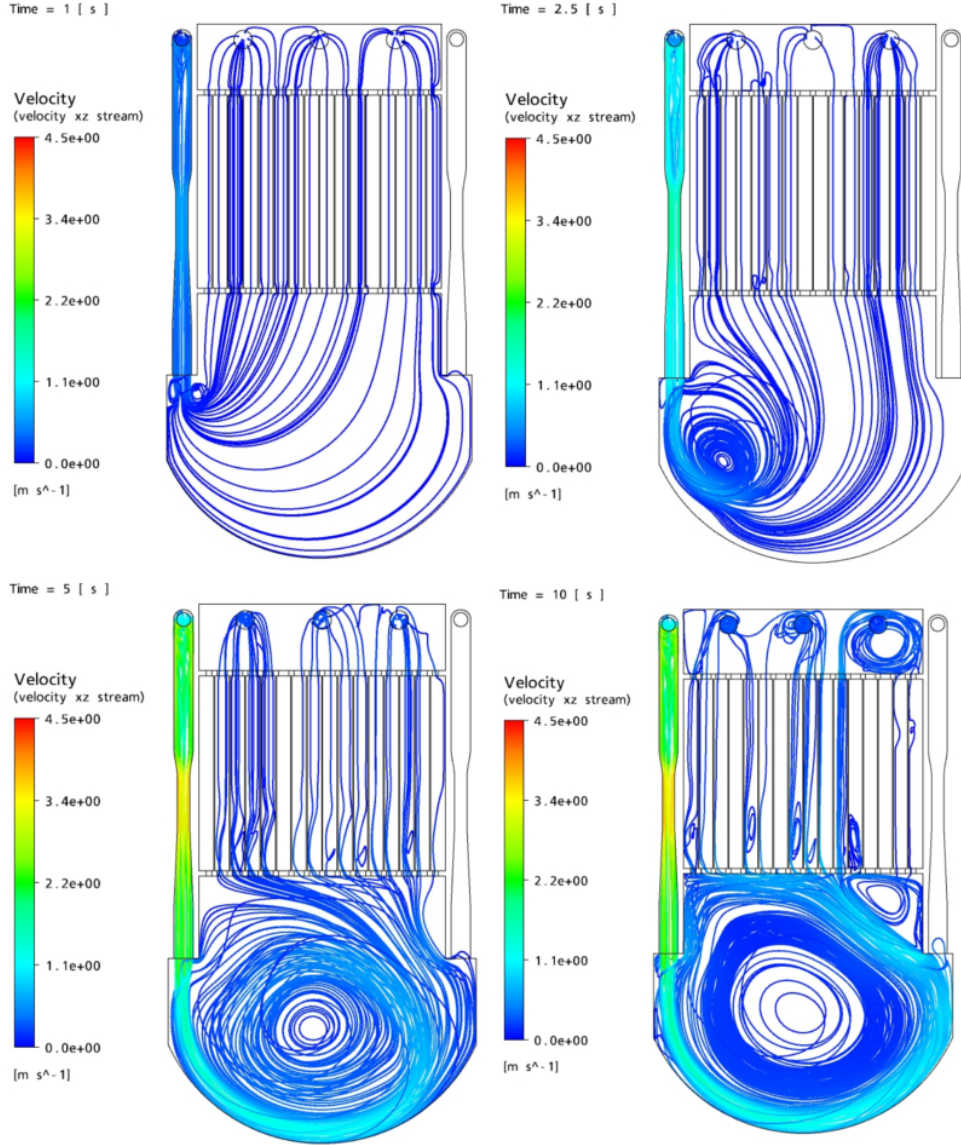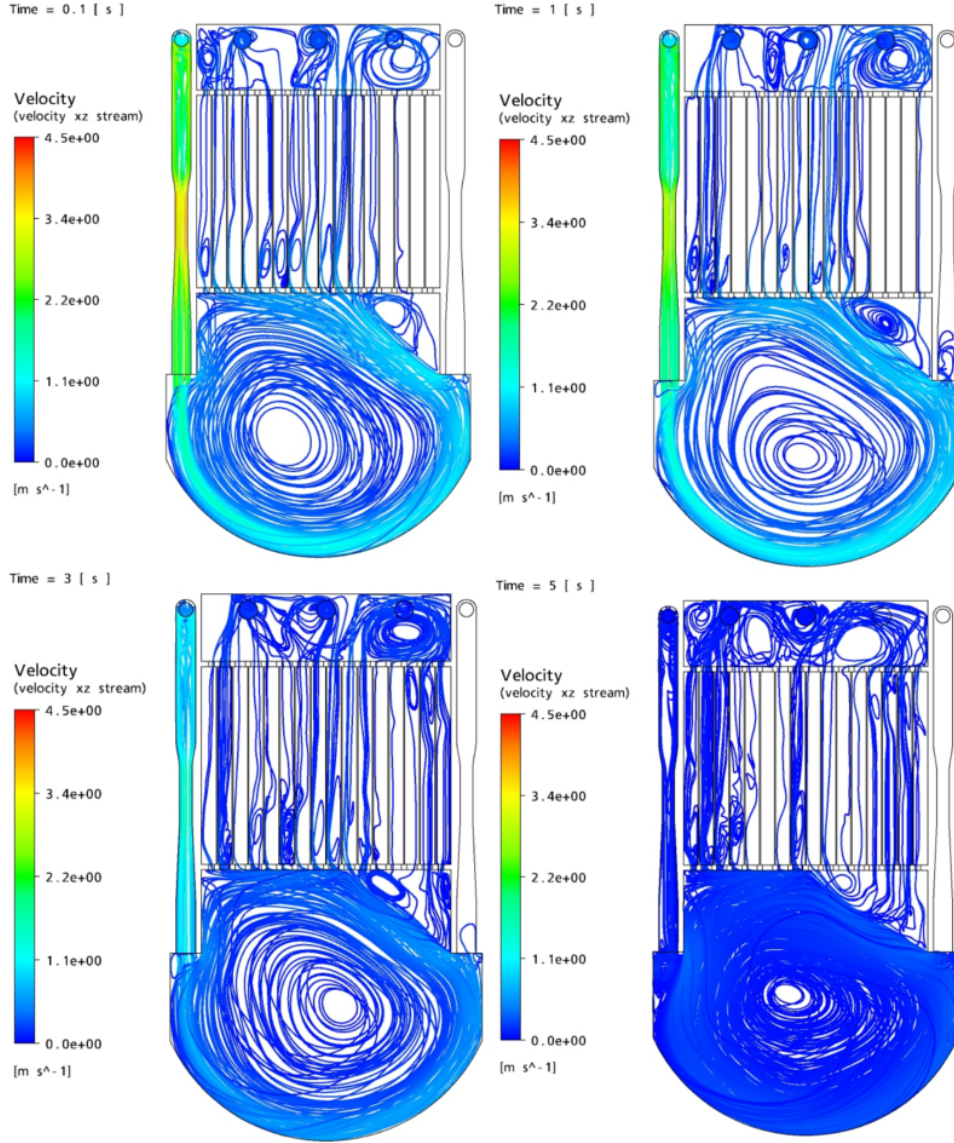
Figure 6.13: Pump start-up: velocity streamlines at different times (1.0 s top left, 2.5 s top right, 5.0 s bottom left, 10.0 s bottom right).

6.2.3 Definition of the test matrix

As mentioned, based on the pre-test CFD simulations, the experimental facility was modified by adding baffles at the exit of the two jet pumps. The finally laid out experimental test matrix, for both steady-state and transient conditions, is given in Tab. 6.1.

The steady-state tests have been designed such to cover all possible flow configurations. The first tests (S1, symmetric boundary conditions) are meant to verify whether an asymmetric steady-state flow regime establishes even when the baffles at the jet pump outlet are in place; moreover, the tests are conducted with different mass flow rates, to see whether, and

Figure 6.14: Pump coast-down: velocity streamlines at different times (0.1 s top left, 1.0 s top right, 3.0 s bottom left, 5.0 s bottom right).

to what extent, the results are influenced. The inlet mass flow rates span a range between 0.5 kg/s ($Re_{JP1} \sim 2.6 \cdot 10^7$) and 1.0 kg/s ($Re_{JP1} \sim 5.2 \cdot 10^7$). In the steady-state tests S2 and S3, special attention is paid to the analysis of the stagnation zones created when employing asymmetric boundary conditions. Test S4 is a tracer-plug recirculation experiment, meant to study the transport of the tracer from the RPV outlets through the loop and back to the RPV outlets (similarly to what was done in Chap. 4 with the double T-junction experiment, except that the geometry here is considerably more complex).

Transient runs T1 and T2 provide the basis for extending the experimental validation of the CFX/TRACE tool to the challenge of the coupling of the momentum equation.

Steady-state	
S1	Symmetric: all inlets and outlets open; 3 mass flow rates (0.50 kg/s, 0.75 kg/s, 1.00 kg/s).
S2	Asymmetric: JP1 and O1 open; 1 mass flow rate (0.75 kg/s).
S3	Asymmetric: JP1, different combinations of outlets open; 1 mass flow rate (0.75 kg/s).
S4	As S2, but with plug recirculation.
Transient	
T1	Asymmetric: JP1, all outlets open. Pump start-up, different current ramps.
T2	Asymmetric: JP1, all outlets open. Pump coast-down, different current ramps.

Table 6.1: Test matrix for the FLORIS facility, as defined after the pre-test simulations.

6.3 Tests

6.3.1 Description of the tests

As for the case of the double T-junction experiment presented in Chap. 4, wire-mesh sensor technology has been employed to visualize the flow by detecting the transport of a tracer in the test section. In the present case, the tracer was tap water mixed with saline solution, while the main fluid was demineralized water. The tests conducted in the FLORIS facility can be categorized in two ways, depending on the way the tracer is injected during the experiment:

- "plug release" - for steady-state tests, i.e. with fixed mass flow rate in the loops; the experiment entailed preparing a tracer plug with a predetermined salt concentration by mixing tap water and saline solution under controlled conditions. The plug was prepared in the bypass section (illustrated in Sec. 6.1) and suddenly released into the system by opening simultaneously the rapid-closure valves through the control system. This operation was found to create a small perturbation in the mass flow as measured by the flow-meter (in the order of a few percent), because some air bubbles were released into the main stream. The effect of such bubbles was found to be negligible, due to their limited size and quantity, and therefore the mass flow could be considered steady, while the measured conductivity was unperturbed by the small void fraction;

- "continuous release" - for transient tests, i.e. with changing mass flow in the loops; the experiment entailed injecting continuously a known quantity of saline solution by means of the syringe pump (Fig. 6.4) just before the entrance to the vessel. The mass flow transient was controlled by the acquisition system, through the pump frequency controllers; a certain ramp was imposed to the current feeding the pumps, in order to vary the angular velocity of the pump rotor and therefore the loop mass flow rate. The flow rates in the two FLORIS loops were measured as function of time by means of flow-meters.

For both types of tests, the tracer concentration was fixed at a sufficiently high value, so that the circulation of the tracer plug (or the dispersion of the continuous injection) inside the vessel could be detected with sufficient accuracy. The experimental data obtained in the various tests are presented in Subsec. 6.3.3 and compared to the simulation results in Sec. 6.4.

6.3.2 Calibration

The wire-mesh sensor electronics needs proper calibration[4] to correctly process the measured data. Therefore, a series of calibration experiments were conducted in FLORIS. The calibration procedure consisted in filling the vessel, under stagnant conditions, with different mixtures of desalinated water, tap water and salt, in order to vary the fluid conductivity. Each mixture had a known conductivity ξ_{mix}, measured using a reference conductivity measurement device. This procedure guaranteed that the conductivity of the fluid was identical at all measurement positions within the FLORIS vessel. Once the vessel was filled with a given fluid mixture, data were acquired for 5 seconds from the wire-mesh sensor and averaged to a single value $M_{mix,i,j}$ for each sensor point, where i and j indicate the coordinates of the given measurement point in the wire-mesh plane. The described procedure was repeated with different mixtures several times. By using a linear relationship between the wire-mesh local measurements $M_{mix,i,j}$ and ξ_{mix}, it is then possible to reconstruct the fluid conductivity ε from a given measurement M of the sensor[5].

The calibration had to be done at each sensor crossing point; here, only the behavior for one point is reported (see Fig. 6.15), since results were similar for the other points. In the figure, two measurement sets are shown, a coarser one (in blue) and a finer one (in red). Notice that, when the conductivity (i.e. tracer concentration) becomes too high, the relation between measured values and fluid conductivity deviates from the linear trend because parasitic currents between neighboring wires become significant. Moreover, during the calibration procedure, it was noticed that the points close to the metallic jet pumps suffered from a damped signal because of the interference with the material of the jet pumps structures.

---

[4] A similar procedure was adopted for the double T-junction experiment described in Chap. 4.

[5] The wire-mesh sensor features a linear relationship between a generic measured value M of the fluid (an integer value elaborated from the electronics, which lies in the range between 0 and 2^{12}) and the corresponding conductivity of the water ξ. In fact, it is possible to relate M and ξ *via* the so-called dimensionless mixing scalar (see, for example, [23, 93]):

$$\vartheta = \frac{\xi - \xi_0}{\xi_1 - \xi_0} = \frac{M - M_0}{M_1 - M_0}$$

where ξ_0 and ξ_1 are two fluid conductivity reference values (usually desalinated water and a chosen mixture), and M_0 and M_1 are the two corresponding values measured by the sensor. It is important to note that this relationship is unique for each point of coordinates (i, j) on the sensor grid; therefore, there will be a matrix of ϑ_{ij} values.

The error analysis related to the mixing scalar is complex and is not detailed here (refer to [94]). However, it has been reported in [94] that the calculated error bands are usually smaller than the fluctuations of the measured values caused by the turbulent nature of the flow. Part of the error comes also from the conductivity measurement device, which has a relative error of $\pm 0.5\%$ on the measured conductivity.
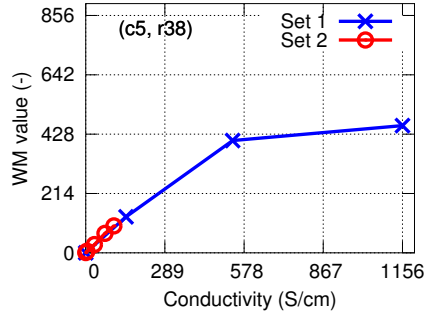
Figure 6.15: Calibration curve for wire-mesh sensor point at column 5, row 38 (jet pump outlet).

6.3.3 Experimental results

The tests were conducted accordingly to the test matrix of Tab. 6.1. Of the various tests, a subset of experiments characterized by different phenomenological behavior has been selected for presentation in this thesis. The chosen scenarios are reported in Tab. 6.2, where the three openings of the vessel O1 to O3 are denoted according to Fig. 6.9. For the transient cases, the minimum mass flow rate was restrained to be above 0.13 kg/s ($Re_{JP1} \sim 6.7 \cdot 10^6$) because of the sensitivity of the mass flow-meters, which is limited to flows higher than 0.11 kg/s.

Scenario	Type	Mass flow rate (kg/s)	$Re_{JP1}(\times 10^7)$	Openings	Injection
Symmetric	Steady-state	0.75 (both inlets)	3.9	I1,I2,O1,O2,O3	Plug rel.
Asymmetric	Steady-state	0.75	3.9	I1,O1	Plug rel.
Recirculation	Steady-state	0.75	3.9	I1,O1	Plug rel.
Pump start-up	Transient	0.13→0.8	0.67→4.2	I1,O1,O2,O3	Cont.
Pump coast-down	Transient	0.8→0.13	4.2→0.67	I1,O1,O2,O3	Cont.

Table 6.2: Selected scenarios for the simulations.

Symmetric scenario

In the "symmetric" scenario, a constant mass flow rate of 0.75 kg/s ($Re_{JP1} \sim 3.9 \cdot 10^7$) is injected in both jet pumps. At a certain time during the experiment, a tracer plug is released into the jet pump JP1 and it travels through the vessel. A series of snapshots, taken at different times during one of the the experiments, is shown in Fig. 6.16. From the path traveled by the tracer plug, the presence of two large symmetric vortices in the lower plenum can be deduced. Also, the formation of a jet impinging the core in the region of the central channels is clearly visible. In addition, on the basis of the tracer distribution, it is possible to observe that an uneven distribution of the mass flow rate exists among the core channels, because the high concentration front travels faster in the central channels than in the peripheral ones.

(a) 8.5 s (b) 9.5 s

(c) 10.5 s (d) 11.5 s

(e) 12.5 s (f) 13.5 s
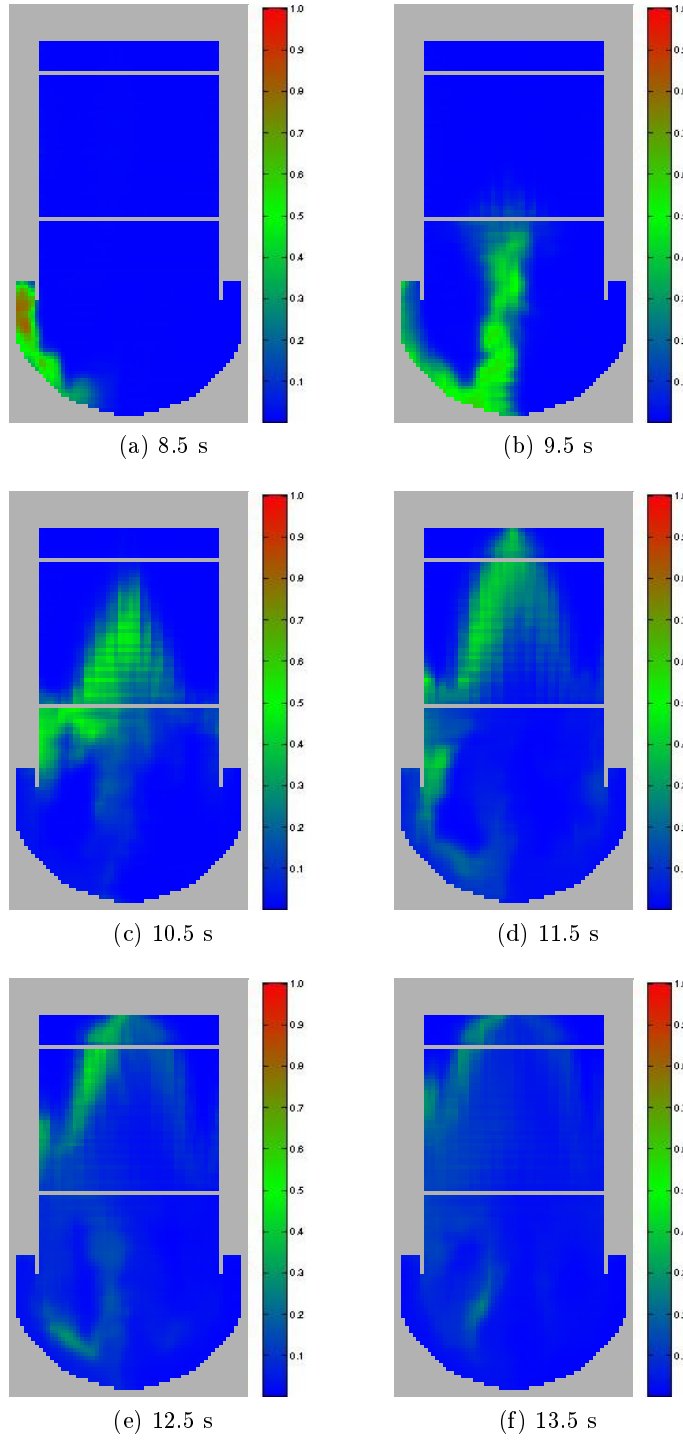
Figure 6.16: Normalized tracer concentration reconstructed from the WM-sensor experimental data for the "symmetric" scenario. Snapshots at different times.
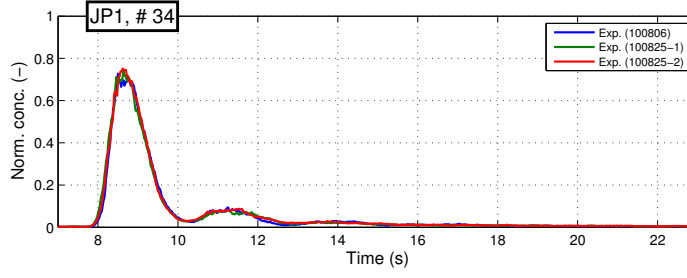
Figure 6.17: Normalized average concentration evolution in JP1, measured at the WM-sensor row 34 (refer to Fig. 6.9). Comparison between different experiments for the "symmetric" scenario.

In Fig. 6.17, the boundary conditions (measured at JP1) are reported. The three separate tests mentioned in the figure were performed using the same boundary conditions, to confirm reproducibility of the experimental results. In the figure, the main peak of the injected tracer plug is clearly visible, followed by a second peak of lower amplitude. The occurrence of the second peak is due to probable stratification in the preparation of the tracer plug, or to the effect of the rapid-closure valves. Collected data show, however, that the experimental procedure is standardized such as to lead to reproducible experiments.

In Fig. 6.18, the time evolution of the tracer concentration at the middle of selected core channels is reported; results for all channels at different core heights are documented in [95]. The curve shapes are similar to the injection curve of Fig. 6.17, featuring a main peak followed by a smaller one. Central core channels (numbers from about 5 to 9), where the jet impinges directly, have higher tracer concentration. The concentration then decreases, moving towards the side channels in both directions. The bias towards the first half of the core, which is on the injection side, is due to the two large vortices that develop in the lower plenum and keep most of the plug circulating on that side. At the same time, it is noticeable, for the same reason, that in the first 8 channels the concentration is usually higher.

Figs. 6.19 and 6.20 show, instead, the tracer concentration evolution at different heights of the core channels 1 and 8, respectively. From these figures, it is possible to see that the mass flow is higher in the central channels and lower in the side channels; this can be deduced by analyzing the propagation of the concentration wave from the inlet of a given channel to its outlet. Another effect noticeable from the readings at different heights of the core is the diffusion of the plug, i.e. the concentration curve becomes lower and wider, due to the turbulent mixing. This effect is relatively small in the central channels, but is more pronounced moving towards the side channels. A hypothesis is that this happens because the velocity profile over the cross section of the channel is relatively uniform in the central channels, while it is not so in the side channels, thus affecting the transport of the tracer plug and the related measurements. Unfortunately, velocity profile measurement are currently not possible in the FLORIS facility, but a support to this hypothesis comes from the simulations
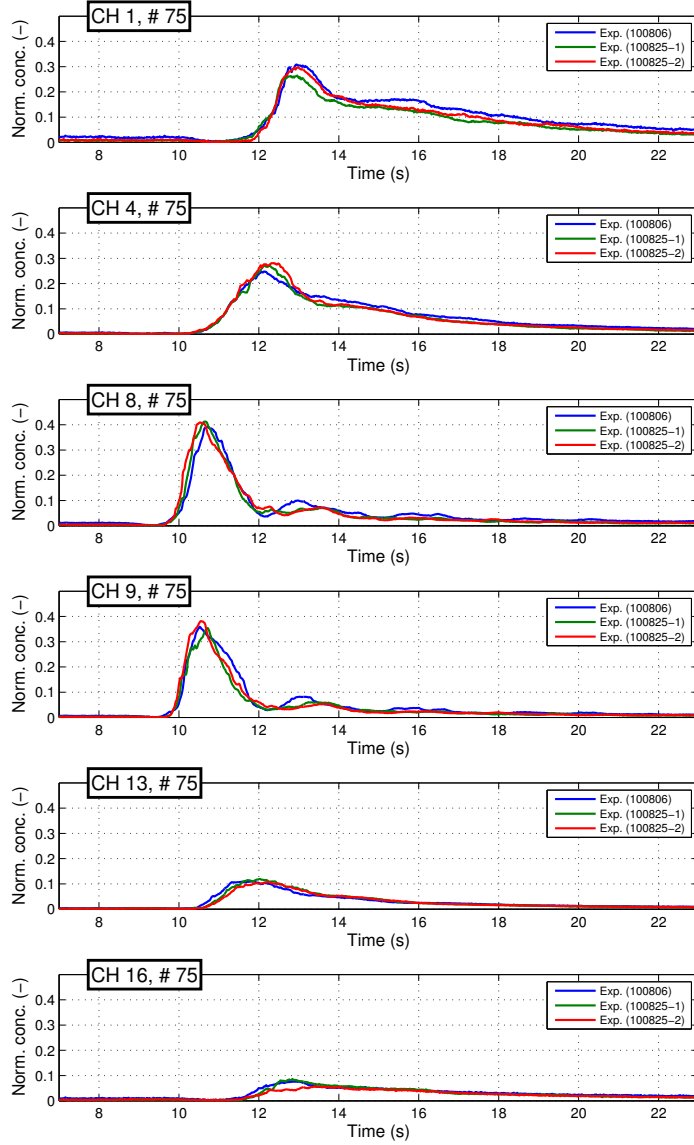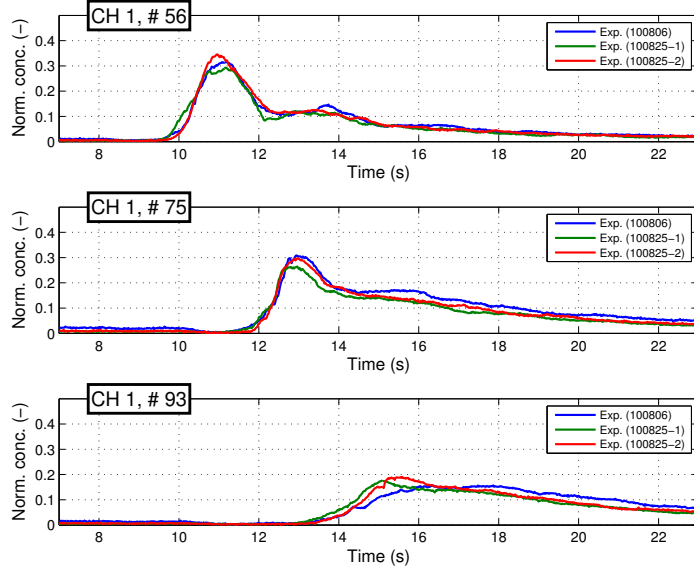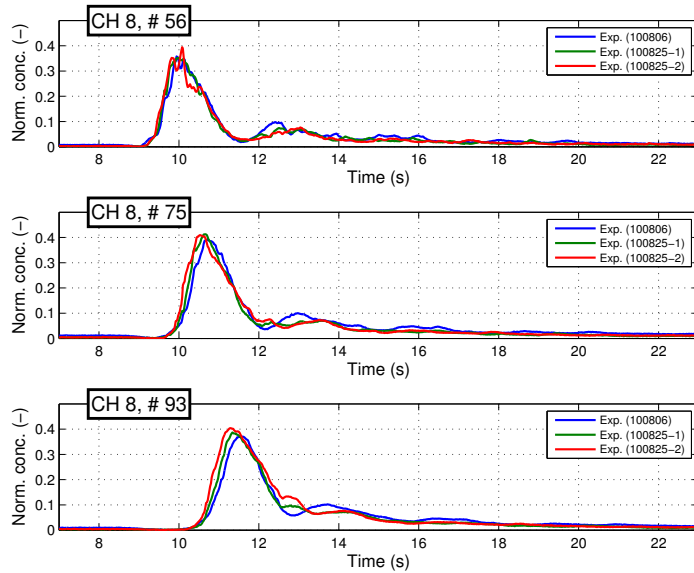
Figure 6.18: Normalized average concentration evolution in the core, measured at the WM-sensor row 75 (core middle) for the core channels 1, 4, 8, 9, 13 and 16 (refer to Fig. 6.9). Comparison between different experiments for the "symmetric" scenario.

presented later in Sec. 6.4.

Asymmetric scenario

In the "asymmetric" scenario, a constant mass flow of 0.75 kg/s ($Re_{JP1} \sim 3.9 \cdot 10^7$) is injected into a single jet pump. At a certain time during the experiment, a tracer plug is released into JP1 and travels trough the vessel. A series of snapshots, taken at different times during one of the experiments, is shown in Fig. 6.21. As predicted with the pre-test simulations presented in Sec. 6.2, it can be clearly seen, from the path traveled by the concentration plug, that an

Figure 6.19: Normalized average concentration evolution in the core, measured at the WM-sensor rows 56, 75 and 93 for the core channel 1 (refer to Fig. 6.9). Comparison between different experiments for the "symmetric" scenario.

Figure 6.20: Normalized average concentration evolution in the core, measured at the WM-sensor rows 56, 75 and 93 for the core channel 8 (refer to Fig. 6.9). Comparison between different experiments for the "symmetric" scenario.

oblique jet impinges upon the core in the region of the central channels. A large vortex in the left part of the lower plenum and a stagnation zone due to the small vortex in the upper right part of the lower plenum are also clearly noticeable. Again, like in the "symmetric" scenario, the high concentration front traveling through the core points to the uneven distribution of the mass flow in the core channels.

In Fig. 6.22, the concentration measured at the outlet of JP1 is reported. Again, two identical experiments have been performed to confirm reproducibility of the experimental results. As for the "symmetric" scenario, the main peak of the injected tracer plug is followed by a second peak of smaller amplitude.

Fig. 6.23 shows the time evolution of the tracer concentration at the middle of selected core channels; results for all channels at different core heights are reported in [95]. It has been observed that core channels from 6 to 10 have a higher concentration, because they are located in the region where the jet formed in the lower plenum directly impacts the core. Channels 11-13 are at the edge of the stagnation zone caused by the small vortex in the lower plenum (see also the velocity streamlines from the pre-test CFD simulation reported in Fig. 6.10a), while channels 14 to 16 are completely within the stagnation zone. No tracer is transported in the latter channels, and the measured concentration is therefore zero.

Figs. 6.24 and 6.25 report the tracer concentration evolution at different heights of the core for channels 1 and 7, respectively. Comparing these figures, one sees that the concentration peak reaches the side channels with a certain delay, since they are further away from the jet's impact location. In both figures, it is noticeable that the diffusion of the plug (i.e. the concentration curve becoming lower and wider) along the core channels, is biased towards the flow direction because of the turbulent mixing. Always from the same figures, the fact that there is a certain mass flow rate distribution across the core channels can be deduced by looking at the propagation speed of the high concentration plug measured along the channel height; in particular, the channels which are directly impacted by the jet are subject to a higher mass flow rate.

Plug recirculation scenario

Since this scenario resembles the "asymmetric" one, similar conclusions can be drawn about the distribution of the concentration in the core channels. The novelty in this experiment lies in the fact that, while in the previous case the liquid was discharged after leaving the vessel, here it is recirculated and reinjected into the jet pump JP1. Since there is only one outlet open, the plug that is recirculated back to JP1 is the one that had previously left the vessel (see Fig. 6.26, peak at about 32-33 s): the recirculation time inside the whole loop is about 22 s (time distance between the two peaks of Fig. 6.26). As expected, the reinjected plug presents a wider, flatter distribution with respect to the original plug injected into JP1 because of the diffusive effect of the turbulent mixing: the maximum concentration of the

(a) 7.5 s   (b) 8.5 s

(c) 9.5 s   (d) 10.5 s
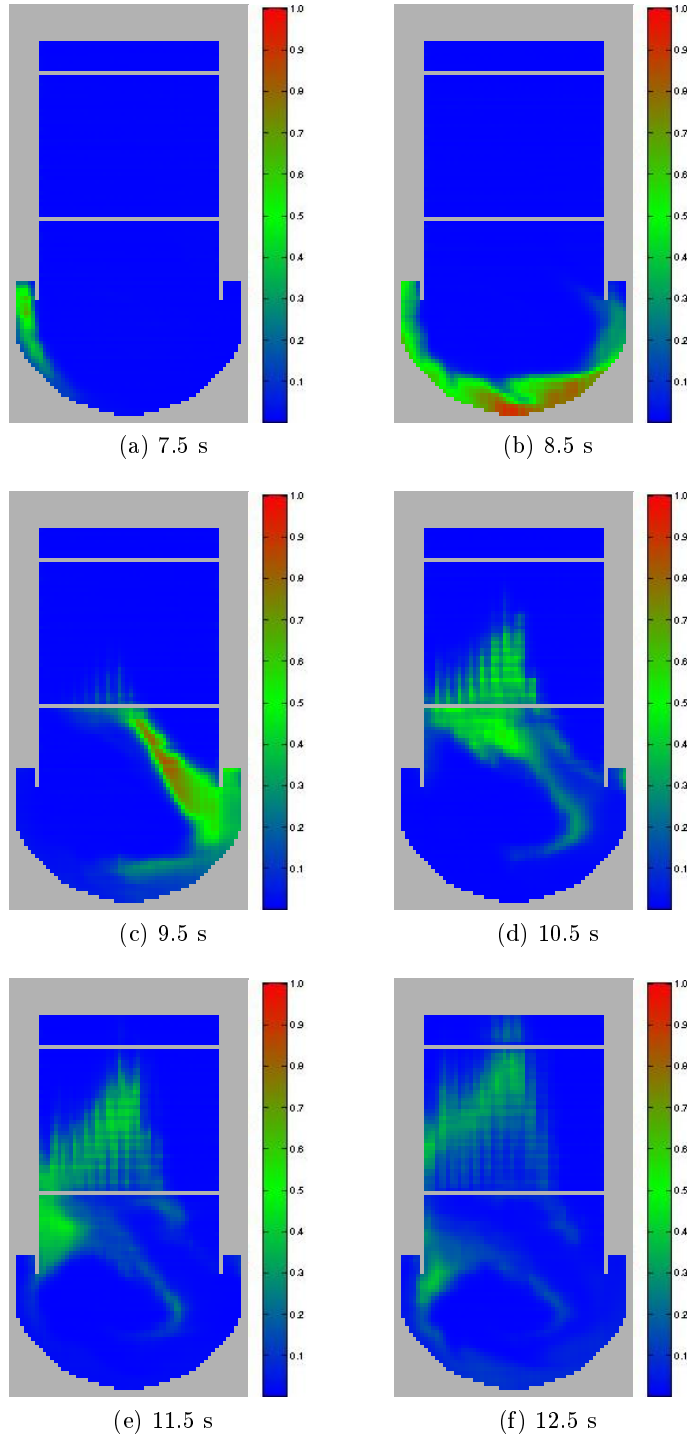
(e) 11.5 s   (f) 12.5 s

Figure 6.21: Normalized tracer concentration reconstructed from the WM-sensor experimental data for the "asymmetric" scenario. Snapshots at different times.
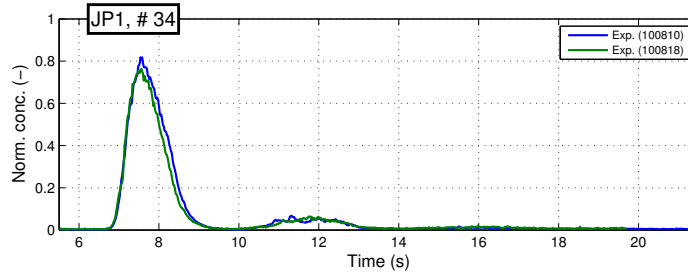
Figure 6.22: Normalized average concentration evolution in JP1, measured at the WM-sensor row 34 (refer to Fig. 6.9). Comparison between different experiments for the "asymmetric" scenario.
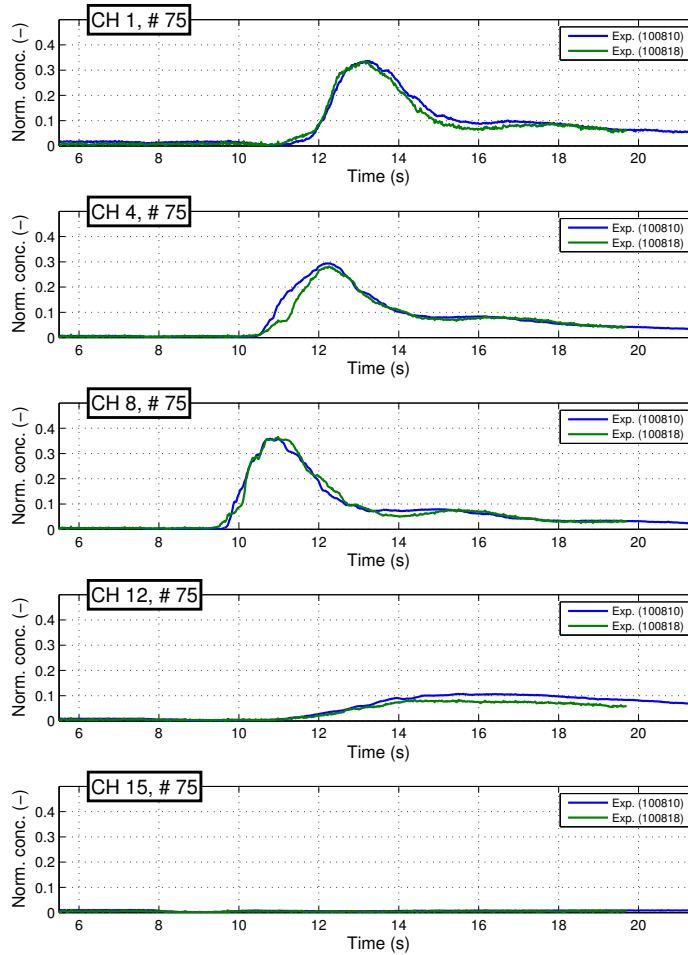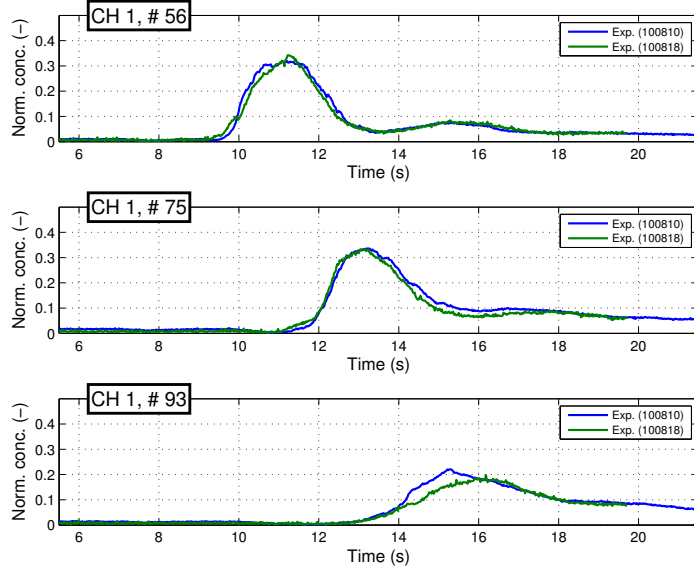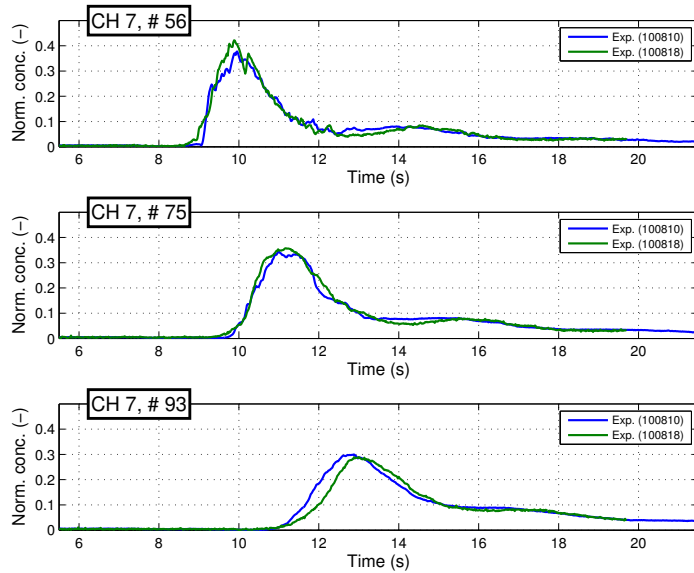

Figure 6.23: Normalized average concentration evolution in the core, measured at the WM-sensor row 75 (core middle) for the core channels 1, 4, 8, 12 and 15 (refer to Fig. 6.9). Comparison between different experiments for the "asymmetric" scenario.

Figure 6.24: Normalized average concentration evolution in the core, measured at the WM-sensor rows 56, 75 and 93 for the core channel 1 (refer to Fig. 6.9). Comparison between different experiments for the "asymmetric" scenario.

Figure 6.25: Normalized average concentration evolution in the core, measured at the WM-sensor rows 56, 75 and 93 for the core channel 7 (refer to Fig. 6.9). Comparison between different experiments for the "asymmetric" scenario.

reinjected plug is about 25% of the original injection maximum. After the reinjection, the plug passes a second time through the core, showing a similar evolution of the distribution within the vessel, since the inlet mass flow rate (and consequently the velocity field inside the vessel) is constant during the entire transient. Fig. 6.27 illustrates the recirculation in selected core channels, at about middle core height. Results for all channels are documented in [95].

Pump start-up scenario

This is the first of the considered transient scenarios and features the establishment of an asymmetric velocity field in the vessel during the start-up of one of the pumps, while the second pump is off-line. The case considered is one in which a current ramp of 0.5 A/s is imposed on the pump, while a continuous tracer injection is taking place. The mass flow rate is 0.13 kg/s at the start and reaches 0.8 kg/s at the end of the transient.

In Fig. 6.28, a series of snapshots taken at different times during the transient are represented. It is seen that, during the transient, the concentration in the vessel decreases with time, since the mass flow rate is increasing. In the same figure is visible the development of a large lower-plenum vortex and of a stagnation zone on the right, as well as the uneven distribution of the mass flow in the core channels, highlighted by the tracer concentration front. The velocity field which develops inside the vessel is asymmetric and approaches a regime similar to that observed for the "asymmetric" scenario, even if in this case all the outlets are open. As stated earlier, the basic phenomenology is the same in the two scenarios.

In Fig. 6.29 are shown the tracer concentration recorded at the WM-sensor row in JP1, as well as the mass flow transient recorded by the flow-meter of the JP1 loop. Even though the tracer injection is continuous, it can be seen that the average value of the tracer recorded by the wire-mesh sensor exhibits a peak. This happens because the injection starts with a low mass flow, insufficient to avoid tracer accumulation in the measurement sections, and proceeds with an increasing flow available for dispersing the tracer. At a certain point of the transient, where the peak appears, the mass flow becomes sufficient to decrease the tracer concentration once again. As time passes, the pump reaches stationary conditions and so does the magnitude of the tracer concentration recorded by the sensor.

Fig. 6.30 shows the tracer concentration at the middle height of the core for selected channels, while Figs. 6.31 and 6.32 represent the tracer evolution at different core heights along channels 1 and 7, respectively. Again, results for all channels at different core heights are reported in [95]. The two figures have features similar to those seen in the corresponding figures of the "asymmetric" scenario: high mass flow rates at the inlet of the central core channels where the jet impinges, and low mass flow rate in channels 1-2 and in the stagnation zone (channels 14-16).
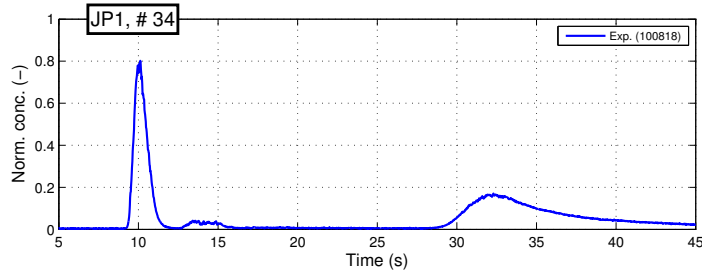
Figure 6.26: Normalized average concentration evolution in JP1, measured at the WM-sensor row 34 (Fig. 6.9). Experiment for the "plug recirculation" scenario.
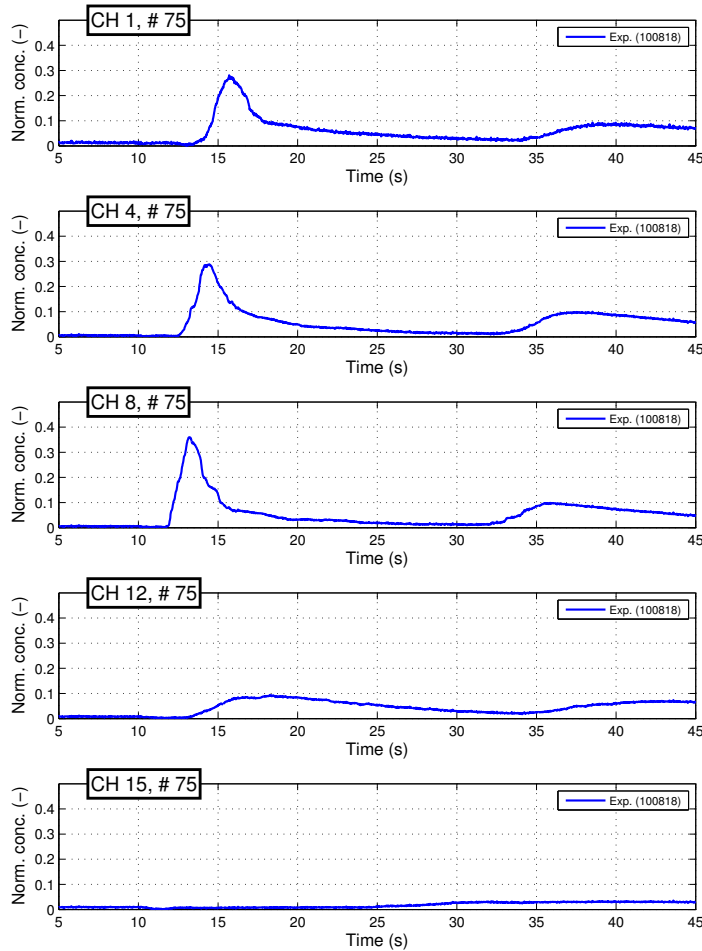

Figure 6.27: Normalized average concentration evolution in the core, measured at the WM-sensor row 75 (core middle) for the core channels 1, 4, 8, 12 and 15 (refer to Fig. 6.9). Experiment for the "plug recirculation" scenario.
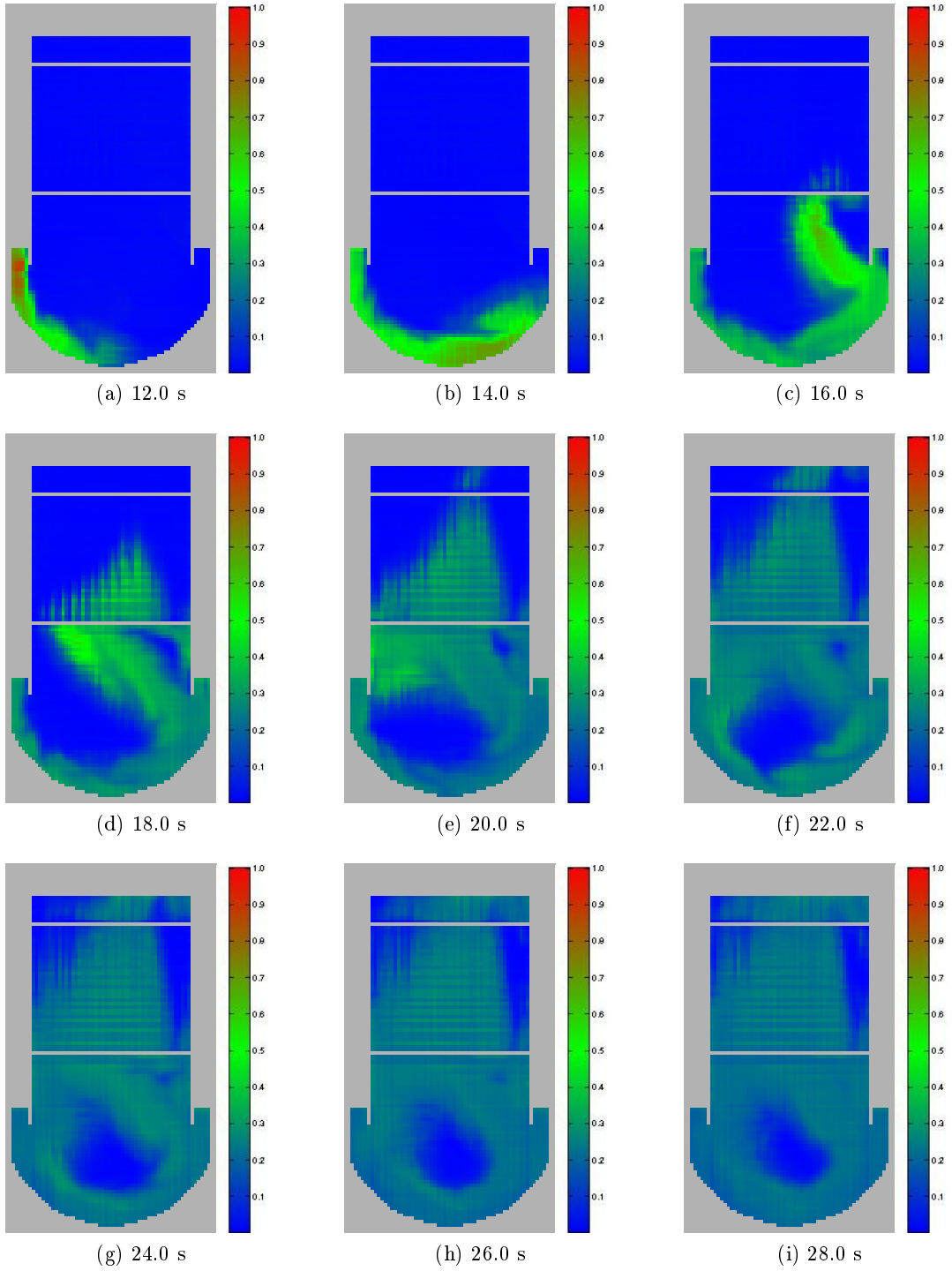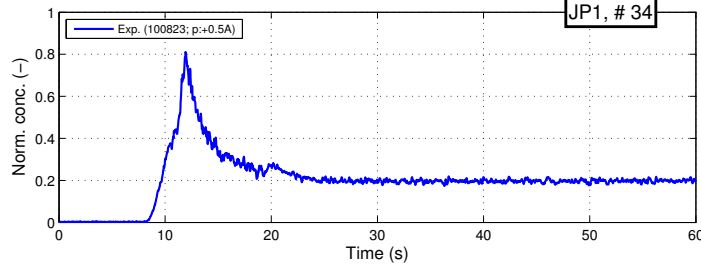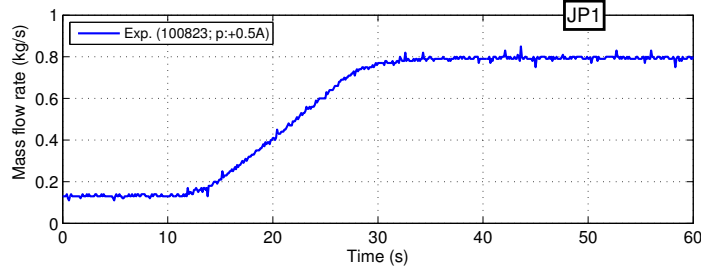
Figure 6.28: Normalized tracer concentration reconstructed from the WM-sensor experimental data for the "pump start-up" scenario. Snapshots at different times.

(a) Normalized average concentration evolution of JP1, measured at the WM-sensor row 34 (see Fig. 6.9).

(b) Mass flow evolution measured in the JP1 loop (see Fig. 6.9).

Figure 6.29: Experimental boundary conditions for the "pump start-up" scenario.
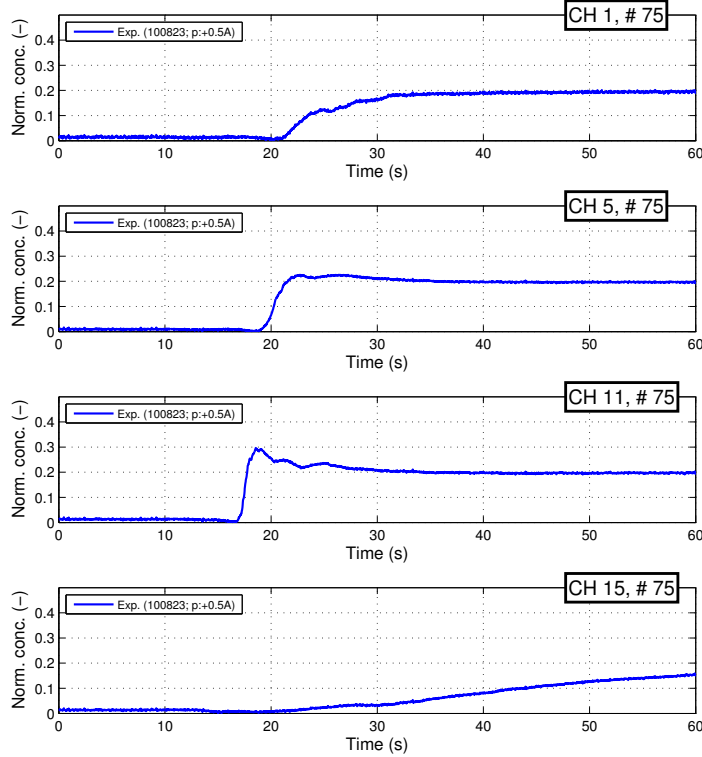
Figure 6.30: Normalized average concentration evolution in the core, measured at the WM-sensor row 75 (core middle) for the core channels 1, 5 11 and 15 (refer to Fig. 6.9). Experiment for the "pump start-up" scenario.
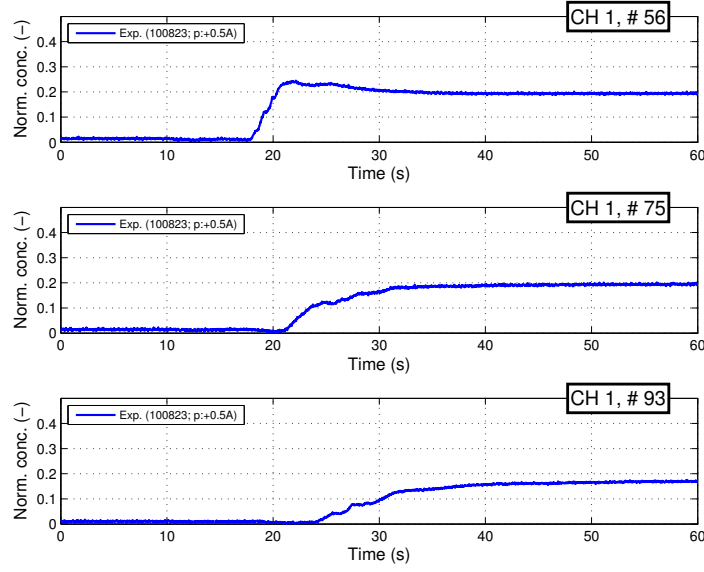
Figure 6.31: Normalized average concentration evolution in the core, measured at the WM-sensor rows 56, 75 and 93 for the core channel 1 (refer to Fig. 6.9). Experiment for the "pump start-up" scenario.
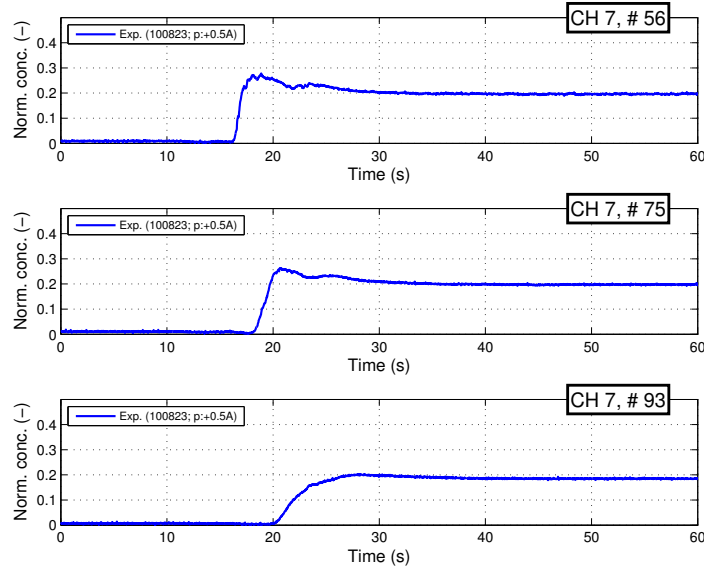
Figure 6.32: Normalized average concentration evolution in the core, measured at the WM-sensor rows 56, 75 and 93 for the core channel 7 (refer to Fig. 6.9). Experiment for the "pump start-up" scenario.

Pump coast-down scenario

This transient scenario features the establishment of an asymmetric velocity field in the vessel during the coast-down of one of the pumps, while the second pump is off-line. The case considered is one in which a current ramp of -0.5 A/s is imposed on the pump; the tracer is injected continuously through the syringe system described previously. At the time when the coast-down is started, the pump in operation has a mass flow rate of 0.8 Kg/s, and this reaches 0.13 kg/s at the end of the transient.

In Fig. 6.33, a series of snapshots taken at different times during the transient are represented. It is seen that the concentration in the vessel increases with time, since the mass flow is decreasing. In the same figure, the large lower-plenum vortex and the stagnation zone on the right are also visible, as is the uneven distribution of the mass flow in the core channels, highlighted by the tracer concentration front. The velocity field which develops inside the vessel is asymmetric and tends to reach a regime similar to that of the "asymmetric" scenario, even if in this case all the outlets are open. As stated earlier, the phenomenology of the experiments is basically the same.

In Fig. 6.34, the tracer concentration recorded at the WM-sensor row 34 in JP1, as well as the mass flow transient recorded by the flow-meter of the JP1 loop, are shown. In accordance with the continuous tracer injection, it can be seen that the average value of the tracer concentration recorded by the wire-mesh sensor increases with time. This happens because the injection starts with a high mass flow, resulting in a low initial concentration measured by the WM-sensor, and proceeds with a decreasing flow, which allows the local tracer concentration to increase. At the end of the transient, the tracer concentration starts to stabilize to a constant level; this happens many seconds after the steady state with reduced mass flow rate has been reached.

From the middle-core average channel concentrations shown for selected channels in Fig. 6.35 (which are significative also for the upper and lower core regions), features similar to those of the "asymmetric" scenario can be seen. Results for all channels are, once again, reported in [95]. In the side channels 1-3, the final concentration is lower, while in the central channels, where the jet impinges directly, the final concentration is higher. Moreover, one can again see the effect of the recirculation zone (around channel 15), where the concentration is practically zero, as also the effect of the uneven distribution of the mass flow rates in the channels, which causes a delayed increase in concentration for the channels where the jet is not impinging directly.

6.4 Simulations and comparisons with experimental data

As for the double T-junction experiments presented in Chap. 4, stand-alone TRACE and CFX simulations, together with coupled CFX/TRACE computations, have been performed
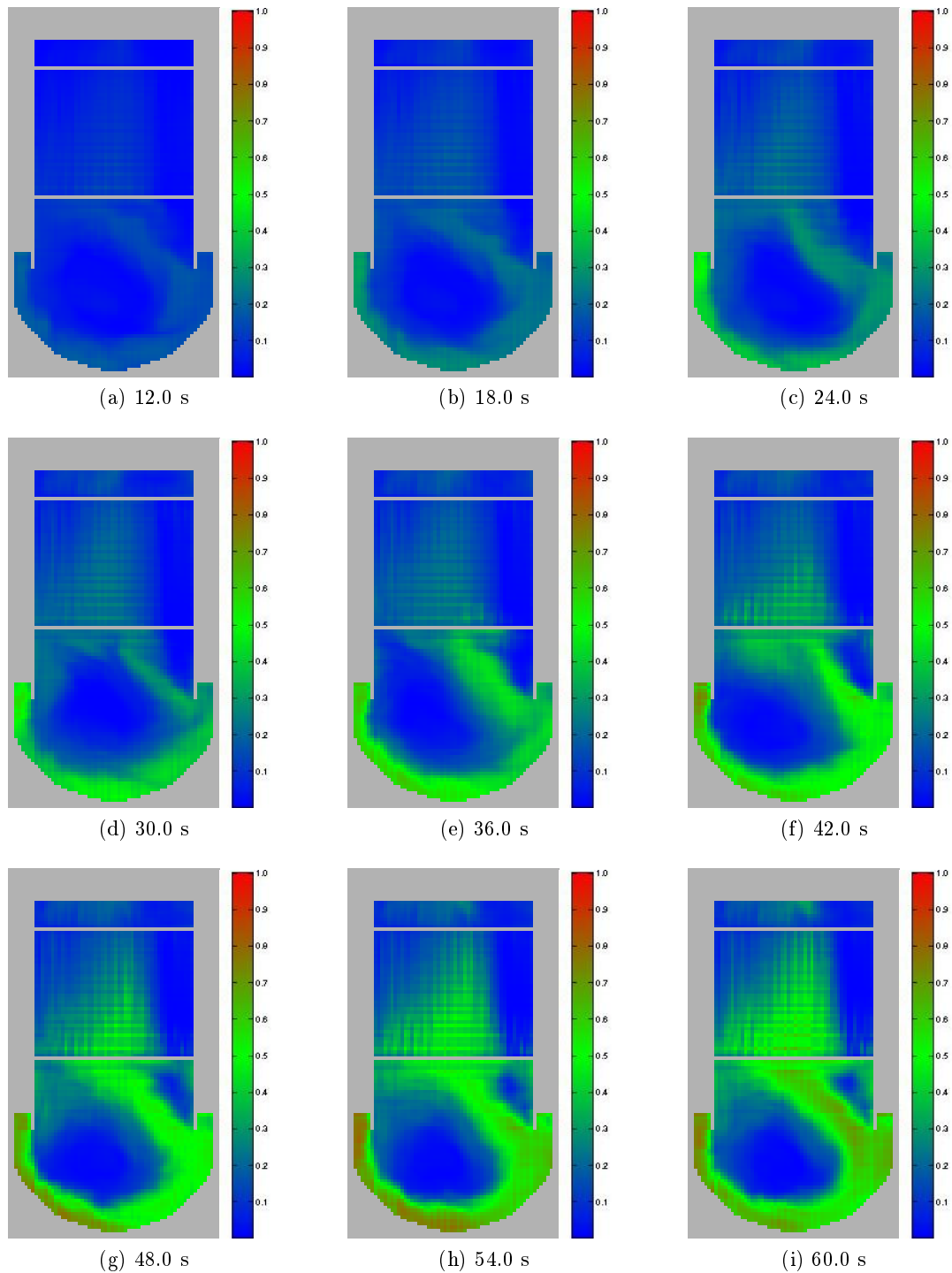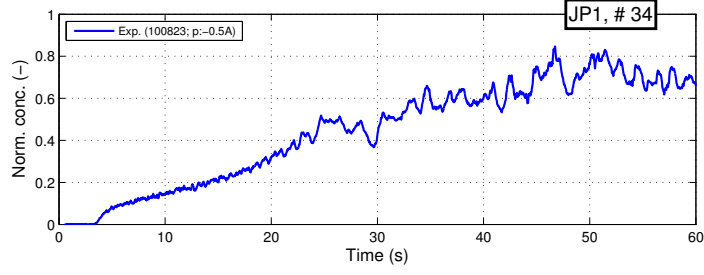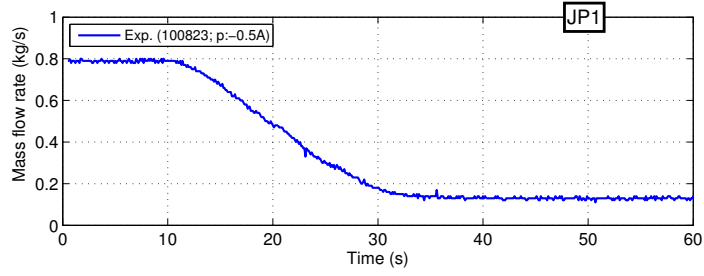
(a) 12.0 s   (b) 18.0 s   (c) 24.0 s

(d) 30.0 s   (e) 36.0 s   (f) 42.0 s

(g) 48.0 s   (h) 54.0 s   (i) 60.0 s

Figure 6.33: Normalized tracer concentration reconstructed from the WM-sensor experimental data for the "pump coast-down" scenario. Snapshots at different times.

(a) Normalized average concentration evolution of JP1, measured at the WM-sensor row 34 (see Fig. 6.9).

(b) Mass flow evolution measured in the JP1 loop (see Fig. 6.9).

Figure 6.34: Experimental boundary conditions for the "pump coast-down" scenario.
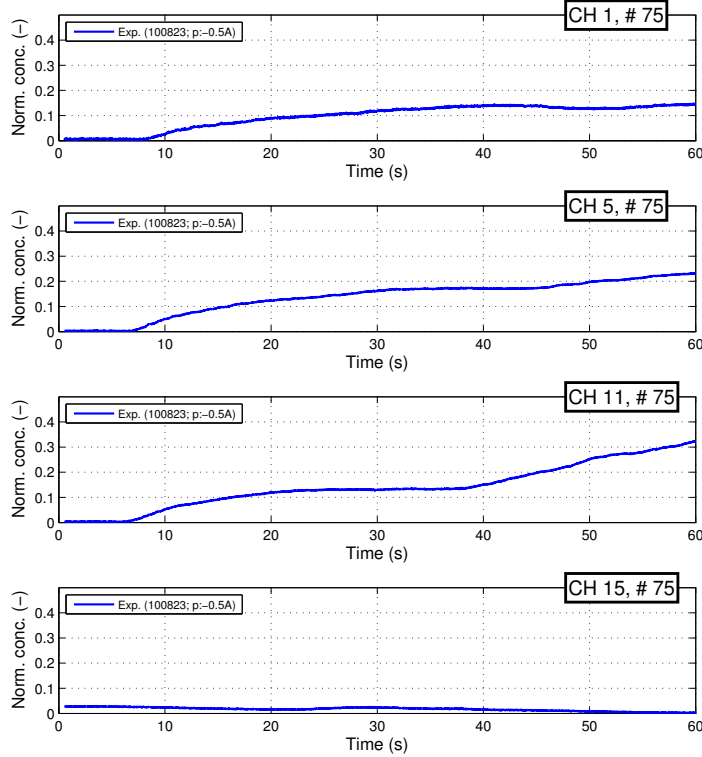
Figure 6.35: Normalized average concentration evolution in the core, measured at the WM-sensor row 75 (core middle) for the core channels 1, 5, 11 and 15 (refer to Fig. 6.9). Experiment for the "pump coast-down" scenario.

for the FLORIS tests. Subsec. 6.4.1 describes the TRACE stand-alone simulations, the results obtained being presented along with the others reported in Subsec. 6.4.2 (CFD stand-alone simulations) and Subsec. 6.4.3 (coupled CFX/TRACE computations). In the latter two subsections are also reported the comparisons with experimental data.

6.4.1   TRACE stand-alone simulations

In TRACE, the FLORIS RPV mock-up has been modeled using a two-dimensional vessel component, connected to the recirculation loop, which is modeled as a system of pipes, valves and pumps (Fig. 6.36). Most of the components have a coarse nodalization (about 10 to 15 cm node-size). In particular, the vessel has been modeled with:

- one node for each core channel, plus two for the jet pumps in the X (horizontal) direction;

- one node in the Y (transversal) direction;

- an adequate number of nodes in the Z (vertical) direction to model all the different cross sections of the jet pumps and of the core. In particular, the inlet and outlet openings of the core channels (which feature a smaller flow area, with respect to the core channels themselves) are modeled in a simplified, zero-dimensional way and an arbitrary[6] pressure drop coefficient of 2.0. Similarly, an arbitrary pressure drop coefficient of 2.0 was assigned to the outlet of the jet pumps, where there is an abrupt change of the cross section.

An *ad-hoc* control system was devised to control the pumps during transient conditions in the simulation, using as input the direct measurements of the mass flow sensors. The tracer injection system was modeled with a fill component, in a similar way as done for the injection in the double T-junction (Chap. 4). In the transient cases, the injection was made directly into the vessel (at the same position as used for its measurement with the WM-sensor), in order to be close to the experimental conditions without having to apply a time-delay correction for the concentration (see App. H).

The simulation cases run are the same as listed in Tab. 6.2. The TRACE stand-alone results are displayed together with the results obtained from the CFD stand-alone simulations and the coupled CFX/TRACE computations (Subsecs. 6.4.2 and 6.4.3, respectively). It should be noted that the QUICKEST scheme, implemented in Chap. 5, was not used in the TRACE stand-alone simulations for the current experiment, because it has not yet been extended to multi-dimensional components, e.g. the 3D model of the RPV mock-up employed here.

---

[6]Due to the symmetry of the vessel and the forced flow inside the recirculation loop, the pressure drop coefficient has negligible effect on the results, which are in any case far from reality due to the limited multi-dimensional capabilities of TRACE (as will be shown later in the comparisons).
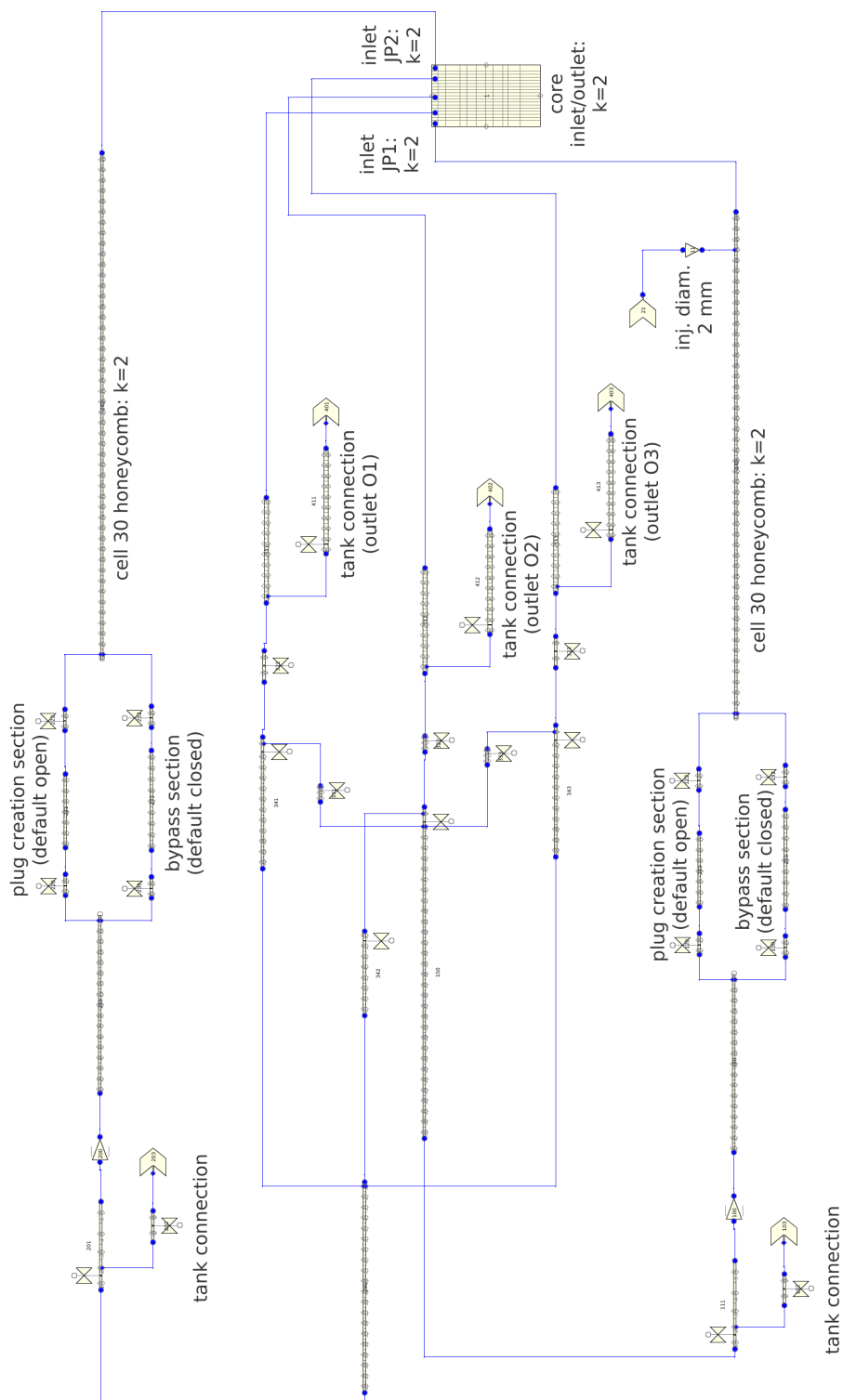
Figure 6.36: TRACE stand-alone model of the FLORIS facility.

6.4.2 CFD stand-alone simulations and experimental comparisons

As compared to the CFD modeling for the pre-test simulations (Sec. 6.2), the initial mesh has been updated by including the baffles at the outlets of the jet pumps and by reducing the mesh size to a total of about 1.7 million elements (against the 6.0 million elements of the pre-test simulations), without compromising the accuracy of the computations and while still respecting the $y^+ < 2$ criterion at the walls. This optimization has led to a considerable decrease in the computational time.

The measured mass flow rate is imposed as boundary condition at the inlet pipes with a flat (uniform) inlet velocity profile. A simulation with a fully developed turbulent inlet velocity profile was also executed, considering the strong effect that this may have on the results (as was found out in Chaps. 3 and 4). However, the 90-degree angle bend existing between inlet loop and jet pump restructures the flow field so strongly that the effect of a given inlet velocity profile is negligible on the transport of the tracer.

The tracer injection is imposed as a uniform concentration over the entire surface at the inlet pipe, since it was seen already in Chap. 4 that the assumption on the concentration profile at the tracer injection location has negligible influence on the final results.

The outlet pressure is imposed to be the same for all the open outlets (atmospheric pressure), in accordance with the readings from the pressure sensors mounted at the outlet locations (the measured pressure drop inside the vessel is about 2 kPa at the considered mass flow rates). In the CFD simulations, the inlet pressure is a result of the mass and momentum balance equations, given the inlet mass flow rate and the outlet pressures; simulations have confirmed the measured value of 2 kPa. Since the test is basically isothermal and fluid properties do not change appreciably over the pressure range in the facility, the average pressure level does not influence the results.

Under transient conditions - according to the simulations carried out with TRACE, which has the capability of simulating the entire loop and does not need a pressure boundary conditions at the vessel outlets, these being a result of the simulation (see Sec. 6.4.3 for details) - the pressure at the outlets has a slightly uneven distribution. It needs to be mentioned that time-dependent pressure boundary conditions, for use in the CFX stand-alone simulations, were not collected during the measurements because of a lack of instrumentation (the pressure tap was used to inject the tracer with the syringe pump). This leaves a constant boundary condition as the only input choice for the model. In any case, pressure differences between the outlets are smaller than the pressure drop within the vessel; simulation results confirm less than 0.1 kPa differences between the outlets (shown later in Figs. 6.74 and 6.78), against about 10 kPa for the whole vessel.

The cases run are again those listed in Tab. 6.2, the results obtained from the CFD stand-alone simulations being described in detail below. Also reported are the comparisons with experimental data and with TRACE stand-alone simulations.

Symmetric scenario

For the "symmetric" scenario (described in Sec. 6.3), a comparison of ANSYS CFX stand-alone results has also been made against a second CFD code, i.e. STAR-CCM+ [92]. The main objective in comparing CFX results to an independent CFD code has been to highlight possible inconsistencies due to the adopted CFD mesh or turbulence model. Thus, CFX results, obtained running in single precision and using a hexahedral mesh and the SST turbulence model, are compared to STAR-CCM+ results, obtained in double precision using a polyhedral mesh and the $\kappa - \varepsilon$ turbulence model. The applied boundary conditions are the same for both simulations and correspond to concentration and mass flow data taken from the selected experiments discussed in the previous section. Since STAR-CCM+ is being considered as "reference" in the code-to-code comparison, its results are presented first below.

STAR-CCM+ stand-alone simulations

In Fig. 6.37, the experimental tracer concentration recorded at the outlet of JP1 at location WM 34 is compared to the simulation results. The profile is well reproduced, thus indicating that correct boundary conditions were set up.

In Fig. 6.38, the results obtained for the tracer concentration at the inlet of channels 1, 4 and 8 are presented for different STAR-CCM+ simulations carried out employing different time steps, solver accuracies and turbulence models. It can be seen that a time step of 0.1 s and a low accuracy for the residuals ($\sim 10^{-4}$, see green curve in Fig. 6.38) result in a considerable delay in predicting the tracer wave. This is indicative of non-converging results with the chosen settings. Allowing the CFD solution to reach a higher accuracy for the residuals ($\sim 10^{-5}$) with the same time step (red curve), or employing smaller integration time steps (here 0.01 s) with the same accuracy of $\sim 10^{-4}$ (cyan curve), gives results which are shifted in time by about the same amount relative to the results obtained with low accuracy and larger time step. The amplitudes, however, differ and appear to depend more on the adopted time step and turbulence model. Although this does not demonstrate that the results are converged, smaller time steps were not adopted because of computational time constraints; however, experience dictates that the shown results should be quite close to the converged solution.

Always in Fig. 6.38, excluding the low-accuracy solution (green curve), it can be seen that the simulation results are more accurate for the central channels (i.e. channel 8), where the jet is impinging, than for the side channels (i.e. channel 1) which are above the recirculation zone and are therefore not in the main flow direction of the tracer. This is mainly due to the inability of the adopted turbulence model to correctly capture the recirculation vortex in the lower plenum and thus the correct velocity at the inlet of the more lateral channels. Indeed, agreement of amplitude and shape of the wave deteriorates when moving towards the side channels.
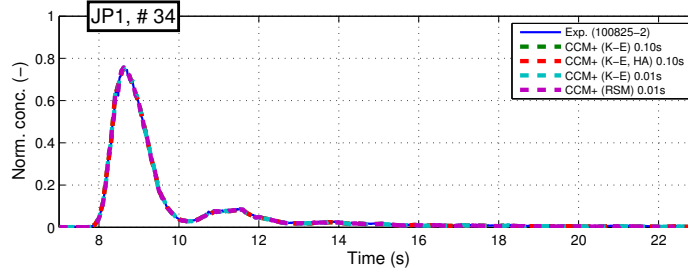
Figure 6.37: Normalized average concentration evolution in JP1 at the WM-sensor row 34 (refer to Fig. 6.9). Comparison between experimental data and different STAR-CCM+ stand-alone simulations for the "symmetric" scenario.
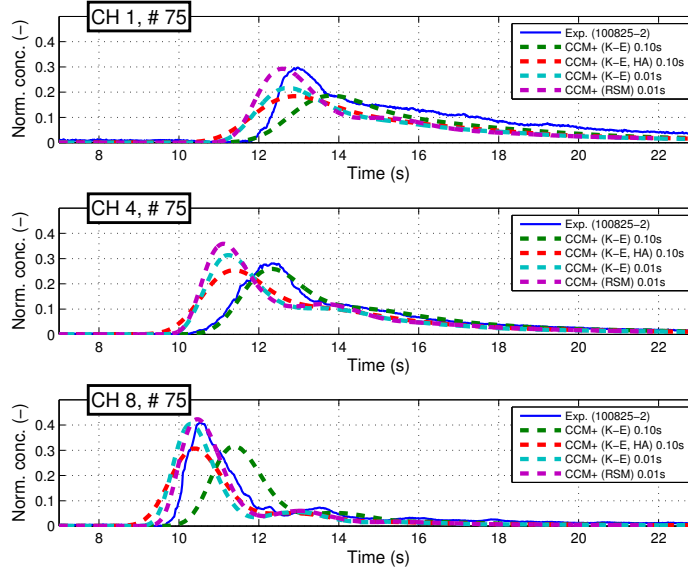

Figure 6.38: Normalized average concentration evolution in the core at the WM-sensor row 75 for the core channels 1, 4 and 8 (refer to Fig. 6.9). Comparison between experimental data and different STAR-CCM+ simulations for the "symmetric" scenario.

Fig. 6.39 shows the absolute time delay of the simulated concentration peaks, relative to the experimental concentration peak as reference, for all of the core channels. By analyzing the more accurate results (i.e. excluding the green curve) and comparing them with the experimental data, it can be seen that the tracer wave entering the core channels is slightly anticipated. This anticipation is larger for the side channels, at whose inlets the recirculation zone is located, and therefore where the main flow direction is not directly oriented towards the core channels. Employing the RS turbulence model instead of the $\kappa - \varepsilon$ turbulence model and adopting the same time step does not result in any significant improvement (see Figs. 6.38 and 6.39).

Fig. 6.40 shows the computed distribution of the mass flow rates at the inlets of the different core channels; this is symmetrical and quite similar for all of the cases. In agreement
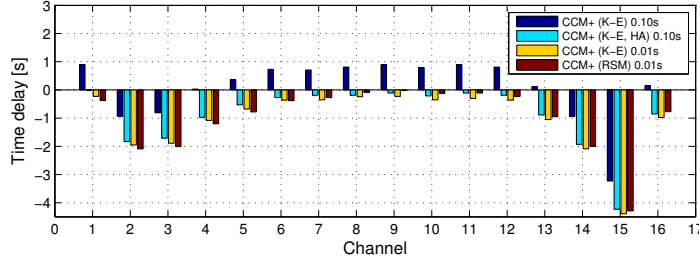
Figure 6.39: Time delay of the maximum average tracer concentration for each core channel at the WM-sensor row 75 (refer to Fig. 6.9), with experimental data taken as reference. Comparison between different STAR-CCM+ stand-alone simulations for the "symmetric" scenario.
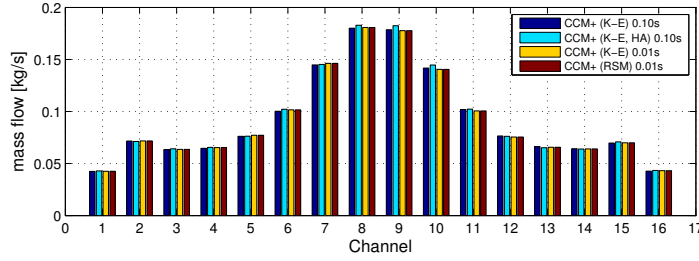

Figure 6.40: Mass flow for each core channel at the WM-sensor row 75 (refer to Fig. 6.9). Comparison between different STAR-CCM+ stand-alone simulations for the "symmetric" scenario.

with the experimental evidence, the computed mass flow rate is higher in the central channels than in the side channels. This can be seen as well in the velocity field contour plot, presented in Fig. 6.41. It is important to note here that the velocity streamlines in the lower part of the sidemost channels are not straight and that they impact upon the channel walls. This may explain why it is difficult to capture the correct tracer concentration in these channels for the simulations shown here and in the following sections. In fact, a $\kappa - \varepsilon$ or SST model has difficulties in correctly capturing the curvature of these velocity streamlines, while a RS model is usually better suited for the task (the channel 1 concentration evolution in Fig. 6.38 is a clear demonstration of this). For the central channels, where instead the streamlines are mostly straight, the $\kappa - \varepsilon$ model (with smaller time step) and the RS model both give practically the same results.

Figs. 6.42 and 6.43 show the maximum normalized concentration reached in each core channel, expressed as absolute and relative[7] value, respectively. From Fig. 6.42, it may be seen that in the second half of the core (channels 9-16) the measured experimental concentration is largely underestimated by the simulations, because the computed velocity field (see Fig. 6.41) is strongly symmetric and most of the injected tracer circulates in the left half of the vessel. Fig. 6.43 shows that in this case the $\kappa - \varepsilon$ model and the RS model perform similarly, with
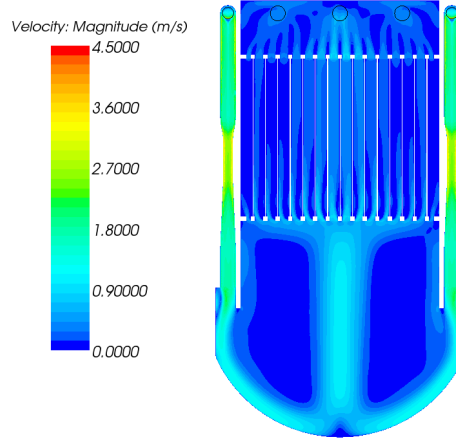
---

[7] To the experimental value.

185

Figure 6.41: Steady-state velocity field for the "symmetric" scenario, computed with STAR-CCM+ stand-alone.
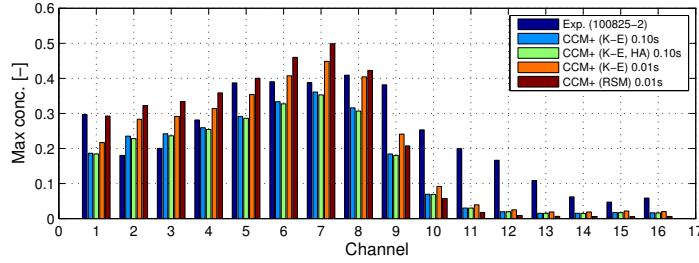

Figure 6.42: Maximum normalized average tracer concentration for each core channel at the WM-sensor row 75 (refer to Fig. 6.9). Comparison between experimental data and different STAR-CCM+ stand-alone simulations for the "symmetric" scenario.
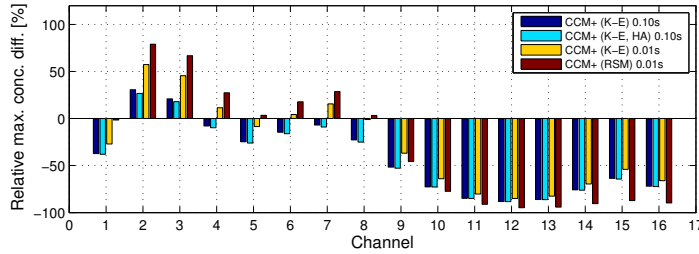

Figure 6.43: Relative difference (with respect to experiment) of the maximum normalized average tracer concentration for each core channel at the WM-sensor row 75 (refer to Fig. 6.9). Comparison between different STAR-CCM+ stand-alone simulations for the "symmetric" scenario.

a maximum concentration difference between them of about 20%. Again, the largest errors are located in the same channels for both models, implying that the computed velocity field is similar and does not correctly reproduce the experiment.

CFX stand-alone simulations

In Fig. 6.44, the experimental tracer concentration recorded at the outlet of JP1 at WM 34 is compared to the simulation results. Again, the profile is well reproduced, thus providing confidence that correct boundary conditions were set up for the calculations.

In Fig. 6.45, the CFX average tracer concentration, obtained with SST and RS turbulent models and with different time steps, is reported for selected core channels; RMS convergence is set to 10^{-4}. As already found for STAR-CCM+, ANSYS CFX results are also found closer to the experimental results for the central channels. It is important to note that, even though the SST solution with 0.1 s time step (red curve) yields results similar to these obtained with the RS model and 0.01 s (cyan curve), it is clearly not converged (it is quite different from the SST solution obtained with 0.01 s time step), and should not be considered. Indeed, non-converged solutions sometimes appear correct just by chance, and this is one of those cases.

Fig. 6.45 presents the results obtained for the tracer concentration at the inlet of channels 1, 4 and 8 for different CFX simulations carried out employing different time steps and turbulence models. Fig. 6.46 shows again the absolute time delay of the simulated concentration peaks, computed by using the experimental concentration peak as reference, for all of the core channels. Similarly to what has been seen in the STAR-CCM+ simulations, there is a significant anticipation of the tracer wave, as may be observed from both figures. The anticipation is larger in the side channels, located above the recirculation zone in the lower plenum; there, the flow streamlines present a strong curvature and CFD RANS models have problems to correctly capture the flow field.

Fig. 6.47 shows the computed mass flow rate distribution for the core channels. In agreement with the experimental evidence, the mass flow rate is higher in the central channels than in the side channels. This can be seen as well in the velocity field contour plot, presented in Fig. 6.48. The absolute values of the core channel inlet velocities are seen to be slightly influenced by the turbulence model adopted in the simulation.

It should be noted that reducing the integration time step adopted in the SST model simulations does not give an appreciable improvement in the time delay of the convected plug or in the channel mass flow predictions. However, it has a significant impact on the maximum concentration reached in each channel, as can be seen from Figs. 6.49 and 6.50, which report the maximum concentration of the tracer plug for each channel, expressed as absolute and relative[8] value, respectively. Considering the simulations with the smaller time step, it may be seen that the tracer concentration at the core channels inlets is underestimated by CFX simulations. In the second half of the core channels, however, the tracer wave amplitude is largely underestimated only if the SST model is used, while the simulation employing the RS model captures the tracer concentration in that section of the core much better.
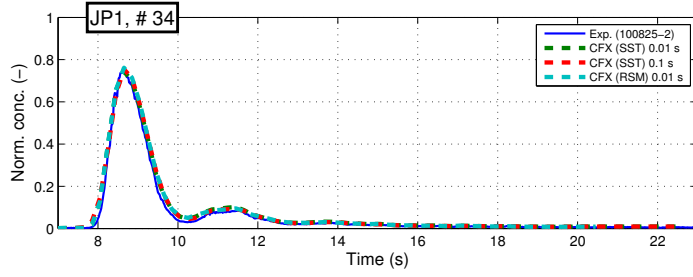
---

[8]To the experimental value.

Figure 6.44: Normalized average concentration evolution in JP1 at the WM-sensor row 34 (refer to Fig. 6.9). Comparison between experimental data and different CFX stand-alone simulations for the "symmetric" scenario.
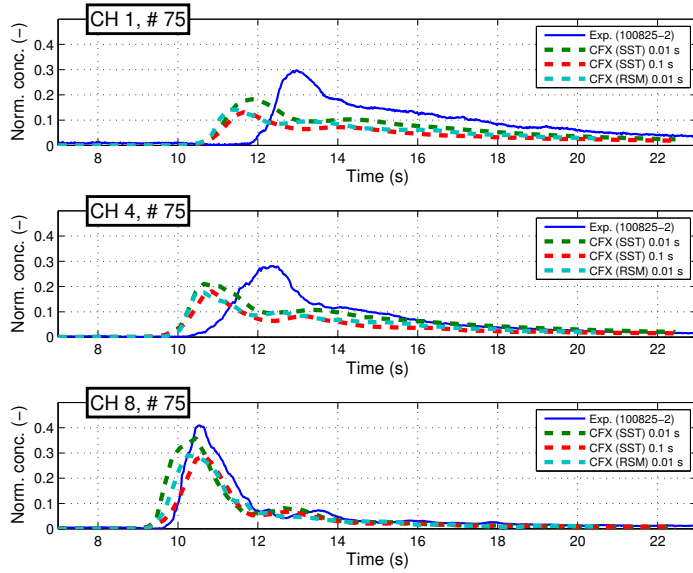

Figure 6.45: Normalized average concentration evolution in the core at the WM-sensor row 75 for the core channels 1, 4 and 8 (refer to Fig. 6.9). Comparison between experimental data and different CFX simulations for the "symmetric" scenario.
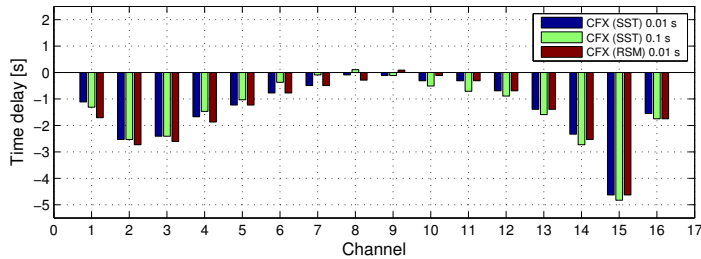

Figure 6.46: Time delay of the maximum average tracer concentration for each core channel at the WM-sensor row 75 (refer to Fig. 6.9), with experimental data taken as reference. Comparison between different CFX stand-alone simulations for the "symmetric" scenario.
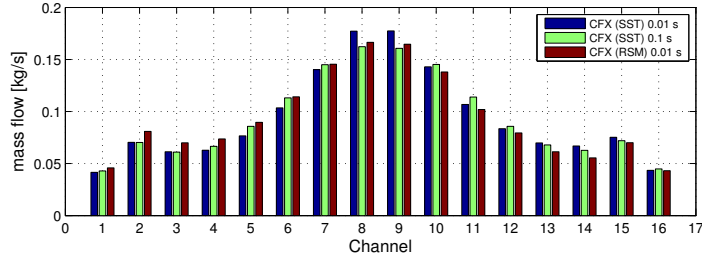
Figure 6.47: Mass flow for each core channel at the WM-sensor row 75 (refer to Fig. 6.9). Comparison between different CFX stand-alone simulations for the "symmetric" scenario.
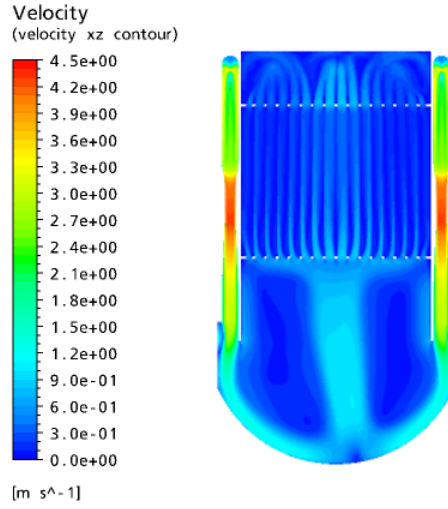

Figure 6.48: Steady-state velocity field for the "symmetric" scenario, computed with CFX stand-alone.
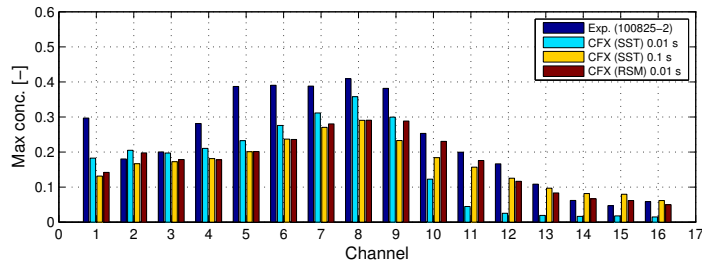

Figure 6.49: Maximum normalized average tracer concentration for each core channel at the WM-sensor row 75 (refer to Fig. 6.9). Comparison between experimental data and different CFX stand-alone simulations for the "symmetric" scenario.
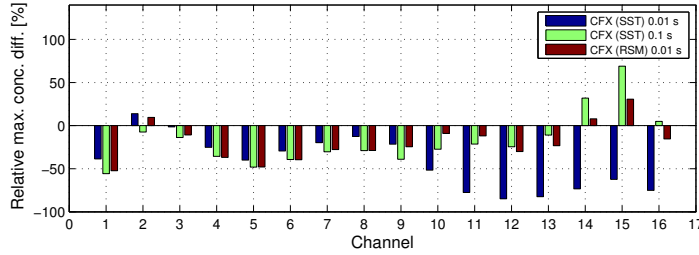
Figure 6.50: Relative difference (with respect to experiment) of the maximum normalized average tracer concentration for each core channel at the WM-sensor row 75 (refer to Fig. 6.9). Comparison between different CFX stand-alone simulations for the "symmetric" scenario.

CFD core channel velocity profiles

The velocity profile in the core channels has a strong impact on the time at which the tracer peak reaches a certain location in the channels, and this could explain the anticipation of the peak observed in the CFD simulations. In fact, for a given average velocity in a certain core channel, if the maximum velocity along the channel cross section is higher, the tracer plug will reach a certain point along the channel sooner. However, no velocity measurements are available in FLORIS, and therefore it is difficult to confirm the hypothesis. It would be clearly worthwhile to include velocity measurements in future FLORIS experiments.

The only information available to support the above hypothesis corresponds to the computed velocity profiles. Fig. 6.51 shows the axial velocity profiles (magnitude with sign) in all core channels and at different core heights, sampled along the central plane between the two FLORIS walls. The profiles are obtained from a CFX simulation. At the core entrance (bottom part of the figure), it is possible to see that the profile is strongly peaked. On the one hand, the peripheral channels have a lower average velocity and the profile peak is more pronounced for them. Therefore, a larger anticipation of the tracer plug is expected there, according to the above hypothesis. On the other hand, in the central channels, where the average velocity is higher, the velocity profile is closer to fully developed conditions and the peaking is much less pronounced than for the lateral channels. Thus, always according to the above hypothesis, the expected anticipation should be smaller. As a matter of fact, this description fits well with what is seen from the simulations (see for example Fig. 6.45). Always according to Fig. 6.51, at the positions further downstream of the core entrance, the velocity peaks become lower, but a fully developed profile is never reached (although channels 8 and 9 get very close to it). Therefore, the anticipation of the tracer plug still increases, but less than in the first half of the core, as can be seen for example from Fig. 6.52, where the tracer plug concentration is shown for different positions in channel 4.

Comparison between stand-alone CFD and TRACE simulations

Fig. 6.53 shows a direct, qualitative comparison of the tracer concentration inside the vessel
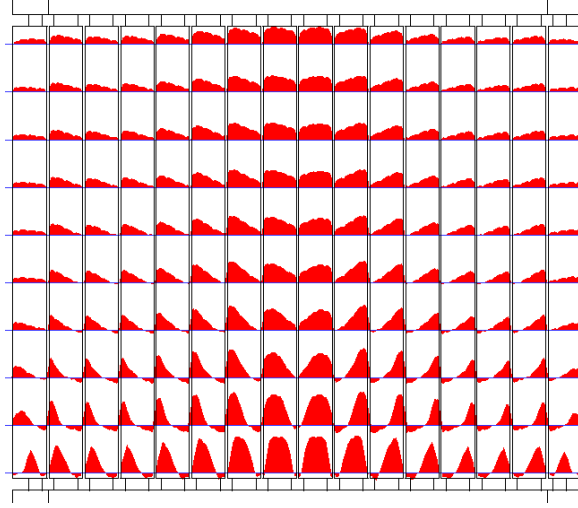
Figure 6.51: Axial velocity profiles (magnitude with sign) sampled at different positions along the core channels and in the central plane between the two FLORIS walls, obtained from the CFX SST simulation with a time step of 0.01 s, for the "symmetric" scenario. Core inlet is at the bottom, core outlet is at the top.

Figure 6.52: Normalized average concentration evolution in the core at the WM-sensor rows 56, 75 and 93 for the core channel 4 (refer to Fig. 6.9). Comparison between experimental data and different CFX simulations for the "symmetric" scenario.

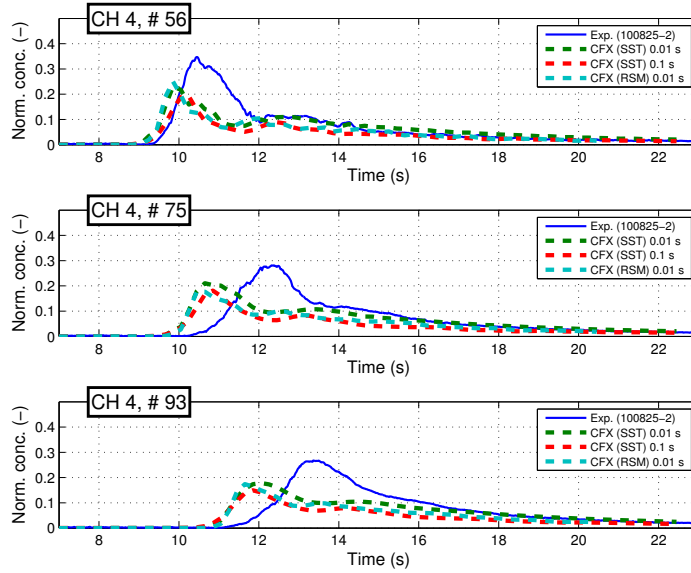at different times during the transient, between the experimental data and the results from the different simulations. It can be seen that both the CFD solutions reproduce quite well the tracer transport inside the lower plenum and the general flow topology, even though a certain anticipation of the tracer front occurs in the simulations. The level of detail of the TRACE nodalization, combined with the deficiencies of the TRACE 3D formulation of the momentum equation, leads, on the other hand, to a very approximate reproduction of the vortices which develop in the lower plenum. Also, as previously pointed out, the TRACE redistribution of the tracer among multiple junctions (i.e. among the core channels, in the present case) is proportional to the computed mass flow rates at the junctions, which leads to a considerable deviation of the tracer splitting among the core channels from the experimental evidence. In this case, simulations tend to be symmetric, and the right half of the core is almost (for STAR-CCM+) or totally (for TRACE) not crossed by the tracer; CFX, if the RS model is employed, is the only exception.

In Fig. 6.54, the tracer concentration recorded at the outlet of JP1 at WM 34 (Fig. 6.9) is compared to the results of the more detailed stand-alone CFD simulations available (described in the previous paragraphs), as also to the TRACE stand-alone solution. The TRACE profile is well reproduced, thus indicating that correct boundary conditions were set up.

Fig. 6.55 shows the results obtained for the tracer concentration evolution at the inlet of channels 1, 4 and 8, again for the more detailed stand-alone CFD simulations available and for the TRACE stand-alone simulation. From the figure, it is clear that TRACE is not able to reproduce the experimental results even qualitatively. This is because, firstly, the TRACE 3D-formulation of the momentum equation is an approximate one, lacking for example turbulence modeling. Secondly, the size of the mesh for which TRACE is designed (e.g. that employed in the present simulation) is usually too large to enable a sufficiently detailed reproduction of the vortices. Thirdly, since it was not possible to use the newly implemented QUICKEST scheme (because of its current limitation to 1D components), significant numerical diffusion effects occur in the TRACE solution.

Fig. 6.56 shows the mass flow rate inside the 16 core channels for the selected simulations. It may be seen that the TRACE velocity field is perfectly symmetric and that the mass flow is almost the same in all the channels (the sidemost channel has a different mass flow because of the different geometry, i.e. the channel inlet area is smaller than that of the other channels); CFD simulations predict instead a symmetric distribution favoring the central channels. Reynolds numbers in the core channels are in the range from $2.4 \cdot 10^6$ (for the side channels) to $1.1 \cdot 10^7$ (for the central channels).

In Fig. 6.57, the time delay of the tracer concentration peak, computed with respect to experimental data, is shown for each of the core channels. It is seen that TRACE predicts a delayed progression of the tracer plug (this is also visible in Fig. 6.55) because of the afore-mentioned mass flow rate distribution. The CFD simulations, on the other hand, anticipate the plug by about the same amount of time. The STAR-CCM+ agreement with experimental

(a) Exp. 8.5 s   (b) CFX 8.5 s   (c) CCM+ 8.5 s   (d) TRACE 8.5 s

(e) Exp. 9.5 s   (f) CFX 9.5 s   (g) CCM+ 9.5 s   (h) TRACE 9.5 s

(i) Exp. 10.5 s   (j) CFX 10.5 s   (k) CCM+ 10.5 s   (l) TRACE 10.5 s

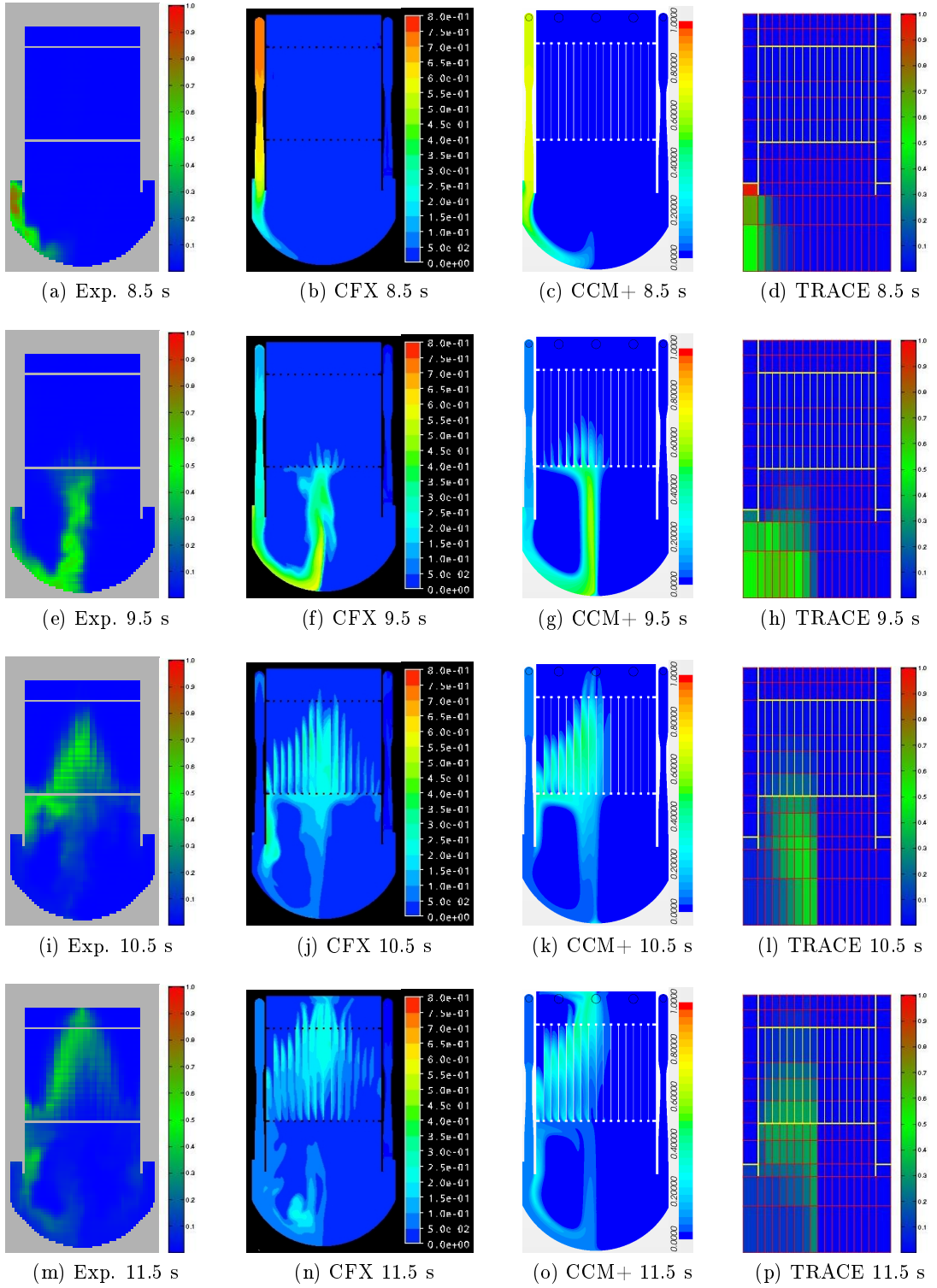(m) Exp. 11.5 s   (n) CFX 11.5 s   (o) CCM+ 11.5 s   (p) TRACE 11.5 s

Figure 6.53: Normalized tracer concentration reconstructed from the WM-sensor experimental data for the "symmetric" scenario, compared with CFX, STAR-CCM+ and TRACE stand-alone simulation results. Snapshots at different times.
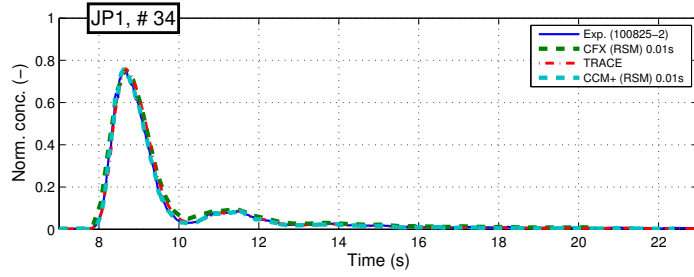
Figure 6.54: Normalized average concentration evolution in JP1 at the WM-sensor row 34 (refer to Fig. 6.9). Comparison between experimental data and results from CFX stand-alone, STAR-CCM+ stand-alone and TRACE stand-alone simulations for the "symmetric" scenario.

Figure 6.55: Normalized average concentration evolution in the core at the WM-sensor row 75 for the core channels 1, 4 and 8 (refer to Fig. 6.9). Comparison between experimental data and results from CFX stand-alone, STAR-CCM+ stand-alone and TRACE stand-alone simulations for the "symmetric" scenario.
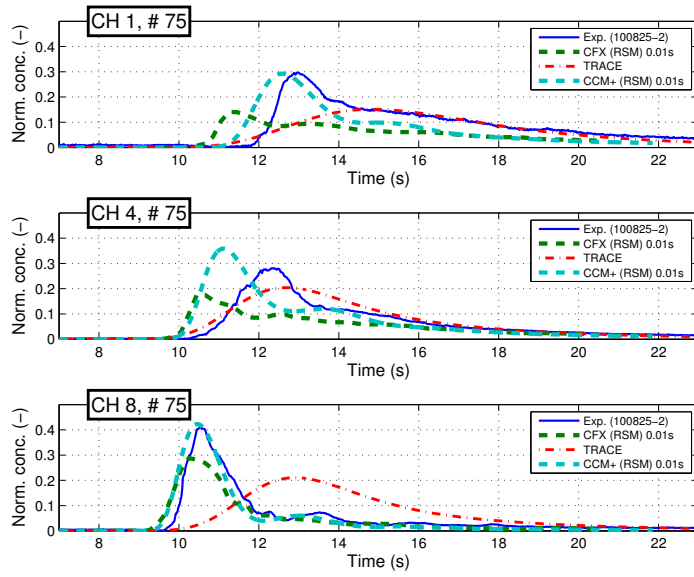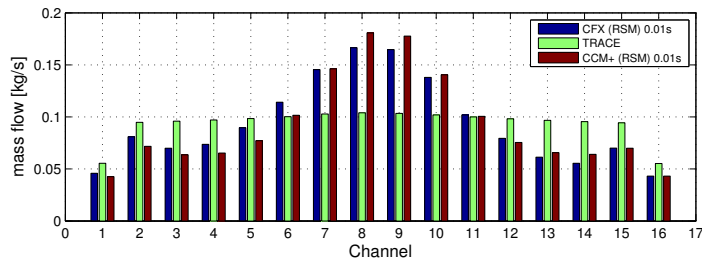

Figure 6.56: Mass flow for each core channel at the WM-sensor row 75 (refer to Fig. 6.9). Comparison between results from CFX stand-alone, STAR-CCM+ stand-alone and TRACE stand-alone simulations for the "symmetric" scenario.
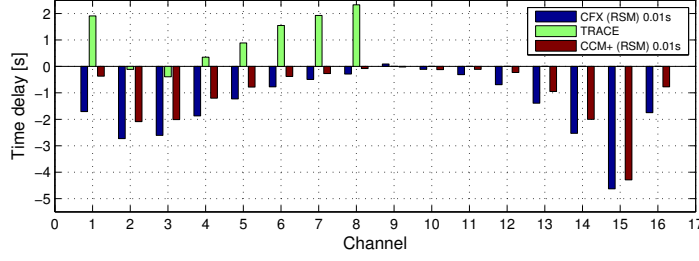
Figure 6.57: Time delay of the maximum average tracer concentration for each core channel at the WM-sensor row 75 (refer to Fig. 6.9), with experimental data taken as reference. Comparison between results from CFX stand-alone, STAR-CCM+ stand-alone and TRACE stand-alone simulations for the "symmetric" scenario.

data is slightly better than that of CFX.

Figs. 6.58 and 6.59 report, respectively, the absolute and relative[9] maximum tracer plug concentration for the core channels. From Fig. 6.58, it may be seen that, in the experiment, there is a greater quantity of tracer flowing in the right half of the vessel than in the simulations, as already noted in the qualitative comparison of Fig. 6.53. The STAR-CCM+ velocity field tends to be more symmetric, thus keeping most of the tracer in the left half of the vessel (where the plug is injected). The CFX simulation, on the other hand, reproduces with greater accuracy the turbulent velocity field in the central part of the lower plenum; consequently, the effect of turbulent mixing, which causes the tracer to spread into the right half of the vessel, is better captured. The TRACE simulation, on the other hand, has a fully symmetric velocity field, which precludes the tracer from spreading to the right half of the vessel. Indeed, TRACE cannot capture the correct splitting of the mass flow between the channels because it splits the tracer concentration accordingly to the mass flow, as was noted in Chap. 4 for the double T-junction experiment. From Fig. 6.59, it may be deduced that STAR-CCM+ largely underestimates the concentration in the right half of the vessel, and generally overestimates it in the left half; a fairly good agreement is reached for the central channels. CFX generally underestimates the maximum concentration in the left half of the core channels; however, it reproduces better the tracer behavior in the right half of the core.

Asymmetric scenario

For the "asymmetric" scenario, most of the considerations previously made for the "symmetric" scenario remain valid.

Fig. 6.60 shows a direct, qualitative comparison of the tracer concentration inside the vessel at different times during the transient, between the experimental data and the CFX and TRACE stand-alone simulations. It can be seen that CFX reproduces quite well the tracer transport inside the lower plenum and the general flow topology; in the lower plenum,
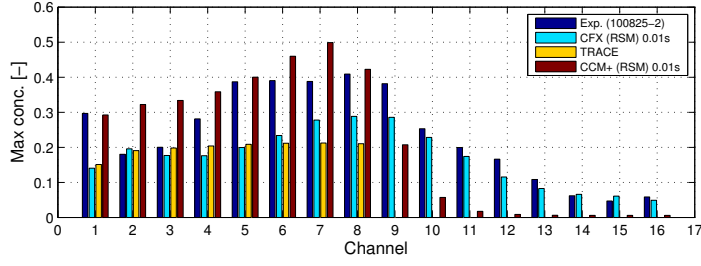
---

[9]To the experimental value.

Figure 6.58: Maximum normalized average tracer concentration for each core channel at the WM-sensor row 75 (refer to Fig. 6.9). Comparison between experimental data and results from CFX stand-alone, STAR-CCM+ stand-alone and TRACE stand-alone simulations for the "symmetric" scenario.
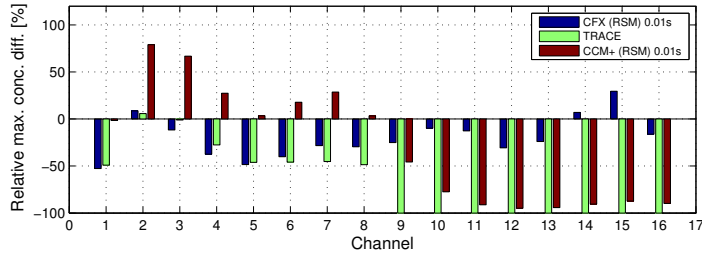

Figure 6.59: Relative difference (with respect to experiment) of the maximum normalized average tracer concentration for each core channel at the WM-sensor row 75 (refer to Fig. 6.9). Comparison between results from CFX stand-alone, STAR-CCM+ stand-alone and TRACE stand-alone simulations for the "symmetric" scenario.

a slight delay in the progression of the maximum concentration is seen for the CFX results, but inside the core the situation is reversed (as shown more clearly in Fig. 6.62). This may be indication that the simplified modeling of the core inlets (and outlets) needs some improving; moreover, it also suggests that the turbulence model employed cannot accurately reproduce the velocity field in the lower plenum. As regards TRACE, the code once again vaguely tries to reproduce the vortices in the lower plenum, but the cell size is too large to provide sufficient detail. From the experimental snapshots, one sees the uneven spread of the tracer in the core channels, as also the formation of a stagnation zone in the right third of the core, as previously described in Sec. 6.3.

Fig. 6.61 reports the tracer concentration at the outlet of JP1, and shows again the correct implementation of the boundary conditions at the jet pump. Fig. 6.62, where the tracer concentration for selected core channels is reported, shows that, apart from the channels in the stagnation zone (from about 12 to 16), the shape of the concentration evolution in the experiment is well reproduced by CFX, although the results do suffer from the delay already noted in the "symmetric" scenario. Once again, one sees the inability of the stand-alone TRACE simulation to correctly predict the concentration in the core channels, both in shape and in amplitude.

(a) Exp. 7.5 s

(b) CFX 7.5 s

(c) TRACE 7.5 s

(d) Exp. 8.5 s

(e) CFX 8.5 s

(f) TRACE 8.5 s

(g) Exp. 9.5 s

(h) CFX 9.5 s

(i) TRACE 9.5 s

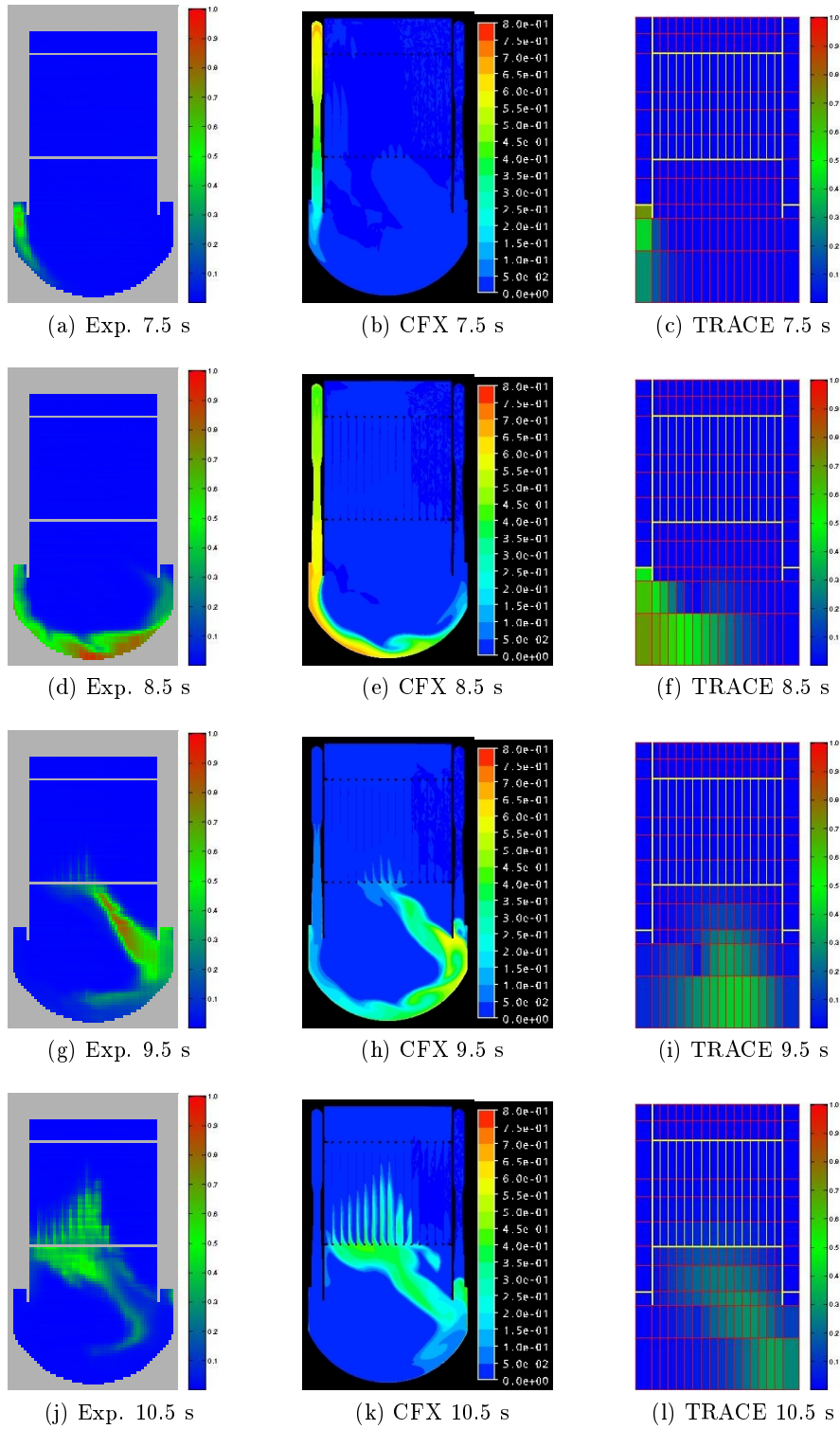(j) Exp. 10.5 s

(k) CFX 10.5 s

(l) TRACE 10.5 s

Figure 6.60: Normalized tracer concentration reconstructed from the WM-sensor experimental data for the "asymmetric" scenario, compared with CFX stand-alone and TRACE stand-alone simulation results.
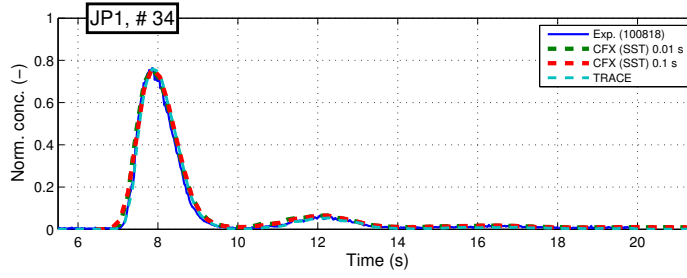
Figure 6.61: Normalized average concentration evolution in JP1 at the WM-sensor row 34 (refer to Fig. 6.9). Comparison between experimental data and results from CFX stand-alone and TRACE stand-alone simulations for the "asymmetric" scenario.

From Fig. 6.63, where the time delay of the tracer concentration peak (computed with respect to experimental data) is shown for each of the core channels, it may be seen that TRACE has a considerable delay for the tracer concentration peak in the core channels 1-11; the rightmost channels should not be considered, since there the concentration is very low and it is difficult to make a proper evaluation (see, for example, Fig. 6.62). The CFX simulation anticipates the concentration peak, as already noted.

Fig. 6.64 displays the mass flow rate in all of the core channels. It shows that the mass flow rate in TRACE is the same for all the channels, i.e. TRACE cannot capture correctly the vortices in the lower plenum of the vessel. As already noted in the "symmetric" scenario, the side channels have a smaller inlet cross-section area and thus a lower mass flow. CFX, on the other hand, predicts the occurrence of the the stagnation zone, with a slightly negative mass flow, and a higher mass flow in the core channels where the jet is directly impinging. The steady-state velocity field is shown in Fig. 6.65.

The maximum tracer concentration (reported in Figs. 6.66 and 6.67 in absolute and relative[10] terms, respectively) is generally underestimated by CFX. This behavior changes at the edge of the stagnation zone. It appears that the channel with the highest maximum concentration is shifted by one channel to the right for the CFX simulation, indicating that the impinging jet is not being reproduced with the correct angle by the CFD code. In TRACE, on the other hand, the tracer concentration is similar in all of the core channels, because the splitting follows the mass flow distribution (Fig. 6.64). As for the "symmetric" scenario, changes in the time step do not significantly affect the mass flow and time delay, while they weakly affect the maximum concentration predicted in each core channel.

Plug recirculation

CFX stand-alone results for this scenario have been found to be similar to those of the "asymmetric" scenario, with respect to the plug injection. However, recirculation results are not available, since a CFD simulation comprising the whole loop would require too much

---

[10] To the experimental value.
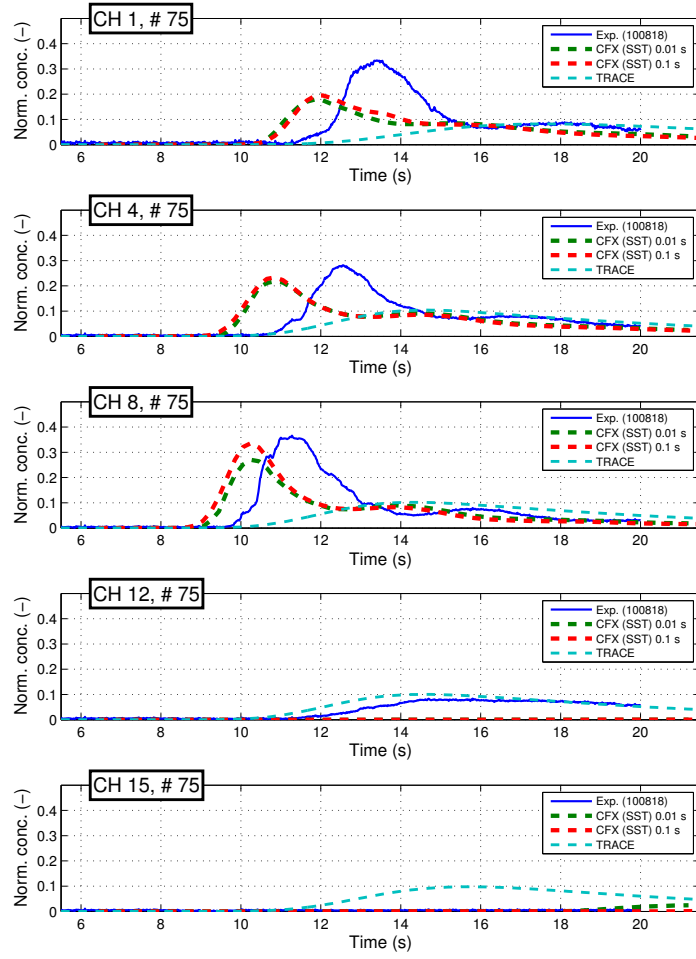
Figure 6.62: Normalized average concentration evolution in the core at the WM-sensor row 75 for the core channels 1, 4, 8, 12 and 15 (refer to Fig. 6.9). Comparison between experimental data and results from CFX stand-alone and TRACE stand-alone simulations for the "asymmetric" scenario.

Figure 6.63: Time delay of the maximum average tracer concentration for each core channel at the WM-sensor row 75 (refer to Fig. 6.9), with experimental data taken as reference. Comparison between results from CFX stand-alone and TRACE stand-alone simulations for the "symmetric" scenario.

Figure 6.64: Mass flow for each core channel at the WM-sensor row 75 (refer to Fig. 6.9). Comparison between results from CFX stand-alone and TRACE stand-alone simulations for the "asymmetric" scenario.
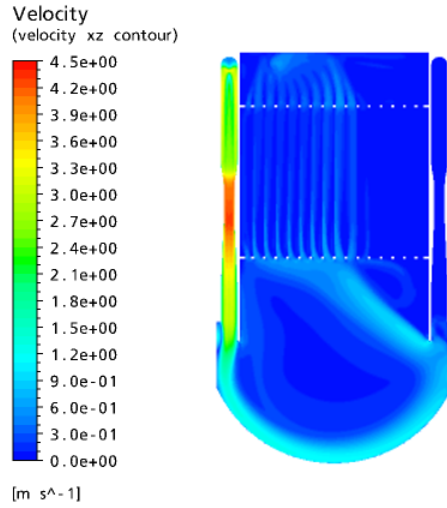
Figure 6.65: Steady-state velocity field for the "asymmetric" scenario, computed with CFX stand-alone.

Figure 6.66: Maximum normalized average tracer concentration for each core channel at the WM-sensor row 75 (refer to Fig. 6.9). Comparison between experimental data and results from CFX stand-alone and TRACE stand-alone simulations for the "asymmetric" scenario.
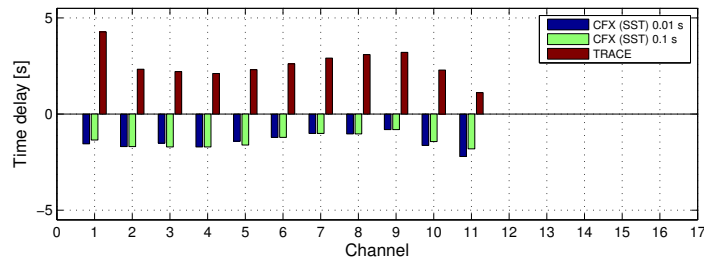
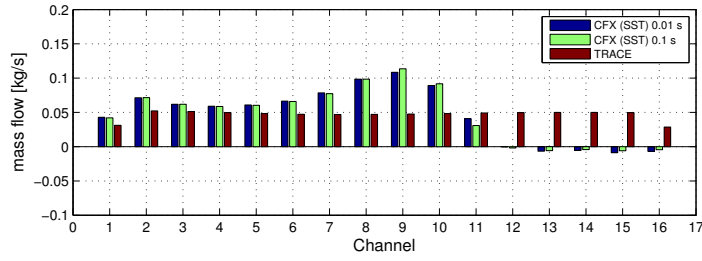Figure 6.67: Relative difference (with respect to experiment) of the maximum normalized average tracer concentration for each core channel at the WM-sensor row 75 (refer to Fig. 6.9). Comparison between results from CFX stand-alone and TRACE stand-alone simulations for the "asymmetric" scenario.
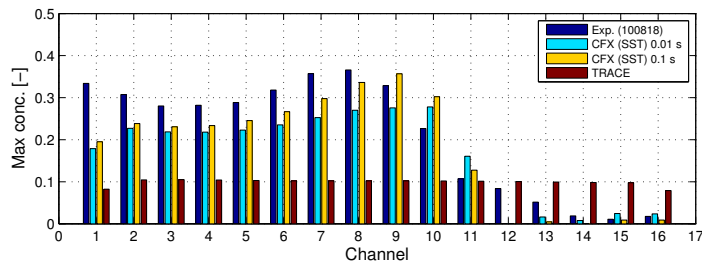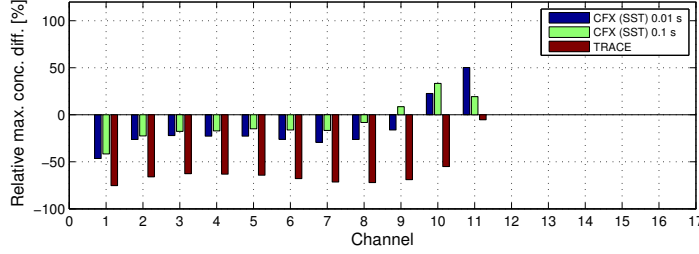
memory and computational power to be carried out. For this reason, the plug recirculation will be modeled and simulated in the next section with the support of the coupled tool.

Pump start-up and shutdown scenarios

Results for these two transient scenarios are presented and discussed together with the coupled simulations in the next section. It is important to note here that the tracer concentration measured at WM 34 (Fig. 6.9) was injected as boundary condition, because it could not be measured directly at the jet pump inlets. In order to get closer to the experimental conditions, the injection was modified with a certain delay in time, so as to take into account the changing mass flow (as explained in App. H).

6.4.3 Coupled CFX/TRACE simulations

To carry out the second phase of the experimental validation of the CFX/TRACE coupled tool, i.e. with respect to the more complex geometry at hand and the coupling of the momentum equation in the case of the transient tests, two possible modeling strategies were considered for the FLORIS facility.

1. In the first option, the entire two-dimensional section of the facility is modeled with the CFD code, including the first 20 cm of the inlet and outlet pipes. The modeling of the pipes makes the imposition of the boundary conditions for the velocity and the pressure at the interface between the model domain to be computed by the CFD code (ANSYS CFX) and that to be computed by the 1D thermal-hydraulic code (TRACE) more straightforward (Fig. 6.68a). The interface between the two domains consists of five separate interfaces, placed at the two inlet pipes and at the three outlet pipes of the RPV model, respectively. The locations of the TRACE-to-CFX interfaces, in correspondence to the RPV inlets, ensure the possibility to convert the cross-section-averaged velocity computed by TRACE into a 2D velocity profile for ANSYS CFX,

at least for the cases where fully developed flow can be assumed (the inlet interfaces are located downstream of a long straight pipe section). The locations of the CFX-to-TRACE interfaces, in correspondence of the RPV outlets, allow one to characterize them with a well defined pressure boundary condition, which is imposed by the presence of a water tank located at about the same height in the system.

2. In the second nodalization option, the CFD computational domain covers simply to the RPV downcomer and lower plenum, so that the location of the CFX-to-TRACE interface corresponds to the inlets of the core channels (Fig. 6.68b). The TRACE-to-CFX interfaces corresponds, as before, to the RPV inlets. The implementation of this modeling strategy is more elaborate due to the higher number of individual interfacing surfaces between the computational domains, and is hence numerically less robust. Moreover, the core inlet section is a coupling junction where the interfacial boundary conditions are difficult to determine and/or to describe accurately (for example, the velocity profile and the pressure field are much more complex than those for a straight pipe). In addition, the repartition of the flow in the upper plenum among the three outlets is challenging for TRACE, since 3D effects in the flow are not negligible, as can be seen from the complex pattern for the velocity streamlines in Figs. 6.10 and 6.11. On the other hand, with this modeling strategy, the CFD domain (and thus the computational mesh) is smaller, so that lower CPU times can be expected.

Weighting the advantages and disadvantages of each of the two above possibilities, it was decided to employ the first option in the present research, the main motivation being that it allows one to study in greater detail the flow field within the entire RPV mock-up and to rule out eventual TRACE deficiencies in modeling the upper plenum. At the same time, it keeps the coupling interface simple and more stable. The trade-off of increased computational costs has been considered to be acceptable for the task.

For the coupled CFX/TRACE simulations, the new CFD mesh of the vessel has been used (described in Subsec. 6.4.2), together with the recirculation loop modeled in TRACE (see Subsec. 6.4.1). The initial tracer injection is imposed as boundary condition into the CFX input file, while the mass flow rate is calculated by the TRACE code (the recirculation loops with the pumps are modeled in the TRACE input file). More details about the set-up of boundary conditions for the "pump start-up" and "pump coast-down" scenarios can be found in App. H. The simulations have been run using the sequential explicit coupling scheme (see Fig. 3.12), in order to limit the running time, and with the newly implemented QUICKEST scheme (Chap. 5) for the TRACE solute transport equation; the latter option plays a role only in the "plug recirculation" scenario, because in this case the tracer concentration is fed back from TRACE to CFX. The coupled simulations have been conducted according to the list of tests of Tab. 6.2. The results are compared to experiment, as also to stand-alone CFD simulations (wherever possible, i.e. for the two transients) and to stand-alone TRACE
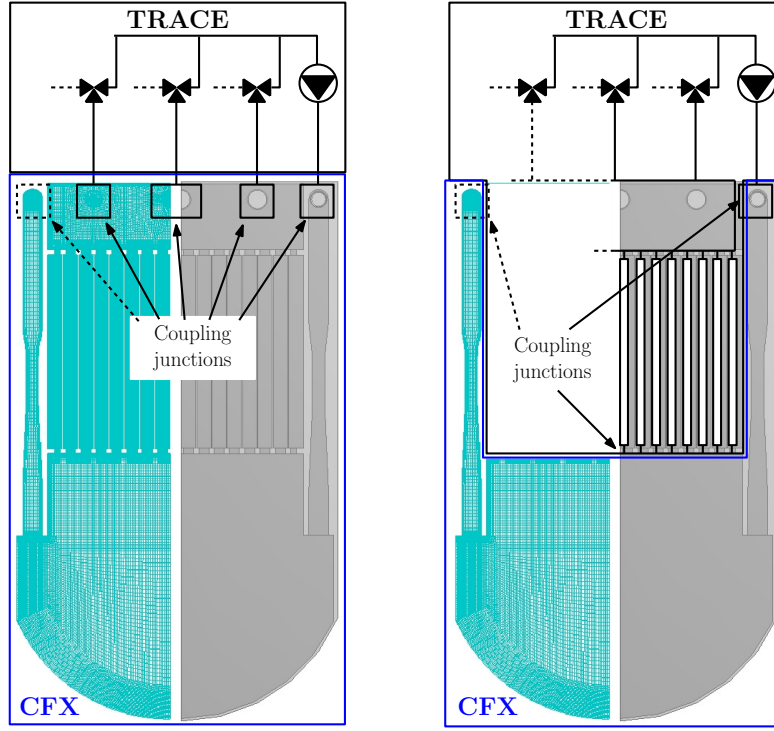
(a) Option 1.   The whole vessel is modeled with CFD and the hydraulic loop with the system code.

(b) Option 2.   Jet pumps and lower plenum are modeled with CFD, while core channels and upper plenum are modeled with the system code. The hydraulic loop is modeled with the system code.

Figure 6.68: Sketch of the possible CFX/TRACE coupling options.

simulations.

Plug recirculation scenario

This scenario, as described in Sec. 6.3, involves the injection of a solute plug at the JP1 vessel inlet, its recirculation through the JP1 loop and its consequent reinjection inside the vessel. The flow field is asymmetric (the second pump is off) and under steady-state conditions, with a mass flow rate of 0.75 kg/s. Fig. 6.69 reports the time evolution of the average concentration at the outlet of the jet pump into which the tracer is injected (in correspondence to the WM-sensor row 34; refer to Fig. 6.9). The first peak of the concentration (between 5 and 15s in the transient) corresponds to the injection of the tracer plug, and therefore both the TRACE stand-alone and the coupled CFX/TRACE solutions match the experimental data. The second large peak occurs after 25s into the transient and is due to the reappearance of the tracer plug, following its recirculation through the facility loop. The CFX/TRACE coupled tool predicts a significantly faster recirculation of the tracer with respect to the experimen-

tal data. This is consistent with the findings discussed previously for the "symmetric" and "asymmetric" scenarios (Sec. 6.3).

Simulations have been carried out employing both the original TRACE version and that with the QUICKEST scheme described in Chap. 5. For the latter, no "physical" diffusion was modeled. By comparing the solutions of CFX/TRACE in Fig. 6.69 with and without the use of the QUICKEST scheme, the effect of the numerical diffusion in the original TRACE solution is clearly visible. By comparing the solution with the QUICKEST scheme against the experimental data, it is also clear that, after reducing the numerical diffusion introduced by the numerical scheme, a physical diffusion term is indeed needed in the tracer transport equation in order to correctly capture the experimental results. This is consistent with the findings discussed in Chap. 5 when validating CFX/TRACE against the double T-junction experiment.

Fig. 6.70 reports the concentration time evolution in selected core channels; the results are similar to those presented for the "asymmetric scenario", considering that the flow config-uration was the same, as also the mass flow rate employed. Similar conclusions can thus be drawn. In addition, the second peak due to the reinjection (not present in the "asymmetric" scenario) is well captured by the coupled simulations, except for the significant anticipation of the tracer front.

Pump start-up scenario

This transient scenario features the start-up of the pump connected to the JP1 inlet, while the other loop is stagnant; the mass flow rate changes from 0.13 kg/s to 0.8 kg/s, while a continuous injection of the tracer takes place at the vessel inlet (refer to Sec. 6.3 for more details). Fig. 6.71 compares concentration snapshots at different times, reconstructed from the experimental data and from the CFX and TRACE stand-alone simulations. The CFX snapshots show a good qualitative agreement between experiment and simulations, as regards the flow field which develops in the vessel during the transient. TRACE, on the other hand, cannot correctly reproduce the flow field, as already discussed in Subsec. 6.4.2.

Fig. 6.72 displays the concentration evolution in JP1. It can be seen that the boundary conditions at the jet pump are correctly implemented, i.e. the injected tracer plug is cor-rectly detected at the WM-sensor row 34 (refer to Fig. 6.9). Since, in the case of CFX and CFX/TRACE simulations, the injection is far from the measurement point[11], the flow tur-bulence smears down the sharp tracer concentration peak; this effect is partially enhanced by the rather large time step. This smearing-down effect, partly visible in the TRACE curve as well, influences the results only with respect to the concentration peak in the core.

---

[11] In the version of CFX employed for this research, it is not straightforward to introduce a tracer source inside the computational domain. Therefore, the concentration in the stand-alone CFX simulations and in the coupled CFX/TRACE simulations has been imposed at the vessel inlet, with a correction for the variable mass flow (see Appendix H).

Figure 6.69: Normalized average concentration evolution in JP1 at the WM-sensor row 34 (refer to Fig. 6.9). Comparison between experimental data and results from CFX/TRACE and TRACE stand-alone simulations for the "plug recirculation" scenario.

Figure 6.70: Normalized average concentration evolution in the core at the WM-sensor row 75 for the core channels 1, 4, 8, 12 and 15 (refer to Fig. 6.9). Comparison between experimental data and results from CFX/TRACE and TRACE stand-alone simulations for the "plug recirculation" scenario.

(a) Exp. 12.0 s   (b) CFX 12.0 s   (c) TRACE 12.0 s

(d) Exp. 16.0 s   (e) CFX 16.0 s   (f) TRACE 16.0 s

(g) Exp.18.0 s   (h) CFX 18.0 s   (i) TRACE 18.0 s

(j) Exp. 24.0 s   (k) CFX 24.0 s   (l) TRACE 24.0 s

Figure 6.71: Normalized tracer concentration reconstructed from the WM-sensor experimental data for the "pump start-up" scenario, compared with CFX and TRACE stand-alone simulation results. Snapshots at different times.

Fig. 6.73 reports the concentration as a function of time for selected core channels. It is seen that CFX stand-alone, as well as the CFX/TRACE coupled tool, correctly predict the appearance of the tracer front at the inlet of the core channels. TRACE, because of its strongly diffusive numerical scheme, is not at all able to capture the sharp tracer concentration front. The TRACE results are also qualitatively different from the experimental measurements. All simulation results, however, settle on the same steady-state value of the tracer concentration, in good agreement with the experimental results. The only exception is the case of the peripheral channels (e.g. channel 15, shown in Fig. 6.73), which are located in the stagnation zone where the flow does not have a predominant direction and the turbulence model employed in the CFD simulations does not correctly capture the flow field.

The discrepancy between CFX and CFX/TRACE concentrations, especially the anticipation in time of the stand-alone code with respect to the coupled tool, can be explained with the fact that, while for the CFX stand-alone simulation the pressure boundary condition is imposed directly at the three outlets and is constant for each of them, in the case of the CFX/TRACE coupled simulation it is imposed at a certain point in the drain pipes, within the TRACE model. The latter location was found to be the most reasonable place to set the boundary condition at atmospheric pressure, considering that it is where the free water surface for the facility lies. The coupled tool computes a certain pressure distribution in the loop, that has to match (and be matched by) the pressure distribution in the FLORIS vessel. Such a pressure field is not constant because of the transient conditions, and thus the pressure at the vessel outlets changes unevenly (see Fig. 6.74, where the computed pressure at the three outlet interfaces is plotted as a function of the time-step number). This clearly shows an important advantage of the coupled simulations over the stand-alone simulations, because the coupled tool is able to dynamically set the interface boundary conditions, i.e. according to the evolution of the system parameters like pressure, mass flow, etc. This was shown in some of the numerical tests in Chap. 3, but the validation was carried out only on the tracer concentration (Chap. 4) and not on the other flow variables (pressure, velocity, etc.). Unfortunately, a direct comparison with differential pressure measurements was also not possible in the FLORIS facility, since the pressure tap at JP1 was used to inject the solute using the syringe pump and the pressure could not be measured.

Pump coast-down scenario

This second transient scenario consists of the shut-down of the pump connected to the JP1 inlet, while the other loop is stagnant; the mass flow rate changes from 0.8 kg/s to about 0.13 kg/s, while a continuous injection of the tracer takes place at the vessel inlet (refer to Sec. 6.3 for more details). Fig. 6.75 compares the concentration snapshots at different times, reconstructed from the experimental data and from the CFX and TRACE stand-alone simulations. The CFX snapshots show a good qualitative agreement between experiment
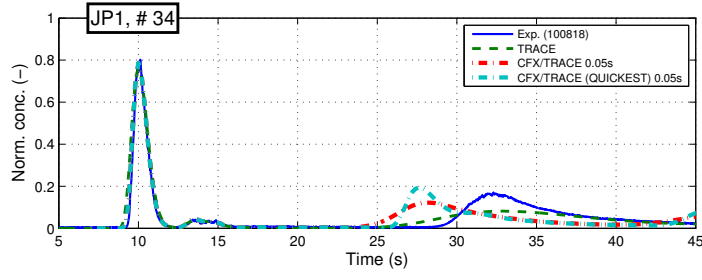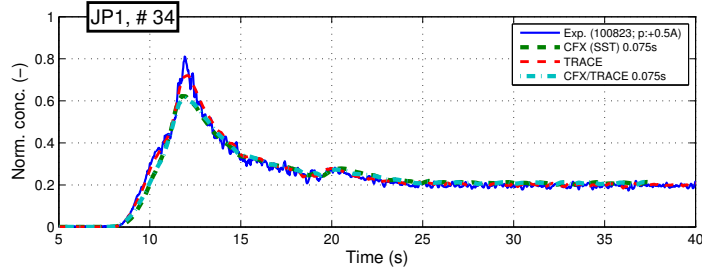
Figure 6.72: Normalized average concentration evolution in JP1 at the WM-sensor row 34 (refer to Fig. 6.9). Comparison between experimental data and results from CFX/TRACE coupled simulations, as well as from CFX and TRACE stand-alone simulations, for the "pump start-up" scenario.
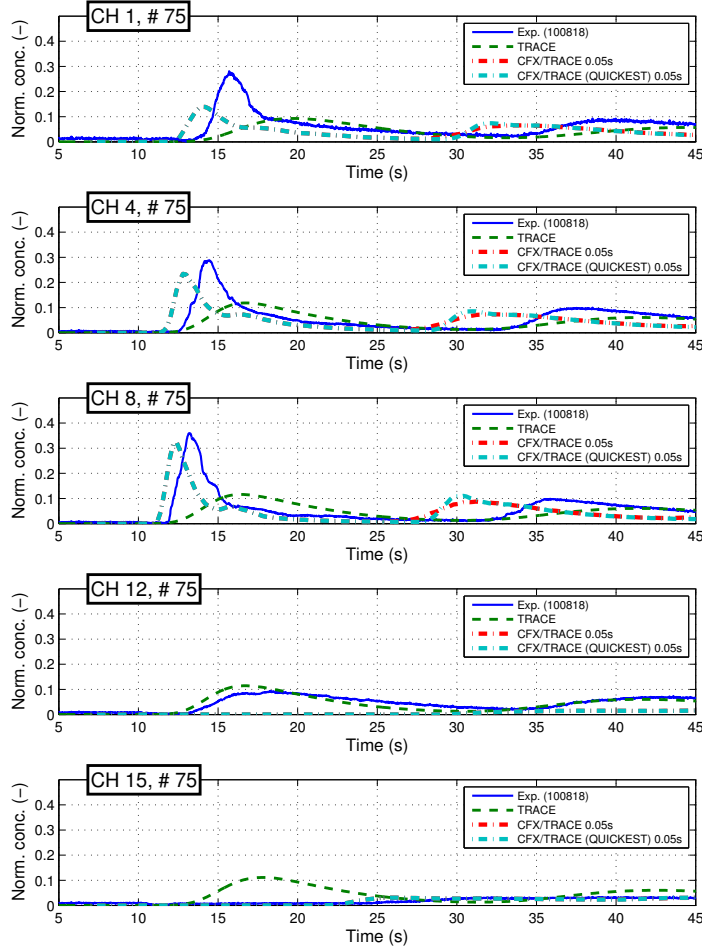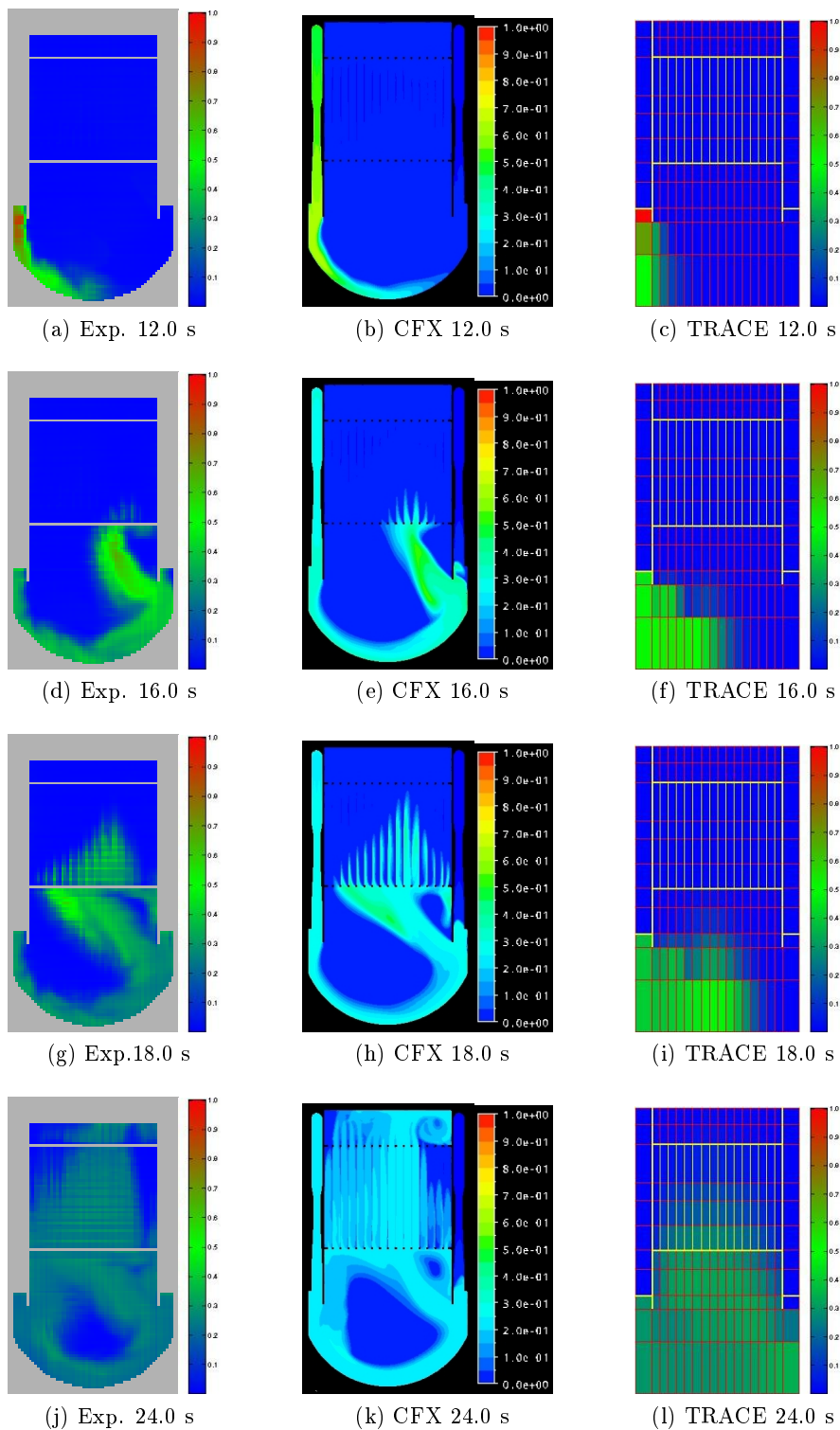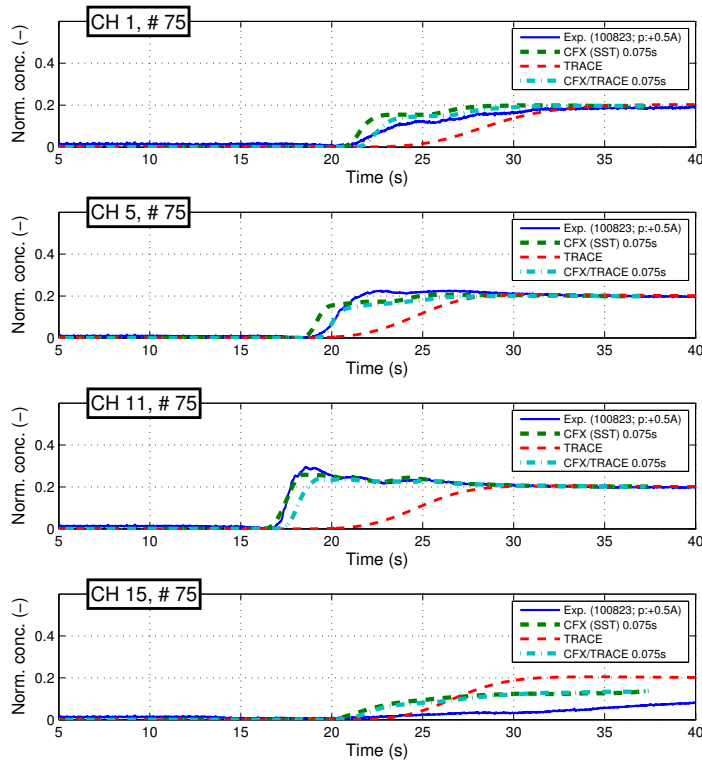

Figure 6.73: Normalized average concentration evolution in the core at the WM-sensor row 75 for the core channels 1, 5, 11 and 15 (refer to Fig. 6.9). Comparison between experimental data and results from CFX/TRACE coupled simulations, as well as from CFX and TRACE stand-alone simulations, for the "pump start-up" scenario.
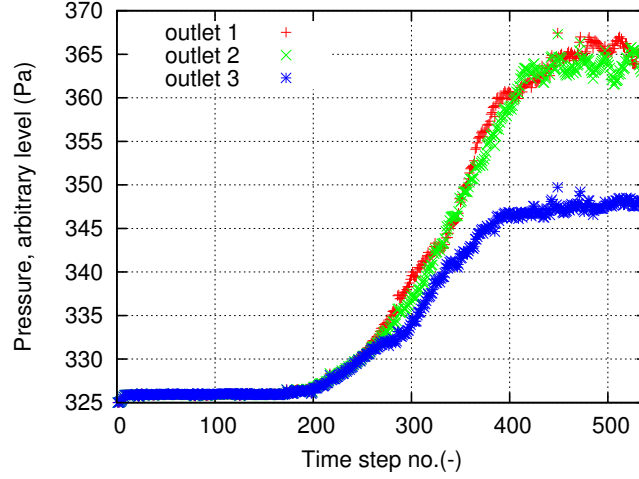
Figure 6.74: Pressure evolution at the three vessel outlets (refer to Fig. 6.9) for the coupled simulation of the "pump start-up" scenario.

and simulations, as regards the flow field which develops in the vessel during the transient. TRACE, on the other hand, cannot correctly reproduce the flow field, as described earlier.

In Fig. 6.76, the concentration evolution in JP1 is shown. It can be seen that the boundary conditions at the jet pump are correctly implemented, i.e. the injected tracer plug is correctly detected at the WM-sensor row 34 (refer to Fig. 6.9).

From Fig. 6.77, where the tracer concentration time evolution is displayed for selected core channels, it may be seen that there is a general overestimation of the tracer concentration in the core channels for both the stand-alone and the coupled simulations. Results are clearly worse than in the "pump start-up" scenario, even though similar flow conditions are present. A possible explanation may be that in the present case the low-velocity flow field, which is established soon and lasts a long time, is not well reproduced by the CFD simulations. In the previous scenario, the low-velocity flow field becomes quickly a high-velocity one, which can be better captured by CFD.

Always in Fig. 6.77, it may be seen that TRACE cannot predict the correct time at which the tracer first arrives at the core inlet, thus delaying the increase in concentration; this delay is not large, however. The same effect is not present for the CFX and CFX/TRACE simulations, indicating that CFD correctly predicts the arrival of the concentration in each channel. Moreover, it can be noted once again that TRACE displays about the same tracer concentration in every core channel, since the mass flow rate computed by the code is similar for all of the channels. The mass flow rate computed by CFD, on the other hand, is different for the different core channels. Moreover, the stagnation zone present in the right third of the core is correctly identified, as was noted previously in the "asymmetric" scenario. For this reason, the concentration plot of channel 15 in Fig. 6.77 has zero concentration for the CFD simulations, while it has a value similar to the other channels for the stand-alone TRACE

(a) Exp. 18.0 s   (b) CFX 18.0 s   (c) TRACE 18.0 s

(d) Exp. 24.0 s   (e) CFX 24.0 s   (f) TRACE 24.0 s

(g) Exp. 30.0 s   (h) CFX 30.0 s   (i) TRACE 30.0 s

(j) Exp. 36.0 s   (k) CFX 36.0 s   (l) TRACE 36.0 s
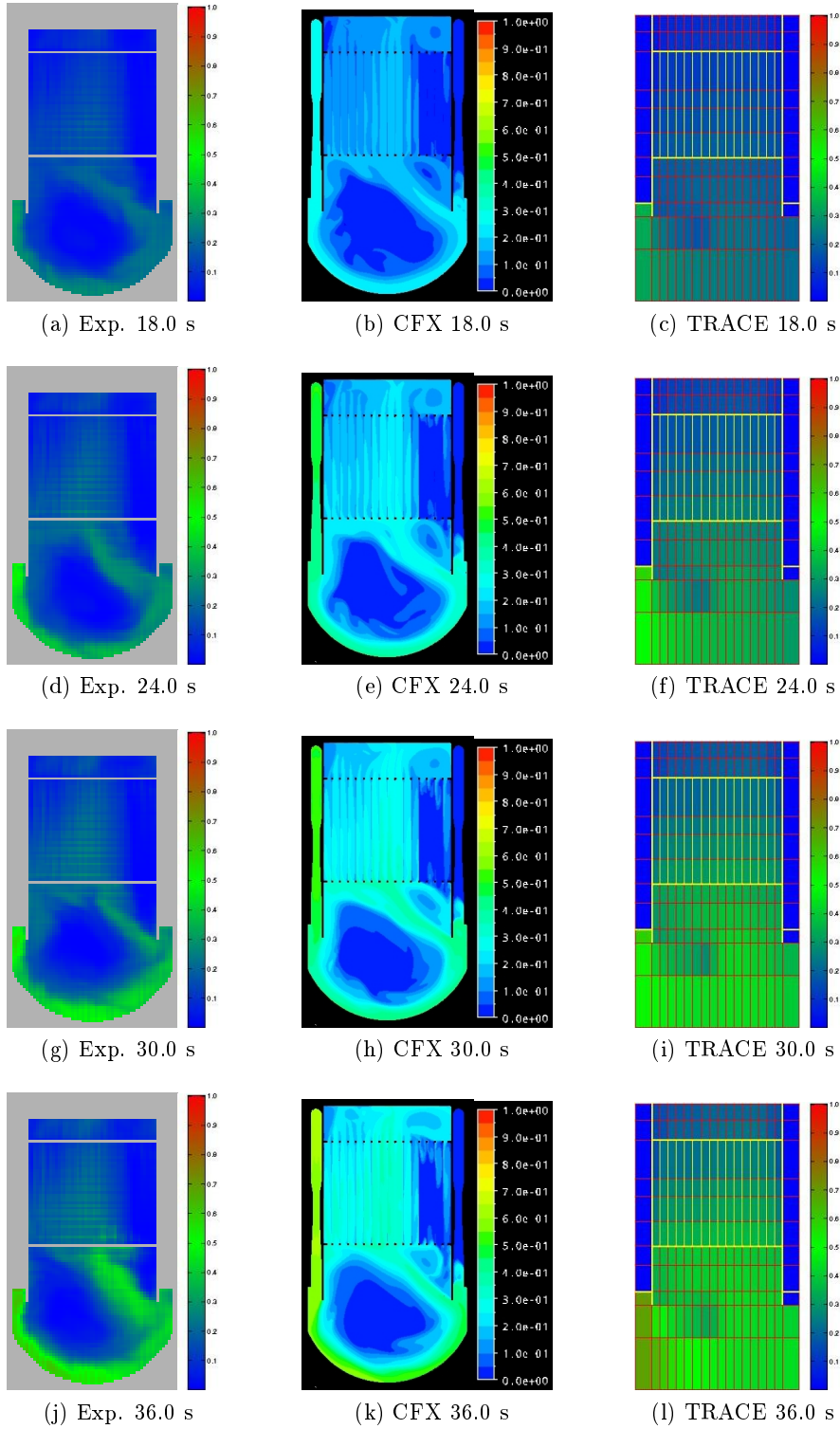
Figure 6.75: Normalized tracer concentration reconstructed from the WM-sensor experimental data for the "pump coast-down" scenario, compared with CFX and TRACE stand-alone simulation results. Snapshots at different times.
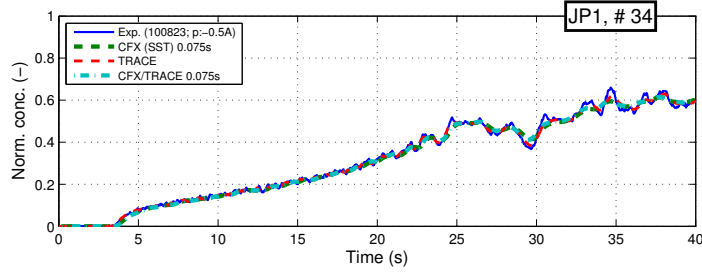
Figure 6.76: Normalized average concentration evolution in JP1 at the WM-sensor row 34 (refer to Fig. 6.9). Comparison between experimental data and results from CFX/TRACE coupled simulations, as well as from CFX and TRACE stand-alone simulations, for the "pump coast-down" scenario.
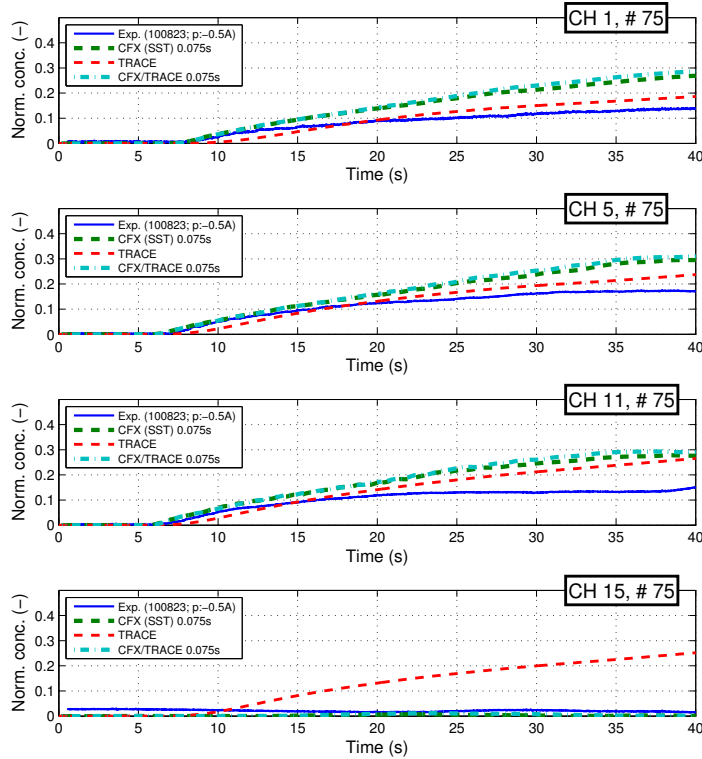
Figure 6.77: Normalized average concentration evolution in the core at the WM-sensor row 75 for the core channels 1, 5, 11 and 15 (refer to Fig. 6.9). Comparison between experimental data and results from CFX/TRACE coupled simulations, as well as from CFX and TRACE stand-alone simulations, for the "pump coast-down" scenario.

simulation.

Finally, Fig. 6.78 shows the pressures computed at the three outlets in the coupled simulation. Although a similar uneven pressure distribution occurs as in the "pump start-up" scenario, there is hardly any discrepancy between CFX and CFX/TRACE in the concentration evolution results shown in Fig. 6.77.
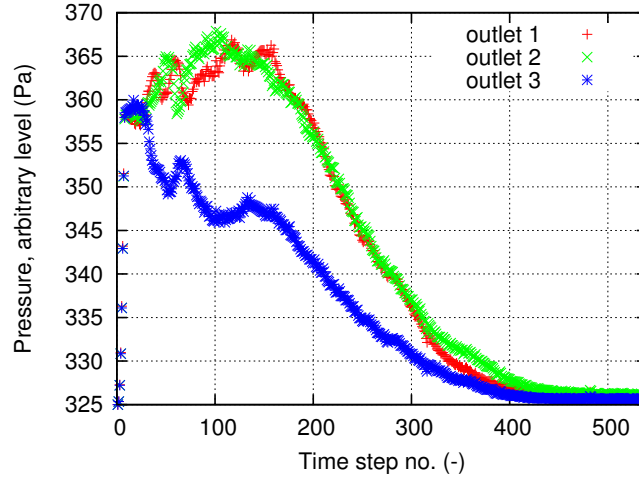
Figure 6.78: Pressure evolution at the three vessel outlets (refer to Fig. 6.9) for the coupled simulation of the "pump coast-down" scenario.

6.5   Chapter summary

Following the setting up and calibration of the data acquisition system, the first qualifying experiments have been carried out for the new FLORIS facility at PSI. The experiments have involved the injection of a controlled quantity of tracer under steady-state and transient flow conditions, and have been used as basis for studying the complex flow field which develops in the lower plenum of the vessel. Analysis of the experiments has first been carried out using stand-alone simulations with TRACE and two independent CFD codes. For the task, a TRACE model of the whole facility (vessel and recirculation loops) and detailed CFD meshes of the vessel were created. An important finding from the stand-alone simulations is that the RANS turbulence models employed in CFD codes still need further improvement and validation, since they were not able to correctly capture the vortices and the related velocity field development in the lower plenum of the FLORIS vessel. The Reynold Stress (RS) model proved to give slightly better results than the SST model, at least for the CFX simulations, but further studies are still needed. Moreover, the complexity of the facility geometry has clearly pointed out the limitations of the 3D modeling capabilities provided by TRACE and the corresponding necessity of employing a coupled tool to capture the flow details in the lower plenum.

Similarly to what was done in the case of the double T-junction experiment (Chap. 4), the CFX/TRACE coupling developed in Chap. 3 has been, for a second time, successfully validated for steady-state conditions, by reproducing the convection of a tracer plug in the vessel and in the recirculation loop of the facility. Clearly, from the viewpoint of the complex geometry, the FLORIS testing has been considerably more stringent. In parallel to the coupled tool validation, the new solute tracking scheme implemented in TRACE (Chap. 5) has been

tested a second time on the new facility, with improved results being obtained, in qualitative agreement with the findings of the previous chapter.

For the first time, the coupling of the momentum equation in CFX/TRACE has been challenged successfully, in that the coupled tool was used for analyzing the two transient tests carried out in FLORIS. In both the "pump start-up" and "pump coast-down" scenarios, the circulation of the tracer under transient flow conditions could be reproduced reasonably well by the coupled tool, thus demonstrating the considerably improved description of the experiments, relative to that possible with the stand-alone codes. More specifically, the two transients analyzed here have clearly brought out the mutual feedbacks between system code and CFD code in the coupled simulations, which cannot be captured by stand-alone simulations. Thanks to this feature, easy-to-measure and more realistic boundary conditions can be defined for the coupled model. This is due to the fact that the automatic feedback between the codes enables the setting up of domain-interface boundary conditions that affect the solving of the momentum equation, i.e. those for the velocity (or mass flow) and the pressure.

Chapter 7

Conclusions and Perspectives

The current doctoral research has been focused on the development and validation of a coupled tool, to combine the advantages of computational fluid dynamics in analyzing complex coolant flows and of state-of-the-art system codes employed for nuclear power plant simulations. As noted already in Chap. 1, such work is very complex and broad-based, and therefore constraints were put on the targeted goals, the modularity of the task being quite helpful in this context. As such, it has been possible to arrive at a working code-set and to proceed to its verification and validation, while focusing on the physical aspects underlying the coupling and on the appropriate interpretation of the results obtained.

This chapter first summarizes the principal findings of the present research (Sec. 7.1). Thereafter, in view of the constraints imposed throughout the development and testing work carried out, as also the new issues encountered, recommendations are made on how the coupled tool could be improved and developed further (Sec. 7.2).

7.1 Main achievements

As explained in Sec. 1.5, the main points of the current research work have been:

1. coupled tool development and verification;

2. validation of the coupled tool through experiments;

3. improvement of the numerical scheme for the TRACE solute tracking equation.

The main findings, under each of the above items, are presented in the following subsections.

7.1.1 Development and verification of the CFX/TRACE coupled tool

Following the state-of-the-art review on coupling methodologies presented in Chap. 2, the coupling between CFX and TRACE was developed as described in Chap. 3. After careful

consideration, the coupling was defined to be on-line, parallel and with non-overlapping domains connected by an interface, which was developed through the PVM software. Moreover, two coupling schemes were tested and implemented: a so-called sequential explicit scheme, in which information is exchanged at the interface once during each time step, and a so-called sequential semi-implicit scheme, in which information is exchanged at the interface several times within the same time step, until a chosen convergence criterion has been satisfied.

The coupled tool was then tested and verified on two chosen transient cases: an open loop configuration and a closed loop configuration. The simulations were conducted on a simple pipe geometry, the aim being to focus on the testing of the code-coupling interfaces and on the numerical stability of the coupling scheme. Parametric studies were carried out in order to test the influence of the chosen integration time step, of the turbulent parameters assigned at the 1D-to-3D coupling interface (i.e. velocity profile and turbulent quantity profiles) and of the coupling scheme employed. From the verification tests, the following conclusions could be drawn:

- While the generic 3D-to-1D interface does not present any problem, since it only requires straightforward averaging procedures, the complementary 1D-to-3D interface introduces new unknowns into the coupled tool. Thus, in order to transform an average scalar value (obtained from the 1D tool) to a 2D distribution (to be used as interface boundary condition for the 3D code), information on the scalar profile over the cross section has to be supplied externally, since the 1D code intrinsically cannot provide this. The degree of influence of the assumed distribution on the results depends on the particular case, because it has been found to be fairly important sometimes (Chaps. 3 and 4), and negligible in other cases (Chap. 6). The results are in fact strongly dependent on the system geometry and on the location of the coupling interface. In any case, this aspect has to be given due consideration, and its importance has to be assessed case by case. Moreover, it has to be noted that different profiles also influence the pressure distribution inside the system.

- The semi-implicit scheme generally has an execution time greater than the explicit scheme, but the results are also influenced by the chosen time step. It was noted in Chap. 3 that, when the same integration time step is used, the semi-implicit scheme yields better accuracy than the explicit scheme. Thus, for a given accuracy, a larger time step can be used with the semi-implicit scheme. However, the better accuracy comes at the cost of a finite number of iterations during the same time step, so that there is clearly a trade-off between time-step iterations and the adoption of larger time steps.

- The explicit scheme is overall more robust, i.e. numerically more stable, than the semi-implicit, but sacrifices a certain precision at the coupling interface to reach that goal.

216

Nevertheless, both schemes require (in certain cases) a pressure-weighting procedure during the interfacial exchange, in order to prevent the pressure at the interface from diverging during the simulation (Chap. 3). This happens because of the way in which the coupling operates, and has also to be evaluated case by case.

7.1.2 Validation of the coupled tool

After the verification, the newly developed coupled tool was validated against experimental data from two different facilities. These installations were designed and built at PSI in the Laboratory for Thermalhydraulics (LTH). They have been instrumented with wire-mesh sensors, aimed at measuring the conductivity of a tracer injected into the flow. The tracer concentration data, recorded during appropriately designed tests, have been used for comparison against simulation results.

The first facility (Chap. 4) has featured a double T-junction component with two branches connected by a recirculation loop. The aim of this mixing experiment was to challenge the coupled tool with the transport of a tracer in a stationary flow field and to show the improvements that such a tool can bring over the stand-alone use of system codes when three-dimensional flow effects play an important role, all this while keeping the geometry as simple as possible, so as to have controlled boundary conditions and reduced computational time. To achieve these objectives, experimental data were compared to CFX and TRACE stand-alone simulations, as well as to CFX/TRACE coupled simulations. The following conclusions could be drawn from this first phase of experimental validation:

- The coupled tool provides an improvement over the TRACE stand-alone simulations, thanks to the capability of CFD to accurately model single-phase, three-dimensional flow fields within relatively simple geometries, like a T-junction.

- The effect of the velocity profile, imposed at the coupling interface, can be quite significant on the results of the CFD simulations. In the case of the double T-junction set-up, for example, the location where the tracer is injected is relatively close to one of the T-junction locations. The experiment was designed such as to achieve a fully developed turbulent velocity profile at this location. However, if a flat velocity profile were imposed at the coupling interface, corresponding to the location of the tracer injection, this velocity profile would have no time to develop before the tracer plug reaches the T-junction zone. As a consequence, the resulting velocity field across the junction would differ from the experimental one, leading to a different tracer distribution in the double T-junction component, and thus to a disagreement in the prediction of the tracer splitting between the main and recirculation loops.

- The TRACE simulations pointed out that the solute tracking equation employed in the system code suffers from considerable numerical diffusion. This issue has been addressed

and resolved in Chap. 5, with the implementation of the QUICKEST-ULTIMATE discretization scheme in TRACE, and considerably improved results were obtained for the double T-junction experiment by employing the new TRACE version in conjunction with the coupled tool.

The second facility, FLORIS (Chap. 6), has featured a scaled-down, simplified, two-dimensional vertical slice of a LWR vessel. The goals of this second mixing experiment have been, on the one hand, to challenge the coupling of the momentum equation by considering the transport of a tracer in a transient flow field, and, on the other hand, to test the challenges that a more complex geometry can pose to the coupled tool and to CFD codes in general. To achieve these goals, experimental data were compared to CFD and TRACE stand-alone simulations, as well as to CFX/TRACE coupled simulations. The key results from these tests have shown the following:

- The coupled tool is able to follow transients in complex geometries and provides considerable improvement over TRACE stand-alone simulations.

- In transient simulations, the feedback between system code and CFD code is appreciable in the coupled tool, and can lead to improved results if the modeling of the boundary conditions is properly done. The ability of the coupled tool to model the complete system makes the definition of more realistic boundary conditions possible for the CFD domain, leaving to the code the task of setting the proper interfacial conditions (fluid pressure and velocity) according to the solution of the momentum equation.

- Although the coupled tool provides a clear extension of the system code capabilities, thanks to the ability of CFD to model three-dimensional components with higher accuracy, the comparison with FLORIS experimental data has nevertheless pointed out certain deficiencies of RANS turbulent models when treating complex geometries. In particular, the difficulty in modeling the flow field in the lower plenum of the RPV mock-up in FLORIS has pointed out the need for improving the turbulence model for treating flows with high curvature and boundary layer detachment.

7.1.3 Implementation of the QUICKEST discretization in TRACE

As mentioned, following the identification of the numerical diffusion issue in TRACE simulations in Chap. 4, a new numerical scheme for the solute tracking equation was introduced into the system code. The QUICKEST scheme, together with the ULTIMATE limiter, developed in the past by Leonard [68, 69, 70] and successfully implemented by Macian [71, 72, 73, 74] in RELAP, was found to represent the appropriate strategy. In the present context, the third-order, upwind, explicit scheme was adapted to the system code's finite-volume scheme and implemented into TRACE for 1D components, the following being the specific considerations made:

- The QUICKEST-ULTIMATE scheme was extended in order to be able to treat an arbitrary number of side junctions.

- The diffusion term, absent in the TRACE solute tracking equation, was modeled and implemented into the new scheme.

After the development and the implementation, the new numerical scheme was successfully verified on simple geometrical configurations and successfully validated against experimental data from the double T-junction and from one of the tests at the German large-scale PKL facility. The following conclusions could be drawn:

- The new numerical scheme considerably reduces the numerical diffusion that was affecting the original scheme employed in the TRACE solute tracker.

- A drawback of the new scheme is the significant increase of the execution time, resulting from the necessity to respect the Courant limit of $C \leq 1$ (while the original numerical scheme in TRACE can converge with $C > 1$).

- The employment of the new scheme, with strongly reduced numerical diffusion, has pointed out the need for modeling turbulent mixing by adding a diffusion term in the transport equation, in order to correctly reproduce experimental results.

7.2 Recommendations for future work

7.2.1 Improvements and possible extensions of the coupled tool

As expressed earlier, several constraints have had to be applied to the development of the coupled tool; moreover, a few new issues were encountered during the verification and validation phases. The modularity of the code-set, however, allows one to add new features during a second phase of development, thereby extending the tool's capabilities, as well as addressing the issues discovered in this work. A partial list of possible new features to be added is presented below:

- With the coupled tool's capability to transfer a scalar value (e.g. a tracer concentration) at the coupling interface already implemented, it should be a relatively easy and straightforward task to implement also the exchange of density and temperature at the same interface. This will open up the possibility to simulate NPP transients closer to actual plant conditions.

- For the same reason as stated in the previous item, the extension of CFX/TRACE to two-phase flows could be envisaged. However, at the 1D-to-3D interface, new challenges arise from the definition of suitable flow quantity profiles in the case of two-phase flows.

For example, each different flow regime would result in a different (statistical) distribution of the void fraction over the coupling interface, which in turn will strongly influence the CFD computation (optimal meshing, solver model used, profiles of the velocity and of the turbulence quantities, etc.). This will require a deeper analysis of the issues involved, and the topic could span over another entire Ph.D. dissertation. However, with the capability to simulate two-phase flow conditions, it will become possible to study most of the accidental transients relevant to LWRs, within the limitations of CFD in modeling multi-phase flows (as discussed in Subsec. 2.2.2).

- New coupling schemes could be implemented, and more robust stabilization techniques could be developed. Furthermore, parallelization of the coupled tool could bring a favorable speed-up in the coupled computations. From some preliminary studies, it has been seen that there could be some interference between the coupling environment and the parallelization environment, and this should be taken into account, studied and, eventually, resolved. It may also be that code modifications have to be made to account for the fact that, in the case of parallel computations, the coupling interfaces are spread over different sub-meshes and not grouped into a single mesh.

- During complex transients, it may happen that the flow through the coupling interface is reversed. The coupled tool has been developed, in principle, to deal with such a condition, but never properly tested in this context. This could be an issue needing further work. Moreover, flow reversal at a coupling interface also affects the velocity profile at the given location, and further studies will be needed concerning the type of profile which is most suitable in a particular situation.

- More advanced work on the correct introduction of velocity and turbulent-quantity profiles at the coupling interfaces could consist in the development of a macroscopic two-equations turbulence model. A recent publication proposes a porous medium approach for averaging the turbulence equations of the $\kappa - \varepsilon$ model over the cell volume and the employment of special closure models to define the corresponding source terms [96]. A proper modeling of sources and sinks in the various components of the system could be carried out with the aid of *ad-hoc* experiments and local CFD computations. This topic could also span over another Ph.D. dissertation.

- The main motivation for the present research has clearly been the future application of the coupled tool to LWR transient analyses. However, a quite straightforward extension of the coupling would be to enable its application to Generation IV liquid metal/salt reactors as well. In this case, the flow is generally single phase and the present coupling can be directly employed. However, the correct fluid properties have to be implemented into both codes. In the case of TRACE, this is already the case for sodium, the FAST project team at PSI, for example, having analyzed the Sodium-cooled Fast Reactor

(SFR) using this code (see, for example, [97]). If sodium properties are implemented into CFX, this could indeed lead to a very useful extension of the coupled tool's capabilities to analyze NPP transients with complex flows.

7.2.2 Further validation of the coupled tool

With reference to the double T-junction experiment, more simulations could be carried out regarding:

- the effects of varying the mass flow ratio between main loop and side loop;

- the effects of employing more accurate turbulence models, i.e. RS-based models instead of RANS models;

- the effects of adding appropriate turbulent-quantity profiles at the coupling interface.

In the context of FLORIS, several improvements of the facility are recommended before carrying out further tests:

- The metallic jet pumps should be replaced with Plexiglas parts, to reduce the interference with the wire-mesh sensor.

- The inlets and outlets of the vessel should also be instrumented with wire-mesh sensors, to improve the data for the boundary conditions to be applied in the simulations.

- The vessel inlets and outlets should be instrumented with pressure indicators, to enhance the scope of the experimental database generated.

Thereafter, for the analysis part, the complex flow field developing inside the lower plenum of FLORIS could be used to:

- test more systematically the RS model;

- benchmark and improve the modeling of turbulence.

7.2.3 First applications to NPP transients with reactivity feedback

The coupled tool could be applied, with few modifications, to simulate a safety-relevant transient of a PWR, like a MSLB or a boron-dilution scenario, both of which were described in Chap. 1. As illustrated in the conceptual scheme of the coupling (see Fig. 1.5), it will be necessary, for such a simulation, to couple the outlet of a CFX RPV model to the inlet of a TRACE core model, so as to enable neutron kinetic computations to be carried out with the system code. For the latter, two possibilities arise: one is to employ simple point kinetics, as directly available within TRACE; the other is to opt for a full 3D-kinetics computation using a time dependent, nodal diffusion code such as PARCS or SIMULATE-3K, both of which

are available in TRACE-coupled form at PSI [98, 99]. With either a point kinetics or a 3D-kinetics representation of the neutronics, the CFX/TRACE configuration has the advantage, with respect to a stand-alone system-code computation, that a more detailed coolant flow distribution can be modeled at the core channel inlets. The resulting improved temperature distribution (in the case of a MSLB simulation), or the improved boron concentration (in the case of a boron dilution scenario), would lead to a more accurate representation of the corresponding reactivity feedback effects occurring in the core, and hence to an improved prediction of the reactor power evolution.

Clearly, in order to fully achieve the needed coupling, the coupled tool has to be modified such that it can account for temperature and density variations (as explained in Subsec. 7.2.1), since these occur in the aforementioned transients and, particularly in the case of the MSLB, have to be considered explicitly. However, in a first phase, without carrying out these modifications to the coupled tool, one could simulate a hypothetical boron-dilution scenario under isothermal coolant conditions, for example due to a malfunction in the CVCS. As a matter of fact, in such a case, the fluid at the RPV inlet nozzle and at the core inlet, where the coupling interfaces are located, is about at the same temperature, and thus fluid properties can be assumed to be constant.

In considering such a hypothetical scenario, a low-concentration boron plug could be injected into one of the cold legs and its transport in the downcomer and lower plenum could be analyzed with CFX and, through the coupled tool, the resulting inlet core concentration, pressure and velocity distributions could be imposed on TRACE as boundary conditions for the neutronics/TH computation.

Regarding the coupling interfaces, the outlet of the RPV lower plenum should be divided into as many sections as the core channels, so that the corresponding one-to-one coupling can be achieved employing the already developed user interface of the coupled tool.

This application will strongly challenge the newly-developed computational tool and will demonstrate its capability to yield, for such transients, improved quality results relative to stand-alone system code computations.

7.2.4 Improvements to the TRACE solute tracking equation

As described in Sec. 7.1, the QUICKEST-ULTIMATE scheme was implemented into the TRACE solute tracking equation, but with some constraints and limitations. This leaves open further improvements which can be made to the code:

- A better integration with the TRACE models that affect the solute concentration inside a cell, e.g. level tracking, stratified flow, etc. In fact, QUICKEST is currently not able to cope with these models, since its development has been based on a (multiphase) homogeneous model of the flow, and therefore a detailed, case-by-case modeling of such phenomena is required.

- The extension to three-dimensional components. This can be achieved by extending the QUICKEST scheme to multi-dimensional geometries (as has been done in other applications of the scheme), or by suitably adapting the current one-dimensional version to the "vessel" component of TRACE.

- Studies on possible diffusion coefficients which could be used for modeling the "physical" diffusion, i.e. the effects of the turbulent mixing, in 1D components. One starting point could be the cited Levenspiel coefficient, but there is a large number of correlations in the open literature based on more accurate physical modeling and on flow parameters, such as the fluid velocity. It should be noted that turbulent mixing depends not only on the velocity but also on the vortex structure, and hence on the complexity of the geometry. Thus, while it may be acceptable to model specific geometries, like 1D pipes, with a diffusion coefficient, the extension of such a concept to complex 3D components may not be straightforward or even possible. In that case, it could be worthwhile to implement a macroscopic turbulent model, as mentioned previously.

Appendix A

Courant-Friedrichs-Lewy stability condition

The Courant-Friedrichs-Lewy condition was discussed by the three authors in a historically relevant paper on the stability and convergence of numerical schemes [77]. This condition is a requirement for the stability of explicit schemes and defines the following limitation of the so-called Courant number:

$$C = \frac{u\Delta t}{\Delta x} \leq 1$$

The above limitation can be seen as a limitation on the speed of propagation u (considered positive here) of the exact solution, which has to be lower or equal to the "speed" of propagation $\frac{\Delta x}{\Delta t}$ of the numerical scheme.

The explanation behind this can be easily seen from the simple problem:

$$PDE \quad \varphi_t + u\varphi_x = 0$$
$$IC \quad \varphi(x,0) = f(x)$$

with exact solution (see App. F for more details):

$$\varphi = f(x - ut)$$

and with discretized solution (explicit upwind scheme)

$$\varphi_{i,n+1} = (1 - C)\varphi_{i,n} + C\varphi_{i-1,n}$$

Clearly, the discretized solution $\varphi_{i,n}$ depends on the values of $f(x)$ at $x_{i-n}, ..., x_i$, while the exact solution is $\varphi(x_i, t_n) = f(x_i - ut_n)$. To avoid the use of less information for the numerical solution than is used for the exact solution, we have to satisfy the condition:

$$x_{i-n} \leq x_i - ut_n$$
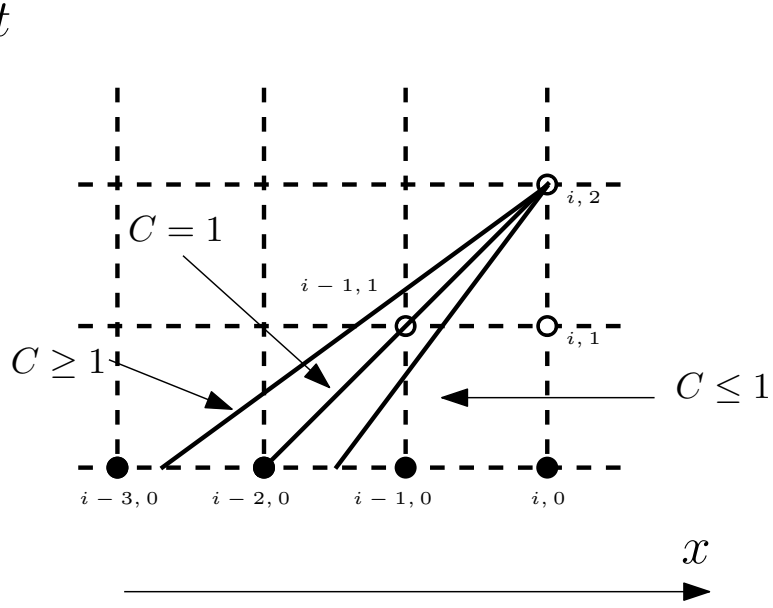
Figure A.1: Illustrated example of the CFL condition.

which translates into (refer to Fig. A.1):

$$(i - n)\,\Delta x \leq i\Delta x - un\Delta t$$

and through simple arithmetical transformation becomes the well known condition $C \leq 1$.

Appendix B

List of the computers used for the simulations

At the Paul Scherrer Institute, three groups of Linux clusters (lccfd, lclrs and lchpc) have been available for computations. In this appendix, a short table of the technical specifications of the machines employed is presented as reference (Tab. B.1).

Machine	CPUs No.	CPU model	Clock [MHz]	Cache [KB]
lccfd01	4	Intel(R) Xeon(R) CPU 5160	3000	4096
lccfd03	4	Intel(R) Xeon(R) CPU 5160	3000	4096
lccfd05	8	Intel(R) Xeon(R) CPU E5450	3000	6144
lccfd07	8	Intel(R) Xeon(R) CPU E5450	3000	6144
lclrs11	4	Dual Core AMD Opteron(tm) Processor 280	2394	1024
lclrs12	4	Dual Core AMD Opteron(tm) Processor 280	2394	1024
lclrs13	4	Dual Core AMD Opteron(tm) Processor 280	2394	1024
lclrs14	4	Dual Core AMD Opteron(tm) Processor 280	2394	1024
lclrs21	8	Intel(R) Xeon(R) CPU E5450	3000	6144
lclrs22	8	Intel(R) Xeon(R) CPU E5450	3000	6144
lclrs31	8	Intel(R) Xeon(R) CPU E5540	2533	8192
lclrs32	8	Intel(R) Xeon(R) CPU E5540	2533	8192
lchpc10	8	Intel(R) Xeon(R) CPU E5540	2533	8192
lchpc11	8	Intel(R) Xeon(R) CPU E5540	2533	8192

Table B.1: Technical specifications of the machines available for the computations.

Appendix C

Numerical diffusion issues

First-order upwind numerical schemes are widely used in system codes because of their simplicity and robustness, the latter aspect being important in order to obtain a stable solution from the system of conservation equations. Unfortunately, such schemes are also affected by numerical errors which are of diffusive character, i.e. the schemes mimic the diffusion term of the convection equations, effectively introducing so-called numerical diffusion into the solution of the problem.

This can be seen through the truncation error analysis of the convection equation [100]. Consider, for the sake of simplicity, the one-dimensional advection equation of a generic function $f(x, t)$, with positive constant velocity u:

$$f_t + u f_x = 0 \tag{C.1}$$

Discretizing Eq. (C.1) using the finite difference method, with explicit advancement in time and first-order upwind for the advective part, the equation becomes:

$$\frac{f_i^{n+1} - f_i^n}{\Delta t} + u \frac{f_i^n - f_{i-1}^n}{\Delta x} = 0 \tag{C.2}$$

where $f_i^n = f(x_i, t_n)$.

Let us define now the following Taylor series expansion:

$$f_{i\pm1}^n = f_i^n \pm \Delta x f_x + \frac{(\Delta x)^2}{2} f_{xx} + O\left[(\Delta x)^3\right]$$

$$f_i^{n+1} = f_i^n + \Delta t f_t + \frac{(\Delta t)^2}{2} f_{tt} + O\left[(\Delta t)^3\right]$$

Now substitute the Taylor series expansions of $f_{i\pm1}^n$ and f_i^{n+1} inside Eq. (C.2). The following

equation results (after some simplifications):

$$f_t + u f_x = -\frac{\Delta t}{2} f_{tt} + \frac{u \Delta x}{2} f_{xx} + O\left[(\Delta x)^2, (\Delta t)^2\right] \tag{C.3}$$

Notice that the LHS of the equation is the convection equation, while the RHS is the error associated with the discretization (which is zero in the exact equation). In order to replace f_{tt} with a spatial derivative term, we differentiate Eq. (C.3) both in time and space, combining the results with the following operation:

$$\bullet_t \ominus u \bullet_x$$

where the dot replaces Eq. (C.3). The result is:

$$f_{tt} + u f_{xt} - u f_{tx} - u^2 f_{xx} = -\frac{\Delta t}{2} f_{ttt} + \frac{u \Delta x}{2} f_{xxt} + \frac{u \Delta t}{2} f_{ttx} - \frac{u^2 \Delta x}{2} f_{xxx} + O\left[(\Delta x)^2, (\Delta t)^2\right]$$

$$f_{tt} = u^2 f_{xx} + O\left(\Delta x, \Delta t\right) \tag{C.4}$$

Substituting now Eq. (C.4) inside Eq. (C.3), it is possible to quantify the error due to the explicit first-order upwind discretization:

$$f_t + u f_x = \frac{1}{2}\left(u \Delta x - u^2 \Delta t\right) f_{xx} + O\left[(\Delta x)^2, (\Delta t)^2, \Delta x \Delta t\right] \tag{C.5}$$

In case of implicit first-order upwind discretization, the error can be computed in the same way and results in:

$$f_t + u f_x = \frac{1}{2}\left(u \Delta x + u^2 \Delta t\right) f_{xx} + O\left[(\Delta x)^2, (\Delta t)^2, \Delta x \Delta t\right] \tag{C.6}$$

From Eq. (C.5) and Eq. (C.6) we can draw several important conclusions:

- The LHS of Eq. (C.5) and Eq. (C.6) is identical to the LHS of Eq. (C.1), while the dominant part of the error (on the RHS) is proportional to f_{xx}, with a coefficient that depends on the time step Δt and on the grid size Δx. Consequently, its behavior is equivalent to that of a diffusion term. Thus, the approximated solution that will be obtained is not that of a pure advection equation, but rather that of a convection equation with a diffusion term whose coefficient is proportional to $\left(u \Delta x \pm u^2 \Delta t\right)$ and therefore dependent on the spatial and temporal discretization adopted. This is why it is referred to as "numerical" diffusion.

- For explicit discretization, the two terms of the numerical diffusion coefficient are competing against each other, so that for particular values of Δx and Δt the error may cancel (or be very low), while for some other the coefficient can be negative. In the latter case, one has the destabilizing effect of a negative diffusion (which is of course

unphysical). For implicit discretization, the two terms sum up with each other, and the destabilizing effect cannot take place; on the other hand, the error can be made smaller only by decreasing the temporal and spatial mesh size.

- Rewriting the error as $u\Delta x \left(1 \pm C\right)$ (where $C = u\Delta t/\Delta x$ is the Courant number), for the explicit case we found the well-known Courant number limitation $C \leq 1$, which has to be respected to avoid a negative numerical diffusion coefficient. The case $C = 1$ is the ideal case where the diffusive error is zero (cell-center to cell-center convection), but such a case is very difficult to obtain in realistic simulations, where the parameters are difficult to control.

As a conclusive remark on numerical diffusion, it is clear that the grid size Δx and the time step Δt play an important role in the magnitude of the artificial diffusion coefficient. In principle, one can adjust these two parameters such as to reduce the numerical diffusion to an acceptable level. In practical problems, however, refinement to an adequate level can be difficult to achieve, not only because of memory consumption and computational time (especially in the case of multidimensional flows [101]), but also because of nonuniformities of the velocity field along the one-dimensional flow path of the thermal-hydraulic model. This is why research is still being carried out on the development of high-order numerical schemes which would allow one to overcome the shortcomings of first-order formulations. A wide variety of improved methods are currently available in the literature. Unfortunately, new problems have to be faced when moving to higher order discretizations, e.g. nonphysical oscillations in the presence of sharp gradients.

Appendix D

Plated-out solute and maximum solute concentration in water

According to [8], solute does not affect hydrodynamics directly. However, the amount of dissolved and plated-out orthoboric acid in the reactor core may affect the hydrodynamics indirectly through the neutronic reactivity feedback caused by the neutronic poison itself.

In TRACE, a simplified model is adopted: if the solute concentration exceeds the orthoboric acid solubility at the liquid temperature in a hydrodynamic cell, TRACE assumes that the excess solute plates out instantly; in the same way, TRACE assumes that the plated-out solute redissolves instantaneously to the maximum allowable concentration if more liquid enters the cell.

D.1   Implementation of the solubility limit

The procedure adopted in the original TRACE code (and in the new version as well) is the following:

1. Inside each cell, the maximum allowed quantity of dissolved solute ϕ_{max} is evaluated as a function of the cell temperature (Sec. D.2).

2. The highest quantity possible of dissolved solute at the end of a time step is the sum of the result of the solute transport equation ϕ^{n+1} and the available mass of plated solute per volume of liquid ϕ_p^n. The final end-of-time-step value of the scalar $\hat{\phi}$ must be the smaller between this limit and the maximum evaluated at point 1.

$$\hat{\phi}^{n+1} = \min\left(\phi^{n+1} + \phi_p^n, \phi_{max}\right)$$

3. As the last step, the remaining inventory of plated-out solute is computed

$$\phi_p^{n+1} = \left(\phi^{n+1} + \phi_p^n\right) - \hat{\phi}^{n+1}$$

D.2 Evaluation of the solubility limit

The maximum allowed quantity of dissolved solute in a cell is a function of the cell temperature; the TRACE default model is a linear function of the temperature, with a minimum and a maximum value of the dissolved concentration.

$$c_{max} = \begin{cases} c_{max} & \text{if} & T \geq T_{sup} \\ c_{min} + \dfrac{c_{max} - c_{min}}{T_{sup} - T_{inf}} \cdot T & \text{if} & T_{inf} \leq T \leq T_{sup} \\ c_{min} & \text{if} & T < T_{inf} \end{cases}$$

and

$$\phi_{max} = (1 - \alpha)\, c_{max} \rho_l$$

The values adopted in TRACE are $T_{sup} = 373$ K, $T_{inf} = 303$ K, $c_{max} = 0.276$ kg$_s$/kg$_l$, $c_{min} = 0.0635$ kg$_s$/kg$_l$.

Appendix E

Upwind discretization for the solute transport equation

For the implementation of the QUICKEST scheme in the code TRACE, some complications arise inside the cells containing side junctions, since the model then departs from the one-dimensional case. Nevertheless, it is possible to consider multiple side junctions per cell while using the one-dimensional QUICKEST scheme by specifying different flow-dependent cases (as shown in Subsec. 5.4.7). However, in certain configurations (for example, total inflow/outflow at the junction cell), the complexity of this special treatment is such that it is desirable to use a local first-order upwind discretization scheme.

Starting from the pure advection equation (the diffusion will be neglected):

$$\underbrace{\frac{\partial \phi\left(\mathbf{x}, t\right)}{\partial t}}_{\text{accumulation term}} = -\underbrace{\boldsymbol{\nabla} \cdot \left(\phi\left(\mathbf{x}, t\right) \mathbf{u}\left(\mathbf{x}, t\right)\right)}_{\text{advection term}}$$

the discretization with the finite volume technique leads to:

$$\int_{\Delta \tau} \int_{\Omega} \phi_t d\Omega d\tau = -\int_{\Delta \tau} \int_{\sigma} \phi \mathbf{u} \cdot \hat{\mathbf{n}} d\sigma d\tau$$

Each term will now be separately analyzed.

E.1   Accumulation term

First the time integration has to be carried out. It is easy to see that:

$$\int_{\Delta t} \phi_t d\tau = \int_{t_n}^{t_{n+1}} \phi_t d\tau = \int_{\phi^n}^{\phi^{n+1}} d\phi = \phi^{n+1} - \phi^n$$

Regarding the volume integration over a cell, the average area A_i of the cell is used:

$$\int_{V_i} \left(\phi^{n+1} - \phi^n\right) dV = A_i \int_{-\frac{\Delta x_i}{2}}^{\frac{\Delta x_i}{2}} \phi^{n+1} dx - A_i \int_{-\frac{\Delta x_i}{2}}^{\frac{\Delta x_i}{2}} \phi^n dx$$

Expanding ϕ in a Taylor series truncated at the first order, the result is:

$$\int_{V_i} \left(\phi^{n+1} - \phi^n\right) dV = A_i \Delta x_i \left(\phi_i^{n+1} - \phi_i^n\right) = V_i \left(\phi_i^{n+1} - \phi_i^n\right)$$

E.2   Advection term

In this case, the first integral to be solved is the surface integral. In the 1D, case the values of ϕ and u are constant on each "surface" (because the surface is reduced to one single point) and therefore their area-averaged values are equal to the values at that point; the result is the following:

$$-\int_\sigma \phi\mathbf{u} \cdot \hat{\mathbf{n}} d\sigma \rightarrow \int_{\sigma_{i-1/2}} \phi u d\sigma - \int_{\sigma_{i+1/2}} \phi u d\sigma - \sum_{k=1}^K \left(\int_{\sigma_{j-1/2}} \phi u d\sigma\right)_{mk} =$$

$$= [A\phi u]_{i-1/2} - [A\phi u]_{i+1/2} - \sum_{k=1}^K [A\phi u]_{j-1/2,k}$$

Integrating in time using a procedure similar to that described in Subsec. 5.4.4 and truncating the series expansion of ϕ at the zeroth order, the result is:

$$[A\phi u]_{i-1/2} - [A\phi u]_{i+1/2} - \sum_{k=1}^K [A\phi u]_{j-1/2,k} =$$

$$\cong \left(A_{i-1/2}\tilde{u}_{i-1/2}\phi_{i-1/2}^n - A_{i+1/2}\tilde{u}_{i+1/2}\phi_{i+1/2}^n - \sum_{k=1}^K \left[A_{j-1/2}\tilde{u}_{j-1/2}\phi_{j-1/2}^n\right]_k\right) \Delta t$$

In the upwind scheme, the value of ϕ on the cell border depends on the velocity direction on that border; in particular, the value of ϕ on the border is taken equal to the value of ϕ at the center of the upwind cell.

$$\phi_{i-1/2}^n = \begin{cases} \phi_{i-1}^n & \text{if} \quad \tilde{u}_{i-1/2}^n \geq 0 \\ \phi_i^n & \text{if} \quad \tilde{u}_{i-1/2}^n < 0 \end{cases}$$

$$\phi_{i+1/2}^n = \begin{cases} \phi_i^n & \text{if} \quad \tilde{u}_{i+1/2}^n \geq 0 \\ \phi_{i+1}^n & \text{if} \quad \tilde{u}_{i+1/2}^n < 0 \end{cases}$$

$$\phi_{j-1/2,k}^n = \begin{cases} \phi_i^n & \text{if} \quad \tilde{u}_{j-1/2}^n \geq 0 \\ \phi_{j,k}^n & \text{if} \quad \tilde{u}_{j-1/2,k}^n < 0 \end{cases}$$

E.3   Final result

Putting together the contribution from both the accumulation and the advection terms and remembering the definition of the Courant number and of the special Courant number, the final result is:

$$\phi_i^{n+1} = \phi_i^n + \tilde{C}_{i-1/2}^i \phi_{i-1/2}^n - \tilde{C}_{i+1/2}^i \phi_{i+1/2}^n - \sum_{k=1}^{K} \tilde{C}_{j-1/2,k}^i \phi_{j-1/2,k}^n$$

Appendix F

First-order PDE solution with the method of characteristics

F.1   Generic problem

Consider the following Initial Value Problem (IVP):

$$PDE \quad a\left(x,t\right)u_x + b\left(x,t\right)u_t + c\left(x,t\right)u = g(x,t) \quad -\infty < x < \infty \quad 0 < t < \infty \quad \text{(F.1)}$$

$$IC \qquad\qquad\qquad u\left(x,0\right) = f\left(x\right) \quad -\infty < x < \infty$$

The solution to this linear first-order equation is based on a physical fact, i.e. that an initial disturbance at some point x propagates along a curve (called characteristic) in the tx-plane.

The idea is to introduce two new coordinates s and τ (to replace x and t) that have the following properties:

- s will change along the characteristic curves

- τ will change along the initial curve (usually the line $t = 0$)

Consider now the new coordinate s; we can represent the characteristics as a function of this parameter, i.e. $x = x\left(s\right)$ and $t = t\left(s\right)$. Then

$$\frac{du\left(x\left(s,\tau\right),t\left(s,\tau\right)\right)}{ds} = u_x\frac{dx}{ds} + u_t\frac{dt}{ds} \tag{F.2}$$

where the derivative is not anymore partial since τ is constant along each one of the characteristics. Comparing Eq. (F.2) with Eq. (F.1), it is easy to see that

$$\frac{dx}{ds} = a\left(x,t\right) \tag{F.3}$$

$$\frac{dt}{ds} = b\left(x,t\right) \tag{F.4}$$

and therefore Eq. (F.1) becomes an ODE in s

$$ODE \qquad \frac{du}{ds} + c(s, \tau)u = g(s, \tau) \qquad\qquad 0 < s < \infty \qquad\qquad \text{(F.5)}$$

$$IC \qquad\qquad u(0) = f(\tau)$$

Therefore, the problem consists in solving, instead of a PDE, three ODEs. With the first one, Eq. (F.5), the solution $u(s, \tau)$ is found. By solving Eqs. (F.3) and (F.4), it is possible to obtain the transformations to return to the tx-plane solution $u(x, t)$

$$x = x(s, \tau)$$

$$t = t(s, \tau)$$

where the constants of integration can be found remembering that $x(s = 0) = \tau$ and $t(s = 0) = 0$.

F.2   Example

In this example the equation of Subsec. 5.6.1 will be solved:

$$PDE \quad \varphi_t + u\varphi_x = 0$$
$$IC \quad \varphi(x, 0) = f(x)$$

The coefficients are $a = u$, $b = 1$, $c = 0$, $g = 0$. Therefore, the three ODEs to be solved are

$$\frac{du}{ds} = 0 \to u = k_0$$

$$\frac{dx}{ds} = u \to x = us + k_1$$

$$\frac{dt}{ds} = 1 \to t = s + k_2$$

Applying the boundary conditions:

$$u(0) = f(\tau) \to k_0 = f(\tau) \to u = f(\tau)$$

$$x(0) = \tau \to k_1 = \tau \to x = us + \tau$$

$$t(0) = 0 \to k_2 = 0 \to t = s$$

the final solution is:

$$\tau = x - ut \to \varphi = f(x - ut)$$

Appendix G

Solution of the advection-diffusion equation

G.1 Generic problem

Consider the following Initial Value Problem (IVP) for the function $\varphi(x,t)$:

$$PDE \qquad \varphi_t = D\varphi_{xx} - u\varphi_x \qquad -\infty < x < \infty \qquad 0 < t < \infty \qquad (G.1)$$
$$IC \qquad \varphi(x,0) = f(x) \qquad -\infty < x < \infty$$

The coefficients D and u are constant. The solution to this equation can be found as described in the following steps.

Change of coordinates

A new set of coordinates ξ and τ is defined:

$$\xi = x - ut \qquad (G.2)$$

$$\xi_x = 1 \qquad (G.3)$$

$$\xi_t = -u \qquad (G.4)$$

$$\tau = t \qquad (G.5)$$

$$\tau_x = 0 \qquad (G.6)$$

$$\tau_t = 1 \qquad (G.7)$$

The derivatives in Eq. (G.12) can be rewritten in terms of the newly defined variables using the chain rule:

$$\varphi_t = \varphi_\xi \xi_t + \varphi_\tau \tau_t = -u\varphi_\xi + \varphi_\tau \qquad (G.8)$$

241

$$\varphi_x = \varphi_\xi \xi_x + \varphi_\tau \tau_x = \varphi_\xi \tag{G.9}$$

$$\varphi_{xx} = (\varphi_x)_x = (\varphi_\xi)_x = \varphi_{\xi\xi}\xi_x + \varphi_{\xi\tau}\tau_x = \varphi_{\xi\xi} \tag{G.10}$$

and substituted into the equation:

$$\cancel{-u\varphi_\xi} + \varphi_\tau = D\varphi_{\xi\xi}\cancel{-u\varphi_\xi}$$

Finally, Eq. (G.12) becomes:

$$
\begin{array}{cclcc}
PDE & \varphi_\tau = D\varphi_{\xi\xi} & -\infty < \xi < \infty & 0 < \tau < \infty & \text{(G.11)} \\
IC & \varphi(\xi, 0) = f(\xi) & -\infty < \xi < \infty &
\end{array}
$$

Notice that the advection term has been removed with the change of variables, and that the IC remains the same in the new coordinate system, since $\xi = x$ if $t = 0$.

Fourier transform conversion and solution of the new problem

Now, let us apply the Fourier transform to Eq. (G.12):

$$\mathcal{F}[\varphi_\tau] = D\mathcal{F}[\varphi_{\xi\xi}]$$

$$\mathcal{F}[\varphi(\xi, 0)] = \mathcal{F}[f(\xi)]$$

In this way, the PDE becomes an ODE and the new IVP is:

$$
\begin{array}{cccc}
ODE & \Phi_\tau = -D\omega^2\Phi & 0 < \tau < \infty & \text{(G.12)} \\
IC & \Phi(0) = F(\omega) &
\end{array}
$$

and the solution of Eq. (G.12) is:

$$\Phi(\tau) = F(\omega)e^{-D\omega^2\tau} \tag{G.13}$$

Finding the inverse transform

The solution of the problem in the ξ, τ coordinate system is found using the inverse Fourier transform of Eq. (G.13):

$$\varphi(\xi, \tau) = \mathcal{F}^{-1}\left[F(\omega)e^{-D\omega^2\tau}\right] \tag{G.14}$$

$$\varphi(\xi, \tau) = \mathcal{F}^{-1}[F(\omega)] * \mathcal{F}^{-1}\left[e^{-D\omega^2\tau}\right] \tag{G.15}$$

$$\varphi(\xi, \tau) = f(\xi) * \frac{1}{\sqrt{2D\tau}}e^{-\xi^2/(4D\tau)} \tag{G.16}$$

$$\varphi\left(\xi,\tau\right) = \frac{1}{2\sqrt{\pi D\tau}} \int_{-\infty}^{+\infty} f\left(\xi\right) e^{-(\xi-\beta)^2/(4D\tau)} d\beta \tag{G.17}$$

where $*$ indicates the convolution of two functions:

$$
\begin{aligned}
\left(f * g\right)\left(x\right) &= \frac{1}{\sqrt{2\pi}} \int_{-\infty}^{+\infty} f\left(x-\beta\right) g\left(\beta\right) d\beta \tag{G.18} \\
&= \frac{1}{\sqrt{2\pi}} \int_{-\infty}^{+\infty} f\left(\beta\right) g\left(x-\beta\right) d\beta \tag{G.19}
\end{aligned}
$$

Conversion to the initial coordinate system

The conversion of Eq. (G.17) to the x, t coordinate system is easily done, and the final solution of Eq. (G.1) is:

$$\varphi\left(x,t\right) = \frac{1}{2\sqrt{\pi Dt}} \int_{-\infty}^{+\infty} f\left(\beta\right) e^{-(x-ut-\beta)^2/(4Dt)} d\beta \tag{G.20}$$

G.2 Example

As an example, the following IVP will be solved:

$$
\begin{aligned}
PDE &\qquad \varphi_t = D\varphi_{xx} - u\varphi_x &\qquad -\infty < x < \infty &\qquad 0 < t < \infty \tag{G.21} \\
IC &\qquad \varphi\left(x,0\right) = C\left[1 - H\left(x\right)\right] &\qquad -\infty < x < \infty
\end{aligned}
$$

where $H\left(x\right)$ is the Heaviside function and C an arbitrary constant:

$$H\left(x\right) = \begin{cases} 0 & if \quad x < 0 \\ 1 & if \quad x \geq 0 \end{cases} \tag{G.22}$$

so that:

$$C\left[1 - H\left(x\right)\right] = \begin{cases} C & if \quad x < 0 \\ 0 & if \quad x \geq 0 \end{cases} \tag{G.23}$$

Going back to Eq. (G.17) and inserting the current IC, the solution in the ξ, τ space becomes:

$$
\begin{aligned}
\varphi\left(\xi,\tau\right) &= \frac{1}{2\sqrt{\pi D\tau}} \int_{-\infty}^{+\infty} C\left[1 - H\left(\beta\right)\right] e^{-(\xi-\beta)^2/(4D\tau)} d\beta \tag{G.24} \\
&= \frac{C}{2\sqrt{\pi D\tau}} \int_{-\infty}^{0} e^{-(\xi-\beta)^2/(4D\tau)} d\beta \tag{G.25}
\end{aligned}
$$

Let us define a new integration variable:

$$\psi = \frac{\xi - \beta}{2\sqrt{D\tau}} \tag{G.26}$$

$$d\psi = -\frac{1}{2\sqrt{D\tau}}d\beta \tag{G.27}$$

$$\psi|_{\beta=0} = \frac{\xi}{2\sqrt{D\tau}} \tag{G.28}$$

$$\psi|_{\beta\to-\infty} \to +\infty \tag{G.29}$$

The integral then becomes:

$$\varphi(\xi,\tau) = -\frac{C}{\sqrt{\pi}}\int_{+\infty}^{\frac{\xi}{2\sqrt{D\tau}}} e^{-\psi^2}d\psi \tag{G.30}$$

$$= \frac{C}{\sqrt{\pi}}\int_{\frac{\xi}{2\sqrt{D\tau}}}^{+\infty} e^{-\psi^2}d\psi \tag{G.31}$$

Remembering the definitions of the error function and of the complementary error function:

$$\mathrm{erf}(x) = \frac{2}{\sqrt{\pi}}\int_0^x e^{-y^2}dy \tag{G.32}$$

$$\mathrm{erfc}(x) = 1 - \mathrm{erf}(x) = \frac{2}{\sqrt{\pi}}\int_x^{+\infty} e^{-y^2}dy \tag{G.33}$$

the solution of the IVP in Eq. (G.21) can be written as:

$$\varphi(\xi,\tau) = \frac{C}{2}\mathrm{erfc}\left(\frac{\xi}{2\sqrt{D\tau}}\right) = \frac{C}{2}\left[1 - \mathrm{erf}\left(\frac{\xi}{2\sqrt{D\tau}}\right)\right] \tag{G.34}$$

and converted to the x, t coordinate system:

$$\varphi(x,t) = \frac{C}{2}\mathrm{erfc}\left(\frac{x-ut}{2\sqrt{Dt}}\right) = \frac{C}{2}\left[1 - \mathrm{erf}\left(\frac{x-ut}{2\sqrt{Dt}}\right)\right] \tag{G.35}$$

Moreover, remembering that:

$$\frac{d}{dx}\mathrm{erf}(x) = \frac{2}{\sqrt{\pi}}e^{-x^2} \tag{G.36}$$

and using the chain rule, the partial derivatives of Eq. (G.35) are:

$$\varphi_x = -\frac{C}{2\sqrt{\pi Dt}}e^{-\left(\frac{x-ut}{2\sqrt{Dt}}\right)^2} \tag{G.37}$$

$$\varphi_t = \frac{Cu}{2\sqrt{\pi Dt}}e^{-\left(\frac{x-ut}{2\sqrt{Dt}}\right)^2} \tag{G.38}$$

The current IVP represents a step-wave traveling with constant velocity u and diffusing with a constant diffusion coefficient D. If we want to know the above derivatives at the

moving center of the step, i.e. at $x = L$ and $t = L/u$, the result is:

$$\varphi_x|_{x=L} = -\frac{Cu^{1/2}}{2\sqrt{\pi D L}}$$

$$\varphi_t|_{t=L/u} = \frac{Cu^{3/2}}{2\sqrt{\pi D L}}$$

It is easy to see that if there is no diffusion, the step will stay sharp and therefore both derivatives will tend to ∞.

Appendix H

Shift of the unsteady boundary conditions in FLORIS simulations

Due to the experimental set-up of the FLORIS facility, the mass flow in each loop is measured well behind the vessel inlets, while the solute inlet concentration can be measured only at the outlet of the jet pumps. This fact has to be taken into account when imposing the mass flow and the solute concentration as boundary conditions in CFX or TRACE.

The mass flow is of little concern, since water can be modeled under the given experimental conditions as an incompressible fluid, and therefore the mass flow can be considered as changing instantaneously throughout the whole system. However, the solute concentration is paired with the mass flow and has to be imposed with the correct timing with respect to the mass flow boundary condition. Again, this is of little concern if the mass flow is constant (i.e. in the "symmetric", "asymmetric" and "plug recirculation" scenarios of Chap. 6), since a miscalculation of the timing simply leads to a shift of the solute injection in time, with no consequences on the solute concentration values to be injected at a certain time. On the other hand, if the mass flow is changing (as happens in the "pump start-up" and "pump coast-down" scenarios of Chap. 6), the timing is fundamental for obtaining correct results during the simulations. The main aim of this appendix is therefore to describe in detail the procedure used to synchronize in time the mass flow and the solute concentration to be used as boundary conditions in the transient simulations of the FLORIS tests.

The evolution of the mass flow $W(t)$ and of the solute concentration $C(t)$ are known from the experiments. The problem is to find, for each given time t^*, the "time-of-flight" t_f^* of the concentration from the inlet of the vessel in our simulation model to the physical measurement point in the facility. This time will be the time by which the solute concentration at time t^* has to be shifted in order to be synchronized with the mass flow used as boundary condition; in other words, to a certain mass flow $W(t^*)$ will correspond a solute concentration $C(t^* - t_f^*)$.

An interesting point is that t_f^* depends on t^* and therefore is changing with time, as long as the mass flow changes too (and this is the reason why it is not a concern to find t_f if the
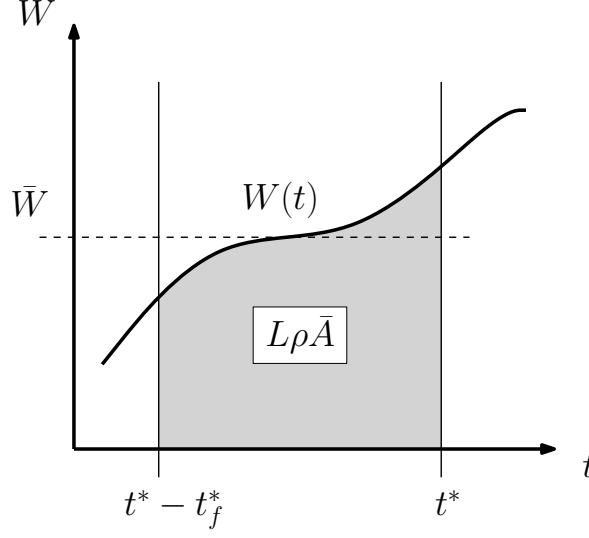
Figure H.1: Mass flow evolution in time and its integral.

mass flow is constant, because it will simply remain constant and one will just have a simple shift in time of the solute injection).

The "time-of-flight" can be defined as:

$$t_f^* = \frac{L}{\bar{v}\left(t^*, t_f^*\right)} \tag{H.1}$$

where L is the distance between the injection point and the concentration measurement point (which is fixed) and $\bar{v}(t^*, t_f^*)$ is the average velocity between the two points. Notice that $\bar{v}$ depends on both t^* and t_f^*, as explained below, and because of this dependence Eq. (H.1) is a nonlinear equation.

The average velocity can be derived from the mass flow as:

$$\bar{v}\left(t^*, t_f^*\right) = \frac{\bar{W}\left(t^*, t_f^*\right)}{\rho \bar{A}} \tag{H.2}$$

where $\bar{W}$ is the average mass flow, ρ is the density (constant in our case) and $\bar{A}$ is the average flow area between injection and measurement points (necessary since the jet pump cross-section area is not fixed; the value is nevertheless constant with time). As can be seen from Fig. H.1, the average mass flow can be calculated in the following way:

$$\bar{W}\left(t^*, t_f^*\right) = \frac{\int_{t^* - t_f^*}^{t^*} W\left(t\right) dt}{t^* - \left(t^* - t_f^*\right)} = \frac{I_W\left(t^*, t_f^*\right)}{t_f^*} \tag{H.3}$$

where I_W is the mass-flow definite integral that depends on its limits (this explains the reason

why the mass flow, and thus the velocity, depends on t^* and the "time-of-flight"). Putting Eqs. (H.1), (H.2) and (H.3) together, we obtain after some simple algebraic passages:

$$I_W\left(t^*, t_f^*\right) = L\rho\bar{A} \tag{H.4}$$

Eq. (H.4) can be solved easily with a numerical solver to obtain the t_f^* for each t^*, and thus the synchronized concentration $C\left(t - t_f\left(t\right)\right)$ to be used as boundary condition together with $W\left(t\right)$. Notice also that Eq. (H.4) means that the area under the mass-flow curve remains constant (because $L\rho\bar{A}$ is constant) for each pair of t^* and t_f^* values.

References

[1] World Nuclear Association, "WNA Website."

[2] Nuclear Engineering International, *NEI handbook 2010*, 2010.

[3] B. L. Cohen, *The nuclear energy option*. Plenum Press, 1990.

[4] IAEA, "50 years of nuclear energy," 2004.

[5] IAEA, "Nuclear technology review 2009," tech. rep., IAEA, 2009.

[6] OECD/NEA, "Nuclear energy outlook 2008," tech. rep., OECD/NEA, 2008.

[7] IEA, "World energy outlook 2008," tech. rep., IEA, 2008.

[8] Office of Nuclear Regulatory Research, *TRACE V5.0 Theory Manual - Field equations, solution methods and physical models*. U.S. Nuclear Regulatory Commission, 2008.

[9] U.S. Nuclear Regulatory Commission, "US-NRC Website."

[10] U.S. Energy Information Agency, "US-EIA Website."

[11] S. Kliem, T. Hoehne, U. Rohde, and F. P. Weiss, "Main steam line break analysis of a VVER-440 reactor using the coupled thermohydraulics system/3D-neutron kinetics code DYN3D/ATHLET in combination with the CFD code CFX-4," in *Proceedings NURETH-9*, Oct. 1999.

[12] S. Salah, C. E. Rossi, and J. M. Geets, "Consequences of asymmetric cold water addition to a PWR core from an inactive loop," in *ANS Transactions*, vol. 14, 1971.

[13] S. Salah, C. E. Rossi, and J. M. Geets, "Three-dimensional kinetic analysis of an asymmetric boron dilution in a PWR core," in *ANS Transactions*, vol. 15, 1972.

[14] D. Alvarez *et al.*, "Boron mixing transient in a PWR vessel: physical studies.," in *CSNI-OCDE Specialists Meeting on Boron Dilution Transients*, Oct. 1995.

[15] T. Burnett, "Westinghouse assessment of reactivity transients due to rapid boron dilution," in *CSNI-OCDE Specialists Meeting on Boron Dilution Transients*, Oct. 1995.

[16] L. Hyvarinen, "An inherent boron dilution mechanism in pressurized water reactors," tech. rep., Finnish Center for Radiation and Nuclear Safety, STUK, 1992.

[17] S. Jacobson, "Reactivity transients after pump start in a boron diluted loop," in *ANS Transactions*, vol. 61, 1990.

[18] J. G. Sun and W. T. Sha, "Analysis of boron dilution in a four-loop PWR," in *CSNI-OCDE Specialists Meeting on Boron Dilution Transients*, Oct. 1995.

[19] P. Gango, "Application of numerical modelling for studying boron mixing in Loviisa NPP," in *CSNI-OCDE Specialists Meeting on Boron Dilution Transients*, Oct. 1995.

[20] P. Gango, "Numerical boron mixing studies for Loviisa nuclear power plant," *Nuclear Engineering and Design*, vol. 177, pp. 239–254, 1997.

[21] R. J. Hertlein, K. Humminger, S. Kliem, H. M. Prasser, T. Hoehne, and F. P. Weiss, "Experimental and numerical investigation of boron dilution transients in pressurized water reactors," *Nuclear Technology*, vol. 141, pp. 88–107, 2003.

[22] F. Alavyoon, B. Hemstroem, N. G. Anderson, and R. I. Karlsson, "Experimental and computational approach to investigating rapid B-dilution transients," in *Proceedings of the CNSI Specialist Meeting on B-dilution Transients*, Oct. 1995.

[23] H. M. Prasser, G. Grunwald, T. Hoehne, S. Kliem, U. Rohde, and F. P. Weiss, "Coolant mixing in a pressurized water reactor: deboration transients, steam-line breaks, and emergency core cooling injection," *Nuclear Technology*, vol. 143, pp. 37–56, 2003.

[24] S. A. Logvinov, V. N. Ulyanovsky, Y. Bezrukov, and A. N. Kozlow, "Mixing of coolant with different boron concentration at the VVER-1000 core inlet during RCP start-up," in *Proceedings of Annual Meeting on Nuclear Technology 2000*, May 2000.

[25] K. T. Kiger and F. Gavelli, "Boron mixing in complex geometries: flow structure details," *Nuclear Engineering and Design*, vol. 208, pp. 67–85, 2001.

[26] C. Queral and I. González, "Analysis of heterogeneous boron dilution sequences," in *Proceedings of the International Conference Nuclear Energy for New Europe*, Sept. 2004.

[27] W. M. J. De Kruijf, "FLUENT and TRAC-PF1 analyses of boron dilution," in *CSNI-OCDE Specialists Meeting on Boron Dilution Transients*, Oct. 1995.

[28] S. Jacobson, *Risk evaluation of local dilution transients in PWRs*. PhD thesis, Linkoping University, 1992.

[29] J. H. Mahaffy, "Numerics of codes: stability, diffusion, and convergence," *Nuclear Engineering and Design*, vol. 145, pp. 131–145, 1993.

[30] R. Schultz, R. A. Riemke, and C. B. Davis, "Comparison: RELAP5-3D systems analysis code & FLUENT CFD code momentum equation formulations," in *Proceedings of ICONE11, 11th Int. Conf. on Nucl. Engineering*, Apr. 2003.

[31] R. Schultz and W. L. Weaver, "Using the RELAP5-3D advanced system analysis code with commercial and advanced CFD software," in *Proceedings of ICONE11, 11th Int. Conf. on Nucl. Engineering*, Apr. 2003.

[32] R. Schultz, W. L. Weaver, R. W. Johnson, D. G. Schonwalter, and N. Basu, "Evaluating fluid behaviour in advanced reactor systems," in *Proceedings of ICONE13, 13th Int. Conf. on Nucl. Engineering*, May 2005.

[33] D. L. Aumiller, E. T. Tomlinson, and R. C. Bauer, "A coupled RELAP5-3D/CFD methodology with a proof-of-principle calculation," *Nuclear Engineering and Design*, vol. 205, pp. 83–90, 2001.

[34] D. L. Aumiller, E. T. Tomlinson, and W. L. Weaver, "An integrated RELAP5-3D and multiphase CFD code system utilizing a semi-implicit coupling technique," *Nuclear Engineering and Design*, vol. 216, pp. 77–87, 2002.

[35] N. Anderson, Y. Hassan, and R. Schultz, "Analysis of the hot gas flow in the outlet plenum of the very high temperature reactor using coupled RELAP5-3D system code and a CFD code," *Nuclear Engineering and Design*, vol. 238, pp. 274–279, 2008.

[36] H. Gibeling and J. H. Mahaffy, "Benchmarking simulations with CFD to 1-D coupling," in *Joint IAEA/OECD Technical Meeting on Use of CFD Codes for Safety Analysis of Reactor Systems, Including Containment*, Nov. 2002.

[37] D. Weber *et al.*, "Extension of integrated neutronic and thermal-hydraulic analysis capabilities of the "numerical nuclear reactor" software system for BWR applications," in *Proceedings PHYSOR 2006*, 2006.

[38] J. C. Gauthier, "Very high temperature reactor: promising nuclear system, specific reactor physics," in *Proceedings of Physor-2004, ANS Top. Meetg. on Reactor Physics*, Apr. 2004.

[39] F. Cadinu, T. Kozlowski, and T. N. Dinh, "Relating system-to-CFD coupled code analyses to theoretical framework of a multiscale method," in *Proceedings ICAPP 2007*, May 2007.

[40] C. L. Waata and T. Frank, "Development of CFD software for the simulation of multidimensional flows in the nuclear reactor cooling system - coupling of ANSYS CFX with 1D system code ATHLET," Tech. Rep. ANSYS TR-08-02, ANSYS Germany, Mar. 2008.

[41] A. Papukchiev, G. Lerchl, C. Waata, and T. Frank, "Extension of the simulation capabilities of the 1D system code ATHLET by coupling with the 3D CFD software package ANSYS CFX," in *Proceedings NURETH-13*, Sept. 2009.

[42] U. Rohde, T. Hoehne, S. Kliem, M. Scheuerer, B. Hemstroem, T. Toppila, T. V. Dury, J. Klepac, J. Remis, P. Muehlbauer, L. Vyskocil, I. Farkas, A. Aszodi, I. Boros, and J.-A. Lycklama a. Nijeholt, "The European project FLOMIX-R: Fluid mixing and flow distribution in the reactor circuit - Final summary report," Tech. Rep. FZR-432 2005, Forschungszentrum Rossendorf, 2005.

[43] U. Rohde, S. Kliem, T. Hoehne, R. I. Karlsson, B. Hemstroem, J. Lillington, T. Toppila, J. Elter, and Y. Bezrukov, "Fluid mixing and flow distribution in the reactor circuit, measurement data base," *Nuclear Engineering and Design*, vol. 235, pp. 421–443, 2005.

[44] T. Mull, K. Humminger, A. Bucalossi, F. D'Auria, P. Monnier, I. Toth, and W. Schwarz, "Final report of the OECD-PKL project," Tech. Rep. NTCTP-G/2007/en/0009, OECD/NEA, 2007.

[45] J. Liebert and R. Emmerling, "UPTF experiment: flow phenomena during full-scale loop seal clearing of a PWR," *Nuclear Engineering and Design*, vol. 179, pp. 51–64, 1998.

[46] F. P. Weiss, H. Watzinger, and R. J. Hertlein, "UPTF experiment: a synopsis of full scale test results," *Nuclear Engineering and Design*, vol. 122, pp. 219–234, 1990.

[47] M. Gavrilas, B. Woods, G. Pertmer, and M. Antkowiak, "Rapid boron dilution transient investigations in a PWR integral test facility," in *Proceedings NURETH-9*, Oct. 1999.

[48] M. Zimmerman *et al.*, "STARS: Safety research in relation to transient analysis for the reactors in Switzerland," Research Report for HSK, Paul Scherrer Institute, 2007.

[49] P. Coddington, R. Macian-Juan, M. Zimmerman, and R. Chawla, "Development, assessment and application of RETRAN-3D for best estimate analysis of nuclear power plant transients," Tech. Rep. TM-41-02-07, Paul Scherrer Institute, May 2002.

[50] Laboratory of Reactor Physics and System Behavior, "STARS Website."

[51] R. Chawla, P. Coddington, F. Jatuff, R. Macian-Juan, M. Murphy, R. Seiler, and M. Zimmerman, "New LRS challenges for 2007-2011," Tech. Rep. AN-41-07-05, Paul Scherrer Institute, 2007.

[52] O. Zerkak, "A RETRAN-3D model applied to a postulated Main Steam-Line Break accident for KKB-I: benchmarking against the NLOOP code results," Tech. Rep. TM-41-05-17, Paul Scherrer Institute, Apr. 2006.

[53] T. V. Dury, B. Hemstroem, and S. V. Shepel, "CFD simulation of the Vattenfall 1/5th-scale PWR model for boron dilution studies," *Nuclear Engineering and Design*, vol. 238, pp. 577–589, 2008.

[54] M. Scheuerer *et al.*, "Evaluation of computational fluid dynamic methods for reactor safety analysis (ECORA)," *Nuclear Engineering and Design*, vol. 235, pp. 359–368, 2005.

[55] M. Andreani *et al.*, "A benchmark exercise on the use of CFD codes for containment issues using best practice guidelines: A computational challenge," *Nuclear Engineering and Design*, vol. 238, pp. 502–513, 2008.

[56] J. H. Mahaffy, "A stability-enhancing two-step method for fluid flow calculations," *Journal of Computational Physics*, vol. 46, pp. 329–341, June 1982.

[57] Office of Nuclear Regulatory Research, *TRACE V5.0 User's Manual - Volume 2: modeling guidelines*. U.S. Nuclear Regulatory Commission, 2008.

[58] ANSYS Inc., *ANSYS CFX Release 11.0 User Manual*, 2006.

[59] G. Yadigaroglu, "Computational fluid dynamics for nuclear applications: from CFD to multi-scale CMFD," *Nuclear Engineering and Design*, vol. 235, pp. 153–164, 2005.

[60] F. D'Auria *et al.*, "Neutronics/thermal-hydraulics coupling in LWR technology, Volume 2: State-of-the-art report," Tech. Rep. 5436, OECD/NEA, 2004.

[61] A. Geist, A. Beguelin, J. Dongarra, R. Manchek, W. Jiang, and V. Sunderam, *A users' guide and tutorial for networked parallel computing*, 1994.

[62] W. L. Weaver, "A mass and energy conserving form of explicit coupling for use with RELAP5-3D," in *2002 RELAP5 International Users Seminar*, Sept. 2002.

[63] W. L. Weaver, E. T. Tomlinson, and D. L. Aumiller, "A generic semi-implicit coupling methodology for use in RELAP5-3D," *Nuclear Engineering and Design*, vol. 211, pp. 13–26, 2002.

[64] ANSYS Inc., *ANSYS CFX Release 11.0 Solver Theory Guide*, 2006.

[65] H. M. Prasser, A. Bottger, and J. Zschau, "A new electrode-mesh tomography for gas-liquid flows," *Flow Measurement and Instrumentation*, vol. 9, pp. 111–119, 1998.

[66] H. M. Prasser, "Novel experimental measuring techniques required to provide data for CFD validation," *Nuclear Engineering and Design*, vol. 238, pp. 744–770, 2008.

[67] R. Zboray, A. Manera, B. Niceno, and H. M. Prasser, "Investigations on mixing phenomena in single-phase flows in a T-junction geometry," in *Proceedings NURETH-12*, Oct. 2007.

[68] B. P. Leonard, "A stable and accurate convective modelling procedure based on quadratic upstream interpolation," *Computer Methods in Applied Mechanics and Engineering*, vol. 19, pp. 59–98, 1979.

[69] B. P. Leonard, "Elliptic systems: finite-difference method IV," in *Handbook of numerical heat transfer*, John Wiley & Sons, Inc., 1988.

[70] B. P. Leonard, "The ULTIMATE conservative difference scheme applied to unsteady one-dimensional advection," *Computer Methods in Applied Mechanics and Engineering*, vol. 88, pp. 17–74, 1991.

[71] R. Macian-Juan, *A study of high order solute tracking in system codes*. PhD thesis, Pennsylvania State University, December 1996.

[72] R. Macian-Juan and J. H. Mahaffy, "Numerical diffusion and the tracking of solute fields in system codes, Part I: One-dimensional flows," *Nuclear Engineering and Design*, vol. 179, pp. 297–319, 1998.

[73] R. Macian-Juan and J. H. Mahaffy, "Numerical diffusion and the tracking of solute fields in system codes, Part II: Multi-dimensional flows," *Nuclear Engineering and Design*, vol. 179, pp. 321–344, 1998.

[74] R. Macian-Juan, K. Ivanov, and J. H. Mahaffy, "Numerical diffusion and the tracking of solute fields in system codes, Part III: Application to a boron dilution transient analysis in the AP600," *Nuclear Engineering and Design*, vol. 179, pp. 345–356, 1998.

[75] Office of Nuclear Regulatory Research, *TRACE V5.0 User's Manual - Volume 1: input specification*. U.S. Nuclear Regulatory Commission, 2008.

[76] T. Barth and M. Ohlberger, "Finite volume methods: foundation and analysis," in *Encyclopedia of Computational Mechanics*, John Wiley & Sons, Ltd., Feb. 2004.

[77] R. Courant, K. Friedrichs, and H. Lewy, "On the partial difference equations of mathematical physics," *Mathematische Annalen*, no. 100, pp. 32–74, 1928.

[78] O. Levenspiel and W. K. Smith, "Notes on the diffusion-type model for the longitudinal mixing of fluids in flow," *Chemical Engineering Science*, vol. 6, no. 4-5, pp. 227–233, 1957.

[79] C. N. J. Sittel, W. D. Threadgill, and K. B. J. Schnelle, "Longitudinal dispersion for turbulent flow in pipes," *Industrial & Engineering Chemistry Fundamentals*, vol. 7, pp. 39–43, Feb. 1968.

[80] W. Barten, A. Manera, and R. Macian-Juan, "One- and two-dimensional standing pressure waves and one-dimensional travelling pulses using the US-NRC nuclear systems analysis code," *Nuclear Engineering and Design*, vol. 238, pp. 2568–2582, 2008.

[81] S. J. Farlow, *Partial differential equations for scientists and engineers*. Dover, 1993.

[82] J. Freixa, F. Reventos, C. Pretel, and L. Batet, "Boron transport model with physical diffusion for RELAP5," *Nuclear Technology*, vol. 160, Nov. 2007.

[83] D. Bertolotto, A. Manera, S. Frey, H. M. Prasser, and R. Chawla, "Single-phase mixing studies by means of a directly coupled CFD/system-code tool," *Annals of Nuclear Energy*, vol. 36, pp. 310–316, April 2009.

[84] J. Freixa and A. Manera, "TRACE and RELAP5 thermal-hydraulic analysis on boron dilution tests at the PKL facility," in *Proceedings NURETH-13*, Sept. 2009.

[85] T. Mull, B. Schoen, and K. Umminger, "Final report of the PKL experimental program within the OECD/SETH project," Tech. Rep. FANP-NGTT1/04/en/04, Framatome ANP, 2004.

[86] T. Mull, B. Schoen, and K. Umminger, "Test PKL III F1.1: Inherent boron dilution during SB-LOCA," Tech. Rep. FANP-NGTT1/05/en/05, Framatome ANP, 2005.

[87] T. Mull, B. Schoen, and K. Umminger, "Test PKL III F1.2: Inherent boron dilution due to reflux-condenser conditions as a function of the primary coolant inventory (RCS pressure: 12 bar)," Tech. Rep. FANP-NTCTPG/07/en/05, Framatome ANP, 2007.

[88] W. M. Bissels, "FLORIS - Flow circulation in the lower plenum and riser," Master's thesis, TEKO Olten, 2008.

[89] S. Kliem, T. Suehnel, U. Rohde, T. Hoehne, H. M. Prasser, and F. P. Weiss, "Experiments at the mixing test facility ROCOM for benchmarking of CFD codes," *Nuclear Engineering and Design*, vol. 238, pp. 566–576, 2008.

[90] S. Kliem, H. M. Prasser, T. Suehnel, F. P. Weiss, and A. Hansen, "Experimental determination of the boron concentration distribution in the primary circuit of a PWR after a postulated cold leg small break loss-of-coolant-accident with cold leg safety injection," *Nuclear Engineering and Design*, vol. 238, pp. 1788–1801, 2008.

[91] Teletronic Rossendorf GmbH, *Wire-Mesh Sensor System WMS200 Manual*. Teletronic Rossendorf GmbH, 2010.

[92] CD-Adapco, *User guide STAR-CCM+ Version 4.06.011*, 2009.

[93] S. Kliem, U. Rohde, and F. P. Weiss, "Core response of a PWR to a slug of under-borated water," *Nuclear Engineering and Design*, vol. 230, pp. 121–132, 2004.

[94] U. Rohde, S. Kliem, B. Hemstroem, T. Toppila, and Y. Bezrukov, "The European project FLOMIX-R: Description of the slug mixing and buoyancy related experiments at the different test facilities - final report on WP2," Tech. Rep. FZR-430 2005, Forschungszentrum Rossendorf, 2005.

[95] D. Bertolotto, "Plots of the tracer concentration time-evolution for the FLORIS facility; comparison between experimental data and simulation results," PSI Memorandum SB-RND-ACT-002-07, Paul Scherrer Institute, 2011.

[96] M. Chandesris and G. Serre, "One dimensional averaged (k-epsilon) turbulence model applied to channel, pipe and rod bundle flows," in *Proceedings NURETH-11*, Oct. 2005.

[97] A. Chenu, *Single and two-phase flow modeling for coupled neutronics/thermal-hydraulics transient analysis of advanced sodium-cooled fast reactors*. PhD thesis, École Polytechnique Fédérale de Lausanne (EPFL), October 2011.

[98] K. Mikityuk, J. Krepel, S. Pelloni, P. Petkevich, and R. Chawla, "FAST code system: review of recent developments and near-future prospects," *Engineering for Gas Turbines and Power*, vol. 132, pp. 102915–1–7, 2010.

[99] K. Nikitin, J. Judd, M. Grandi, A. Manera, and H. Ferroukhi, "Peach Bottom 2 turbine trip simulation by TRACE/S3K coupled code," in *Proceedings PHYSOR 2010*, May 2010.

[100] D. A. Anderson *et al.*, *Computational Fluid Mechanics and Heat Transfer*. Computational and Physical Processes in Mechanics and Thermal Sciences, Taylor & Francis, 2nd ed., 1997.

[101] M. A. Leschziner, "Practical evaluation of three finite differences schemes for the computation of steady-state recirculating flows," *Computer Methods in Applied Mechanics and Engineering*, vol. 23, p. 293, 1980.

Acknowledgments

with administrative matters, to K. Hofer for his enlightening views on Swiss culture and society, and to my co-workers in the Ph.D. students' office, namely, A. Epiney, G. Girardin, P. Petchevich, A. Chenu and K. Sun.

I would also like to thank my entire family for the support they provided me through my entire life and especially during the doctorate years. In particular, I would like to acknowledge the contributions of my girlfriend Gemma and of my two parrots Rösti and Spätzli, who provided, respectively, the more than welcome necessary support and the (mostly) unwanted distractions during the last year of this long journey.

A final acknowledgment goes to all of my long-time friends and to all the people I have met during the last five years, whom I didn't directly mention here, but who have contributed in different ways to my life and hence to this thesis.

To everybody who made this work possible, a big thank you!

Curriculum Vitae

Davide Bertolotto

Personal information

Contact:	Zürcherstrasse 47		**Date of birth:**	October 13th, 1981
	5400, Baden, Switzerland		**Place of birth:**	Torino, Italy
	+41 (0)76 2130156		**Nationality:**	Italian
	davide.bertolotto@gmail.com			

Education

2007 - Present	*Ph.D. in Energy*	
	Thesis	Coupling a system code with computational fluid dynamics for the simulation of complex coolant reactivity effects
	Location	École Polytechnique Fédérale de Lausanne (EPFL), Lausanne, Switzerland & Paul Scherrer Institute (PSI), Villigen, Switzerland
2003 - 2005	*M.Sc. in Nuclear and Energy Engineering*	
	Thesis	Thermal-hydraulic test and analysis of the Advanced Stability Experiment at ENEA Frascati
	Location	Politecnico di Torino, Turin, Italy
2000 - 2003	*B.Sc. in Energy Engineering*	
	Thesis	Thermal-hydraulics and dryout in boiling water reactor fuel assemblies
	Location	Politecnico di Torino, Turin, Italy

Training

2008	*Frederic Joliot & Otto Hahn Summer School on "Physics, Fuels and Systems"*	
	Organiz.	Commissariat à l'Énergie Atomique et aux Énergies Alternatives (CEA), Cadarache, France & Karlsruhe Institute of Technology (KIT), Karlsruhe, Germany
2007	*Short Course on Modeling and Computation of Multiphase Flows*	
	Organiz.	Eidgenossische Technische Hochschule Zürich (ETHZ), Zurich, Switzerland
2006	*Basic Course on FLUENT*	
	Organiz.	ANSYS Italia S.r.l., Milan, Italy
2006	*Summer School on CFD: finite volumes, finite elements, compressible flows*	
	Organiz.	Unione Italiana Termofluidodinamica (UIT), Italy

Teaching experience

2007 - Present	*Laboratory assistant*	
	Task	Reactor experiments and radiation measurements (Physics Bachelor students, Nuclear Engineering Master students) at the CROCUS reactor
	Location	École Polytechnique Fédérale de Lausanne (EPFL), Lausanne, Switzerland

Professional experience

2006	*Research assistant*	
	Task	Research collaboration on low-temperature superconductor thermal-hydraulics
	Location	Politecnico di Torino, Turin, Italy
2005	*Trainee*	
	Task	Set-up of ASTEX (Advanced STability EXperiment), test of LHC (Large Hadron Collider, CERN) current leads
	Location	Research Center ENEA Frascati, Rome, Italy

Publications

Journal papers

D. Bertolotto, A. Manera, R. Macian, R. Chawla, *Improvement of the one-dimensional dissolved-solute convection equation using the QUICKEST-ULTIMATE algorithm*, Nuclear Engineering and Design 241 (245-256), 2011. http://dx.doi.org/10.1016/j.nucengdes.2010.10.021

D. Bertolotto, A. Manera, S. Frey, H.-M. Prasser, R. Chawla, *Single-phase mixing studies by means of a directly coupled CFD/system-code tool*, Annals of Nuclear Energy 36 (310–316), 2009. http://dx.doi.org/10.1016/j.anucene.2008.11.027

Conference papers

D. Bertolotto, A. Manera, R. Chawla, *Development and validation of a coupled CFD/system-code tool, ENEN Ph.D. Event*, International Congress on Advances in Nuclear Power Plants (ICAPP), Nice, FR, May 2-5 2011.

D. Bertolotto, V. Petrov, A. Manera, W. M. Bissels, H.-M. Prasser, R. Chawla, *Set-up of a Validation Strategy for the Coupled Code CFX/TRACE in the FLORIS Facility with the Aid of CFD Simulations*, International Congress on Advances in Nuclear Power Plants (ICAPP), San Diego, California, US, June 13-17 2010.

D. Bertolotto, A. Manera, R. Chawla, *CFD simulation of a single-phase mixing experiment*, ENEN Ph.D. Event, International Young Nuclear Congress (IYNC), Interlaken, CH, September 21-26 2008.

D. Bertolotto, A. Manera, S. Frey, H.-M. Prasser, R. Chawla, *Single-phase mixing studies by means of a directly coupled CFD/system-code tool*, International Conference on the Physics of Reactors (PHYSOR), Interlaken, CH, September 14-19, 2008.

L. Savoldi, **D. Bertolotto**, R. Zanino, *Analysis of helium buoyancy and stagnation risk in the ITER TF coils*, 21-th International Cryogenic Engineering Conference (ICEC21), Prague, CZ, July 17-21, 2006.

Awards

2009	*Best 3rd year presentation at NES Ph.D. Day*	
	Organiz.	Paul Scherrer Institute (PSI), Villigen, Switzerland
2008	*Conference paper selected for publication in the Annals of Nuclear Energy*	
	Organiz.	International Conference on the Physics of Reactors (PHYSOR), Interlaken, Switzerland